The Search for Supersymmetry in Complex Hadronic States Using the ATLAS Detector

Aaron Paul O'Neill

Christ Church
University of Oxford

A thesis submitted for the degree of
Doctor of Philosophy

Trinity 2021

Abstract

The standard model of particle physics is incomplete. A well motivated solution to several of its issues, including the absence of dark matter, is a theoretical extension called supersymmetry. Supersymmetric particles may be produced in the 13 TeV collisions recorded by the ATLAS experiment at the LHC. The presence of a dark matter candidate particle would be signified by the presence of missing transverse momentum, $E_{\mathrm{T}}^{\mathrm{miss}}$, in an event. A quantity designed to find very weakly interacting particles escaping the detector. This thesis first analyses the performance of $E_{\mathrm{T}}^{\mathrm{miss}}$ and its significance, $\mathcal{S}(E_{\mathrm{T}}^{\mathrm{miss}})$, with the complete ATLAS p–p Run 2 dataset with $\sqrt{\mathrm{s}} = 13$ TeV. A direct search for SUSY particles is then presented. This search is aiming to find new physics in events with large jet multiplicities, no leptons and a moderate amount of $E_{\mathrm{T}}^{\mathrm{miss}}$. The dominant background in this analysis comes from QCD multi-jet events that have very little real $E_{\mathrm{T}}^{\mathrm{miss}}$. Instead, the $E_{\mathrm{T}}^{\mathrm{miss}}$ will be from mismeasurement and resolution effects. The $E_{\mathrm{T}}^{\mathrm{miss}}$ significance is used to suppress contributions from these events in the signal regions. In addition a new jet definition is employed to improve the reconstruction of jets used in the analysis. No deviation from the standard model is observed. The results are used to calculate exclusion limits in terms of simplified models, the largest excluded mass for the gluino is 2 TeV assuming a massless lightest neutralino. This limit was found using a two step cascade decay of the gluino to SM particles and the lightest neutralino. The final section of the thesis is concerned with finding a method to discriminate between quark and gluon initiated jets in ATLAS. Many new physics searches seek signatures with only quarks in the final state and so gluons can be considered a background. The ability to discriminate between the two types of jets greatly improves the discovery power of these analyses.

The Search for Supersymmetry in Complex Hadronic States Using the ATLAS Detector

Aaron Paul O'Neill

Christ Church

University of Oxford

A thesis submitted for the degree of

Doctor of Philosophy

Trinity 2021

Abstract

The standard model of particle physics is incomplete. A well motivated solution to several of its issues, including the absence of dark matter, is a theoretical extension called supersymmetry. Supersymmetric particles may be produced in the 13 TeV collisions recorded by the ATLAS experiment at the LHC. The presence of a dark matter candidate particle would be signified by the presence of missing transverse momentum, $E_{\mathrm{T}}^{\mathrm{miss}}$, in an event. A quantity designed to find very weakly interacting particles escaping the detector. This thesis first analyses the performance of $E_{\mathrm{T}}^{\mathrm{miss}}$ and its significance, $\mathcal{S}(E_{\mathrm{T}}^{\mathrm{miss}})$, with the complete ATLAS p–p Run 2 dataset with $\sqrt{\mathrm{s}} = 13\,\mathrm{TeV}$. A direct search for SUSY particles is then presented. This search is aiming to find new physics in events with large jet multiplicities, no leptons and a moderate amount of $E_{\mathrm{T}}^{\mathrm{miss}}$. The dominant background in this analysis comes from QCD multi-jet events that have very little real $E_{\mathrm{T}}^{\mathrm{miss}}$. Instead, the $E_{\mathrm{T}}^{\mathrm{miss}}$ will be from mismeasurement and resolution effects. The $E_{\mathrm{T}}^{\mathrm{miss}}$ significance is used to suppress contributions from these events in the signal regions. In addition a new jet definition is employed to improve the reconstruction of jets used in the analysis. No deviation from the standard model is observed. The results are used to calculate exclusion limits in terms of simplified models, the largest excluded mass for the gluino is 2 TeV assuming a massless lightest neutralino. This limit was found using a two step cascade decay of the gluino to SM particles and the lightest neutralino. The final section of the thesis is concerned with finding a method to discriminate between quark and gluon initiated jets in ATLAS. Many new physics searches seek signatures with only quarks in the final state and so gluons can be considered a background. The ability to discriminate between the two types of jets greatly improves the discovery power of these analyses.

Declaration

This dissertation is the result of the author's own work, except in the few cases where explicit reference is made to the work of others, and has not been submitted for another qualification to this or any other university. This thesis does not exceed the page limit.

Aaron Paul O'Neill

Acknowledgements

Getting to this point was by no means a solo effort and I have had the fortune to live an exciting and varied life, and to meet many incredible people along the way. I will acknowledge some folks directly and my apologies that I cannot fit everyone in here (I would need another thesis or two to do that) but I would like everyone to know that all your interactions, advice and conversations have made me the man I am today. For that, I am eternally grateful.

I would like to begin with thanks to my teachers at Carrickfergus Grammar School, even though I was not the most ideal student they could have asked for. They should all know that I really did enjoy my time there and although I did not show it, they did plant the seeds for my love of mathematics and physics.

There are many reasons I decided to join the Royal Marines, some of them I myself cannot fathom; the long cold/wet/dry/terrifying/painful stretches were at best a test of my character. That said, I regret nothing and wouldn't change a moment of it. Thank you to every Royal I had the pleasure to serve with. All of the nights ashore, adventures and general mischief are something I will never forget. In particular thank you to Sergeant "Tell" Ansell for keeping me sane and safe during the tour in Afghanistan and my Uncle Kenneth Faloon for the "wear your side-armour" order at the start of the tour.

After studying A-Levels in my spare time in the Royal Marines I achieved the results necessary (*just*) to attend Queen's University Belfast. There I truly fell in love with the field of physics thanks to the amazing efforts of all the lecturers and staff in the physics department. Thanks in particular to Prof Mihalis Mathioudakis for offering me a summer internship on solar flares and during the course of which became a dear friend and mentor. Also to Dr Tom Field for all his help in my application to Oxford and to both Tom and Mihalis for their reference letters which, must have been amazingly flattering because I was accepted. Education included, the best thing that came out of QUB was meeting Robert Graham and Zak Morris, two of the most wonderful men I have ever encountered. There are far too many in-jokes and adventures to broach here not to mention the pool nights at the student union; “sure, we’ll just go for one”. Just know that the pair of you will always be in my heart and I look forward to the madness to come. I would like to thank Tanith Panayotou for all her support and encouragement that made my university days such a success.

This thesis was completed while studying at the University of Oxford and I can say that I had the absolute pleasure to be supervised by Prof Alan Barr, one of the most intelligent people on the face of this Earth. I cannot thank you enough for all your advice, teaching and supervision over the course of the DPhil. Not just in the art of being a particle physicist but in all aspects of life. I was able to transform from wide eyed fresher with imposter syndrome into a confident researcher and that, in very large part, is thanks to you Alan. Particle physics is a collaborative effort and on the Oxford side I would like to thank all the members of the SM+ group: Claire Gwenlan, Jon Burr, Jesse Liu, Mike Nelson, Gabriel Gallardo, Jonas Würzinger, Claudia Merlassino, Ynyr Harris, Ludovic Fraser-Taliente and Eimear Conroy. I would also like to thank the entire Oxford ATLAS group, it was a pleasure to be in the presence of such fine minds and in particular thank you Todd Huffman for all your help while I organised the Oxford ATLAS group meetings.

In Oxford my studies did not just include an exposure to physics but also thanks to Annahita Brooks for teaching me the ways of art and allowing me to help in the construction of her exhibition, my time in the art department was a welcome break during my spare time even if there were a few very late nights. Moving to Switzerland for my attachment to CERN was no easy trip and I am extremely grateful to the Brooks-Vogt family for making me feel instantly at home and welcoming me into theirs. Edyta, Frank, Annahita and Bella you were truly beyond hospitable and it really made my time in Switzerland, thank you for the wonderful trips all over the country and of course Freiburg, *Auf geht’s Freiburg schieß ein Tor.*

While at CERN I had the pleasure to meet the UK LTA gang and made many close friends including the “lunch bunch”. Friday beers in R1 were always one of the highlights of the week and the can’t miss social event in CERN. Particular thanks must go to Matous Vozak, my house mate and partner in crime. In the most amazing stroke of luck I was placed in a house with one of the most kind souls I have ever encountered and made a lifelong friend. Moving back to Oxford afforded me the opportunity to become reacquainted with my college, Christ Church, and all the amazing folks there. One of the highlights of this time were the beer brewing nights as part of the “Beyond Standard Malt” brewing company. Thank you to Eimear Conroy for all the craic and putting up with my, dreadful, attempt to learn

Irish. I was also very fortunate and landed on my feet with two amazing house mates in Oxford; Elizabeth Brown and Andrew Stevens. Football has been a large part of my life for many years and it was made all the more enjoyable by pub trips with Alan Riddles; “Norn Iron” fan and companion extraordinaire. During a considerable part of the DPhil I was kept sane with our weekly Dungeons and Dragons sessions crewed by a hardy band of rogues and scoundrels; Sam, Zak, Maty and adroitly dungeon mastered by the ruthless Robert Graham.

A quick return to some thanks to the physics groups in ATLAS, this work would not have been possible without the invaluable conversations, advice and seemingly endless patience with my questions. The Jet $E_{\mathrm{T}}^{\mathrm{miss}}$ group felt like a family from the very beginning, it is also the best Karaoke group in CERN. So many to thank but in particular: Chris Young, Chris Delitzsch, Steven Schramm, Max Swiatlowski and Holly Pacey. The multi-jets analysis team were all incredible and although we did not find SUSY I had a blast trying, thank you in particular to Marco Valente for all the amazing help and patience.

There is no way I could have achieved any of this without the love and support of my family and in this respect I am again blessed, much love to the Faloons and the O’Neills. Two of my closest friends definitely belong in the family section, many thanks to Joshua Dodge and Connor McIlroy for all the good times. Unfortunately my father could not be around for many of my achievements but he was always with me in spirit and dearly missed. Some of the biggest thanks go to my Granny Agnes, Mum Lana and Brother Josh. Thank you to my Granny for always supporting me in all my endeavours. Thanks Mum for all the encouragement and conversations you genuinely made me feel like a superhero and to my dearest brother Joshua “Jo” O’Neill, I am willing to bet that no brother has loved another in the way I do you, thank you for everything. You have all made this possible and I cannot thank you enough, it is truly and deeply appreciated.

Sláinte,

Aaron

Preface

Working in the ATLAS collaboration means that no publication is produced alone and the work I have been involved with is no exception. Below I have summarised a list of publications and my contributions therein as well as other work related to detector performance this also applies to the relevant chapters in the thesis.

- **Missing transverse momentum performance using the full run II pp data set at 13 TeV.** I was able to produce the first full Run 2 performance plots for $E_{\mathrm{T}}^{\mathrm{miss}}$ and its significance in ATLAS under the guidance of Maximilian Swiatlowski and Jeanette Lorenz `https://atlas.web.cern.ch/Atlas/GROUPS/PHYSICS/PLOTS/JETM-2019-03/`.

- **Missing Transverse Momentum Significance For Full Run 2 using 13 TeV pp data: LHCC poster.** Summarised the full Run 2 $E_{\mathrm{T}}^{\mathrm{miss}}$ results in the LHCPP poster session [1].

- **Search for new phenomena in final states with large jet multiplicities and missing transverse momentum using $\sqrt{s} = 13\,\mathrm{TeV}$ proton-proton collisions recorded by ATLAS in Run 2 of the LHC.** Search for physics beyond the standard model, in the form of supersymmetry (SUSY), in final states with many jets, no leptons and moderate amounts of $E_{\mathrm{T}}^{\mathrm{miss}}$. In this analysis I was heavily involved in the production of NTuples and propagating these through the entire analysis chain. I performed some quark-gluon discrimination studies as well as producing all the validation plots required by the SUSY group.

  This analysis was the first SUSY analysis to use particle-flow jets (PFlow), I also calculated the PFlow signal systematics, and so a comparison was made with the older ATLAS jet definition (EMTopo). I produced all of the EMTopo results and the comparison was finalised by another analysis team member.

  Finally I was responsible for the HEP data entry and another form of analysis preservation, RECAST. The latter required the production of several containers that operated at each stage of the analysis to allow new signal models to be reinterpreted in terms of the analysis [2]. This paper makes up the chapter *The Search for Supersymmetry in States with Many Hadronic Jets*.

- **40th International Conference on High Energy Physics - When Jets MET SUSY: ATLAS searches for squarks and gluinos.** These public slides aimed to highlight the impact improvements in detector performance have on the discovery power of new physic searches [3]. The presentation was also converted into a note to be included in the Proceedings of Science for the entire conference [4].

- **Missing Transverse Momentum Performance in Run 2.** I have been working on a complete publication to summarise the $E_{\mathrm{T}}^{\mathrm{miss}}$ performance over Run 2 along with the $E_{\mathrm{T}}^{\mathrm{miss}}$ + pile-up subgroup. This publication is currently in progress. This paper as well as the previous $E_{\mathrm{T}}^{\mathrm{miss}}$ based work forms the basis of the *Missing Transverse Momentum and Its Significance in the ATLAS Detector* chapter.

- **Search for R-parity-violating supersymmetric particles in multi-jet final states produced in proton-proton collisions at $\sqrt{s} = 13\,\mathrm{TeV}$ recorded by ATLAS in Run 2 of the LHC.** This is a new analysis that aims to find R-parity violating decays of gluinos to many jets in the ATLAS detector. I produced the R-parity violating signal grids with 6 jets that are used in the quark-gluon discrimination chapter.

In addition to this work that made it in to publications I was also heavily involved in the design and construction of the $E_{\mathrm{T}}^{\mathrm{miss}}$ software packages used to analyse the performance of the missing transverse momentum.

I was able to work on the problem of quark-gluon discrimination, a long standing and challenging problem in particle physics. This work has not made it to publication by the time of writing of this thesis and this is almost entirely my own work excepting where stated otherwise. I owe a great debt of gratitude to Ludovic Frazer-Taliente for his outstanding help in this effort as well as the extremely useful conversations and insight he brought to this work.

In this thesis any figure, plot or diagram that is not of my own making will be marked as such with a statement like "Figure taken from" followed by the relevant citation. Plots I have produced that have then been made public by ATLAS are marked with **ATLAS** or **ATLAS Preliminary**.

Contents

List of Figures

. . . every saint and sinner in the history of our species,
lived there on a mote of dust, suspended in a sunbeam.

— Carl Sagan -*Pale Blue Dot: A Vision of the Human Future in Space, 1997*

1
Introduction

We humans are an innately curious bunch, though not always to our benefit, it is a quality that in part *defines* us. This trait is in no way unique to our species but it is something that *Homo sapiens* excels at. From humble beginnings, the first early humans crafted simple tools, spear heads, in the Olduvai Gorge. The slow steady march of evolution would bring forth the modern human and the world was forever changed. A rapid increase in brain size and postnatal brain growth coupled with our ability to cover great distances initiated a planetary wide spread of, what is now, the most abundant primate species on the Earth. This spread is impressive enough on its face but what humans did along the way was unprecedented. People began to notice a connection with their environment and; the weather, the stars and seasons. Some of the earliest human carvings and drawings, the Lascaux cave drawings for example, are thought to represent constellations.

While at first these celestial objects were considered to be spirits and gods, thoughts soon turned to understand exactly what everything around us really *was*. This is where this journey begins and underpins the work contained in this thesis, at the smallest scales what is the universe made of? The idea of tiny indivisible pieces making up all things past and present is not a new one and in fact it existed in natural philosophy from the 6th century BC. The Jain leaders of ancient India conceived of a non-living universe of matter called "pudgala" consisting of an infinity of particles called "permanu" each occupying a space-point. Never ones to be left out, the ancient Greeks also had a say in the matter with Democritus theorising that everything was built from "atoms", the word arising from the ancient Greek for indivisible. The atoms of this period are in reality more closely related to molecules in modern day parlance.

A methodical approach to science is apparent in the early works of the mathematician Ibn al-Haytham, working in the Islamic Golden Age, where he conducted experiments in optics and expounded a particle theory of light. Following on from this Francis Bacon rebelled against the notion of answering scientific questions with deduction and instead called for proof by repeatable observation. The application of the experimental method initiated a cascade of discoveries including those of Galileo Galilei during the scientific Revolution. At the end of this period the very first subatomic particle was discovered by J.J. Thomson, and other physicists; the electron.

The field of particle physics, as it is known today, exploded into life with a series of ground-breaking and revolutionary discoveries in the experimental and theoretical realms. The discovery, and subsequent splitting, of the atom revealed a need to inject higher and higher energies into experiments to access smaller and smaller scales. The revelation that an entirely new kind of physics ruled at these minuscule sub-atomic lengths, Quantum physics, was, in a word, revolutionary. The predictions of quantum mechanics, and subsequently quantum field theory, required increasingly large, elaborate and powerful machines to probe. A group of European nations gathered together to form a laboratory dedicated to this very purpose which culminated in the discovery of the Higgs boson in 2012 [5][6], the final piece of the most complete theory of particle physics to date; the Standard Model.

A thoroughly deserved pat on the back for all involved since the Olduvai Gorge. Yet, physicists continue to work on our understanding of the universe as the Standard Model is not a complete theory and has some glaring omissions. This thesis focusses on experimental techniques that can be used to find the answers to these questions as well as a direct search for new physics that lies beyond the standard model and a method to differentiate between two fundamental particles.

An overview of the Standard Model of particle physics is presented in Chapter 2, which also goes on to present some of the issues with the SM and finally presents a proposed extension to the SM in the form of supersymmetry (SUSY). Chapter 3 summarises the Large Hadron Collider (LHC) and the ATLAS experiment, the apparatus used to collect the data analysed in this thesis.
The standard model contains some weakly interacting particles that may escape the detector without being detected, new physics models often predict a new invisible particle that would have a similar behaviour. Chapter 4 presents the performance of a technique that can infer the presence of such invisible particles and how confident one can be that this is a real invisible particle and not due to mismeasurement.
A search for physics beyond the standard model is presented in Chapter 5, SUSY predicts the possible production of very massive particles called gluinos at the LHC. These particles may then decay in long chains of hadronic particles as well as some invisible stable particles. Identifying the difference between fundamental quarks and the force carrier of the strong force, the gluon, would enhance measurements of the SM and increase the discovery power of many searches for new physics. A technique to address this is presented in Chapter 6. Finally, the entire thesis is summarised in Chapter 7.

The story so far: In the beginning the Universe was created. This has made a lot of people very angry and been widely regarded as a bad move.

— Douglas Adams - *The Restaurant at the End of the Universe, 1980*

2 Particle Physics Theory

Contents

2.1 Introduction

The primary concern of this thesis is experimental particle physics but in order to understand the predictions and why certain measurements are made it is necessary and enlightening to introduce the fundamental theory of particle physics. Physics is an almost miraculous science that makes possible things that were once thought to belong only in the realm of magic.

Attempting to understand the universe at its most basic level is something humans have done from the very birth of consciousness. This fundamental research has been the driving force behind industrial, economic and technological progress for our entire history. Although the immediate applications of such discoveries are not always apparent; without fail such knowledge contributes to the betterment of humanity in due course, even if that journey takes a few wrong turns. One needs only take a cursory glance around their immediate surroundings to see the impact of core particle physics research; no television without the discovery of the electron, no coin sized computer chips of tremendous power without quantum mechanics and no world wide web without CERN.

Figure 2.1: A steel sculpture by Gayle Hermick called "Wandering the Immeasurable" located outside the main Meyrin site at CERN. Image taken from [7].

All this made possible by thousands upon thousands of scientists of singular purpose equipped with a soul deep curiosity and the power of a keen mind. This journey is wonderfully captured in the sculpture "wandering the immeasurable", Figure 2.1, situated outside the main site of the European centre for nuclear research on the outskirts of Geneva, Switzerland.

This chapter illustrates the current state-of-the-art model that details our collective knowledge of the subatomic universe; known as the standard model (SM) of particle physics. The particle content of the model as well as their interactions are summarised alongside some phenomenological consequences of the theory. This picture is not quite complete and so the various issues that remain are discussed and a proposed solution to many of the current problems is covered last, in the form of supersymmetry (SUSY). Much of this chapter was written with the aid of many excellent and indispensable sources; the section on the standard model used References [8–18], the section on supersymmetry is based upon References [19–21].

2.2 The Standard Model of Particle Physics

The Standard Model (SM) of particle physics is one of, if the not *the*, most successful theories ever devised. It is a mathematical model that describes all the particles known to exist and the interactions between them.

The SM states that all *normal matter* in the universe is constructed of a remarkably small set of subatomic particles. These are split into two groups: the fermions, half-integer spin particles that make up matter (the *matter particles*) and integer spin force mediating particles known as *bosons*. The entire content of the standard model is succinctly drawn in Figure 2.2 [1]. It is striking to see everything we see around us in day to day life and in the universe at large described in such a small table, this table distils the pure essence of the SM and leaves out the mathematical beauty of this rather brilliant theory.

[1]Except the Graviton as this is the theoretically predicted mediator of gravitation and sits outside the SM.

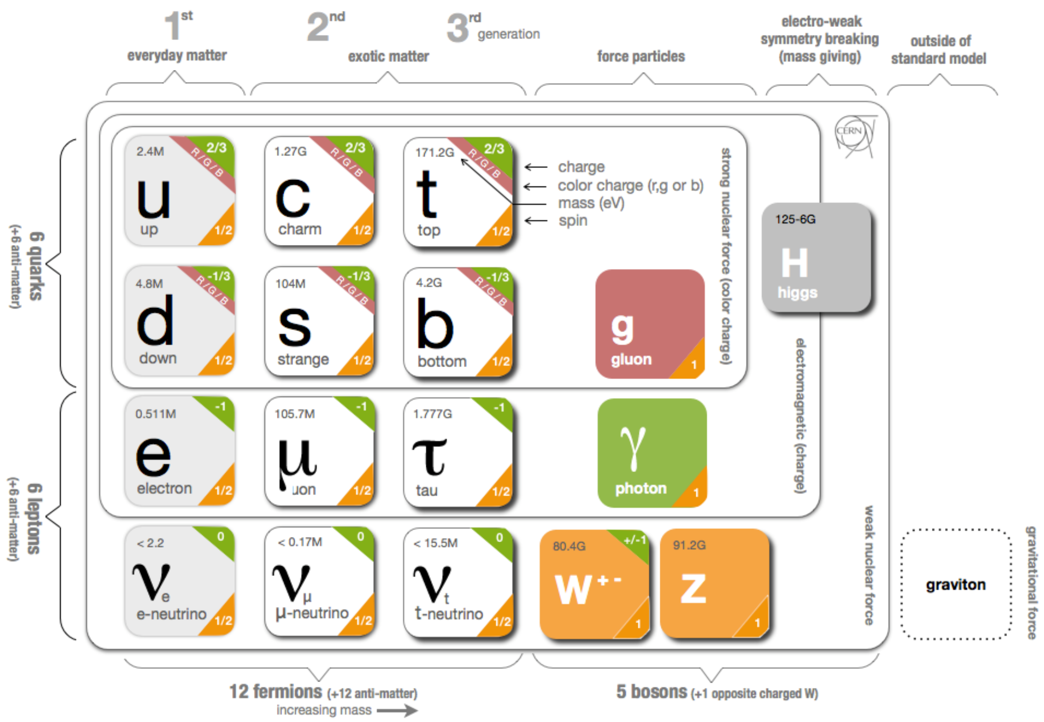

Figure 2.2: The particle content of the standard model of particle physics. Figure taken from [22].

The Standard Model is a Quantum Field Theory (QFT), a set of theoretical physics frameworks that allow quantum physics and special relativity to be combined. In QFT the most fundamental units are the quantum fields that pervade the entire universe and elementary particles are quantisations of those fields. The various fields are able to interact depending on certain qualities and so form the particles and waves that older theories were built upon. The elementary particles can be divided into four categories:

1. **Quarks**: These consist of 6 spin 1/2 fermionic particles and the same number of anti-particles. The complete quark sector can be subdivided into 3 generations each more massive than the last. The quark particles are known as: *up* (u), *down* (d), *charm* (c), *strange* (s), *top* (t) and *bottom* (b). Quarks interact with all force mediating fields in the standard model carrying; the electromagnetic and weak charges, and the strong charge (the only SM

fermions to do so). The quarks also interact with the Higgs field, all of these characteristics are detailed in Figure 2.2.

2. **Leptons**: These are also a set of 6 spin one-half fermions that all feel the weak force and have a set of 6 anti-matter partners. The first three leptons *electron* (e), *muon* (μ) and *tau* (τ) interact with the Higgs field and carry electromagnetic charge. These three again come in three generations of increasing mass, each generation is coupled with a corresponding neutrino. The neutrinos are a unique type of lepton as they only interact weakly and do not carry the any electronic charge.

3. **Bosons**: Particles that mediate the various forces by way of 5 spin-1 gauge bosons. The *gluon* (g) mediates the strong force responsible for binding quarks into baryons, the weak force is mediated by the $W^{\pm}$ and Z bosons and finally the electromagnetic force is transmitted by the *photon* (γ)

4. **Higgs Boson**: A scalar, or spin-zero, boson that provides particles with mass. In this regard it is unique as it only interacts with massive particles and not a gauge charge as is the case with the spin-one bosons. Through a mechanism known as *spontaneous symmetry breaking* (SSB) the Higgs boson provides mass to the weak bosons ($W^{\pm}$ and Z), the quarks and the leptons. This mechanism is discussed further in the Appendix, A.0.2.

With the exception of the top, quarks do not exist in isolation due to the nature of the strong force. Instead they form a family of composite particles called hadrons containing a certain number of valence quarks bound by gluons. The top quark is an exception to this rule as it decays faster than these composite states can form. Hadrons are subdivided into two primary families; baryons made of an odd number of quarks (typically three) and mesons which, consist of an even number of quarks (normally two). More exotic combinations of quarks have been found to exist like tetraquarks, a combination of four quarks, discovered by the Belle collaboration [23] and a composite state of five quarks called a pentaquark was more recently discovered by the LHCb collaboration [24].

Almost all *free* hadrons are unstable and decay to another state. Examples of baryons are the proton and neutron, the proton is believed to be the exception to the unstable nature of hadrons as it is stable or has an exceptionally long lifetime ($> \mathcal{O}(10^{29})$ years [11]) while a free neutron will decay with a mean lifetime of $\tau_{\mathrm{n}} = 879.4 \pm 0.6$ seconds [11]. Examples of mesons are objects like the pions ($\pi^{\pm}$ and π^{0}), combinations of up and down type quarks, mesons are unstable.

Interestingly, hadrons also contain a constant flux of quark and anti-quark pairs, along side the valence quarks, produced in gluon splittings and annihilating within the hadron to gluons. This behaviour forms a *quark sea* of virtual quarks that are normally contained within the hadron but under particular circumstances may hadronise outside of the composite state, in a high energy collision for example.

More rigorously the SM is built from three symmetry groups combining to form:

$$SU(3)_C \otimes SU(2)_L \otimes U(1)_Y. \tag{2.1}$$

This group describes the strong, weak and electromagnetic interactions and these are mediated by a set of gauge fields. The strong interaction, or *Quantum Chromodynamics* (QCD), is described by the $SU(3)_C$ group. At energies above 246 GeV the electroweak interactions remain unified as $SU(2)_L \otimes U(1)_Y$, below this limit it breaks down into the weak interaction and electromagnetism (*Quantum Electrodynamics*, QED).

To describe the interactions and behaviours of these fields one can employ the Lagrangian, an equation that describes the dynamics of a system. In classical mechanics a system will follow the principle of least action, where the action is the time integral of the Lagrangian,

$$\mathcal{S} = \int_{t_1}^{t_2} L dt \tag{2.2}$$

In classical mechanics this formulation will find $\mathcal{S}$ for a particular path in a system and the path followed will be the one with the smallest value of $\mathcal{S}$. In reality the requirement is that the path be an extremum. For quantum field theory the picture is a bit different and one must consider all paths possible as they all contribute. The evolution of a system between two times is then described as a probability amplitude that is proportional to the sum over all paths between the two space-time points. The contribution of a particular path has a phase (or weight) proportional to the action $e^{\frac{i\mathcal{S}}{\hbar}}$ [15].

2.2.1 Scattering and Cross Section Measurements

Before discussing the complete standard model it is useful to set an objective in terms of physical measurements. The LHC and in particular the ATLAS experiment (Chapter 3) has an amazing capability to make precision measurements of cross-sections, σ, and event rates for a great many final states and across a broad range of momenta. In order to make the connection between experimental observations and the underlying theory one can make use of the basic principal of scattering physics [13],

$$\sigma = \frac{1}{I} \int |\langle f|\mathcal{M}|i\rangle|^2 d\Pi_f. \tag{2.3}$$

Here, the initial state of the protons is given by $|i\rangle$ with some flux I. The final states of the particles, $|f\rangle$, reside in a differential Lorentz-invariant phase space denoted by $d\Pi_f$. The final component is the particle scattering matrix $\mathcal{M}$, which allows the probability for a process of the form $P\left(|i\rangle \rightarrow |f\rangle\right)$ to be calculated using the quantum amplitude $\langle f|\mathcal{M}|i\rangle$.

The scattering matrix $\mathcal{M}$ is related to the path integral that was just discussed in the previous section. The path integral is performed over the set of field configurations

$$\langle f|\mathcal{M}|i\rangle \sim \int \mathcal{D}x e^{i\mathcal{S}}, \tag{2.4}$$

in natural units. In this format the term $\mathcal{D}x$ represents the integration over all paths. Again the action, $\mathcal{S}$, is a key component of this calculation and so the remainder of the chapter will be concerned with the theoretical construction of the Lagrangian density that in turn allows for the computation of the action by the relation shown in Equation 2.2 and hence the cross-section for any process of interest.

2.2.2 Gauge Symmetries

As we have seen the Standard Model is readily expressed in terms of symmetries but what is meant by a "symmetry" exactly? In the SM a symmetry exists if a transformation is applied and the predictions of the theory do not change. According to Noether's theorem [25][26] any continuous symmetry of the Lagrangian will generate a conservation law. This simple statement immediately highlights the importance of symmetries. For example, invariance under transformations of the Poincaré group (symmetry of special relativity); translations, rotations and Lorentz boosts generate the conservation of momentum, angular momentum and the centre of mass position.

One of the most important symmetries in the Standard Model are the gauge symmetries and these can be readily demonstrated using the Dirac Lagrangian for a free fermion with spinor, ψ:

$$\mathcal{L}_0 = \bar{\psi}\left(i\partial\!\!\!/ - m\right)\psi. \tag{2.5}$$

The transformation under a global $U(1)$ symmetry is,

$$\psi \xrightarrow{\mathrm{U(1)}} e^{iq\Lambda}\psi, \tag{2.6}$$

where $\Lambda \in \mathbb{R}$ (a constant, *global* symmetry). This shows that the Lagrangian is invariant under such a transformation. If this symmetry is now forced to be *local* by making the parameter Λ dependent on space-time coordinates, $\Lambda(x^\mu)$, the invariance is broken by the derivative by $\partial\!\!\!/\psi \xrightarrow{\mathrm{U(1)}} e^{iq\Lambda}(\partial\!\!\!/ + iq\partial\!\!\!/\Lambda)\psi$. To regain our footing and retain invariance one must alter the derivative to be *gauge covariant*:

$$D_\mu = \partial_\mu - iqA_\mu \tag{2.7}$$

and now there is a vector field that transforms as $A_\mu \xrightarrow{\mathrm{U(1)}} A_\mu + \partial_\mu\Lambda$. Local $U(1)$ invariance is now preserved and there is an interaction term in the Lagrangian that represents the interaction between the Dirac fermion with charge q and the electromagnetic field four-vector potential, A_μ. Now there is interaction between the fermions through a photon field but to be a propagating field one needs to add a gauge-invariant kinematic term:

$$\mathcal{L}_K = -\frac{1}{4}F_{\mu\nu}(x)F^{\mu\nu}(x) \tag{2.8}$$

where $F_{\mu\nu} \equiv \partial_\mu A_\nu - \partial_\nu A_\mu$ represents the strength of the electromagnetic interaction. It is worth noting that there is a possible mass term for the gauge field, $\mathcal{L}_m = \frac{1}{2}m^2 A^\mu A_\mu$, but this violates symmetry and so the photon is predicted to be massless ($m_\gamma < 1 \times 10^{-18}$ eV [11]). Similar arguments can be applied to the other symmetry groups and these local group symmetries are usually known as *gauge symmetries*.

2.2.3 The Standard Model Lagrangian

The standard model Lagrangian can be written in remarkably succinct form as is wonderfully summarised in [14], the formulation is as follows:

$$\mathcal{L} = \underbrace{-\frac{1}{4}\mathbb{F}_{\mu\nu}\mathbb{F}^{\mu\nu}}_{\substack{\text{Guage Bosons}\\ \text{(Force Carriers)}}} + \underbrace{i\bar{\psi}D\!\!\!\!/\psi}_{\substack{\text{Interaction}\\ \text{between}\\ \text{matter}\\ \text{particles}}} + \underbrace{\psi_i y_{ij}\psi_j\phi + h.c.}_{\substack{\text{Mass of}\\ \text{the fermions}}} + \underbrace{|D_\mu\phi|^2}_{\substack{\text{Guage boson}\\ \text{masses}}} \underbrace{-V(\phi)}_{\substack{\text{Higgs self-}\\ \text{interactions}}} \tag{2.9}$$

In brief summary each of these components can be outlined as:

1. $-\frac{1}{4}\mathbb{F}_{\mu\nu}\mathbb{F}^{\mu\nu}$: Is the term that governs the gauge fields, which are adjoint representations of the gauge groups. This is a Yang-Mills theory which is a gauge theory based on reductive Lie algebra. Importantly the field strength

can be found using the commutator of the covariant derviatives and this is described in Section 2.2.4.

2. $i\bar{\psi}\not{D}\psi$: Is a kinetic term for quarks and leptons that also encodes their interactions with the gauge fields. This term acts on Weyl fields ψ and $\not{D}$ is equivalent to $\gamma^\mu D_\mu$ in Feynman slash notation.

3. $\psi_i y_{ij} \psi_j \phi + h.c.$: This determines the coupling of the fermion fields to the Higgs field and as such generates mass for them, Hermitian conjugate (*h.c.*) is the same but for anti-matter particles. The unitary matrix y_{ij} sets the fermion masses as well as their flavour mixing angles, in the quark sector it is known as the *quark mixing matrix* or the Cabibbo-Kabayahi-Masakawa matrix, CKM [11] for short. Finally the complex scalar ϕ is the Higgs field, see below.

4. $|D_\mu \phi|^2 - V(\phi)$: These terms are marked separately in Equation 2.9 but really can be thought of as two components of the Higgs sector. The first term $|D_\mu \phi|^2$ is another kinetic term and this is also the mechanism by which the weak bosons gain mass through symmetry breaking. The second component, $-V(\phi)$, is the Higgs potential that sets the scale of electroweak symmetry breaking and the Higgs self-interaction.

2.2.4 The Gauge Sector

One can investigate these terms in slightly more detail to gain a phenomenological understanding of the theory as a whole. In an expanded form of the first term in Equation 2.9 one can look more directly at the self interacting component of the gauge boson fields [10]:

$$\mathcal{L}_{Gauge} = -\frac{1}{4}\mathbb{B}_{\mu\nu}\mathbb{B}^{\mu\nu} - \frac{1}{4}\mathbb{W}^i_{\mu\nu}\mathbb{W}^{\mu\nu}_i - \frac{1}{4}\mathbb{G}^{\mu\nu}_a\mathbb{G}^a_{\mu\nu} \tag{2.10}$$

where repeated indices are always summed. The field strength tensors represent each symmetry group and can be summarised as follows. The $U(1)_Y$ interactions are represented by the $\mathbb{B}$ tensor and have a very similar form to the electromagnetic term discussed in Section 2.2.2,

$$\mathbb{B}_{\mu\nu} = \partial_\mu B_\nu - \partial_\nu B_\mu. \tag{2.11}$$

The tensor $\mathbb{W}$ handles the $SU(2)_L$ group interactions,

$$\mathbb{W}^i_{\mu\nu} = \partial_\mu W^i_\nu - \partial_\nu W^i_\mu + g\epsilon^{ijk} W^j_\mu W^k_\nu, \tag{2.12}$$

where i, j and k run from $1 \rightarrow 3$ and represent the three components of the gauge field. g is the weak interaction coupling strength. Finally the non-abelian theory of $SU(3)_C$ has a field strength tensor represented by:

$$\mathbb{G}^{\mu\nu}_a = \partial^\mu G^\nu_a - \partial^\nu G^\mu_a + g_s f^{abc} G^\mu_b G^\nu_c. \tag{2.13}$$

In a similar fashion to $SU(2)_L$ there is a strong interaction coupling strength, g_s, and a set of anti-symmetric structure constants for $SU(3)_C$ contained in f^{abc}. In the case of the strong interactions the indices a, b and c run in integer steps from 1 to 8. In both the $SU(2)_L$ and $SU(3)_C$ groups there are structure constants of ϵ^{ijk} and f^{abc} respectively. These are obtained from the commutation relations and the generators of the symmetry, in general the generators of a $SU(N)$ group satisfy the commutation relation,

$$\frac{1}{2}\left[t^A, t^B\right] = i f^{ABC} t^C, \tag{2.14}$$

where f^{ABC} represents the structure constants of the $SU(N)$ group.

The second term of Equation 2.9 contains the fermionic fields and how they interact with one another via the bosons. These matter fields are summarised in Table 2.1 but in brief these are L_i, ℓ_{R_i}, Q_i, u_{R_i} and d_{R_i} where the index i runs over the three generations. Using this notation one can expand on the second term of Equation 2.9 to give the fermion-gauge-interaction (FGI) Lagrangian density:

$$\mathcal{L}_{FGI} = i\bar{L}_i \not{D} L_i + i\bar{\ell}_{R_i} \not{D} \ell_{R_i} + i\bar{Q}_i \not{D} Q_i + i\bar{u}_{R_i} \not{D} u_{R_i} + i\bar{d}_{R_i} \not{D} d_{R_i}. \tag{2.15}$$

Under the $SU(2)_L$ symmetry the left-handed leptons combine into the L_i doublets and the left-handed quarks form the Q_i doublets. The right-handed quarks and leptons, excluding the neutrinos, are singlets under $SU(2)_L$.

	Generation (i)			Electrical Charge	Weak Isospin	Weak Hypercharge
	1	2	3	Q	T_3	Y_W
L_i	$\begin{pmatrix} e_L \\ \nu_e \end{pmatrix}$	$\begin{pmatrix} \mu_L \\ \nu_\mu \end{pmatrix}$	$\begin{pmatrix} \tau_L \\ \nu_\tau \end{pmatrix}$	$\begin{pmatrix} -1 \\ 0 \end{pmatrix}$	$\begin{pmatrix} -\frac{1}{2} \\ \frac{1}{2} \end{pmatrix}$	$\begin{pmatrix} -1 \\ -1 \end{pmatrix}$
ℓ_{R_i}	e_R	μ_R	τ_R	-1	0	-2
Q_i	$\begin{pmatrix} u \\ d \end{pmatrix}$	$\begin{pmatrix} c \\ s \end{pmatrix}$	$\begin{pmatrix} t \\ b \end{pmatrix}$	$\begin{pmatrix} \frac{2}{3} \\ -\frac{1}{3} \end{pmatrix}$	$\begin{pmatrix} \frac{1}{2} \\ -\frac{1}{2} \end{pmatrix}$	$\begin{pmatrix} \frac{1}{3} \\ \frac{1}{3} \end{pmatrix}$
u_{R_i}	u_R	c_R	t_R	$\frac{2}{3}$	0	$\frac{4}{3}$
d_{R_i}	d_R	s_R	b_R	$-\frac{1}{3}$	0	$-\frac{2}{3}$

Table 2.1: The fermion content of the standard model in terms of chiral fields with the electroweak charges associated with the $SU(2)_L \otimes U(1)_Y$ symmetry. Right-handed neutrinos are omitted from this table as they will carry none of these charges, and hence not interact, if they exist.

The interactions of the gauge bosons and the fermions are encoded in the *covariant derivative*:

$$D_\mu = \partial_\mu - \frac{1}{2} i g' Y B_\mu - i g T_3 \sigma^i W^i_\mu - \frac{1}{2} i g_s S \lambda^a G^a_\mu \tag{2.16}$$

where the Y_W weak hypercharge is the generator of the $U(1)_Y$ group and T_3 is the third component of the weak isospin that is $\pm\frac{1}{2}$ for left-handed fermions while it is zero for right-handed fermions. The electric charge is related to the weak hypercharge and weak isospin by

$$Q = T_3 + \frac{1}{2} Y_W. \tag{2.17}$$

Equation 2.16 also contains a set of generators. The first set are the generators of the $SU(2)_L$ group, $\frac{1}{2}\sigma^i$, where σ^i are known as the *Pauli matrices*:

$$\sigma_1 = \begin{pmatrix} 0 & 1 \\ 1 & 0 \end{pmatrix}, \quad \sigma_2 = \begin{pmatrix} 0 & -i \\ i & 0 \end{pmatrix}, \quad \sigma_3 = \begin{pmatrix} 1 & 0 \\ 0 & -1 \end{pmatrix}. \tag{2.18}$$

The final set of generators are for the $SU(3)_C$ group, $\frac{1}{2}\lambda^a$, where λ^a are the Gell-Mann matrices.

Another important component of Equation 2.16 are the three sets of coupling constants; g_s, g and g' for the $SU(3)_C$, $SU(2)_L$ and $U(1)_Y$ groups respectively. Finally, to ensure that the correct fields act on the appropriate particles certain terms can be set to zero for specific particles using T_3 and S. The weak term only acts on left-handed fermions and so T_3 is zero for right-handed particles. So that the strong field only acts on quarks, S is 1 for quarks and 0 for leptons.

This derivative must be invariant under $SU(3)_C \otimes SU(2)_L \otimes U(1)_Y$ symmetry transformations. The fermion and boson transformations are summarised in Table 2.2.

Symmetry	Fermion	Boson
$U(1)_Y$	$\psi \rightarrow \exp\left[i\Lambda_Y(x)Y\right]\psi$	$B_\mu \rightarrow B_\mu + \frac{1}{g'}\partial_\mu\Lambda_Y(x)$
$SU(2)_L$	$\psi \rightarrow \exp\left[i\Lambda_L^i(x)\sigma^i\right]\psi$	$W_\mu^i \rightarrow W_\mu^i + \frac{1}{g}\partial_\mu\Lambda_L^i(x) + \epsilon^{ijk}W_\mu^j\Lambda_L^k(x)$
$SU(3)_C$	$\psi \rightarrow \exp\left[i\Lambda_C^a(x)\lambda^a\right]\psi$	$G_\mu^a \rightarrow G_\mu^a + \frac{1}{g_s}\partial_\mu\Lambda_C^a(x) + f^{abc}G_\mu^b\Lambda_C^c(x)$

Table 2.2: A summary of the symmetry groups and the transformations of the fermions and bosons under each group.

2.2.5 Electroweak Sector

Considering only the electroweak interactions the EW Lagrangian can be written as:

$$\begin{aligned}\mathcal{L}_{EW} = &-\frac{1}{4}\mathbb{B}_{\mu\nu}\mathbb{B}^{\mu\nu} - \frac{1}{4}\mathbb{W}^i_{\mu\nu}\mathbb{W}_i^{\mu\nu} \\ &+ i\bar{L}_i \not{D} L_i + i\bar{\ell}_{R_i}\not{D}\ell_{R_i} + i\bar{Q}_i\not{D}Q_i + i\bar{u}_{R_i}\not{D}u_{R_i} + i\bar{d}_{R_i}\not{D}d_{R_i},\end{aligned} \tag{2.19}$$

removing the strong force interaction term from the covariant derivative in Equation 2.16 to leave only the EW terms.

For a more complete summary of the neutral and charged currents of the electroweak sector, the Higgs mechanism, QCD and a discussion on renormalisation see Appendix A.

2.2.6 Cross Sections at the LHC

At the LHC the main aim is to measure cross sections of processes as summarised in Equation 2.3, these measurements over the LHC data taking runs are summarised in Figure 2.3. The standard model predictions agree phenomenally well with experimental results, however, there are a few issues that remain.

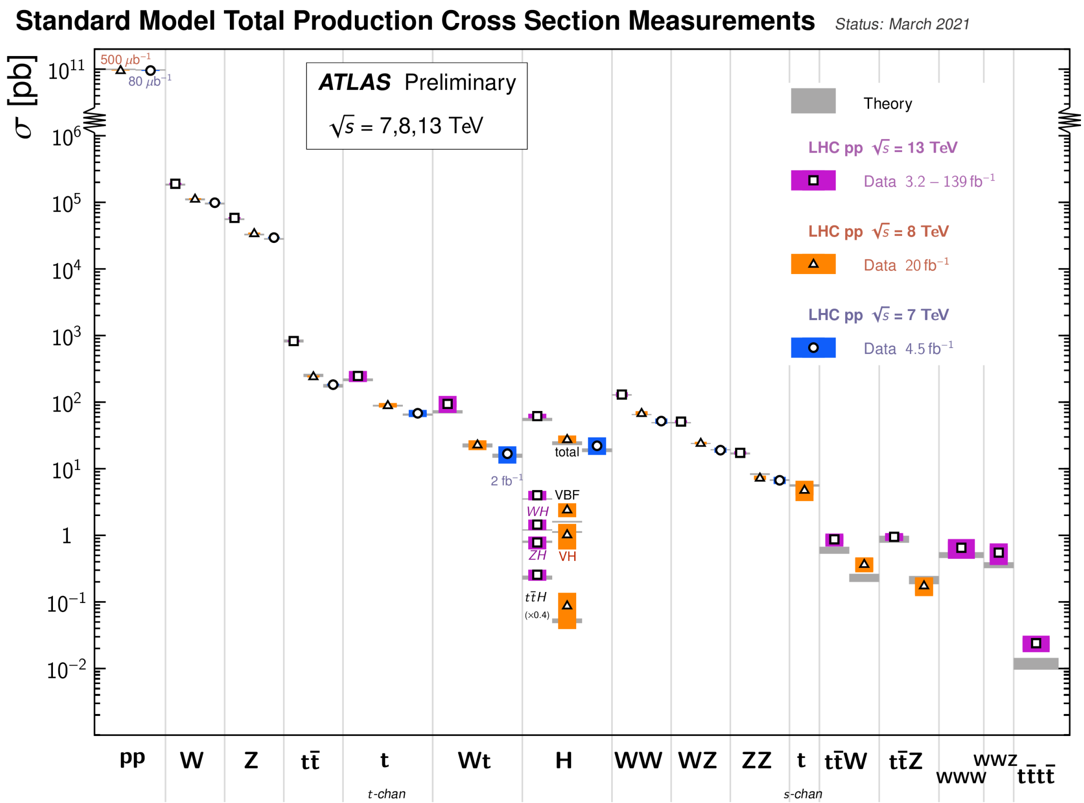

Figure 2.3: Summary of the total fiducial cross sections measured by the ATLAS experiment for various SM processes during operations of the LHC compared to simulation. In this case the term fiducial simply translates to 'within detector acceptance'. Figure taken from [27].

2.3 Problems With the Standard Model: Not *Quite* the Whole Story

While the standard model has been a stunningly successful theory there are a few omissions and issues. One of the main issues in the SM is that there are no gravitational interactions included. This is not an obstacle for the predictions of the model at energies currently achievable experimentally. Although gravitation is a powerful force from the perspective of day to day human life, at the quantum scale it is extremely weak and only becomes relevant at energies approaching the Planck scale, $\mathcal{O}(10^{19}\,\mathrm{GeV})$. While the problem is not severe in this context the theory cannot be complete until the formulation of quantum gravity is included in the standard model. Summarised briefly below are some of the other challenges facing the standard model of particle physics.

Dark Matter

The phenomenon known as *dark matter* is not covered by the standard model. Only about 4% of the universe is made up of the "ordinary" matter described by the SM. The rest is predicted theoretically to be composed of dark matter (22%) and *dark energy* (74%). Dark matter theory explains some of the anomalous measurements of galactic rotation curves as well as some unexplained gravitational lensing effects [28][29]. Observations constrain some of the properties of dark matter. If it is a particle it needs to be more massive than the weakly interacting SM particles (the neutrinos) so that it is non-relativistic and able to form the large scale structures responsible for observed galactic structures. Such a massive particle would also have to interact with the gravitational force and possibly through the weak interaction. As it is "dark" such a field would have to be decoupled from the photon otherwise it would be luminous and easily observed and nor would it couple to the strong force. Theories for dark matter particles tend to postulate a single weakly interacting massive particle (WIMP) or a suite of particles, like a dark sector SM, to explain the observations.

The Hierarchy Problem

In Appendix A.0.2 the Higgs mechanism is discussed and it is noted that the mass of the Higgs depended on the potential term and the vacuum expectation value (VEV) but this is really a free parameter in the SM. In reality the mass of the Higgs also depends on the radiative loop corrections described by:

$$m_H^2 = m_{H,0}^2 + \delta m_{H'}^2. \tag{2.20}$$

The $\delta m_{H'}$ correction term in this relation is very sensitive to new physics which is expected to be between the electroweak scale and the Planck scale. The mass of the Higgs boson has been measured to be 125 GeV [5][6] and so this indicates that there is a precise cancellation between $m_{H,0}$ and $\delta m_{H'}$, is known as the *fine tuning problem*.

Unification of the Forces

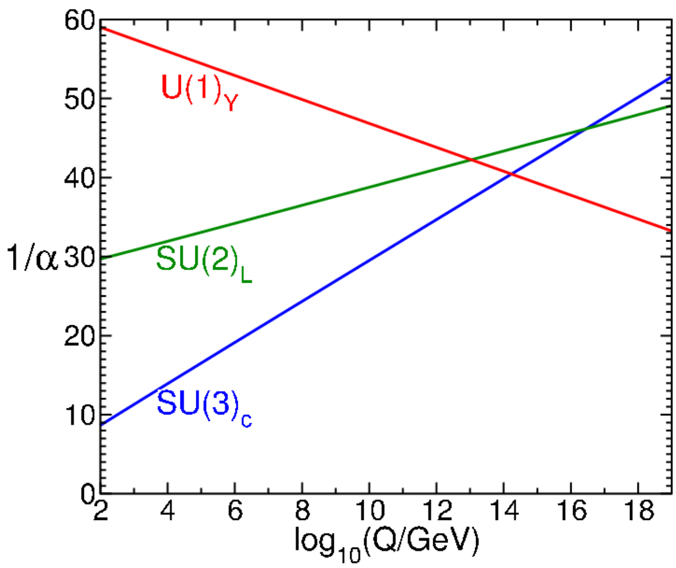

Figure 2.4: The coupling strengths for the various symmetry group components of the standard model of particle physics. Figure taken from [30].

The standard model is based on a set of gauge symmetry groups, $SU(3)_C \otimes SU(2)_L \otimes U(1)_Y$, and motivated by an argument for theoretical simplicity it would be desirable to have the groups be set in a single gauge group and so unify into a single force at high enough energy. The inverse coupling strengths for the three gauge groups as a function of Q are seen in Figure 2.4 and it is clear that the SM predicts no unification. There are models that predict ways around this and one such theory, supersymmetry, is discussed in Section 2.4.

Neutrino Masses

The SM as presented here does not contain a mechanism to generate masses for the neutrinos. The mass terms are necessary to describe the phenomenon of neutrino oscillations whereby neutrinos oscillate between the three generations as the propagate [31]. There are readily available methods to add in these masses, however there is not yet enough experimental evidence to determine if neutrinos acquire mass with Dirac or Majorana terms [32].

Matter Anti-matter Asymmetry

The fact that matter dominates over anti-matter indicates that there is a mechanism for *charge-parity*, CP, violation at high energies and this resulted in a baryon asymmetry at the beginning of the universe. The standard model does allow for a small amount of CP violation in the CKM matrix (Appendix Equation A.9) although this is not enough to explain the level of asymmetry required to create the cosmos as we know it. Sakharov proposed a set of conditions that would be required to produce matter and anti-matter asymmetry in different amounts [33]. These conditions furnish physicists with clues about how such a mechanism should behave although a solution to this issue remains illusive.

Free Parameters and Grand Unification: One Theory to Rule Them All?

There is no unique way to define the free parameters of the SM but in one approach there are 19, including: three lepton masses, six quark masses, three CKM mixing angles, one CKM CP violation phase, three gauge couplings, one QCD vacuum angle, the Higgs expectation value and the Higgs mass. The number of free parameters again increases if one includes a mechanism for neutrino masses. The CP-violating term in the QCD sector (Appendix A.0.3) provides another stumbling block to a complete theory. When one probes the vacuum structure of QCD a vacuum angle appears and contained within this is a CP-violating term. This parameter appears to be zero or very close to it when it can range from $0 \rightarrow 2\pi$ and this is known as the *strong CP problem* [34]. The theory of QCD seems to *preserve* CP symmetry and this issue again relates to the baryon asymmetry discussed previously.

From an aesthetic point of view one would desire a way to generate these parameters and not have them as dials with which one simply tunes the mathematics to the observable universe. Thinking of how the electromagnetic and weak interactions are unified above a certain energy within a $SU(2)_L \otimes U(1)_Y$ symmetry that is then broken. One could imagine that the SM $SU(3)_C \otimes SU(2)_L \otimes U(1)_Y$ symmetry is actually a broken component of a higher order symmetry like $SU(5)$ [35]. In this regime the running couplings of the SM would overlap at some energy instead of missing each other as we saw in Figure 2.4.

Lepton Flavour and the Secrets of the Muons

The SM as covered here indicates that the coupling of leptons to the bosons should be independent of the flavour of the lepton, otherwise known as *lepton universality*. Recent observations have provided some tension in the assumption of lepton flavour universality [36][37]. This tension is not as yet statistically significant to the level of discovery but they do indicate there may be yet another issue just below the surface.

Another discrepancy appears in the magnetic moment, M, of the muon. Particles that carry spin, S, have a magnetic moment and for the muon it is defined as:

$$M_\mu = g_\mu \frac{e}{2m_\mu} S_\mu \tag{2.21}$$

m_μ is the mass of the muon, e is the unit electrical charge and g_μ is the muon g-factor which is close to two. The muon g-factor is modified by radiative quantum corrections that make it move slightly away from two. This anomalous moment can be quantified with,

$$\alpha_\mu = \frac{g_\mu - 2}{2} \tag{2.22}$$

which can be measured with phenomenal accuracy. Such a measurement was performed at the "$g - 2$" experiment at Fermilab which confirmed an earlier experiment at Brookhaven National Laboratory (E821). The collaboration found that their measurement in combination with the previous efforts of E821 for the muon anomalous magnetic moment [38],

$$\alpha_\mu = 116592061(41) \times 10^{-11}(0.35\text{ppm}). \tag{2.23}$$

This combined value increased the tension between theory and experiment to 4.2σ, which is very close to the particle physics "gold standard" of 5σ significance. There are efforts currently under way to improve this significance further in the coming years. This measurement can be explained if there are massive particles contributing to the radiative corrections in g_μ.

2.4 Supersymmetry: An Elegant Solution

The Standard Model is a remarkably successful theory and one that is able to predict many fundamental behaviours of nature as discussed at the end of the last section there are still many unanswered questions and issues in the theory; dark matter and energy, unification of the forces and gravity. The huge gap in energy between the electroweak and gravitational scale would also suggest that new physics phenomena should appear somewhere between these two bounds.

A well motivated extension to the SM that aims to solve many of the aforementioned problems is *supersymmetry* or SUSY [39–41]. This extension introduces a new symmetry for the fermions and bosons. Such a symmetry can be easily motivated by considering the *hierarchy problem*, discussed in Section 2.3, and the loop corrections to the mass of the Higgs. Two diagrams demonstrating the first order corrections for a fermion and a scalar are shown in Figure 2.5. These diagrams result in a mass correction for fermions of the form [19],

$$\delta m_H^2 = -\frac{|\lambda_f|^2}{8\pi^2}\Lambda_{UV}^2 + \dots \tag{2.24}$$

where λ_f is the fermion's Yukawa coupling and Λ_{UV}^2 is some high energy cut off scale at which new physics enters. This was also mentioned in the discussion of renormalisation, Section A.0.4. The scalar loop in Figure 2.5b also has a correction of [19],

$$\delta m_H^2 = \frac{|\lambda_S|^2}{16\pi^2}\left[\Lambda_{UV}^2 - 2m_S^2 \ln\left(\frac{\Lambda_{UV}}{m_S}\right) + \dots\right]. \tag{2.25}$$

One notes the difference in sign between the two corrections that arises from the spin statistics differences between the two fields.

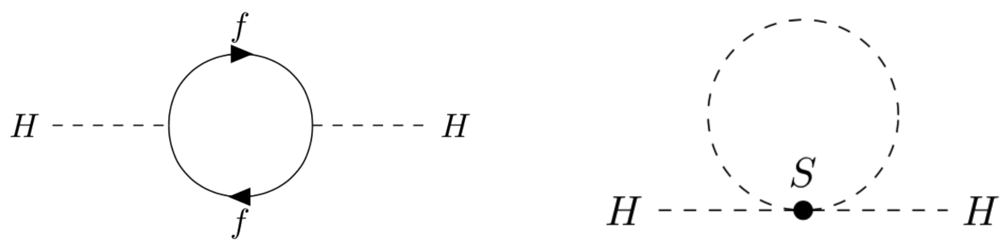

(a) Fermion **(b)** Scalar

Figure 2.5: First order loop corrections to the Higgs mass. The loop for a fermion and a scalar are shown on the left and right respectively.

The quadratic divergences cancel with the introduction of two scalar fields with $\lambda_S = |\lambda_f|^2$. This can be achieved by introducing a new symmetry that relates fermions to bosons with an anti-commutating spinor operator, $\mathcal{Q}$, that generates such transformations as [19]:

$$\mathcal{Q}|\text{Fermion}\rangle = |\text{Boson}\rangle \quad \text{and} \quad \mathcal{Q}|\text{Boson}\rangle = |\text{Fermion}\rangle. \tag{2.26}$$

This simple relation *is* the symmetry in supersymmetry and it has some important ramifications for the theory. The relation of Equation 2.26 means that the generators $\mathcal{Q}$ and $\mathcal{Q}^\dagger$ form an algebra of anti-commutating and commutating relations [19]:

$$\{\mathcal{Q}, \mathcal{Q}^{\dagger}\} = \mathcal{P}^{\mu} \tag{2.27}$$

$$\{\mathcal{Q}, \mathcal{Q}\} = \{\mathcal{Q}^{\dagger}, \mathcal{Q}^{\dagger}\} = 0 \tag{2.28}$$

$$[\mathcal{P}^{\mu}, \mathcal{Q}] = \left[\mathcal{P}^{\mu}, \mathcal{Q}^{\dagger}\right] = 0 \tag{2.29}$$

where $\mathcal{P}^{\mu}$ is the four-momentum generator and the spinor indices have been suppressed. Now this requires that each particle in the standard model has a *superpartner*. In the case of the fermions there are two scalar fields generated, S_R and S_L, one for the left and right handed components. These partners of the fermions are generally called *sfermions* and are comprised of *sleptons* and *squarks*. The spin 1/2 partners of the bosons are typically known as *gauginos*. The Higgs sector is slightly more complex as one now requires that there are two standard model Higgs doublets, one coupling to the up-type quarks and the other to the down-type. Furthermore, there will be a set of four supersymmetric partners of the Higgs known as *Higgsinos*.

2.4.1 Particle Content of Minimal Supersymmertric Standard Model (MSSM)

As has been briefly highlighted this symmetry generates new particles. To be more rigorous one must form new sets of *supermultiplets* under the action of $\mathcal{Q}$ to give the complete particle content of a supersymmetric standard model.

In this case we shall focus on the *Minimal Supersymmertric Standard Model* (MSSM) [42–44] which, is the minimal number of particles and interactions required by the content of the Standard Model. The *squarks* and *sleptons* are called such as they are the scalar superpartners of their SM counterparts. These together form chiral supermultiplets corresponding to the left- and right-handed components of the fermionic fields. This imposes the condition that the *sfermions* are in fact spin-0 scalars and not spin-1 vector bosons. The symbolic representation of these new fields are represented by a tilde ($\sim$) over the SM symbol. For example the electron field, e, has two complex scalar fields for the left- and right-handed components, the *selectrons*; $\tilde{e}_L$ and $\tilde{e}_R$. This holds for all the superpartners of the fermion fields.

Moving to the gauge sector it is clear that the bosons must be partnered to spin-1/2 *gaugino* fields. In general the superpartners of the bosons are named by appending "ino" to the end of the SM particle's name; gluon becomes *gluino*. The final convention of note is that the symbol for these gauginos again use the tilde: $g \rightarrow \tilde{g}$.

To avoid the so called *gauge anomaly*, whereby the loop diagrams of a Higgs supermultiplet break gauge symmetry, one must modify the Higgs field slightly. Imposing the condition that the sum over the hypercharges of the fermionic fields must be zero the gauge anomaly can be avoided. If there are two Higgs supermultiplets with $Y = \pm 1/2$ then the sum over the fermion components causes the anomaly to vanish. With this modification there are two separate Higgs doublets in the SM: (H_u^+, H_u^0) and $\left(H_d^+, H_d^0\right)$. These fields give rise to the masses of the up-type and down-type quarks respectively. Now by extension the new Higgs doublets form a set of fermionic superpartners called higgsinos that are $SU(2)_L$ doublet left-handed Weyl spinor fields [19] denoted by $\left(\tilde{H}_u^+, \tilde{H}_u^0\right)$ and $\left(\tilde{H}_d^+, \tilde{H}_d^0\right)$. The Higgs fields are able to acquire vacuum expectation values through spontaneous symmetry breaking and together these satisfy, $v^2 = v_u^2 + v_d^2$ and the ratio of these two values are gives $\tan\beta = v_u/v_d$. Once electroweak symmetry is broken the three spare degrees of freedom for the Higgs are taken in to the gauge bosons as the Higgs mass mechanism, Appendix A.0.2. There are some remaining degrees of freedom which form 5 fields: two charged scalars $H^\pm$, two neutral scalars called h^0 and H^0 (the lighter field h^0 is identified with the SM Higgs) and one neutral pseudoscalar A^0.

Finally turning our attention back to the electroweak sector with a gauge symmetry of $SU(2)_L \otimes U(1)_Y$ contains the, now familiar, spin-1 gauge bosons $W^\pm$, W^0 and

B^0 which in turn have spin-1/2 superpartners: $\tilde{W}^{\pm}$, $\tilde{W}^0$ the *winos*, and $\tilde{B}^0$ the *bino*. The neutral higgsinos and the neutral electroweak gauginos mix to form a set of four mass eigenstates called *neutralinos* ($\tilde{\chi}_i^0$). The charged higgsinos may also combine with the charged winos to form two mass eigenstates called *charginos* ($\tilde{\chi}_i^{\pm}$) with a charge of plus or minus one.

This summarises the contents of the MSSM as well as a brief treatment of the dynamics of the model. The content of the MSSM is summarised in Table 2.3.

Name	Symbol	Spin-0	Spin-1/2	Spin-1	$SU(3)_C$, $SU(2)_L$, $U(1)_Y$
Chiral Supermultiplets					
Squarks, Quarks (Three Generations)	Q_L	$\begin{pmatrix}\tilde{u}_L\\ \tilde{d}_L\end{pmatrix}$	$\begin{pmatrix}u_L\\ d_L\end{pmatrix}$		$\left(\mathbf{3},\mathbf{2},\frac{1}{6}\right)$
	$\bar{u}_R$	$\tilde{u}_R$	u_R		$\left(\bar{\mathbf{3}},\mathbf{1},-\frac{2}{3}\right)$
	$\bar{d}_R$	$\tilde{d}_R$	d_R		$\left(\bar{\mathbf{3}},\mathbf{1},\frac{1}{3}\right)$
Sleptons, Leptons (Three Generations)	L_L	$\begin{pmatrix}\tilde{e}_L\\ \tilde{\nu}_e\end{pmatrix}$	$\begin{pmatrix}e_L\\ \nu_e\end{pmatrix}$		$\left(\mathbf{1},\mathbf{2},-\frac{1}{2}\right)$
	$\bar{\ell}_R$	$\tilde{e}_R$	e_R		$(\mathbf{1},\mathbf{1},1)$
Higgs, Higgsinos	H_u	$\begin{pmatrix}H_u^+\\ H_u^0\end{pmatrix}$	$\begin{pmatrix}\tilde{H}_u^+\\ \tilde{H}_u^0\end{pmatrix}$		$\left(\mathbf{1},\mathbf{2},\frac{1}{2}\right)$
	H_d	$\begin{pmatrix}H_d^+\\ H_d^0\end{pmatrix}$	$\begin{pmatrix}\tilde{H}_d^+\\ \tilde{H}_d^0\end{pmatrix}$		$\left(\mathbf{1},\mathbf{2},-\frac{1}{2}\right)$
Guage Supermultiplets					
Gluino, Gluon	$\mathcal{G}$		$\tilde{g}$	g	$(\mathbf{8},\mathbf{1},0)$
Winos, W Bosons	$\mathcal{W}$		$\tilde{W}^{\pm}$, $\tilde{W}^0$	$W^{\pm}$, W^0	$(\mathbf{1},\mathbf{3},0)$
Bino, B Boson	$\mathcal{B}$		$\tilde{B}^0$	B^0	$(\mathbf{1},\mathbf{1},0)$

Table 2.3: Particle content of the MSSM before electroweak symmetry breaking where each particle set has the charges associated with each of the SM symmetries.

Considering Table 2.3, there are 32 separate particle masses in the MSSM (excluding the gravatino, the superpartner of the undiscovered graviton) all of which remain undiscovered at the time of writing.

2.4.2 R-parity

A very important quantity in the theory of supersymmetry is R-parity [45],

$$P_R \equiv (-1)^{3(B-L)+2S} = \begin{cases} +1 & \text{Standard Model Particles} \\ -1 & \text{Supersymmetric Particles} \end{cases}, \tag{2.30}$$

where B is the baryon number, L is the lepton number and S is the spin of the particle. This symmetry is imposed in order to reproduce some phenomenologically important features. In the SUSY Lagrangian one can include terms that would violate lepton and baryon number and this has direct consequences on the stability of the proton. With these terms unsuppressed the proton could decay rapidly via $p \to \pi^0 e^+$, however, the proton is thought to be stable or have an extraordinarily long lifetime, greater than 10^{34} years [46]. R-parity conservation forbids these terms and so makes the proton stable.

R-parity conservation also means that the lightest SUSY particle (LSP) is stable. Such a particle would be an ideal particle candidate to explain dark matter [47]. In many supersymmetric theories the neutralino is the LSP and such a particle would be massive and weakly interacting which, as we have seen, are two primary conditions for a dark matter particle. The final consequence of R-parity is that SUSY particles are produced in pairs at a collider such as the LHC. A more thorough introduction of R-parity can be found in [48].

2.4.3 Spontaneous Supersymmetry Breaking

Supersymmetry is not an exact symmetry because if this were the case then the masses of the superpartners would be identical to the masses of their SM counterparts and hence would have been discovered already. SUSY must be a broken symmetry and this can be achieved via explicit symmetry breaking terms contained in the

Lagrangian or by some spontaneous symmetry breaking as occurs in the Higgs mechanism. The breaking of the symmetry can reintroduce quadratic divergences into the Higgs mass correction terms and so many consider a soft SUSY breaking to be the solution. In this case one introduces a new mass scale, m_{soft}, with the breaking of the symmetry coming about in much the same way that the spontaneous symmetry breaking of the Higgs mechanism brings about the electroweak scale. The Lagrangian of the MSSM now comes in a slightly different form,

$$\mathcal{L} = \mathcal{L}_{\text{SUSY}} + \mathcal{L}_{\text{soft}}, \tag{2.31}$$

with all the gauge coupling as well as Yukawa interactions in $\mathcal{L}_{\text{SUSY}}$. The second term in Equation 2.31 breaks the symmetry but does contain all of the mass terms for the SUSY partners. This scale should not be far above the TeV scale, as it would again fail to solve the hierarchy problem. There are more complete descriptions of SUSY breaking mechanisms in References [19][20].

2.4.4 The Phenomenological MSSM and Simplified Models

The MSSM with soft SUSY breaking contains all possible SUSY breaking parameters that do not reintroduce the quadratic divergences in the Higgs mass correction. These terms are the masses for the gauginos and sfermions, and the bilinear and trilinear couplings [19]. All told, when one combines these with the terms for unbroken supersymmetry, there are over 100 free parameters.

This number of free parameters presents a problem. Such a theory is not predictive and it can simply be tuned to the observed universe. To improve the situation experimental results can be used to restrict the number of parameters with a set of conditions [49][44]:

1. No new source of CP-violation
2. No flavour changing neutral currents
3. First and second generation universality

These conditions linked with the assumption that the LSP is the lightest neutralino, $\tilde{\chi}_1^0$, allow the number of free parameters to be reduced by an order of magnitude. Further detail on these conditions are given in Reference [44] along with the free parameters, of which there are now 19.

The list of conditions given above reduces the number of free parameters and is known as the *phenomenological minimal supersymmetric Standard Model* or pMSSM [50]. In practice searches for new physics at a collider experiment set up regions of interest using powerful variables to isolate potential signal events but how does one link an observed experimental excess to the underlying theoretical structure? *Simplified models* were created to address exactly this issue. They operate on the assumption that only a few masses are kinematically accessible and only a few branching ratios are of importance and are typically fixed. These models are intended as a first characterisation of the data and are of use even if the true theoretical structure is far more complex than the simplified model.

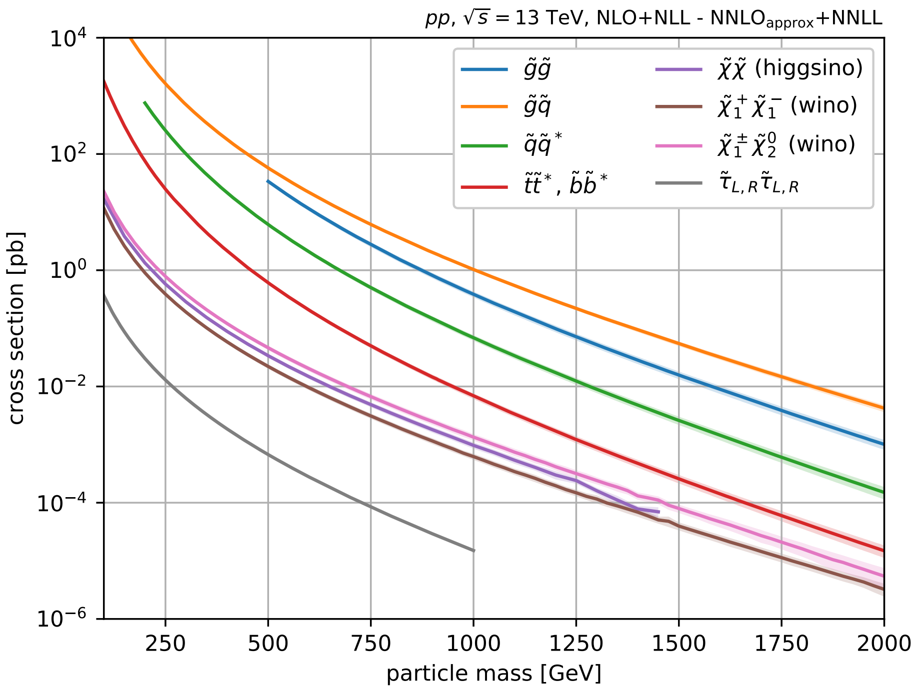

Figure 2.6: SUSY cross sections for the LHC operating at $\sqrt{s} = 13\,\text{TeV}$. Figure reproduced from [51].

Simplified models can be used to calculate the production rates of certain processes at the LHC, as in Figure 2.6. This figure shows the strong and electroweak production modes with $\sqrt{s} = 13\,\text{TeV}$ and the strongly produced particles dominate. Some of the cross-sections are large because the gauge symmetry and SUSY generators commute and so SUSY particles have the same coupling as their SM counterparts. The production cross-sections for all the SUSY channels seen in Figure 2.6 decrease with increasing mass. Limited by the centre-of-mass energy of the parton-parton interaction. When naturalness [52] is considered SUSY is expected to appear at the TeV scale and so particles may well be within reach of this machine.

2.4.5 Conclusions

This chapter introduced the theoretical framework that is the current understanding of our universe at its most fundamental scales. While the Standard Model of particle physics is an incredibly accurate theory and many of its predictions were discussed. There are some omissions like gravitation, dark matter and naturalness. An extension to the SM in the form of supersymmetry was summarised. This beyond-the-SM-physics model postulates another symmetry between fermions and bosons and the consequences of this were described. Supersymmetry predicts a suite of new particles and when the argument for naturalness is considered these particles should begin to appear at the TeV scale and so, excitingly, may be within reach of current experimental particle physics technologies.

If you would be a real seeker after truth, it is necessary that at least once in your life you doubt, as far as possible, all things.

— René Descartes *Principles of Philosophy, 1644*

3

CERN, The LHC and The ATLAS Experiment

Contents

3.1 The Large Hadron Collider: LHC

Using the 26.7 km tunnel excavated for the LEP experiment between 1984 and 1989 the Large Hadron Collider is a two-ring-superconducting-hadron accelerator [53] situated on the Franco-Swiss boarder near Geneva, Switzerland. The tunnel lies at a depth between 45 m and 170 m underground and has a slight incline of 1.4% sloping down from the Jura mountain to towards Lac Léman. On average the tunnel depth is approximately 100 m. The "ring" is comprised of eight straight sections and eight arcs with two 2.5 km transfer tunnels that link the LHC to the injector complex between the CERN Meyrin and Prévessin sites. Figure 3.1 shows an aerial photograph of the world's largest and highest energy collider with the four principal experiments highlighted on the circumference as well as some other key features.

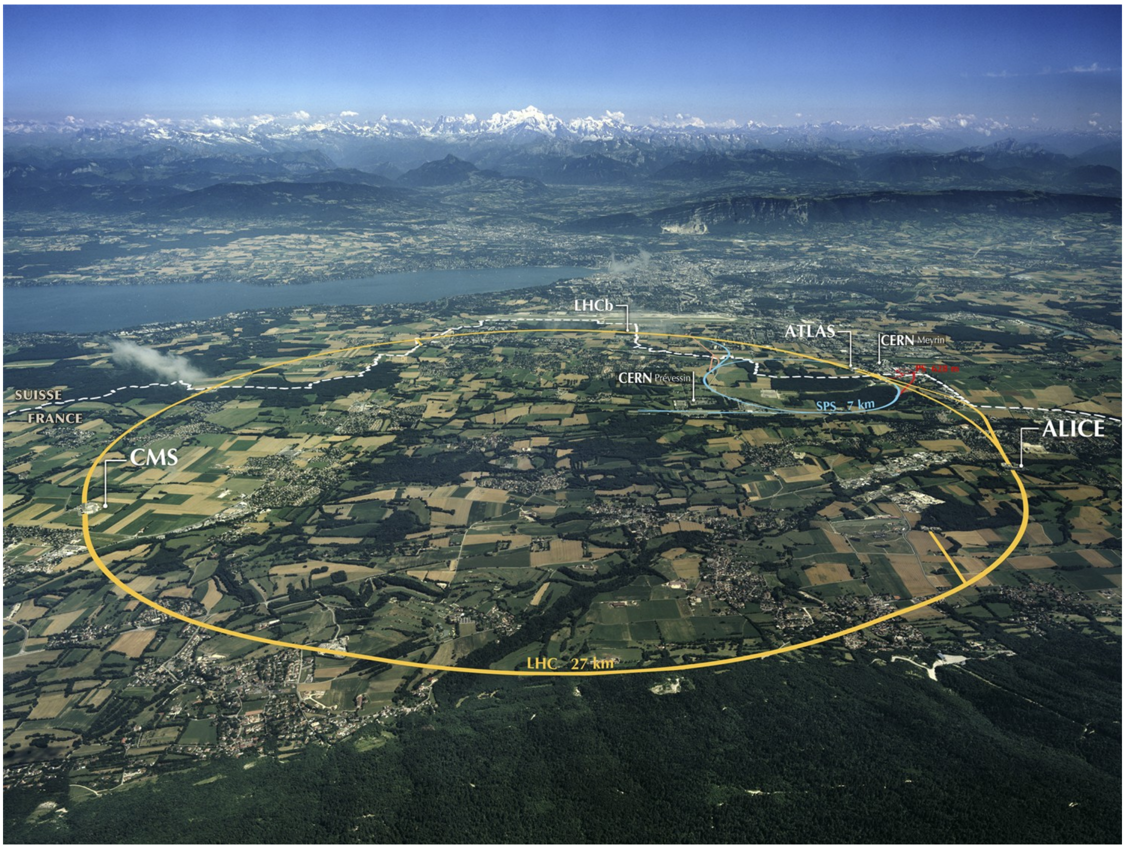

Figure 3.1: An aerial photograph taken in 2008 of the LHC's 27 km ring [53] with the four largest experiments as well as the two main CERN sites in Meyrin and Prévessin marked. Also visible in the image is the Swiss-French boarder which gives an impression of the sheer scale of this machine. Now part of the LHC accelerator complex, the smaller 7 km ring of the super proton synchroton is visible in blue. Image taken from [54].

The LHC has two contra-rotating beams. These beams intersect at four collision points and at each of these points there is an experiment. Briefly, and in no particular order, the experiments are:

- ATLAS [55] and CMS [56], two general purpose experiments located at opposite sides of the ring, Figure 3.1. Each designed to flexibly take advantage of the large range of physics provided by p–p collisions at high luminosities.
- ALICE [57] is dedicated to heavy-ion physics and the resulting high density phase of matter called quark-gluon plasma.
- LHCb [58] is an asymmetric detector built to record the debris from collisions in the forward direction only. The experiment specialises in the measurement of CP violation that can appear in the interactions of hadrons containing a bottom quark.

Two basic ingredients are needed for any circular accelerator; electric fields for acceleration in the longitudinal direction of the beam and magnetic fields to change the trajectory of the beam or "bending". The accelerating electric fields come in the form of Radio Frequency (RF) cavities, devices that oscillate the electromagnetic fields very rapidly to provide a kick of acceleration to charged particles entering them. The bending magnets provide a magnetic field transverse to the direction of travel of the beam and so by the Lorentz force exert a force perpendicular to both the beam velocity and magnetic field, towards the centre of the ring. Figure 3.2 is a simplified schematic diagram of the entire accelerator complex with start-up dates and the circumferences of the circular accelerators. The penultimate stage is the Super Proton Synchrotron (SPS) which takes the beam up to a peak energy of 450 GeV, ready for injection into the two LHC beam pipes.

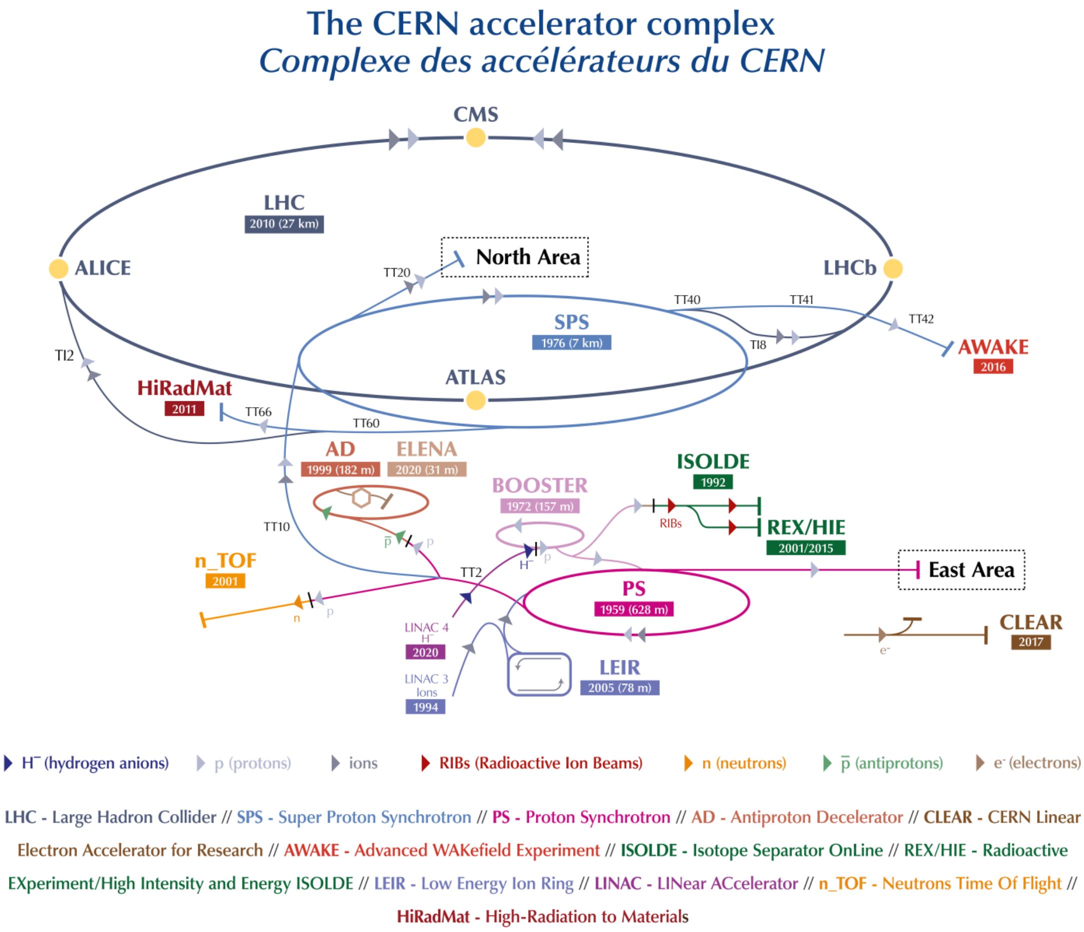

Figure 3.2: A simplified schematic view of the CERN accelerator complex. For p–p collisions protons enter LINAC2 (now LINAC4 on this figure), next on to the BOOSTER, Proton Synchrotron (PS) and then the Super Proton Synchrotron (SPS) before finally arriving at the LHC. Figure taken from [59].

RF cavities are used to accelerate the beam and so the beams cannot be continuous and are instead clumped together into bunches. Nominally there would be 2808 bunches, each bunch containing $\sim 10^{11}$ protons, circulating in each beam. The bunches are not evenly spaced around the circumference of the ring but are grouped together in "trains", the structure of these is dictated by the filling scheme.

Due to restrictions imposed by the superconducting dipole magnets the energy has been increased in steps over the years of operation. In 2011 the center-of-mass energy, $\sqrt{s}$, was 7 TeV and increased in 2012 to 8 TeV (these years are known as

Run 1). From the year 2015 to 2018 (Run 2) the center-of-mass energy made a large jump up to 13 TeV with the two beams closely approaching their design of 6.5 TeV each. Between each of the runs the machine has a period of time known as a Long Shutdown (LS) during which time upgrades can be made like those that allowed $\sqrt{\mathrm{s}}$ to jump from 8 TeV to 13 TeV. The second Long Shutdown (LS2) began in 2018 and is expected to end in 2022 with the beginning of Run 3.
The intensity of the colliding proton beams is a very useful quantity to know. This is also known as the instantaneous luminosity, $\mathcal{L}$, and when multiplied by the cross section, σ, for a particular process gives the expected rate of that process:

$$\frac{\mathrm{d}N}{\mathrm{d}t} = \sigma\mathcal{L}. \tag{3.1}$$

For any collider the instantaneous luminosity can be written, in a very general way, as

$$\mathcal{L} = \frac{N_b n_p^2}{A} f_{\mathrm{rev}} \tag{3.2}$$

where the number of bunches is N_b, the number of particles of each of the two interacting bunches is n_p (assuming it is the same in each bunch), the overlapping area of the bunches is A and finally the frequency of revolution in the ring is f_{rev}. There are several other factors that can be accounted for in this expression by modifying A such as; the beam profile (usually assumed to be Gaussian), transverse beam emittance, a luminosity reduction factor to account for the crossing angle of the bunches and so on [53][60]. Integrating both sides of Equation 3.1 with respect to time produces the number of events

$$N = \sigma L, \tag{3.3}$$

and here L is the integrated luminosity luminosity of the machine,

$$L = \int \mathcal{L} dt. \tag{3.4}$$

Units of L are given in units of inverse cross section, where typically the unit of cross section is the barn ($1\,\mathrm{b} = 10^{-28}\,\mathrm{m}^2 = 10^{-24}\,\mathrm{cm}^2$) and more commonly the picobarn

(1 pb $= 10^{-12}$ b) and the femtobarn (1 fb $= 10^{-15}$ b). Equation 3.3 highlights the importance of maximising the luminosity as the higher the luminosity the more signal events one can produce and. If a process has a very low cross section the probability of observing it are increased with a larger luminosity. There are several ways to improve the situation; increase the number of protons per bunch, increase the number of bunches or reduce the overlap area A by squeezing the bunches into a smaller transverse area at the interaction point (IP). These are some of the very methods that will be used to increase the luminosity by a huge amount during the high-luminosity LHC (HL-LHC) era, as well as a method to rotate the bunches to overlap completely and so remove the crossing angle luminosity reduction [61].

Over the course of Run 2 (2015-2018) the LHC was able to deliver 156 fb^{-1} of which ATLAS was able to record 147 fb^{-1} (Figure 3.3). This thesis analyses the “good for physics” 139 fb^{-1} subset which has a luminosity uncertainty of 1.7% [62].

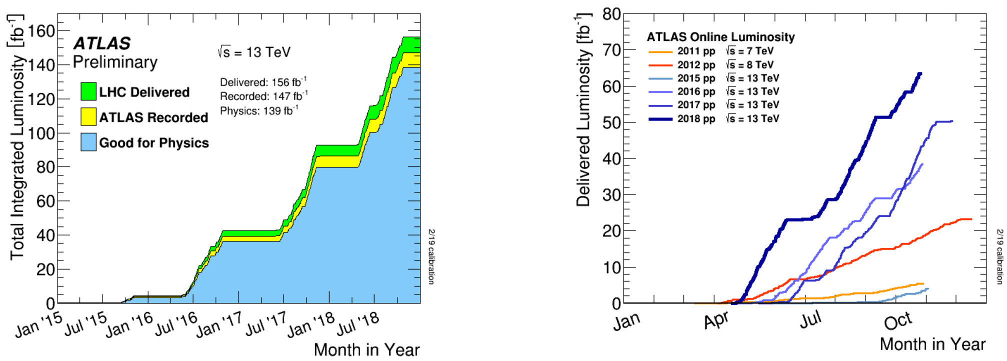

(a) Total Integrated Luminosity Data Quality

(b) Delivered Luminosity versus Time (2011-2018)

Figure 3.3: The total integrated luminosity delivered to ATLAS in terms of the data quality (a) and the delivered luminosity to ATLAS as a function of time for each of the data taking years (b). Figure taken from [63]

3.1.1 Pile-up

While increasing the luminosity is good for many reasons, including the detection of extremely rare processes, there are some drawbacks. Increasing the number of interactions per bunch crossing will eventually have a negative impact on the experiments as it becomes more and more difficult to disentangle the interesting processes from other interactions in a busy environment. These other interactions are referred to as pile-up and are considered to be contamination of an event. There are two types of pile-up effects:

- **In-time pile-up** is the presence of extra signals due to multiple interactions happening in the *same* bunch crossing. This can be suppressed by using information from the tracker (Section 3.2.2) to ensure signals are coming from the desired interaction.

- **Out-of-time pile-up** are signals originating from the previous or following bunch crossings. This largely affects the calorimeters (Section 3.2.3) as signals propagate outward it may be the case that signals from the previous bunch crossing are still present or that the signals from the following have entered.

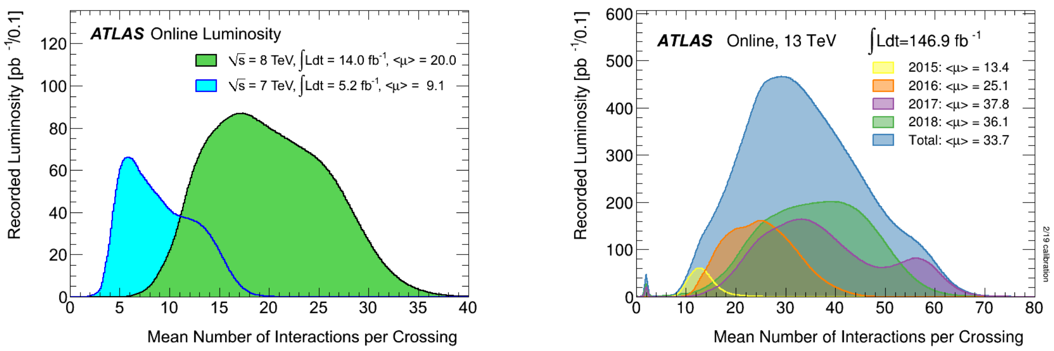

(a) Run 1 $\langle \mu \rangle$ [64] **(b)** Run 2 $\langle \mu \rangle$ [63]

Figure 3.4: The mean number of interactions per bunch crossing recorded by ATLAS during Run 2 data taking. The mean corresponds to the mean of a Poisson distribution of interactions per bunch crossing calculated for each crossing. Each of the years are shown individually as well as the total distribution.

The mean number of interactions per bunch crossing, $\langle \mu \rangle$ shown in Figure 3.4. This $\langle \mu \rangle$ is in fact the mean of the Poisson distribution of the number of interactions per crossing for each bunch

$$\mu = \frac{\mathcal{L}_b \, \sigma_{\text{inel}}}{f_{\text{rev}}}. \tag{3.5}$$

Where the instantaneous luminosity per bunch is $\mathcal{L}_b$, the inelastic cross section for p–p collisions is σ_{inel} which is set to be 80 mb at 13 TeV (71.5 mb at 7 TeV and 73.0 mb at 8 TeV) and as before f_{rev} is the revolution frequency of the LHC [64][63]. A second way to measure the pile-up is to use the number of reconstructed primary vertices in an event, N_{PV} (vertex reconstruction is discussed in Section 3.4.1). Figure 3.4 shows that $\langle\mu\rangle$, and hence the pile-up, has been increasing year on year since Run 1 and this issue is only going to get worse as the LHC moves into the high-luminosity era.

3.2 The ATLAS Detector

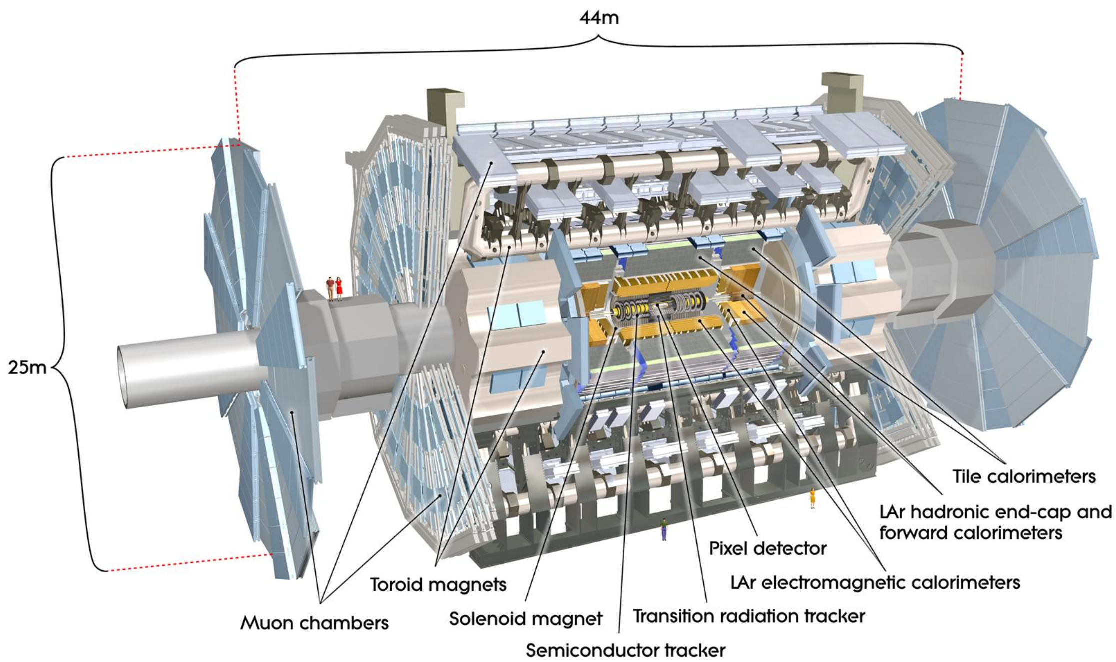

Figure 3.5: A computer generated image of the ATLAS experiment with cut out sections to make all detector subsystems visible. Figure taken from [55].

ATLAS (A Toroidal LHC ApparatuS) [55] is a cylindrical multi-purpose nearly hermetic detector located on the circumference of the LHC at one of the collision points. The detector is 45m long and 25m high and weighs in at approximately 7000 tonnes. It is designed to take advantage of the many physics opportunities provided by the LHC beams, proton or heavy ion, with capabilities ranging from precision measurements to new physics searches. A complete diagram detailing the overall layout of the apparatus is shown in Figure 3.5.

The beams enter the experiment through each of the end caps and are collided in the center of the cylinder which is the nominal interaction point. The detector is forward-backward symmetric from the perspective of the nominal IP. Working outwards from the IP ATLAS has a layered structure which can be subdivided by each detector subsystem:

- The first piece is the inner tracker (Section 3.2.2) that gives high positional resolution measurements of charged particles coming from the p–p collisions. The tracker is immersed in a 2 T magnetic field from a solenoid to allow the momentum of the particles to be determined.

- The calorimeters (Section 3.2.3) surround the tracker. The central calorimeters are split into two types; a high granularity liquid-argon (LAr) electromagnetic calorimeter and a hadronic scintillator-tile calorimeter.

- The muon spectrometer (Section 3.2.4) encompasses the calorimeters and sits within air-cored toroids. These toroids along with two end-cap magnets provide the magnetic field structure of ATLAS which generates the bending power in the rest of the experiment outside the tracker's solenoid.

Moving outwards from the beam line the detector can be subdivided very broadly into central Barrel Region (BR) sections that are cylinders around the beam axis and End-Cap (EC) sections that are wheels sitting perpendicular to the beam covering the forward (backward) regions. To maximise the impact of ATLAS, and increase the range of physics possible, good resolution in all subsystems was required [55], summarised in Table 3.1 along with the $|\eta|$ (definition in Section 3.2.1) coverage of that system.

Subsystem	Required Resolution	$\lvert\eta\rvert$ Coverage
Tracker	$\frac{\sigma_{p_\mathrm{T}}}{p_\mathrm{T}} = 0.05\% p_\mathrm{T} \oplus 1\%$	2.5
EM Calorimeter	$\frac{\sigma_E}{E} = \frac{10\%}{\sqrt{E}} \oplus 0.7\%$	3.2
Hadronic Barrel and end-cap	$\frac{\sigma_E}{E} = \frac{50\%}{\sqrt{E}} \oplus 3\%$	3.2
Hadronic Forward	$\frac{\sigma_E}{E} = \frac{100\%}{\sqrt{E}} \oplus 10\%$	$3.1 < \lvert\eta\rvert < 4.9$
Muon Spectrometer	$\frac{\sigma_{p_\mathrm{T}}}{p_\mathrm{T}} = 10\,\%\,@\,p_\mathrm{T} = 1\,\mathrm{TeV}$	2.5

Table 3.1: The resolutions and coverage that would be required to fully exploit all the available physics opportunities at the LHC, p_T and E in this table have units of GeV unless otherwise stated [55].

Each of these detector components is described in detail in the following sections of this chapter.

3.2.1 The Coordinate System

ATLAS uses a right handed coordinate system with the origin fixed at the nominal interaction point at the centre of the detector. The z-axis points along the beam line, x points in towards the centre of the LHC leaving y to point vertically upwards as shown in Figure 3.6. The azimuthal angle ϕ is the rotation around the z axis in the $x - y$ plane and the polar angle θ is measured from z. The $x - y$ plane is usually referred to as the “transverse” plane and it is useful to define certain measurements in this plane, such as the momentum:

$$p_\mathrm{T} = \sqrt{{p_\mathrm{x}}^2 + {p_\mathrm{y}}^2}. \tag{3.6}$$

As well as the transverse plane the detector can be sliced in the $y - z$ plane, the so called “longitudinal” plane. Both the transverse and longitudinal planes are illustrated in Figure 3.6 at the top left and bottom right respectively.

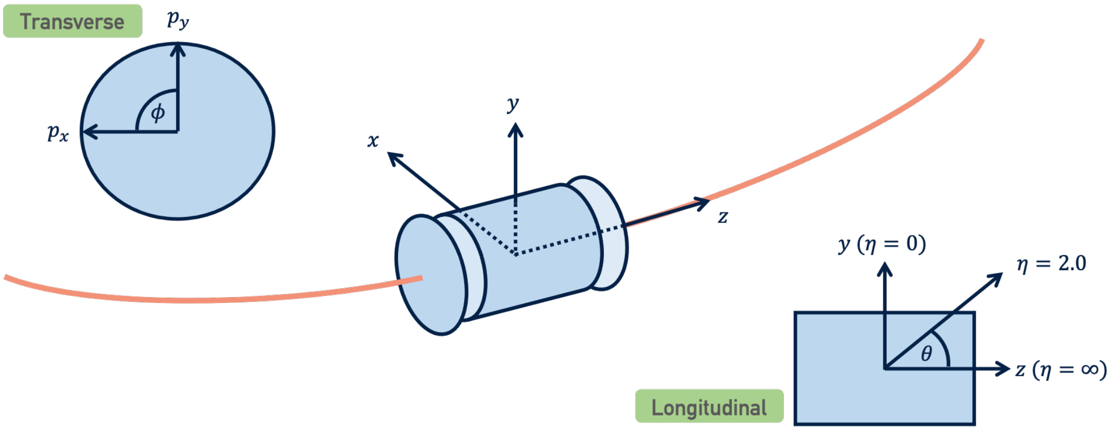

Figure 3.6: A simplistic schematic of the ATLAS experiment where the red sweeping line indicates the LHC beamline and the Cartesian coordinate system is overlaid on the barrel of the experiment. Two important planes are shown; the transverse plane (top left) and the longitudinal plane (bottom right). The transverse plane shows the two components of momentum as well as the azimuthal angle, the longitudinal shows some examples of the pseudo-rapidity, η.

The colliding partons have differing momentum fractions along the beam-line, in the z direction, and this fraction is generally unknown. So, it is useful to define a quantity called rapidity,

$$y = \frac{1}{2} \ln \left(\frac{E + p_z}{E - p_z} \right). \tag{3.7}$$

The difference between the rapidity of two particles, Δy, is invariant under longitudinal Lorentz boosts and so avoids the issue of partons, with an unknown momentum fraction in z, having to be boosted into their rest frame. This is also the motivation behind defining the momentum in the transverse plane, as in Equations 3.6, as this quantity is invariant under longitudinal boosts.

Under the approximation that the particle is travelling close to the speed of light, or that that the mass of the particle is negligible compared to its momentum, one can approximate the rapidity using the pseudo-rapidity:

$$\eta = -\ln \left(\tan \left(\frac{\theta}{2} \right) \right). \tag{3.8}$$

This coordinate is used for light high energy particles as it is simple to measure θ as the angle between the particle's three-momentum and the beam axis, z. Combining η and the azimuthal angle ϕ gives a coordinate space known as $\eta - \phi$ space. In this plane distance between objects ΔR, with coordinates (η_1, ϕ_1) and (η_2, ϕ_2), can be easily computed as:

$$\Delta R_{12} = \sqrt{(\Delta\eta_{12})^2 + (\Delta\phi_{12})^2} = \sqrt{(\eta_1 - \eta_2)^2 + (\phi_1 - \phi_2)^2} \tag{3.9}$$

The coordinate system described here gives and easy method to locate signals within the detector which, is hermetic in ϕ and has excellent coverage in the forward regions up to $|\eta| < 4.9$.

3.2.2 The Inner Detector

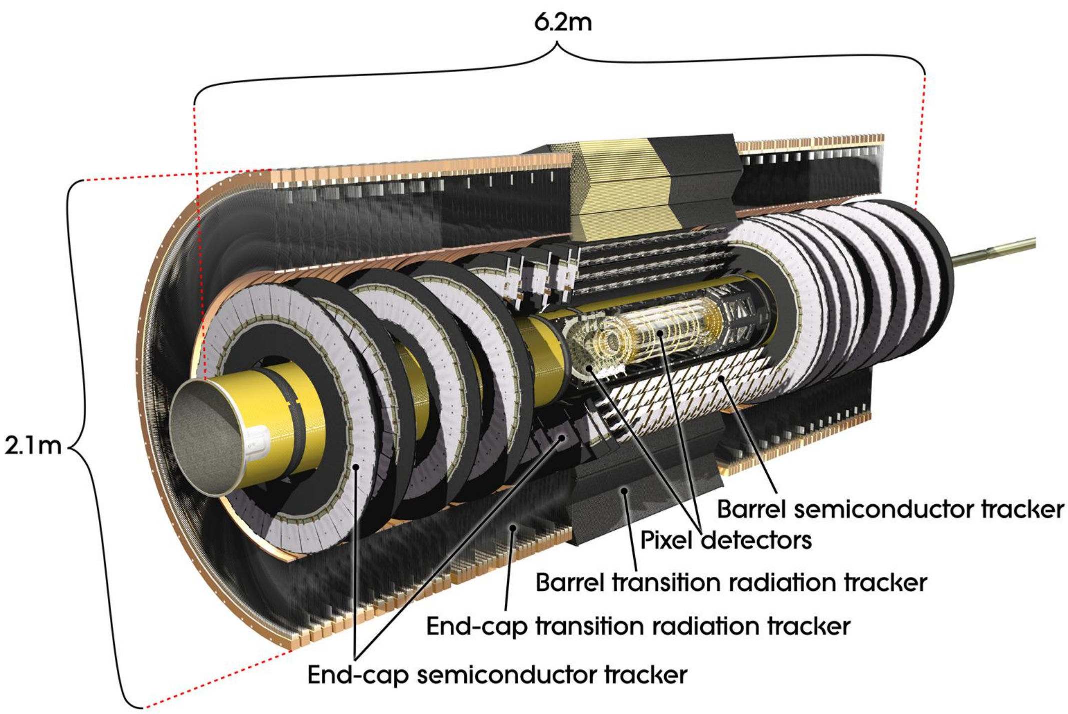

Figure 3.7: Computer generated image of the complete inner detector with cut aways to reveal the innermost components. Figure taken from [55].

The ATLAS Inner Detector (ID) is the innermost component of the detector and as such it is the first instrument particles produced in the collisions will encounter.

The ID is designed to detect charged particles with excellent momentum resolution as well as primary and secondary vertex identification for charged tracks, nominally, above 0.5 GeV but can go as low as 0.1 GeV within $|\eta| < 2.5$ [55].

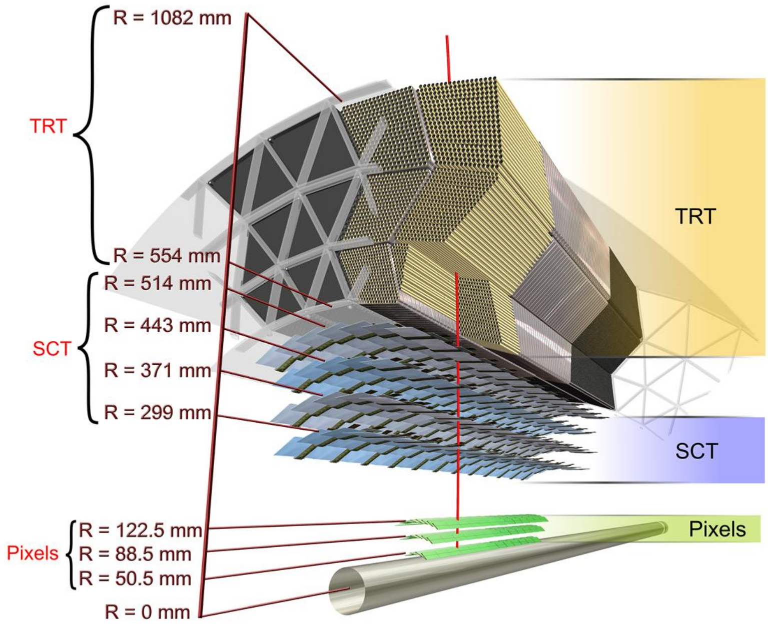

Figure 3.8: Transverse cutaway section of BR of the ID showing the structural components and the measurements indicating physical size. Figure taken from [55].

The ID is contained within a cylindrical envelope of length 7.024m, along the beam-pipe, and radius 1.15m and the overall structure is shown in Figure 3.7. The ID can be further subdivided into three sub-detectors, Figure 3.8; the silicon pixel detector (PD), the semiconductor tracker (SCT) and the transition radiation tracker (TRT). These components are listed moving outward from the beam-pipe and each has a barrel and end-cap component, each will be discussed further in the coming sections. Outside of the TRT is the outer envelope of the ID and beyond that is the solenoid coil that immerses the entire ID in a 2 T magnetic field that provides the bending force for charged particles, as illustrated in Figure 3.9. Overall the resolution of the ID is as designed and stated in Table 3.1.

The amount of material used to construct the tracker must be as minimal as possible to reduce secondary scattering from the incident particles. The sensors must also be extremely radiation hard so as not to degrade entirely or fail over the many years of LHC operations. Figure 3.8 shows the central barrel region of the ID with structural elements and gives a clear representation of the location of each of the sub-detectors with respect to the beam-line.

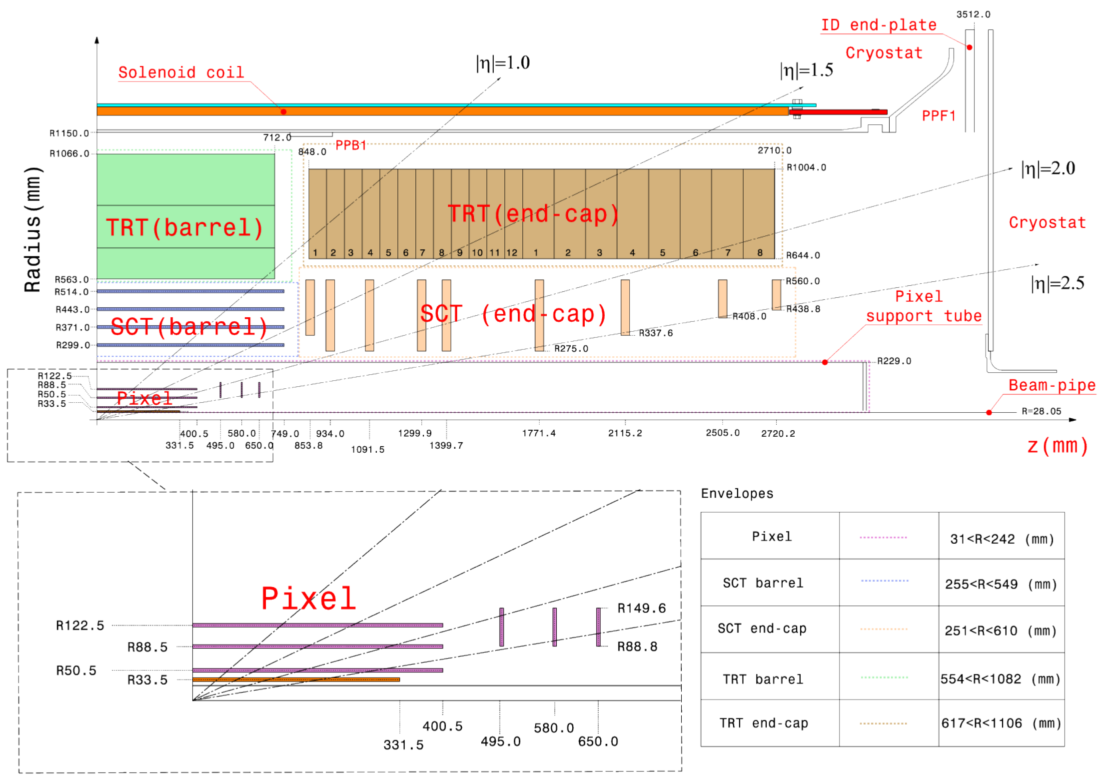

Figure 3.9: One quarter of the ATLAS detector in plan view. Figure taken from [55].

Silicon Pixel Detector

At the very heart of ATLAS is the pixel detector and this is essential for making precise track and vertex measurements. The pixel detector consists of 1744 modules arranged in three barrel layers and two end-caps each with three disc layers, these can be seen clearly in Figure 3.9. Each module consists of 16 front-end chips each with 2880 electronics channels that read out to the trigger and data acquisition system. The pixels on the sensor tiles are, generally, $50 \times 400\,\mu\text{m}^2$ (some 10% of pixels, close to the front-end chips are $50 \times 600\,\mu\text{m}^2$) and are formed of reverse-bias diodes. As a charged particle passes through a pixel electron-hole pairs are created and these drift in opposite directions due to an applied electric field and a current can be read out as a binary decision "hit" or "no hit". This provides excellent resolution to resolve interaction vertices and is able to resist the high levels of radiation present this close to the beam-line. To mitigate the negative effects of the high radiation environment the detector has a set of operating conditions; the operational temperature needs to be within a range of $-5°$C to $-10°$C and the applied bias voltage can be increased from 150 V to 600 V over the 10 years of operations depending on the position of the sensor and the integrated luminosity among other considerations.

During 2012-2013, the first long shut down (LS1), an extra pixel layer was inserted between the new smaller radius beam-pipe and the first pixel barrel layer called the Insertable B-Layer (IBL) [65][66]. The IBL was added to maintain or improve the tracking and flavour tagging performance despite the irreversible radiation damage. The IBL is composed of 14 carbon fibre staves that are 2 cm wide and 64 cm long and each stave is tilted by 14° in ϕ. The staves surround the beryllium beam-pipe at an average radius of 33 mm with a wide pseudo-rapidity coverage of $|\eta| \leq 3$. The staves each have a carbon dioxide cooling tube and 32 front end chips bonded to the silicon sensors [66].

Semiconductor Tracker

The Semiconductor Tracker (SCT) comprises four cylindrical barrel layers approximately 30cm from centre of the beam-pipe, as shown in Figure 3.8, the closest two end-caps each containing 9 disc layers. Both BR and EC structures are visible in Figure 3.9. In total, there are 4088 modules in the SCT that cover a surface of $63\,\mathrm{m}^2$ in an almost hermetic fashion providing a minimum of four precision measurements. The strips are 6 or 12 cm long and have a pitch of $80\,\mu$m.

Continuing to use the silicon pixel technology over such a large area would have been prohibitively expensive and so for reasons of cost and reliability single sided p-in-n technology was used. This strip technology is reliable, simply read out and requires a bias voltage, initially, of 150 V which may be increased to 350 V over the 10 years of operation. The individual silicon strips provide two-dimensional information and so to gain some sensitivity along z in the BR and in the EC. Each module contains two layers tilted at a stereo angle of 40 mrad. The resulting resolution for the SCT is $17\,\mu$m in $R - \phi$ and $580\,\mu$m in z or R [55].

Transition Radiation Tracker

Moving radially outwards from the SCT the Transition Radiation Tracker (TRT) is encountered next and this is the outermost component of the ID (Figure 3.8). The TRT extends the central tracking of ATLAS out to a radius of approximately 1 m and provides acceptance up to $|\eta| < 2$ [55].

The TRT is comprised of polyimide drift tubes 4 mm in diameter with a single $31\,\mu$m gold-plated tungsten wire running through the center. The tubes nominally contain a gas mixture of 70% Xenon, 27% carbon dioxide and 3% molecular oxygen and the straw wall is held at a 1.5 kV potential difference from the central anode wire [67]. In total there are around 300,000 drift tubes in the TRT and these provide 30 2D space point measurements, on average, with a resolution of $120\,\mu$m. The tubes come in two different lengths; 52,544 straws of 1.44 m for the barrel region and 245,760 straws of 0.37 m for the end-cap discs arranged radially, perpendicular to the beam-pipe [67].

As a charged particle traverses the TRT it ionises the gas mixture leaving a trail of free electrons and ions. The electrons then drift in the electric field to the wire where they are amplified and read out as a signal. In between the drift tubes material is placed to cause transition radiation; in the barrel there are polymer fibres and in the end-cap there is foil. Encountering these abrupt changes in refractive index relativistic particles will emit transition radiation especially for large relativistic gamma factor of the particles, $\gamma = E/m$, which is strongest for electrons. This difference in emission thus aids in particle identification.

3.2.3 Calorimetry

Immediately after the solenoid coil containing the ID are the calorimeters. Calorimeters are designed to measure the energy of incident particles by completely absorbing them within the calorimeter's volume. Calorimeters can measure charged and neutral particle energies, while the tracker only detects charged particles. Calorimeters cannot measure the energy of very weakly interacting particles that would pass through the apparatus, neutrinos and muons for example. How ATLAS deals with these two particles will be discussed later.

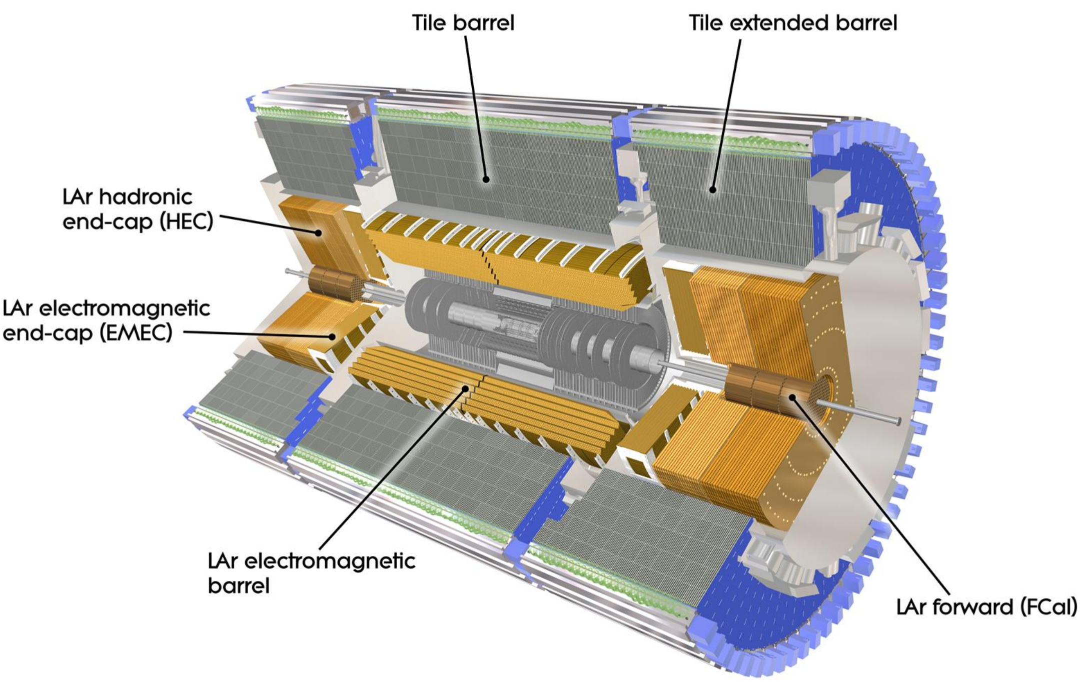

Figure 3.10: Structure and arrangement of the ATLAS calorimeter systems with cut out sections. Figure taken from [55].

ATLAS uses the sampling-calorimeter technique, the calorimeters are segmented in the transverse plane and in ϕ to allow for the measurement of shower shape and so aid in the task of particle identification. This segmentation also aids in the

determination of particle energy flow direction. The magnitude of the measured signal from the showers is proportional to the energy of the incident particles in the case of electrons, positrons and photons. This is not the case for hadronic showers which need to have a calibration procedure applied after data collection is complete and this process is described in Section 3.4.
Figure 3.10 illustrates the ATLAS calorimeter layout and positioning central barrel and forward end-cap calorimeters. The calorimetry covers the entire ϕ range and coverage extends up to $|\eta| < 4.9$ and is able to contain the entirety of the particle showers with minimal leakage into the muon spectrometer.

The required resolutions of each of the detector systems was summarised in Table 3.1, the resolution of the various types of calorimeters used in ATLAS is an important figure of merit and provides a clean way to compare performance between calorimeter types. The generic formulation of calorimeter resolution is:

$$\frac{\sigma_E}{E} = \frac{A}{\sqrt{E}} \oplus \frac{B}{E} \oplus C \tag{3.10}$$

where A, B and C are the stochastic term, the noise term, and a constant term respectively while $\oplus$ denotes a quadratic sum and E is measured in GeV. Each of these parameters is dependent on η [68]. These factors account effects that contribute to the resolution term:

- **A, Stochastic Term:** The number of particles generated in a shower is random and so there will be energy fluctuations measured as the shower evolves (dominating for hadrons). This term also accounts for the sampling nature of the measurement (dominates for electrons and photons).

- **B, Noise Term:** The readout electronics have an inherent noise. Pile-up contributes to this noise term in several ways. The out-of-time pile-up contributes through the signal shaping functions being used. The in-time pile-up fluctuations are connected to the Possion-fluctuated number of proton collisions per bunch crossing.

- **C, Constant Term:** ATLAS is built to a very high specification however, there will be imperfections in the construction. The response of the detector is not perfectly uniform and there will be energy lost in "dead material" such as the structural elements of the detector. One of the most important contributions to the constant term comes from channel-to-channel variations arising from electronic gain fluctuations.

The resolution of the EM calorimeter, expanding on the required values in 3.1, is $A = 10\%$, $B = 0.1\%$ and $C = 0.7\%$ [68][69]. For the hadronic calorimeter; $A = 50\%$, $B = 1\%$ and $C = 3.4\%$ for pions in the central region of the detector [70].

The Liquid Argon Electromagnetic Calorimeter

ATLAS uses sampling calorimeter technology and for the electromagnetic calorimeter there is a lead absorber with a liquid argon (LAr) active medium. The main purpose of this detector is to measure the energies of particles producing electromagnetic showers of electrons, positrons and photons. The layers adopt an "accordion" sampling geometry as this allows for short cables, uniformity (no azimuthal cracks) and good signal extraction, visible in Figure 3.11a in the barrel module schematic. Three cryostats cool the calorimeter.

The structure of the system is divided into barrel and end-cap regions as has been the case for all sub-detectors up to this point. The electromagnetic barrel (EMB) section is in three layers covers up to $|\eta| < 1.475$. An example of one of the barrel modules is presented in Figure 3.11a with the granularity of each cell marked on, the tree layers of the module are clearly visible and the number of radiation lengths (X_0) is also indicated. The electromagnetic end-cap (EMEC) covers the range $1.4 < |\eta| < 3.2$ [55].

The middle and outer layers of the LAr calorimeter are built of cells with a high granularity of 0.0245×0.025 and 0.0245×0.05 respectively in $\Delta\phi \times \Delta\eta$. This granularity is excellent for distinguishing electrons and photons coming from neutral and charged pions which, is of importance as pions are the most commonly produced particle at the LHC.

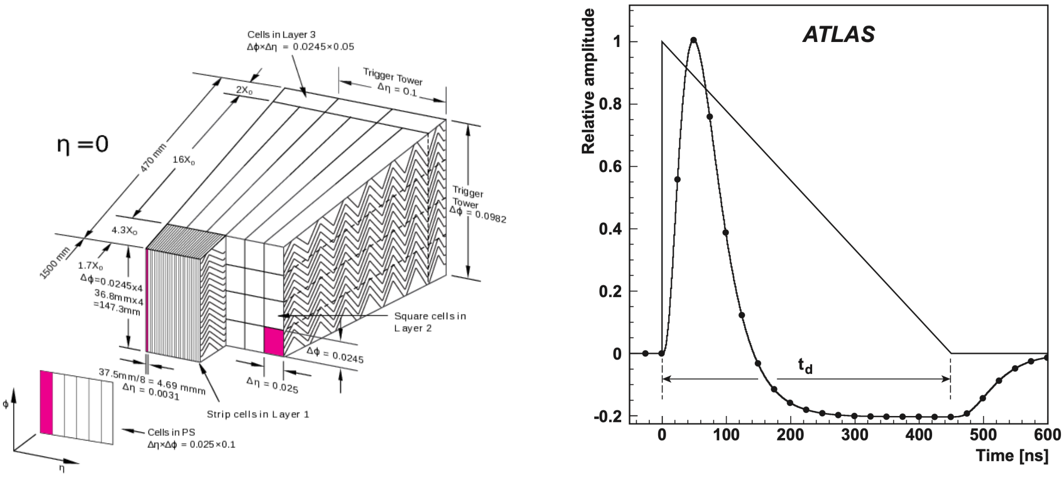

(a) LAr Calorimeter Barrel Module Schematic

(b) LAr Signal Amplitude Against Time

Figure 3.11: A EM calorimeter module and the idealised pulse shape for signal extraction. Figure taken from [55]

Using liquid argon calorimetery has many advantages: detector uniformity, linear response, radiation hardness, and high granularity. There are several drawbacks including; poor stochastic term resolution (property of sampling calorimeters), difficult cryogenics, and slow charge collection time. At a nominal operating voltage of 2 kV the charge collection can be 450 ns, an obvious issue given that the LHC bunch separation is 25 ns. This slow collection in extracting physics signals and triggering the detector is addressed by integrating the signals over a shorter, fixed time, of 25 ns. This approach creates an ideal pulse shape as illustrated in Figure 3.11b. The accordion sampling geometry mentioned previously also helps in the effort to reduce the charge collection and readout time, having longer readout cables could increase the signal collection time by tens of nanoseconds and increase signal fluctuations.

The Hadronic Calorimeters

ATLAS employs several different systems for the hadronic calorimetry. In this section the tile calorimeter and liquid argon end-cap calorimeter (HEC) are discussed and the forward calorimeters are left to the next section. The tile calorimeter [71] is another sampling calorimeter with steel absorber layered with scintillator as the active medium, Figure 3.13. The tile calorimeter surrounds the EM calorimeter in the barrel region ($|\eta| < 1$) 5.8 m in length and also has two extended barrel regions ($0.8 < |\eta| < 1.7$) each 2.6 m, marked in Figure 3.10, giving a total coverage of $|\eta| < 1.7$.

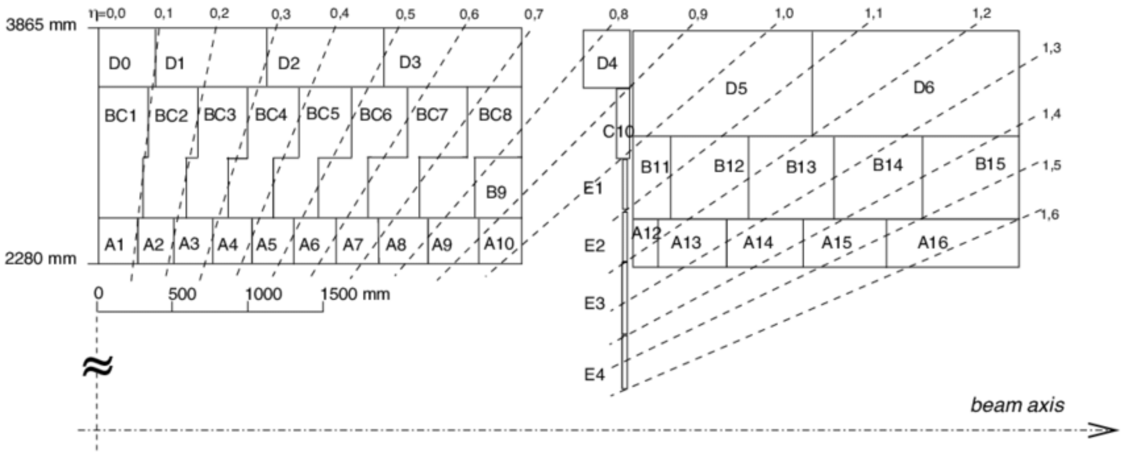

Figure 3.12: Schematic showing the structure of the tile calorimeter and its segmentation in η. Figure taken from [55].

This outer most component of the calorimeter is designed to measure particles like protons, neutrons and pions. Charged particles in the showers initiated by the steel absorber produce photons in the scintillator which are collected using wavelength-shifting optical fibres and transmitted to photomultiplier tubes, located at the top of the modules, that produce a signal output. The barrel layers are again in three layers as shown in Figure 3.12, the two innermost layers are subdivided into towers of 0.1×0.1 in $\Delta\eta \times \Delta\phi$ and the last layer towers have corresponding dimension 0.2×0.1. The calorimeter is fitted with three calibration systems: a ^{137}Cs radioactive source, laser and charge injection [55].

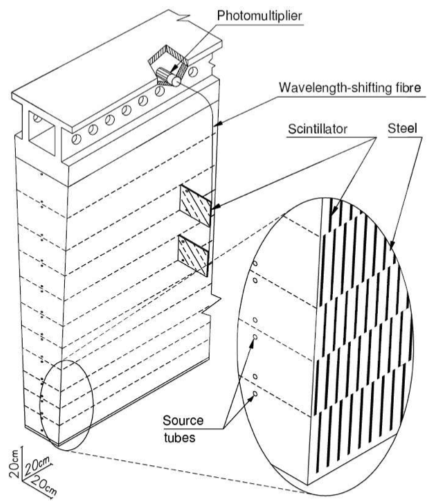

Figure 3.13: The structure of a tile calorimeter module. The layering of steel absorber with plastic scintillator with optical readout channels and photomultiplier tube at the top is shown. Figure taken from [55].

In the more forward regions the environment becomes increasingly radioactive, due to the proximity to the beam-pipe. For this reason a more radiation-hard configuration is employed with copper absorber and LAr active medium. In the range $1.5 < |\eta| < 3.2$ are the hadronic end-cap calorimeters (HEC), visible in Figure 3.10 while Figure 3.14b shows the schematic view of the HEC by itself in different planes.

The HEC consists of two wheels positioned perpendicularly to the beam-line, each wheel is made up of 32 identical wedge shaped modules a single module is illustrated in Figure 3.14a. The outer radius of the HEC wheels remains constant at 2.03 m. The front wheel modules are made up of 24 copper plates each 25 mm thick with a 12.5 mm front plate. The rear wheels have thicker copper plates at 50 mm and 16 plates in total. The inner radius of the HEC varies; the first 9 plates of HEC1 have an inner radius of 372 mm while all remaining plates of HEC1 and 2 have an inner radius of 475 mm.

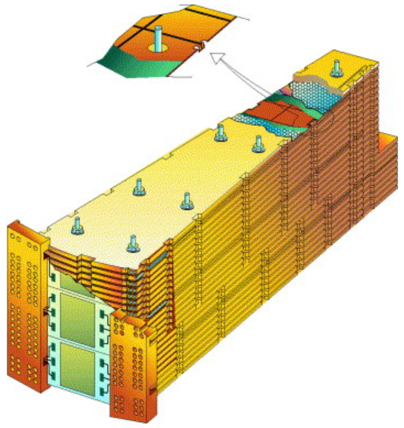

(a) Module of the Front Hadronic End-Cap Calorimeter

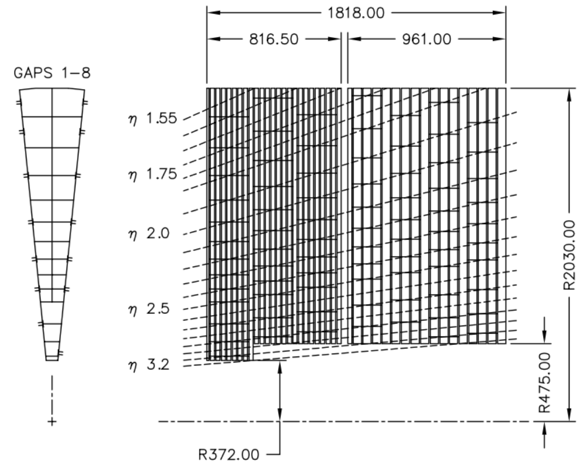

(b) Hadronic End-Cap Calorimeter Schematic

Figure 3.14: A single module of the hardronic end-cap calorimeter (a) and the general schematic in $R-\phi$ (b, left) and $R-z$ (b, right). Figure taken from [55]

The gaps between the copper plates are consistently 8.5 mm and three electrodes divide each gap into four LAr drift regions. Each of the drift zones are supplied with their own high voltage and the central electrodes contains a pad which serves as the readout for the HEC module. The arrangement is such that the pads form a semi-pointing geometry which is shown by the η lines on Figure 3.14b. The readout cell size is dependent on η for $|\eta| < 2.5$ the cells have dimension 0.1×0.1 in $\Delta\eta \times \Delta\phi$ and 0.2×0.2 for larger values of $|\eta|$ [55].

The Forward Calorimeters

In the most forward regions of the detector are the two forward calorimeters (FCal) covering a range of $3.1 < |\eta| < 4.9$. The FCals are located in the same cryostats as the hadronic end-cap calorimeters and so the design is closely integrated to minimise energy loss in the gaps between the two. The very forward position of the FCal, at high $|\eta|$, means that the modules are exposed to very high particle fluxes and so need to be very radiation hard. For this reason the modules have smaller liquid argon caps to combat ion build-up issues while keeping the detector module very dense. The small LAr gaps are achieved by using an electrode structure of small diameter rods centred in tubes that are parallel to the beam direction all inset in an absorber material. The FCal is split into three 45 cm modules; the first is an electromagnetic module (FCal1) with a copper absorber and the second two are hadronic modules (FCal2 and FCal3) with tungsten absorber material. Figure 3.15 shows the amount of material in radiation lengths (X_0) for each of the calorimeter subsystems in terms of η. The LAr gaps forming the active regions of the detectors are 0.269 mm, 0.376 mm and 0.508 mm for FCal1, FCal2 and FCal3.

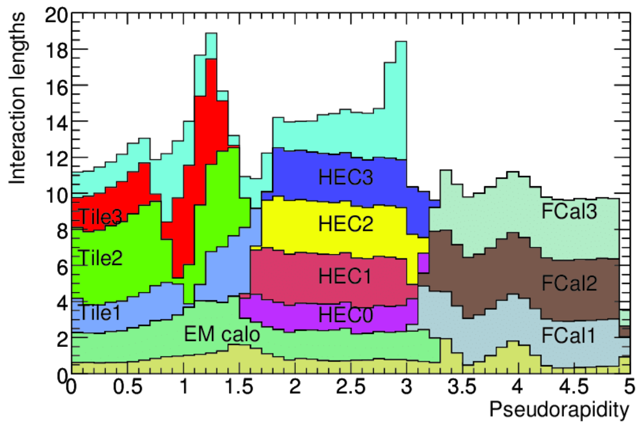

Figure 3.15: The amount of material in radiation lengths, X_0, as a function of pseudo-rapidity. Figure taken from [55].

3.2.4 The Muon Spectrometer

As muons pass through the inner tracker and the calorimeters they lose very little energy and so another method is added to detect them, the muon spectrometer (MS). This forms the outer layer of the experiment and is one of the most prominent features visible in Figure 3.5. A more technical plan drawing highlights the most important features of the spectrometer in Figure 3.16.

The muon spectrometer operates by bending the muons in the bending plane $(\eta - z)$ and taking highly accurate positional measurements. Combining positional data and the known magnetic field the MS was designed to measure muons up to $|\eta| < 2.7$ and with a minimum resolution of 10% for 1 TeV muons (Table 3.1) and this was found to be very closely met in 2017 and 2018 data [72].

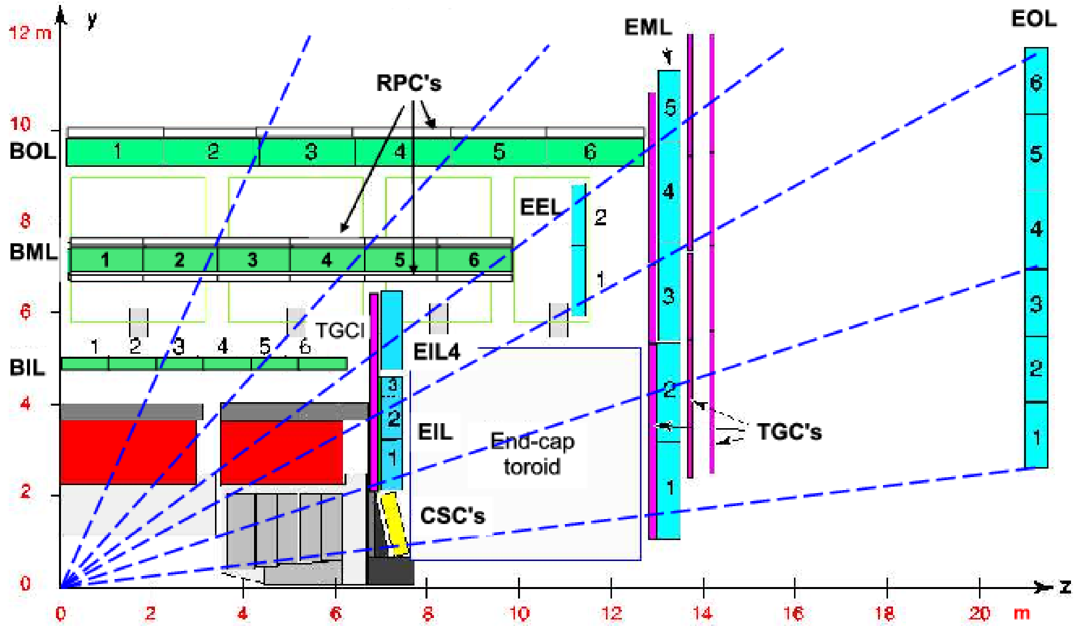

Figure 3.16: Profile view of one quarter of the ATLAS muon spectrometer. Figure taken from [55].

Broadly speaking the MS comprises a magnet system, precise tracking chambers and fast triggering detectors. Toroidal magnets are split into two systems: in the center of the experiment are the end-cap toroids producing a 1 T field on average and on the outer regions there are 8 air-cored toroids circling the barrel region and delivering an average field of 0.5 T (visible in Figure 3.5 and Figure 3.17). In the barrel region, $|\eta| < 2.0$, there are three layers of precision tracking chambers. The three concentric cylinders of the barrel are located at the base of the toroids, inside the toroids and at the outer edge of the toroids at about 5 m, 7.5 m and 10 m respectively. Figure 3.17 illustrates this clearly as well as showing that each layer consists of a set of octants, each octant having two different extensions with a large and a small sector to provide an overlap in ϕ that improves coverage. The two end-cap regions (Figure 3.16) have muon chambers arranged into 3 large wheels perpendicular to the z-axis at 7.4 m, 10.8 m and 21.5 m from the interaction point.

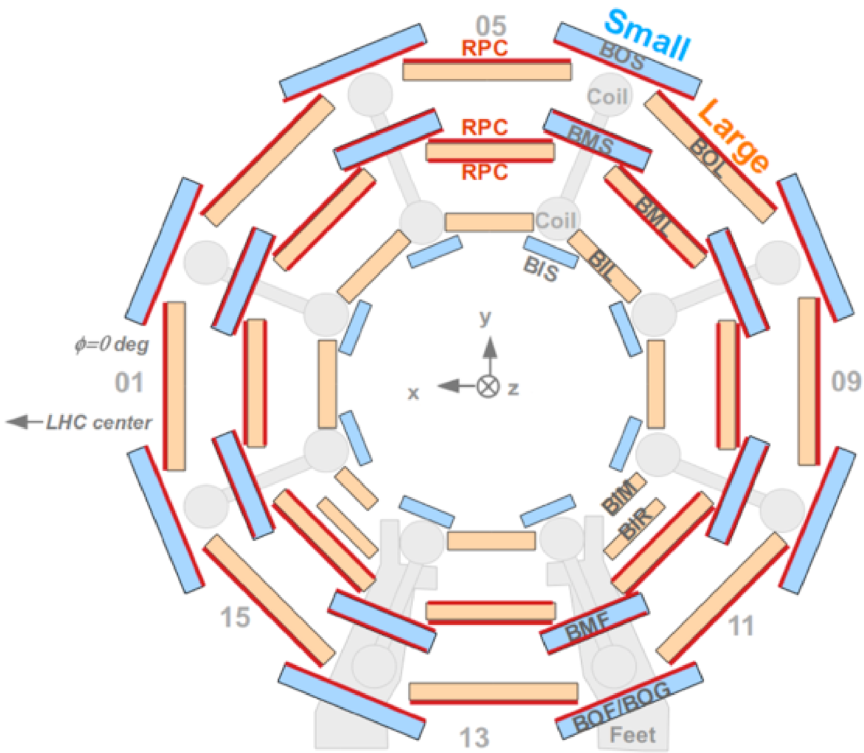

Figure 3.17: Cross sectional view of the ATLAS muon spectrometer showing the octagonal structure and positioning of the tracking chambers in the barrel region. Figure taken from [73].

Precision Tracking Chambers

The curvature of the muons in the magnet system combined with high precision positional measurements provided, in the most part, by the monitored drift tubes (MDT) allow for highly accurate determination of the muon momentum. The MDTs are cathode tubes filled with a gas mixture of argon and carbon dioxide at a pressure of 3 bars with a central anode wire (tungsten-rhenium at 3080 V) and these allow for a resolution of around 80 μm per tube. Figure 3.18a shows a cross section of one of the MDTs with passing muon and a simple diagram depiction of a passing muon ionising the gas mixture which then drifts in the electric field. The tubes are combined into modules 2 or 4 tubes deep as shown in Figure 3.18b and the resolution of each module is around 35 μm. This impressive accuracy requires that the position of the tubes in the modules is closely and constantly monitored, Figure 3.18b also shows the optical alignment system. Not only do the tubes themselves need to be kept at a straightness better than 100 μm, the relative positions of the neighbouring modules must also be monitored and another optical system is employed for this purpose. These systems combined allow the position of muons to be recorded with an accuracy of 50 μm, half the width of an average human hair [55].

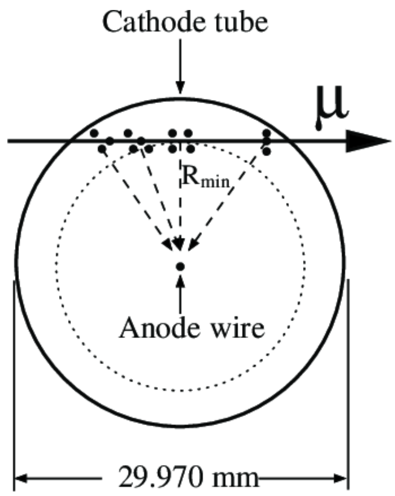

(a) Cross Section of a Monitored Drift Tube

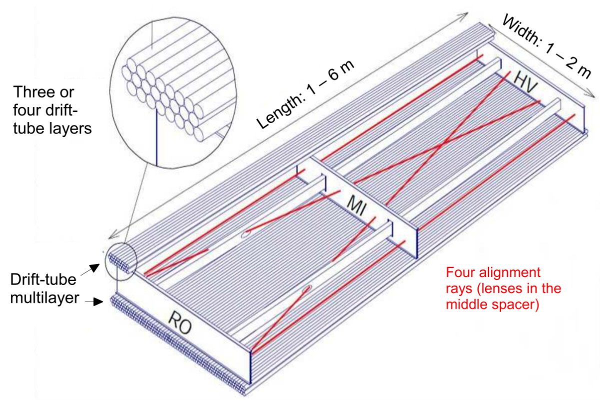

(b) Diagram of Monitored Drift Tube Module

Figure 3.18: Cross section of a single monitored drift tube with charge production caused by passing muon (a) and the structure of a complete module with alignment rays. Figure taken from [55]

The maximum drift time in the MDTs can be up to 700 ns meaning another system is required for fast triggering. In the innermost wheel of the end-caps another detector technology is used as this region is expected to have a higher flux of muon. For this purpose cathode strip chambers (CSC) are employed because they have a much shorter drift time of 40 ns. The CSCs are multi-wire proportional chambers and the cathodes are split into smaller strips for improved positional resolution, 60 μm per CSC plane [55].

Overall the resolution of the MDT and CSC systems in combination is $35 - 49\,\mu$m per chamber in the $\eta - z$ bending plane which gives the required resolution of $\sim$ 10% up to several TeV [74].

Fast Trigger Chambers

The positional resolution of the MDT and CSC modules is excellent but the long drift time means that another system must be used to trigger within the 25 ns spacing of the proton bunches. The trigger system extends up to $|\eta| < 2.4$: Resistive Plate Chambers (RPC) cover the barrel region up to $|\eta| < 1.05$ and Thin Gap Chambers (TGC) extend the rest of the way, $1.05 < |\eta| < 2.4$.

The RPCs are a pair of parallel resistive plates with a 2 mm spacing and an electric field of 4.9 kV/mm, illustrated in Figure 3.19a. As a charged particle passes through avalanches quickly form to give a signal output with a response time of 1.5 ns. The TGCs are multi-wire proportional chambers with a larger separation between the wires than between the wire and the cathode, illustrated in Figure 3.19b. This small pitch combined with a highly quenching gas mixture of CO_2 and $n-C_5H_{12}$ (n-pentane) allows operation in a quasi-saturated mode giving sufficient pattern recognition and a rapid response time of 4 ns [55].

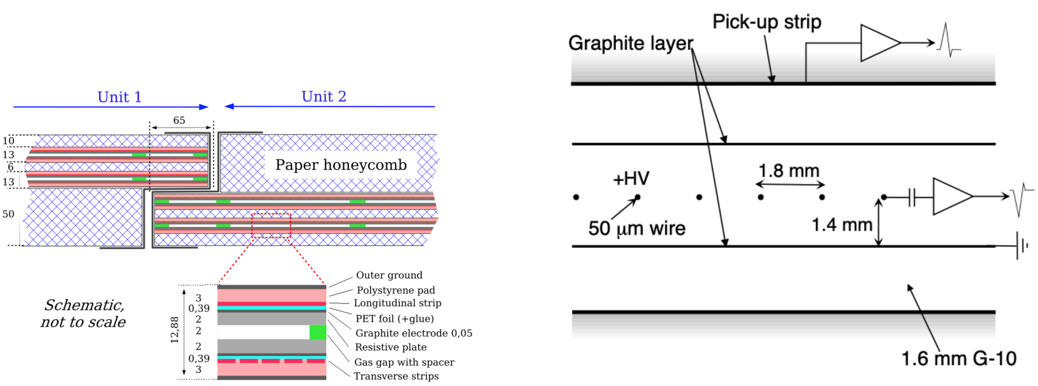

(a) Resistive Plate Chamber Cross Section **(b)** Thin Gap Chamber Schematic

Figure 3.19: The two components of the MS fast trigger system, RPC (a) and TGC (b). Figure taken from [55]

3.3 Data Acquisition, the Trigger System: Itchy Trigger Finger

Proton-proton collisions occurring every 25 ns, corresponding to a rate of 40 MHz, would generate an unmanageable amount of data for storage and analysis so there needs to be a method for selecting the most interesting events from this torrent. The Trigger and Data Acquisition System (TDAQ) is able to select the interesting events based on known characteristics from those that are less so. The TDAQ in Run 2 comprises two systems, the **Level-1 Trigger** (L1) and the **High Level Trigger** (HLT)[75].

The Level 1 Trigger

A hardware based trigger takes in data from the sub-detectors and performs a first set of selections on a very basic object reconstruction. The L1 is divided into three components: L1Calo which operates on calorimeter information, L1Muon utilising the muon spectrometer and L1Topo that applies more complex analysis to jets, electrons, taus and muons after L1Calo. These objects are then sent to the Central Trigger Processor (CTP), these are all illustrated in the Level-1 section of Figure 3.20. This first stage reduces the rate from 40 MHz to 100 kHz before events are passed to the High Level Trigger.

The High Level Trigger

The high level trigger has access to the full detector read out at L1 rate and this system is software based and can apply more complex selections and cuts. Using more sophisticated object reconstruction the rate is reduced from the L1 rate of 100 kHz to around 1 kHz. Events selected by the L1 trigger undergo processing immediately via event buffering provided by the Read-Out System (ROS). The HLT itself consists of a farm of 2800 CPU cores which apply offline-like event reconstruction to the full detector readout with partial track reconstruction, Figure 3.20. Events selected by the HLT are split into different data streams (physics, debug, etc.) before being sent to local storage to be processed by a Tier-0 facility.

The Main Physics Stream is the primary data used for physics analysis. It is split again into different categories based on the physics objects in the event: $b-$jets, electrons, muons, etc. An Express stream uses a small amount of the bandwidth to rapidly reconstruct the data using offline data processing to assess data quality and provide calibration information.

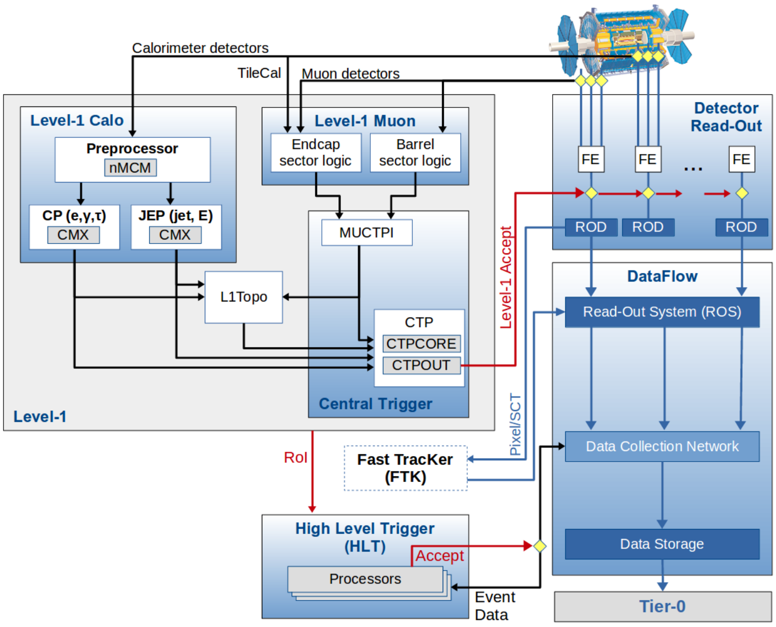

Figure 3.20: Diagram of the ATLAS Trigger and Data Acquisition System in Run 2. Figure taken from [75].

3.4 Object Reconstruction

The core goal of ATLAS is to use the electrical signals from detection to reconstruct all stable and interacting particles produced in a particular $p-p$ collision. With these candidate objects various Standard Model processes, and possibly Beyond the SM interactions, can be studied. After the reconstruction is complete physicists have a collection of events containing “physics objects”, this section will detail the process of building these objects.

Figure 3.21 shows how different particles interact with ATLAS, dashed lines indicate that the particle does not interact with that part of the detector while the solid lines shows that it does.

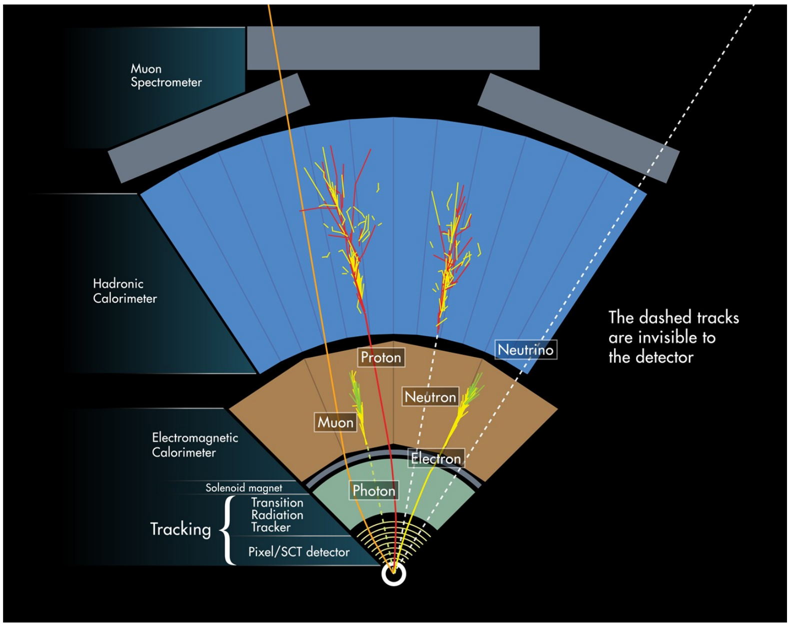

Figure 3.21: A single “wedge” of the detector is shown in the transverse plane with each of the sub-detectors visible, working outwards from the beam-pipe: the ID, electromagnetic calorimeter, hadronic calorimeter and the muon spectrometer. Figure taken from [76]

3.4.1 Tracks and Vertices

Tracks are defined in relation to some reference point, this is typically the beamspot (the average beam position in the detector where p–p collisions occur), and using a set of track parameters: d_0, z_0, ϕ, θ and q/p. Here d_0 is the transverse impact parameter defined as the closest point in the transverse plane to the reference position, z_0 is the longitudinal impact parameter and this is similar to d_0 but in the longitudinal plane. The angles ϕ and θ are the azimuthal and polar angles seen before and finally the ratio q/p is the reconstructed track charge, q, over the track momentum, p.

The reconstruction of tracks begins in the innermost pixel layer using what is known as an “inside-out” approach. The track reconstruction algorithm seeks a track seed which is formed of three space points in unique layers of the pixel or SCT sub-detectors of the ID, as shown in Figure 3.22a. These then constitute the track candidates once they have passed various quality cuts, like momentum, number of hits etc. The tracks are extended into the TRT with classical track extrapolation and when this can be done the track is said to have a TRT extension. A second step in the tracking involves forming tracks from the TRT in regions seeded by electromagnetic calorimeter. These tracks are then extended inwards towards the SCT and pixel detectors. TRT tracks that do not have any silicon hits are retained for photon reconstruction, discussed in Section 3.4.3. These tracks then make up the final reconstructed track collection [77].

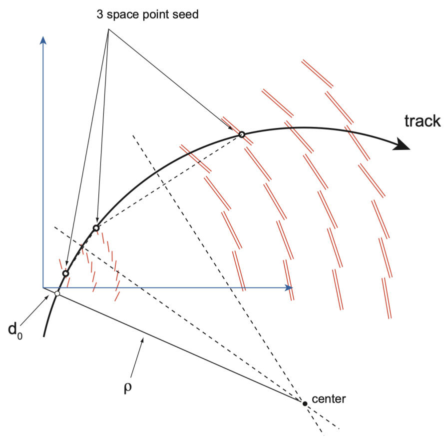

(a) Schematic of Track Seeding Technique [78]

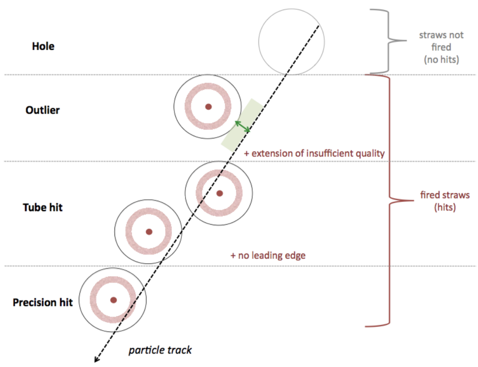

(b) TRT Hits Definitions [77]

Figure 3.22: Schematic of how tracks in ATLAS are seeded, here ρ is the radius of the circle described by the track (a) and the definition of TRT hits (b).

With this track collection the interaction in the bunch crossing with the highest energy, the hard-scatter, can be found by defining primary vertices (PVs). The primary vertices are determined in two steps; vertex finding and vertex fitting [79]. Once a collection of PVs has been found their total number is called N_{PV}, this is a good indicator of pile-up in an event. The hard-scatter interaction is defined as the PV with the highest $\sum p_{\mathrm{T}}^2$ of tracks associated with it. This is defined for each PV but the vertex with the highest value is more likely to be the location at which the interesting physics was produced. All other vertices are then labelled as pile-up vertices.

3.4.2 Electrons

Electrons are reconstructed using information from the EM calorimeter and tracks from the ID. The trajectory of the tracks is projected out to the calorimeter and at that point, or nearby, a calorimeter cluster should be found. ATLAS uses topo-clustering as the standard constituents for electrons and photons (as well as hadronic jets). The clustering algorithm gathers cells that are adjacent to form three-dimensional clusters, these clusters ideally represent the energy and direction of the incident particles. The primary observable used to cluster the cells is the cell energy significance [80]

$$\varsigma_{\text{cell}}^{\text{EM}} = \frac{E_{\text{cell}}^{\text{EM}}}{\sigma_{\text{noisecell}}^{\text{EM}}} \tag{3.11}$$

where $E_{\text{cell}}^{\text{EM}}$ is the measured cell energy and $\sigma_{\text{noisecell}}^{\text{EM}}$ is the expected cell noise. The EM scripts denote that the two variables are measured at the electromagnetic scale [80]. The algorithm clusters the cells as follows:

1. Clustering begins from a seed cell in the calorimeter, which is a cell with its energy significance above a particular threshold, S, $|\varsigma_{\text{cell}}^{\text{EM}}| > S$. For Run 2 data taking $S = 4$.

2. Now the cluster grows outwardly by adding all neighbouring cells that satisfy $|\varsigma_{\text{cell}}^{\text{EM}}| > N$. N is the threshold for growth control and was set at $N = 2$ for Run 2.

3. The cluster boundaries are set by adding cells that meet the condition $|\varsigma_{\text{cell}}^{\text{EM}}| > P$. P is the principal cell filter and in Run 2 this was $P = 0$.

This method is commonly known as the *4-2-0 ATLAS topo-clustering algorithm* [81]. Clusters with a longitudinal and lateral shower profile consistent with that of an EM shower are used to form regions-of-interest (ROIs). Standard track reconstruction is performed in the ID and these tracks can then be matched to the ROIs, while considering the effects of bremsstrahlung in the detector, to seed a supercluster [81].

Superclustering [81] is an improved method of reconstructing electrons (and photons) introduced in 2017 and it replaced a "sliding-window" technique [82].

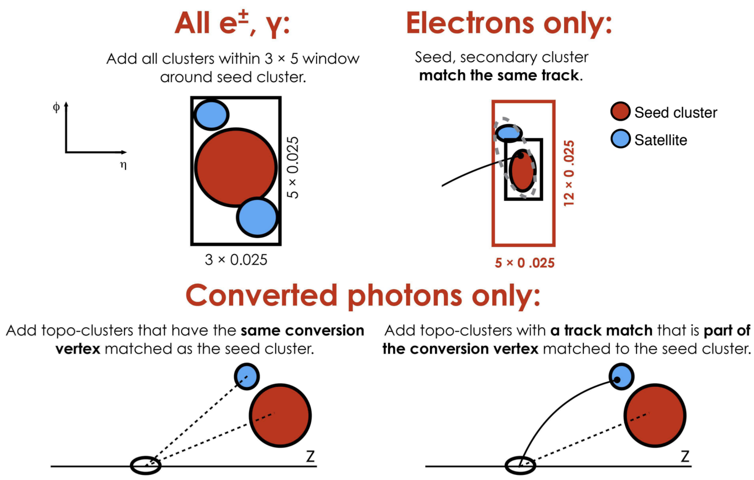

Figure 3.23: Depiction of the superclustering algorithm for electrons and photons. Figure taken from [81]

The electrons are then calibrated using regression boosted decision trees (BDT) trained to correct the energies of the uncalibrated electron candidates [83]. To ensure high purity of electrons a set of quality requirements are applied to them [81], these are commonly referred to as "working points". This is done using a likelihood discriminant and allows the definition of **Loose**, **Medium** and **Tight** quality working points. Isolation working points are also defined by comparing the energy in a cone or region around the electron to the energy of the electron itself [81].

3.4.3 Photons

Reconstruction of photons follows a similar procedure to that of the electrons. The topo-clusters are seeded in a similar manner [83] but then differ in how tracking information is used. To seed a photon supercluster the topocluster must have a slightly higher transverse energy of $E_{\mathrm{T}} > 1.5\,\mathrm{GeV}$ [81].

There are two main photon reconstruction types; a photon can be reconstructed as being converted — and the resulting particles will leave tracks in the ID modules that can be subdivided into single or double-track conversions — or the photon will remain unconverted and appear only as an EM calorimeter deposit [82]. The calibration procedure for photons is also very similar to that of the electrons and the working points are constructed in a similar manner [81].

3.4.4 Muons

Muons are reconstructed using signals from the ID and muon spectrometer (MS) independently. The ID tracks are reconstructed for muons in exactly the same fashion as all other tracks as described in Section 3.4.1. The tracks reconstructed in the MS and ID are combined to form the final collection of muons.

Muons, like electrons and photons, then have some corrections applied to achieve the high precision in momentum and resolution necessary. The correction factors are derived by studying $Z \rightarrow \mu\mu$ and $J/\psi \rightarrow \mu\mu$ in data and Monte Carlo.

Once the muons are reconstructed various restrictions can be imposed to ensure the purity of the muons in much the same way as was done for the electrons. These quality requirements are designed to select signal muons instead of those coming from a background process like the decay of hadronic particles such as kaons or pions. The quality of the tracks, in the ID and MS, that were used to construct the muon is used to define a set of quality working points [84].

3.4.5 Hadronic Jets

Quarks and gluons produced in $p{-}p$ collisions produce jets of hadrons. To construct the jets one can split the process into two broad steps:

1. Use the raw detector signals that come from the energy depositions of the shower in the calorimeter to form constituents.

2. Use these constituents to form groups of particles that represent the jets themselves.

The topo-clustering method is used to form the standard jet constituents, which is the same for electrons and photons; described in Section 3.4.2.

Jet Clustering

The reconstructed topoclusters are then fed into a jet reconstruction algorithm. These algorithms need to be infrared and collinear (IRC) safe meaning that the final jet collection must not be modified by unresolved emissions. One of the most common families of jet finding techniques are the k_t algorithms and in particular the anti-k_t [85]. In this thesis two R values are used to cluster: small-R ($R = 0.4$) and large-R ($R = 1.0$) jets. The smaller variety are the workhorses of many analyses and represent jets coming from quarks or gluons while the larger type are very useful for capturing quarks coming from the decay of heavy boosted particles, W bosons for example.

Electromagnetic Topocluster (EMTopo) Jets

The process described previously is the case for Electromagnetic Topocluster (EMTopo) jets and as seen the inputs to the anti-k_t algorithm are reconstructed topological clusters of calorimeter cells [80]. EMTopo jets were the recommended jet type in ATLAS for quite some time however, the calorimeter is particularly sensitive to pile-up contributions which can alter the jet's four-momentum.

Particle Flow (PFlow) Jets

A new approach known as "particle flow" (PFlow) aims to combine the measurements from the tracker and the calorimeter to form signal inputs for clustering. These signals in the ideal case represent the individual particles which can then be combined into jets. Put simply, the energy of the charged tracks associated with the PV is subtracted from matched calorimeter depositions. Once this is complete there is a collection of "particle flow objects" (charged and neutral) on which reconstruction is performed. A complete flow chart describing the algorithm's operation is given in Figure 3.24.

The first advantage of the PFlow approach is that the spatial resolution for the charged PFlow objects from the tracker is much improved and aids in the reduction of pile-up. Secondly, the momentum resolution of the tracker is superior at low p_{T}, allowing softer particles to be included in the reconstruction of a jet that would not pass the cuts in the topocluster method [70]. As the energy of the particles increases the calorimeter resolution becomes superior (Table 3.1).

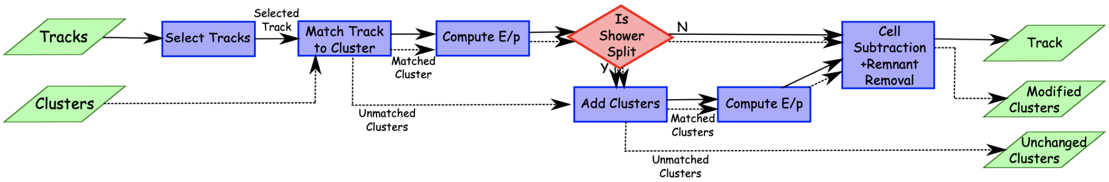

Figure 3.24: A flow chart describing the operation of the particle flow algorithm. Figure taken from [70].

The combination of these two subsystems adds the benefits of both systems while reducing the drawbacks of either in isolation. Figure 3.25 displays a comparison of the absolute uncertainty, $\sigma\left(p_{\mathrm{T}}\right)/p_{\mathrm{T}}$, for PFlow and EMTopo jets in p_{T} and η (Note: on these plots a calibration is applied, as outlined in the next section). The p_{T} distribution highlights the reduction in uncertainty for PFlow at low momentum and then comparable values with EMTopo at high values of p_{T}. In pseudo-rapidity PFlow jets perform better across most of the range of η.

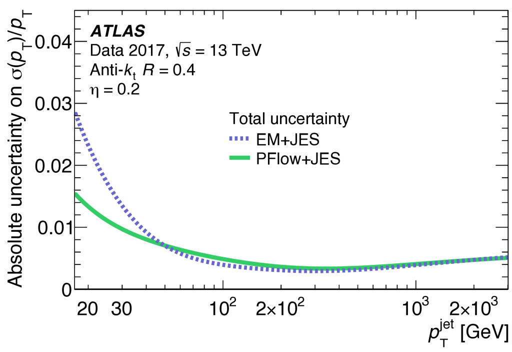

(a) Absolute Uncertainty in p_{T} for EMTopo and PFlow

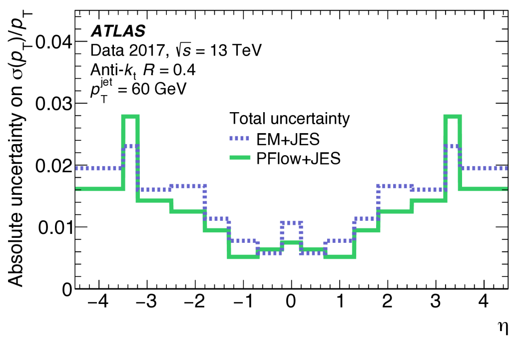

(b) Absolute Uncertainty in η for EMTopo and PFlow

Figure 3.25: The absolute uncertainty for PFlow (with jet energy scaling (JES)) jets, in green, and EMTopo + JES, in blue, as a function of jet p_{T} (left) and the jet pseudo-rapidity or η (right). In the $p_{\mathrm{T}}^{\mathrm{jet}}$ distribution all of the jets considered have $\eta = 0.2$ and in the η the jets have $p_{\mathrm{T}} = 60\,\mathrm{GeV}$. Figure taken from [86].

Jet Calibration

The measured energy of the electromagnetic particles (electron, positron and photon) is at the right scale but this is not the case for hadronic particles as the energy of these is underestimated. Weakly interacting particles produced in the hadronic shower can go undetected in the calorimeters and there are other effects like energy leakage, etc. The four-momentum vectors of the jets must be calibrated using the Jet Energy Scale (JES) calibration, a flow chart of this process is shown in Figure 3.26. This calibration restores the jet energy, momentum and mass to that of the truth scale [86].

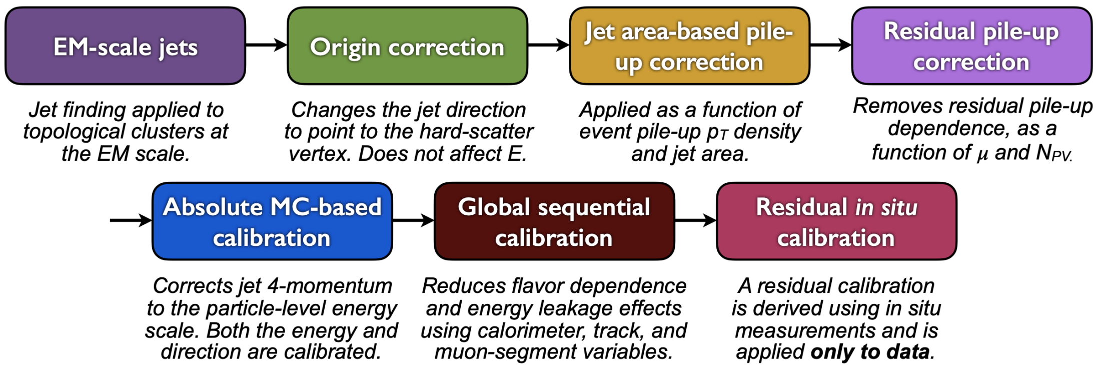

Figure 3.26: Flow diagram showing the process for calibrating the jets to EM-scale, this correction is applied to the full four-momenta of the jets. Figure taken from [86].

Pile-up Jets

The large number of p–p collisions that can occur in a single bunch crossing can alter the objects reconstructed in an event. For jets, pileup can cause the reconstruction of additional jets referred to as pile-up jets. There are two primary sources of pile-up jets:

1. **Stochastic Pile-up Jets**: Random particle fluctuations in the calorimeters occurring in a coherent manner with no particular source and these can be reconstructed as additional jets.

2. **QCD Pile-up Jets**: These are indeed real jets but originate from another single p–p pile-up interaction.

The two types of pile-up are shown in Figure 3.27. To mitigate these ATLAS uses a discriminant called the Jet Vertex Tagger (JVT), this tagger operates using a k-Nearest Neighbour (kNN) algorithm to construct a two-dimensional likelihood using two variables [87]. The first is,

$$R_{p_{\mathrm{T}}} = \frac{\sum_k p_{\mathrm{T}}^{\mathrm{track}_k}(\mathrm{PV}_0)}{p_{\mathrm{T}}^{\mathrm{jet}}}, \tag{3.12}$$

the p_{T} sum of the tracks associated with a jet which also come from the PV, normalised by the calibrated jet p_{T}. For pile-up jets $R_{p_{\mathrm{T}}}$ approaches zero. The second variable is

$$\mathrm{corrJVT} = \frac{\sum_k p_{\mathrm{T}}^{\mathrm{track}_k}(\mathrm{PV}_0)}{\sum_l p_{\mathrm{T}}^{\mathrm{track}_l}(\mathrm{PV}_0) + \frac{\sum_{n\geq 1}\sum_l p_{\mathrm{T}}^{\mathrm{track}_l}(\mathrm{PV}_n)}{k \cdot n_{\mathrm{track}}^{\mathrm{PU}}}}, \tag{3.13}$$

where $\sum_k p_{\mathrm{T}}^{\mathrm{track}_k}(\mathrm{PV}_0)$ is a p_{T} sum of the tracks coming from the hard-scatter vertex that are associated to the jet in question, similar to that described in $R_{p_{\mathrm{T}}}$. The second term in the denominator sums the p_{T} of the tracks in the jet coming from each of the pile-up vertices. The total number of pile-up tracks in an event is $n_{\mathrm{track}}^{\mathrm{PU}}$ and k is a constant factor set to be $k = 0.01$ [87]. JVT selections are applied to jets with $p_{\mathrm{T}} > 20\,\mathrm{GeV}$ and $|\eta| < 2.8$.

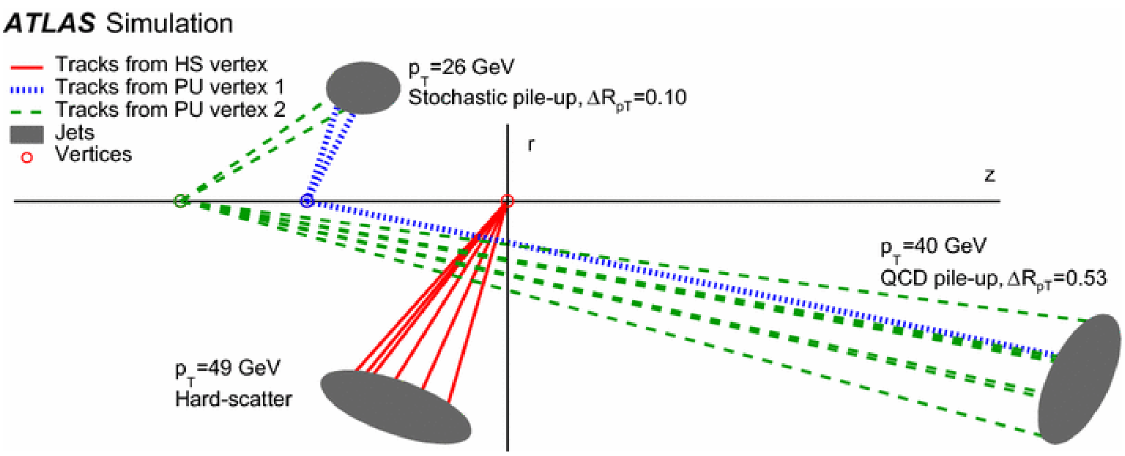

Figure 3.27: Sketch illustrating the various types of pile-up jets with their $R_{p_{\mathrm{T}}}$ values as well as the hard-scatter jet. Figure taken from [88].

Flavour Tagging

The jet collections described above may also be tagged as resulting from a bottom quark using the MV2c10 algorithm [89]. MV2c10 combines track-based variables to form a multivariate discriminant designed to identify jets as being b-flavoured while rejecting those of c or light-flavour in simulated $t\bar{t}$ events. Jets are deemed to be b-flavour if they pass a 70% efficiency working point provided that they have satisfied the JVT conditions along with the kinematic and detector cuts of $p_{\mathrm{T}} > 20\,\mathrm{GeV}$ and $|\eta| < 2.5$. As this algorithm is optimised using simulation, scale factors are applied to correct for the differences in selecting b-jets in data [89].

Finally, jets which do fail a set of quality requirements are vetoed from further analysis to remove contributions from Beam Induced Background (BIB), cosmic rays and calorimeter noise [90].

This thesis primarily uses PFlow jets in the analyses but EMTopo jet collections are used to benchmark the performance gain from the use of particle flow.

3.4.6 Missing Transverse Momentum, $E_{\mathrm{T}}^{\mathrm{miss}}$

The author worked extensively on the performance of missing transverse momentum, $E_{\mathrm{T}}^{\mathrm{miss}}$, and its significance in the ALTAS experiment, producing the first full Run 2 data performance result in ATLAS, and so Chapter 4 is dedicated to the derivation and study of this fascinating quantity.

3.5 Conclusion

Circulating $\sim 10^{11}$ protons per bunch at unprecedented energies in one of the largest machines ever constructed by human kind and colliding them has allowed physicists to probe the smallest scales of matter with incredible accuracy.

This chapter described how such a feat is achieved and in turn how ATLAS is able to measure electronic signals coming from particles produced in $p{-}p$ collisions. Each of the detector components and their purposes were introduced to give an overview of the experiment. Measuring these interactions is but one facet of this complex process. The flood of data that is produced by colliding proton bunches every 25 ns cannot be recorded and so a fast two component trigger system isolates events with the most interesting physics signatures for future analysis.

The primary function of ATLAS is to convert these electrical impulses from subatomic particle interactions into candidate objects that represent the particles of the initial interaction. Each object of interest undergoes a process of reconstruction, calibration and quality selection before all objects in an event are stored. With this phenomenal amount of data physicists, including the author, can test properties of the standard model. Not only that; through hard work, perseverance, dedication to the scientific method, and a hint of luck perhaps find the new physics beyond the SM that lurks just behind this incredible theory.

An expert is a person who has found out by his own painful experience all the mistakes that one can make in a very narrow field.

— Niels Bohr -*Life Magazine, 9th of September 1954*

4
Missing Transverse Momentum and Its Significance in ATLAS

Contents

4.1 Introduction

Missing transverse momentum, $E_{\mathrm{T}}^{\mathrm{miss}}$, is an extremely important quantity in the ATLAS experiment [55]. In the simplest terms it is a measurement of the momentum carried out of the detector by invisible, or non-interacting, particles. In this case "invisible" is meant from the perspective of the detector's eye view, and an invisible particle is one that does not interact with any of the subsystems of ATLAS via the fundamental forces that the experiment relies upon to detect particles.

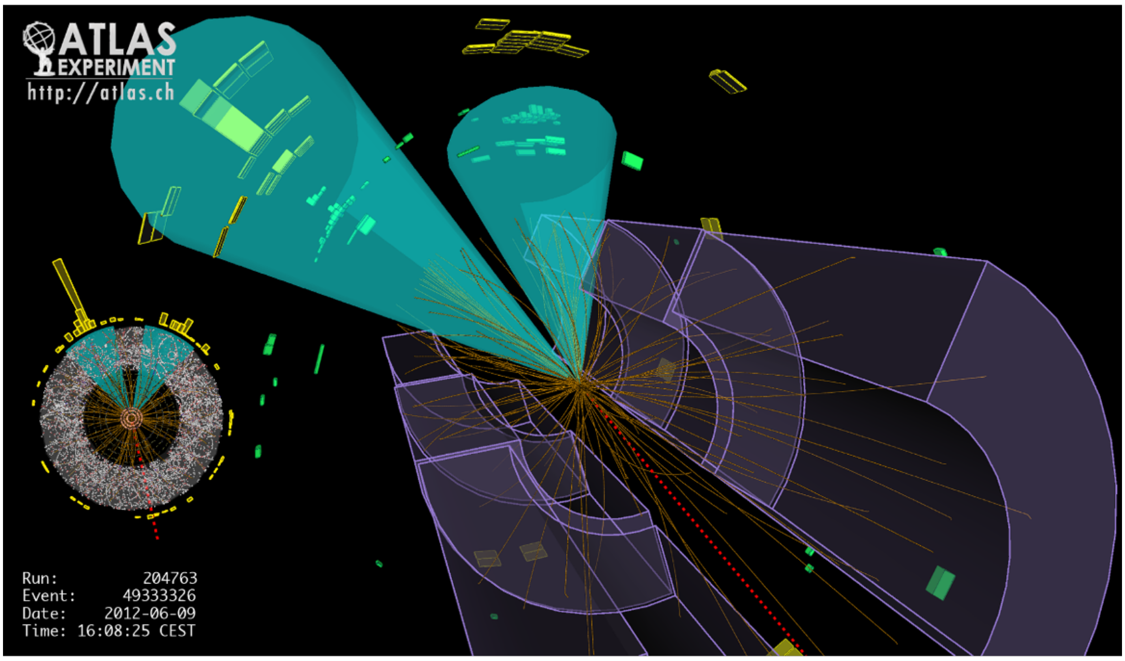

Figure 4.1: An event recorded in the ATLAS experiment that shows two jets, represented by the blue cones, and the calculated $E_{\mathrm{T}}^{\mathrm{miss}}$ seen by the red dashed line. Figure taken from [91].

If one were to make a slightly more rigorous statement: $E_{\mathrm{T}}^{\mathrm{miss}}$ is the momentum imbalance in a plane perpendicular to the LHC beam line and centred on the nominal interaction point. From this perspective $E_{\mathrm{T}}^{\mathrm{miss}}$ seems a rather straightforward but it is in fact a complex event-level quantity that involves significant signals from every component of the detector; tracks from the ID, calorimeter energy deposits and signals in the muon spectrometer. In adding all of these signals together one must rely on having a hermetic detector, to a good approximation, and avoid double counting of energy deposits in different subsystems from the same particle. This calculation is challenging but at the same time it is extremely well motivated. In the standard model (SM) of particle physics there is only one known class of particle that will carry momentum entirely undetected out of the detector, the neutrinos.

Figure 4.1 shows a di-jet event, with the two blue cones representing the reconstructed jets. The red dashed line shows where the momentum imbalance is and could indicate a non-interacting particle escaped detection along this trajectory. If one looks at the small inset image of Figure 4.1, showing the transverse plane of the detector, an intuitive sense of what $E_{\mathrm{T}}^{\mathrm{miss}}$ can be gained.

If dark matter (DM) is formed of a kind of particulate matter then these particles would interact very weakly, perhaps only via the gravitational force. One example, of a theory that predicts dark matter particles is supersymmetry, a well-motivated extension of the SM, which predicts the existence of a stable non-interacting particle called the lightest supersymmetric particle. Many SM measurements, like the determination of Higgs boson properties in different decay channels ($H \to WW$ for example), also greatly benefit from a good understanding of $E_{\mathrm{T}}^{\mathrm{miss}}$ reconstruction.

The momentum in the transverse plane is very close to zero before the interaction of the protons, so summing across the momentum of all detected signals in this plane after the event should also be zero. A value different from this indicates that some momentum has been carried away without registering a signal. The calculation is hindered by particles escaping detector acceptance, since ATLAS does not completely cover the full 4π steradians of the solid angle, also signals from other proton interactions in the same bunch crossing (in-time pileup) and even signals from the preceding or subsequent bunch crossings (out-of-time pileup).

4.2 Stuff You Should Know About $E_{\mathrm{T}}^{\mathrm{miss}}$

Since the very beginning of p–p data taking at the LHC in 2010 ATLAS has developed robust and accurate techniques to compute the missing transverse momentum in the detector [92][93]. During the data-taking period known as Run 1 (2010 to 2012) during which the p–p centre of mass energy was 7 TeV, the calculation was split into contributions from the calorimeter and signals in the muon spectrometer [92].

Importantly $E_{\mathrm{T}}^{\mathrm{miss}}$ is calculated in the transverse plane of the detector. Figure 4.2 shows that the momentum of a particle can be projected onto the transverse plane with two components of momentum (p_x and p_y). Ideally, if all particles in an event could be reconstructed perfectly in an entirely hermetic detector then the missing transverse momentum is a negative vector sum of the transverse momenta of all the particles in an event,

$$E_{\mathrm{x(y)}}^{\mathrm{miss}} = - \sum_{i\,\in\,\mathrm{particles}} p_{x(y),i}. \tag{4.1}$$

In this form one would have a set of observables constructed from this calculation including; a missing transverse momentum vector

$$\mathbf{E}_{\mathrm{T}}^{\mathrm{miss}} = \left(E_{\mathrm{x}}^{\mathrm{miss}}, E_{\mathrm{y}}^{\mathrm{miss}}\right), \tag{4.2}$$

the magnitude of this vector as well as a direction in azimuthal angle (ϕ, Figure 4.2),

$$E_{\mathrm{T}}^{\mathrm{miss}} = \left|\mathbf{E}_{\mathrm{T}}^{\mathrm{miss}}\right| = \sqrt{{E_{\mathrm{x}}^{\mathrm{miss}}}^2 + {E_{\mathrm{y}}^{\mathrm{miss}}}^2} \tag{4.3}$$

and

$$\phi^{\mathrm{miss}} = \arctan\left(\frac{E_{\mathrm{y}}^{\mathrm{miss}}}{E_{\mathrm{x}}^{\mathrm{miss}}}\right). \tag{4.4}$$

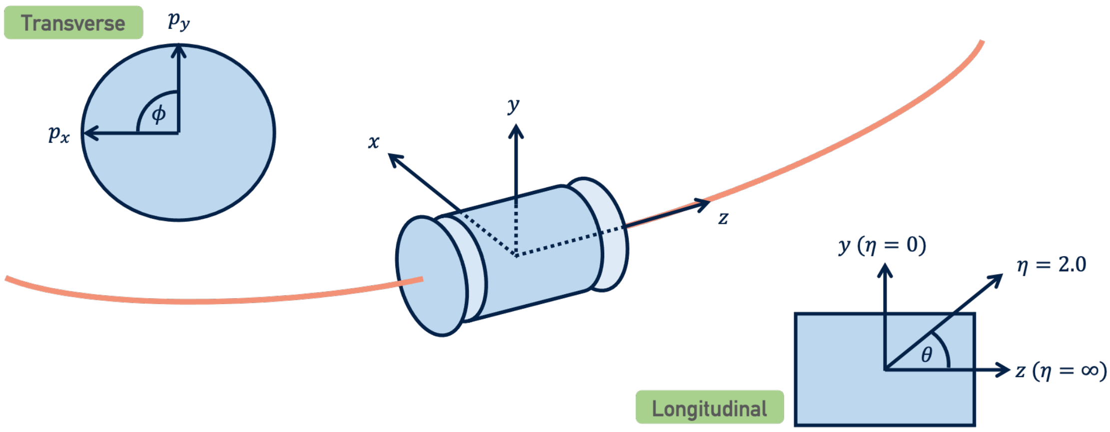

Figure 4.2: A simplistic schematic of the ATLAS experiment where the red sweeping line indicates the LHC beamline and the Cartesian coordinate system is overlaid on the barrel of the experiment. Two important planes are shown; the transverse plane (top left) and the longitudinal plane (bottom right). The transverse plane shows the two components of momentum as well as the azimuthal angle, the longitudinal shows some examples of the pseudo-rapidity, η. For a complete picture of the ATLAS detector refer to Chapter 3.

In reality particles are not reconstructed perfectly and the detector is not completely hermetic.

4.3 Run 2: A League Above

During Run 1 (2010-2012) there were increases in centre of mass energy and the average number of interactions per bunch crossing, $\langle\mu\rangle$, and Run 2 is no exception to this. A large increase in beam energy allowed the accelerator to collide protons with $\sqrt{s} = 13\,\text{TeV}$, approaching the original design capacity. The number of interactions per bunch crossing also increased to further complicate matters. Figure 4.3 illustrates the pile-up distribution for the entirety of the run, in blue, there is a large range in the mean number of interactions per bunch crossing and importantly a sizeable number of events with $\langle\mu\rangle > 50$.

Following on from the lessons learned in Run 1 [92][93], $E_{\mathrm{T}}^{\mathrm{miss}}$ evolved to cope with the changing conditions. Higher collision energy means higher p_{T} neutrinos and the possibility of producing massive BSM particles, and the (Blues Brothers-esque car) pileup of proton collisions occurring in every bunch crossing means more energy deposition in the detector not coming from the hard-scatter one is attempting to calculate $E_{\mathrm{T}}^{\mathrm{miss}}$ for.

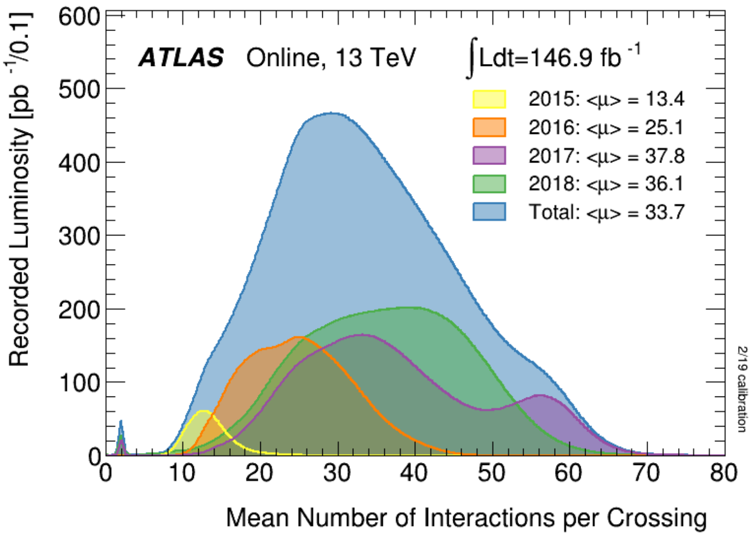

Figure 4.3: The mean number of interaction per bunch crossing weighted by the luminosity during Run 2. The distribution for the complete Run 2 luminosity is shown as well as the distributions for each year of data taking. Figure taken from [63]

Reconstruction of $E_{\mathrm{T}}^{\mathrm{miss}}$ is performed in two separate parts; the first is the contribution from all fully calibrated and well defined physics objects (hard objects) coming from the hard-scatter (HS) vertex. The second component is the soft term, comprising all detector signals associated to the HS but not with any of the pre-defined physics objects. $\mathbf{E}_{\mathrm{T}}^{\mathrm{miss}}$ is then the negative vector sum over these two components

$$\mathbf{E}_{\mathrm{T}}^{\mathrm{miss}} = \underbrace{- \sum_{i \in \text{Hard Objects}} \mathbf{p}_{\mathrm{T}}^{i}}_{\mathbf{E}_{\mathrm{T}}^{\text{miss, Hard}}} \underbrace{- \sum_{i \in \text{Soft Signals}} \mathbf{p}_{\mathrm{T}}^{i}}_{\mathbf{E}_{\mathrm{T}}^{\text{miss, Soft}}} . \tag{4.5}$$

The first term is the hard term which contains a vector sum of all the transverse momenta for each accepted physics object

$$\mathbf{E}_{\mathrm{T}}^{\text{miss, Hard}} = - \sum_{\text{Electrons}} \mathbf{p}_{\mathrm{T}}^{e} - \sum_{\text{Photons}} \mathbf{p}_{\mathrm{T}}^{\gamma} - \sum_{\tau \text{ leptons}} \mathbf{p}_{\mathrm{T}}^{\tau} - \sum_{\text{Muons}} \mathbf{p}_{\mathrm{T}}^{\mu} - \sum_{\text{Jets}} \mathbf{p}_{\mathrm{T}}^{\text{jets}} . \tag{4.6}$$

The second component of eq. 4.5 is the soft term. The track soft term (TST) is formed by using all of the tracks associated with the HS vertex and not with the particles or jets [94]. The $E_{\mathrm{T}}^{\mathrm{miss}}$ observables seen earlier in Equations 4.2, 4.3 and 4.4 can then be determined. Combining the soft term with the complete hard term expression, the entire $\mathbf{E}_{\mathrm{T}}^{\mathrm{miss}}$ reconstruction is:

$$\mathbf{E}_{\mathrm{T}}^{\mathrm{miss}} = \underbrace{\underbrace{-\sum_{\substack{\text{Selected}\\\text{Electrons}}} \mathbf{p}_{\mathrm{T}}^{e}}_{\mathbf{E}_{\mathrm{T}}^{\mathrm{miss,\,e}}} \underbrace{-\sum_{\substack{\text{Selected}\\\text{Photons}}} \mathbf{p}_{\mathrm{T}}^{\gamma}}_{\mathbf{E}_{\mathrm{T}}^{\mathrm{miss,}\,\gamma}} \underbrace{-\sum_{\substack{\text{Selected}\\\text{Taus}}} \mathbf{p}_{\mathrm{T}}^{\tau}}_{\mathbf{E}_{\mathrm{T}}^{\mathrm{miss,}\,\tau}} \underbrace{-\sum_{\substack{\text{Selected}\\\text{Muons}}} \mathbf{p}_{\mathrm{T}}^{\mu}}_{\mathbf{E}_{\mathrm{T}}^{\mathrm{miss,}\,\mu}} \underbrace{-\sum_{\substack{\text{Selected}\\\text{Jets}}} \mathbf{p}_{\mathrm{T}}^{\mathrm{jets}}}_{\mathbf{E}_{\mathrm{T}}^{\mathrm{miss,\,jet}}}}_{\text{Hard Term}} \underbrace{\underbrace{-\sum_{\substack{\text{Unused}\\\text{Tracks}}} \mathbf{p}_{\mathrm{T}}^{\mathrm{soft}}}_{\mathbf{E}_{\mathrm{T}}^{\mathrm{miss,\,Soft}}}}_{\text{Soft Term}} . \tag{4.7}$$

To give an indication of the amount of activity in an event one can measure the scalar sum of all transverse momenta,

$$\sum E_{\mathrm{T}} = \underbrace{\sum_{\substack{\text{Selected}\\\text{Electrons}}} p_{\mathrm{T}}^{e} + \sum_{\substack{\text{Selected}\\\text{Photons}}} p_{\mathrm{T}}^{\gamma} + \sum_{\substack{\text{Selected}\\\text{Taus}}} p_{\mathrm{T}}^{\tau} + \sum_{\substack{\text{Selected}\\\text{Muons}}} p_{\mathrm{T}}^{\mu} + \sum_{\substack{\text{Selected}\\\text{Jets}}} p_{\mathrm{T}}^{\mathrm{jet}}}_{\text{Hard Term}} + \underbrace{\sum_{\substack{\text{Unused}\\\text{Tracks}}} p_{\mathrm{T}}^{\mathrm{soft}}}_{\text{Soft Term}} \tag{4.8}$$

where $E_{\mathrm{T}} = |\mathbf{E}_{\mathrm{T}}|$ and $p_{\mathrm{T}} = |\mathbf{p}_{\mathrm{T}}|$. This quantity allows the evaluation of the overall scale to assess the hardness of an event in the transverse plane. The hard terms in $E_{\mathrm{T}}^{\mathrm{miss}}$ and $\sum E_{\mathrm{T}}$ (Equations 4.7 and 4.8) are typically pile-up resistant as they are composed of fully reconstructed and calibrated physics objects and these calibrations include a pile-up correction. The soft term can have considerable pile-up dependence if the calorimeter deposits are used. This is one of the main reasons for using tracks coming from the hard scatter vertex as the soft term. This suppresses the amount of energy from in-time pile-up activity entering the $E_{\mathrm{T}}^{\mathrm{miss}}$ calculation and almost completely eliminates contributions from out-of-time pile-up.

The ordering of the objects is very important and must be considered to avoid double counting of energy deposits associated with more than one reconstructed particle. The reconstructed and calibrated objects have an ordering of priority to enter the $E_{\mathrm{T}}^{\mathrm{miss}}$ calculation, this is kept the same as the early Run 2 analysis [94]. First in line are the electrons (e) followed by photons (γ), hadronically decaying taus (τ_{had}), muons (μ) and finally the jets. Passing the objects in this way maintains flexibility for the various physics analyses so if one were to not include a particular type of electron, or any of the object types, this would change the values of $E_{\mathrm{T}}^{\mathrm{miss}}$ and $\sum E_{\mathrm{T}}$. In this configuration the desired electron, or object type, collection can be easily passed to the $E_{\mathrm{T}}^{\mathrm{miss}}$ calculation, this also allows for systematic variations to be easily included.

All electrons that pass selection criteria are included in the $E_{\mathrm{T}}^{\mathrm{miss}}$ first. If a lower priority object shares a calorimeter deposit with a higher order particle that has already been accepted for the $E_{\mathrm{T}}^{\mathrm{miss}}$ calculation that lower order object is rejected entirely. Muons are slightly more complex to deal with and only non-isolated muons will overlap with other objects (mostly jets and taus) and share calorimeter energy deposits. The full treatment of muons is discussed in Section 4.4.4. The soft term is of lowest priority formed from the tracks not associated with any physics object and enters the $E_{\mathrm{T}}^{\mathrm{miss}}$ calculation last. A short summary of the priority of each object type along with the selections is given in Table 4.1.

4.4 Object Selection

A more detailed description of the objects that are used in this analysis of the performance of $E_{\mathrm{T}}^{\mathrm{miss}}$ for the full Run 2 dataset is presented in this section. A short summary of the selections is given in Table 4.1 and one should note that other object selections can be used that best suit a particular analysis which highlights the flexibility of this approach to $E_{\mathrm{T}}^{\mathrm{miss}}$.

4.4.1 Electrons

Reconstruction of the electrons is performed using seeded clusters in the electromagnetic (EM) calorimeter that are matched to an inner detector track. These matched tracks and clusters are identified as electrons using a likelihood-based algorithm [81]. In this analysis the electrons are required to have $p_{\mathrm{T}} \geq 25\,\mathrm{GeV}$ and $|\eta| < 2.47$. To remove electrons from the crack region between the barrel and

Priority	Object	Selections	Comments
1	e	$\|\eta\| < 2.47$, $p_{\mathrm{T}} > 25\,\mathrm{GeV}$, $\|d_0\| < 5.0\,\mathrm{mm}$, $\|z_0 \sin(\theta)\| < 0.5\,\mathrm{mm}$	All $e^{\pm}$ passing quality and kinematic selections.
2	γ	$\|\eta\| < 1.37$ or $1.52 < \|\eta\| < 2.47$, $p_{\mathrm{T}} > 130\,\mathrm{GeV}$	All γ passing quality and kinematic selections, and without signal overlap with (1).
3	τ_{had}	$\|\eta\| < 2.5$, $p_{\mathrm{T}} > 20\,\mathrm{GeV}$	All τ_{had} passing quality and kinematic selections, and without signal overlap with (1) or (2).
4	μ	$\|\eta\| < 2.7$, $p_{\mathrm{T}} > 25\,\mathrm{GeV}$, $\|d_0\| < 5.0\,\mathrm{mm}$, $\|z_0 \sin(\theta)\| < 0.5\,\mathrm{mm}$	All μ passing quality and kinematic selections, and following the μ-jet overlap removal procedure.
5	jet	$p_{\mathrm{T}} > 20\,\mathrm{GeV}$, $\|\eta\| < 4.5$, $JVT > 0.59$: EMTopo, $p_{\mathrm{T}} < 60\,\mathrm{GeV}, \|\eta\| < 2.4$, $fJVT < 0.5$: EMTopo, $p_{\mathrm{T}} < 50\,\mathrm{GeV}, 2.4 < \|\eta\|$, $JVT > 0.5$: PFlow, $p_{\mathrm{T}} < 60\,\mathrm{GeV}, \|\eta\| < 2.4$	All jets passing quality and kinematic selections, without signal overlap with (1)-(3), and following the μ-jet overlap removal procedure.
6	ID track (soft term)	$p_{\mathrm{T}} > 400\,\mathrm{MeV}$, $\|d_0\| < 1.5\,\mathrm{mm}$, $\|z_0 \sin(\theta)\| < 1.5\,\mathrm{mm}$, $\Delta R(\mathrm{track}, e/\gamma\mathrm{cluster}) > 0.05$, $\Delta R(\mathrm{track}, \tau_{\mathrm{had}}) > 0.2$.	All hard-scatter ID tracks passing quality and kinematic selections, without signal overlap with (1), (3)-(5).

Table 4.1: Summary of the ordering and selections imposed on each of the objects that go into computing $E_{\mathrm{T}}^{\mathrm{miss}}$ and $\sum E_{\mathrm{T}}$. The transverse and longitudinal impact parameters (d_0 and z_0) play an important role in ensuring that tracks entering the soft term are coming from the hard scatter vertex. The ordering is kept the same as it was in the earlier analysis of 13 TeV data [94].

end-cap calorimeter, they satisfy the "LooseAndBLayerLLH" quality selections [95] and impact parameter restriction of $|z_0 \sin\theta| < 0.5\,\text{mm}$ and $d_0/\sigma(d_0) < 5$. The signal electrons have to be isolated according to the "GradientLoose" working point and pass the "TightLLH" quality criteria [96].

4.4.2 Photons

Reconstruction of photons follows a similar procedure to that of the electrons using EM calorimeter deposits with $|\eta| < 2.47$ and also excluding the EM calorimeter transition region $1.37 < |\eta| < 1.52$. The topo-clusters are seeded in the same manner [83] but after this the inclusion of tracking information is the main difference. There are two main photon reconstruction types; a photon will be reconstructed as being converted and the resulting particles will leave tracks in the ID modules that can be subdivided into single or double-track conversions or the photon will remain unconverted and appear only as an EM calorimeter deposit [82].

Calibration of the photons and electrons is done in the same manner [97]. "Tight" identification settings as well as the "FixedCutTight" isolation criteria are applied and finally a transverse momentum restriction of $p_{\mathrm{T}} > 130\,\text{GeV}$.

4.4.3 Hadronic Taus

Hadronically decaying taus are reconstructed using tracks from the ID, EM and hardronic calorimeter clusters. To reconstruct a τ-lepton jets are fed in to the algorithm and a boosted decision tree then differentiates between jets caused by other particles and those coming from τ-leptons [98]. Candidate τ particles are required to pass the "Medium" working point [98], have $p_{\mathrm{T}} > 20\,\text{GeV}$ and $|\eta| < 2.5$. Taus which fail to meet these requirements can still enter the $E_{\mathrm{T}}^{\mathrm{miss}}$ calculation as jets and those that decay leptonically to and electron or muon will enter the calculation under those object types.

4.4.4 Muons

Muons are found by combining hits in the muon spectrometer's (MS) various subsystems where coordinates can be measured in, and orthogonal to, the bending plane of the detectors magnetic field. These hits are combined to form segments in each of the MS layers that may then be gathered into track candidates and after a χ^2 fit these candidates are accepted if the requisite selections are met. Independently of the MS reconstruction the tracks in the inner detector (ID) are processed and in most cases a combined fit is achieved by extrapolating the MS track inwards and associated with an ID track [84].

Muons must have $p_\mathrm{T} > 25\,\mathrm{GeV}$ and $|\eta| < 2.7$. To suppress muons originating from secondary vertices the muons must have a transverse impact parameter with $|d_0| < 5.0\,\mathrm{mm}$ and a longitudinal impact parameter that satisfies $|z_0 \sin\theta| < 0.5\,\mathrm{mm}$. The muon candidates must also have passed the overlap removal procedure and pass the "Medium" quality criteria [84]. Extending these criteria signal quality muons must also satisfy the conditions of "FCLoose" isolation [84].

4.4.5 Jets

Two jet reconstruction methods are used in this analysis, EMTopo and PFlow jets (Section 3.4.5 and Section 3.4.5). Both of these methods reconstruct using the anti-k_t jet algorithm [85] using a radius of $R = 0.4$ [1] in $\eta - \phi$ space. In the case of EMTopo jets the input to the anti-k_t algorithm are reconstructed topological clusters of calorimeter cells [80].

For particle flow (PFlow) jet collections are formed using inputs from the calorimeter and the tracker that ideally represent individual particles. The energies of any charged particles, found by matching the tracker signals to a cluster of cells in the calorimeter, are removed from the calorimeter to leave neutral PFlow objects. Reconstruction is then performed on these remaining calorimeter energy deposits

[1] The radius of the jet is defined as $R = \sqrt{(\Delta\eta)^2 + (\Delta\phi)^2}$

and tracks (charged PFlow objects) associated to the hard scatter (HS) vertex.

The first advantage of the PFlow approach is that the spatial resolution for the charged PFlow objects from the tracker is much improved and aids in the reduction of pile-up. Secondly, the momentum resolution of the tracker is superior at low p_{T} allowing softer particles to be included in the reconstruction of a jet that would not pass the cuts in the topo-cluster method [70].

4.4.6 $E_{\mathrm{T}}^{\mathrm{miss}}$ Soft Term

The soft term, first encountered in Section 4.3, can be reconstructed in a variety of ways but in this thesis it will be limited to two: the *track soft term* (TST) and the *calorimeter soft term* (CST). The TST tends to perform better than the equivalent calorimeter soft term due to the increase in pile-up dependence of the calorimeter.

Track Soft Term

Tracks and vertices are selected as in Section 3.4.1 and each event is required to have at least one primary vertex. These tracks, if they are not associated with a physics object and have $|\eta| < 2.5$, then enter the $\mathbf{E}_{\mathrm{T}}^{\mathrm{miss,\,Soft}}$ term. To avoid overlap with the other physics objects an overlap removal procedure is applied, tracks that satisfy:

1. $\Delta R\,(\text{track}, e \text{ or } \gamma \text{ cluster}) < 0.5$
2. $\Delta R\,(\text{track}, \tau) < 0.5$
3. associated with a muon
4. ghost associated with a jet

are not included in $\mathbf{E}_{\mathrm{T}}^{\mathrm{miss,\,Soft}}$. The selection of tracks in this way means that the TST is highly resistant to pile-up however it will not include contributions from neutral particles.

Calorimeter Soft Term

The other method for constructing $\mathbf{E}_{\mathrm{T}}^{\mathrm{miss,\,Soft}}$ uses the calibrated calorimeter clusters that are not associated with any physics objects. In this thesis the default soft term will be the TST unless otherwise stated.

4.5 Datasets

4.5.1 Data

The analyses presented in this chapter used the full Run 2 data set with a total integrated luminosity of $139\,\mathrm{fb}^{-1}$. The data collected were from proton-proton collisions with 25 ns bunch spacing at a centre-of-mass energy of 13 TeV. The uncertainty on the total luminosity is 1.7% [62], estimated using the LUCID-2 detector [99]. Only high quality data collected with a fully operational detector were used and a set of quality criteria are applied to reduce instrumental noise and the impacts of cosmic ray events.

4.5.2 Monte Carlo Simulation

The principal event type analysed here is $Z \to \ell\ell$, explained more completely in Section 4.6, so a set of Monte Carlo simulations were curated to predict the data. Monte Carlo simulations are used to model SM processes that can then be normalised using the predictions for their cross sections.

The $Z \to \ell\ell$ events were modelled using two generators. In the first instance events were generated with the Powheg-Box [100] using a matrix element calculation at next-to-leading order (NLO). To generate the parton shower and the underlying event the matrix element was passed to Pythia8 [101] using the AZNLO tuned parameter set [102]. The parton distribution functions (PDFs) came from the CTEQ6L1 [103] PDF set. The second method employs Sherpa [104] for the matrix element, parton showering and underlying event and the PDFs came from the NNPDF3.0 NNLO PDF [105].

Other processes contributing to the $Z \to \ell\ell$ events like $t\bar{t}$, single top quarks and diboson are also simulated. The $t\bar{t}$ events used the POWHEG-BOX [100] to simulate the matrix element and the parton showering was performed with PYTHIA8 [101] with the NNPDF2.3 LO PDF set and the A14 ATLAS tune [106]. Events with single top quarks used the same setup and tune as the $t\bar{t}$ processes. Dibosons (WW, WZ, ZZ) were produced using the POWHEG and PYTHIA8 scheme, using the AZNLO tuned parameter set [102], but using the CT10 PDF set. All simulated events were passed through the ATLAS detector simulation infrastructure [107] which is based on GEANT4 [108] to determine the detector response.

4.6 Event Selection

The performance of the $E_{\mathrm{T}}^{\mathrm{miss}}$ can be estimated by isolating certain event types known to have particular properties related to the true values of true $E_{\mathrm{T}}^{\mathrm{miss}}$. This thesis will focus on the leptonic Z decays as these are assumed to have $E_{\mathrm{T}}^{\mathrm{miss,\,true}} = 0$.

4.6.1 $Z \to \ell\ell$

For evaluating $E_{\mathrm{T}}^{\mathrm{miss}}$ performance, the $Z \to \ell\ell$ final state is very well motivated as events can be selected with extremely high signal to background ratio. As well as this the Z boson is well understood, and it may have its kinematics measured to high precision. There are, in actual fact, two channels considered for the leptonically decaying Z boson, $Z \to \mu\mu$ and $Z \to ee$. There is a well defined expectation value for the Z decay to electrons or muons, $E_{\mathrm{T}}^{\mathrm{miss,\,true}} = 0$. This is because neutrinos are only produced in very rare heavy flavour decays in the hadronic recoil off the Z; for this reason one can say that, almost always, $Z \to \ell\ell$ has no genuine $E_{\mathrm{T}}^{\mathrm{miss}}$.

The scale and resolution of the $E_{\mathrm{T}}^{\mathrm{miss}}$ is well defined in this channel and reflects the resolution of object reconstruction of the physics objects. This final state is also well reconstructed in the presence of pile-up for further motivation. For the $Z \to \mu\mu$ case the performance of the muon-jet overlap removal can be gauged. All of the aforementioned reasons apply to both data and MC and so the performance will be tested using data-MC comparisons.

There are two different sets of conditions to select $Z \to ee$ and $Z \to \mu\mu$ events although they are grouped under the banner of $Z \to \ell\ell$. The conditions to reconstruct the Z itself are the same but the selections on the lepton types do differ. In order to select events for recording a set of triggers are employed. In the case of the muons events must pass one of three high-level muon triggers with different p_{T}^{μ} and isolation requirements [109] which are summarised in Table 4.2. The next level of selection comes at the offline stage and requires that there be exactly two muons that pass the conditions and selections described in Section 4.4.4. The two muons must have opposite charge and both satisfy $p_{\mathrm{T}}^{\mu} > 25\,\mathrm{GeV}$.

Muon Trigger Name	p_{T}^{μ} Condition	Isolation Requirement
`HLT_mu20_iloose_L1MU15`	$p_{\mathrm{T}}^{\mu} > 20\,\mathrm{GeV}$	"Loose", $p_{\mathrm{T}}^{\mathrm{cone}}/p_{\mathrm{T}}^{\mu} < 0.12$
`HLT_mu26_ivarmedium`	$p_{\mathrm{T}}^{\mu} > 26\,\mathrm{GeV}$	"Medium", $p_{\mathrm{T}}^{\mathrm{cone}}/p_{\mathrm{T}}^{\mu} < 0.06$
`HLT_mu50`	$p_{\mathrm{T}}^{\mu} > 50\,\mathrm{GeV}$	No Isolation Requirement

Table 4.2: A summary table of the muon triggers used to select $Z \to \mu\mu$ events for $E_{\mathrm{T}}^{\mathrm{miss}}$ performance studies. The isolation requirements are a ratio between the scalar sum of all tracks within a cone of $\Delta R = 0.2$ around the muon and not including the muon track itself ($p_{\mathrm{T}}^{\mathrm{cone}}$) to the momentum of the muon (p_{T}^{μ}).

The electrons used to isolate $Z \to ee$ events must also satisfy a set of triggers with their own conditions [110]. In a similar fashion to the muons the electrons need to fulfil all the quality conditions outlined in Section 4.4.1 and the event must have exactly two oppositely charged electrons with $p_{\mathrm{T}}^{e} > 25\,\mathrm{GeV}$.

For both $Z \to ee$ and $Z \to \mu\mu$ events the reconstructed invariant mass of the di-muon or di-electron events must be close to the mass of the Z boson, $|m_{\ell\ell} - m_Z| < 25\,\mathrm{GeV}$ where $\ell\ell$ is $\mu\mu$ or ee.

4.7 $E_{\mathrm{T}}^{\mathrm{miss}}$ Performance in Run 2

The performance of the defined $E_{\mathrm{T}}^{\mathrm{miss}}$ observables will be studied using a set of data-MC comparisons in the channels outlined in Section 4.6. The decay of Z bosons to muons is considered and shown in terms of the primary missing transverse momentum variables: $E_{\mathrm{T}}^{\mathrm{miss}}$, $E_{\mathrm{x}}^{\mathrm{miss}}$, $E_{\mathrm{y}}^{\mathrm{miss}}$ and ϕ^{miss} from Equations 4.2, 4.3 and 4.4.

Aside from processes that can pass all the selection cuts and be accepted as a $Z \rightarrow \mu\mu$ event with a real neutrino present, the measured $E_{\mathrm{T}}^{\mathrm{miss}}$ will be a reflection of resolution and reconstruction effects. This limit on the resolution of the detector, the inability to reconstruct each of the object terms perfectly and the fact that contributions from pile-up cannot be completely eliminated result in there being an experimental bias to observe non-zero values of $E_{\mathrm{T}}^{\mathrm{miss}}$.

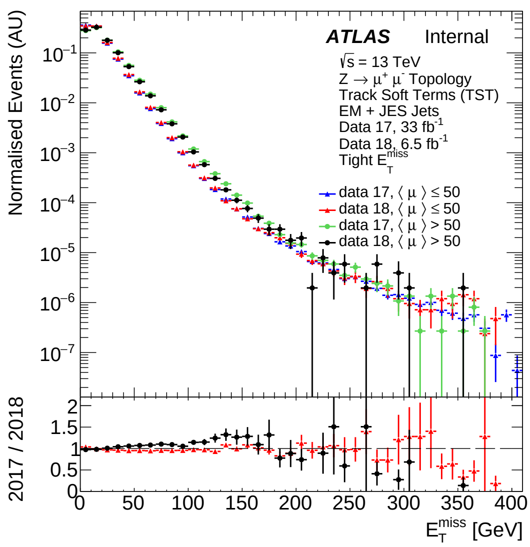

Figure 4.4: To ensure that $E_{\mathrm{T}}^{\mathrm{miss}}$ reconstruction was running properly a small subset of 2018 data was compared to the 2017 data with different $\langle\mu\rangle$ conditions applied before the $E_{\mathrm{T}}^{\mathrm{miss}}$ calculation to check high and lower pile-up conditions.

Given that several different processes can contribute to the final state in question by satisfying all the object requirements and cuts this needs to be accounted for in the Monte Carlo simulations. These other processes need to be weighted according to the cross-section of the process as well as having the pile-up profile scaling factor applied.

The MC in general is scaled using all of these factors to a standard luminosity of $1\,\mathrm{pb}^{-1}$ then the simulation can be scaled to the luminosity of the data it is being compared to, for Run 2 plots the MC is scaled to $139\,\mathrm{fb}^{-1}$ of recorded ATLAS data.

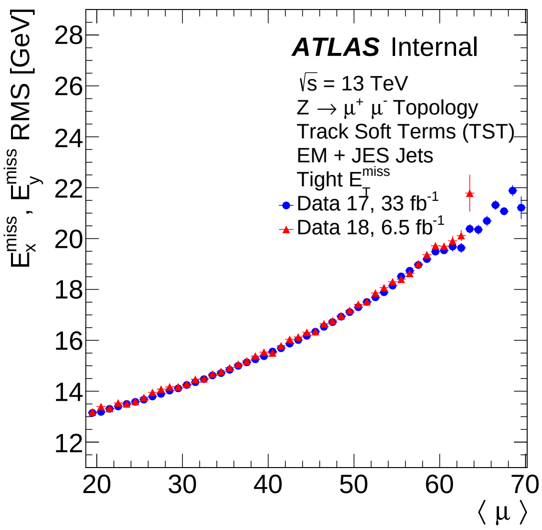

Figure 4.5: The $E_{\mathrm{x}}^{\mathrm{miss}}$ and $E_{\mathrm{y}}^{\mathrm{miss}}$ components have their RMS taken as a function of $\langle\mu\rangle$. These two components are then combined in a quadratic sum to give the single line. The agreement between the two years is excellent indicating that reconstruction between years was consistent.

At the beginning of data taking in 2018 the author performed quality checks to ensure that the $E_{\mathrm{T}}^{\mathrm{miss}}$ reconstruction was consistent with the previous year's data taking. These plots used only a small amount of the 2018 data that had been recorded in 2018 but that are instructive apart from this in a few ways. Figure 4.4 highlights the pile-up dependence of the $E_{\mathrm{T}}^{\mathrm{miss}}$; when $\langle\mu\rangle > 50$ the distribution shifts out to the right indicating that the busier environment is contributing to the $E_{\mathrm{T}}^{\mathrm{miss}}$ calculation. The two years are in good agreement and some differences are due to the difference in pile-up profile between each year, see Figure 4.3. The RMS of the two $E_{\mathrm{T}}^{\mathrm{miss}}$ components can be plotted as a function of average number of interactions per bunch crossing for the same small test set, as in Figure 4.5. This is also illustrative of the $E_{\mathrm{T}}^{\mathrm{miss}}$ dependence on $\langle\mu\rangle$ as the RMS of the two components increases with $\langle\mu\rangle$. The lack of red data 2018 points at high $\langle\mu\rangle$ come as a result of the smaller quality test data set being used.

Figure 4.6 has the full set of $E_{\mathrm{T}}^{\mathrm{miss}}$ observables for the $Z \to \mu\mu$ event selection discussed in Section 4.6.1. Each of these plots, and many of those later in this chapter, have a similar arrangement. The Run 2 distributions all consider the full data set of $139\,\mathrm{fb}^{-1}$ at $\sqrt{\mathrm{s}} = 13\,\mathrm{TeV}$ and the various background are broken down into three components (for the $Z \to \ell\ell$ events) that are labelled in the right hand legend. The data are represented by the black points while the MC contributions are given by the coloured histograms stacked on top of one another. The upper left corner contains information about the event selection, luminosity and centre of mass energy as just discussed it does also contain information about the jets used. The second piece of information on jets is the `incljet` line that can be seen in Figure 4.6 and this is shorthand for "inclusive jets" and indicates that all jets passing the requirements of Section 4.4.5 enter the $E_{\mathrm{T}}^{\mathrm{miss}}$ calculation.

The $Z \to \mu\mu$ simulation label, in dark blue, has an extra piece of information beside the legend entry and this is the particular generator used to produce the MC sample and indicates that there can be different generators used for this sample as detailed in Section 4.5. The MC simulation for the two $Z \to \ell\ell$ channels can be either POWHEG + PYTHIA8 [100][101] or SHERPA [104]. The lower part of the plots have a ratio for each bin where the number of data entries is divided by the number of MC entries in that same bin. The ratio plot has a few extra features; the first being that the data points have statistical error represented by the vertical black lines, secondly the statistical error for the MC is indicated by the grey slashed regions around the red line that benchmarks a ratio of unity and hence perfect agreement between prediction and measurement. It is important to note that the plots in Figure 4.6 have only statistical error.

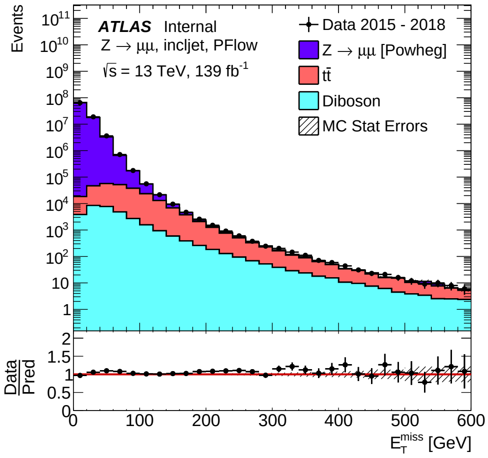

(a) $E_{\mathrm{T}}^{\mathrm{miss}}$

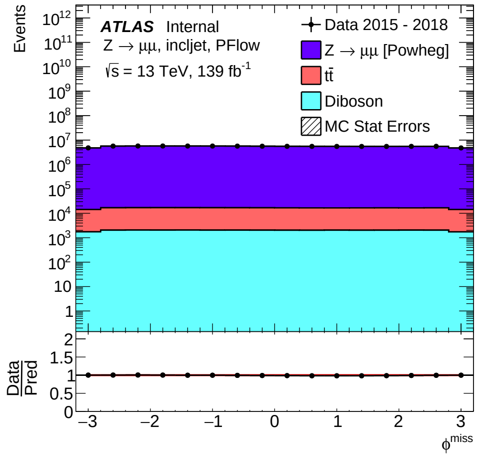

(b) ϕ^{miss}

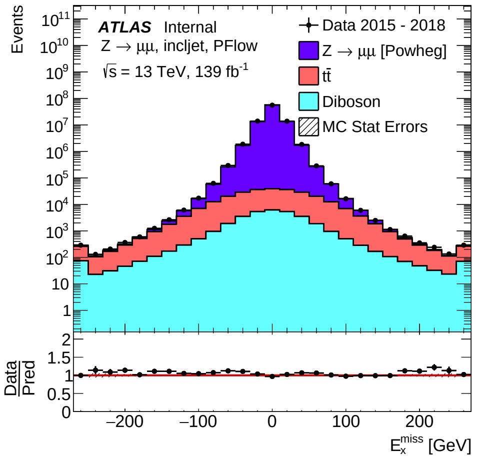

(c) $E_{\mathrm{x}}^{\mathrm{miss}}$

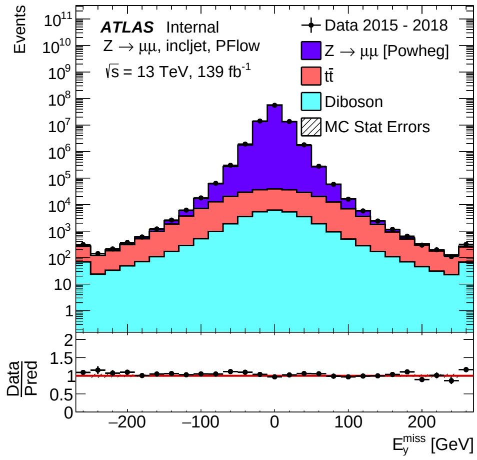

(d) $E_{\mathrm{y}}^{\mathrm{miss}}$

Figure 4.6: $E_{\mathrm{T}}^{\mathrm{miss}}$ observables for the $Z \to \mu\mu$ event selection, shown in histograms comparing data and prediction by MC using the entire Run 2 dataset corresponding to an integrated luminosity of $139\,\mathrm{fb}^{-1}$. The coloured histograms represent the various processes that can contribute to this channel; $Z \to \mu\mu$, $t\bar{t}$ and diboson processes including WW, ZZ and WZ. The data are overlaid with the black points and the lower panel has the ratio between data and prediction as well as the statistical error for both. The bins with an upturn in the number of events at the outer edges of (c) and (d) are the overflow bins and capture all events where $E_{\mathrm{x}}^{\mathrm{miss}}$ and $E_{\mathrm{y}}^{\mathrm{miss}}$ were beyond $[-250, 250]$ GeV.

Each of the sub-figures in Figure 4.6 gives one of the aforementioned observables of $E_{\mathrm{T}}^{\mathrm{miss}}$. Let's first consider the distribution of $E_{\mathrm{T}}^{\mathrm{miss}}$ itself shown in Sub-Figure 4.6a, the bulk of the distribution is dominated by the $Z \to \mu\mu$ MC and this is to be expected as the selection efficiency is $\sim 99.5\%$. The low values of $E_{\mathrm{T}}^{\mathrm{miss}}$ are consistent with the hypothesis that $E_{\mathrm{T}}^{\mathrm{miss,\,true}} = 0$ with some resolution effects and the experimental bias to observe non-zero values of $E_{\mathrm{T}}^{\mathrm{miss}}$. Moving toward the tail of the histogram, $E_{\mathrm{T}}^{\mathrm{miss}} > 150\,\mathrm{GeV}$, the processes that will have a real high p_{T} neutrino produced in flavour changing currents like $t \to Wb \to \ell\nu b$ (and similarly for the anti-top in $t\bar{t}$ production) and satisfy the event selection requirements dominate. Overall the agreement between data and prediction is remarkable and in the bulk of the distribution the modelling is extremely close to the data. In the tails there are some more fluctuations caused by the mis-modelling in $t\bar{t}$ MC but the agreement across the entire spectrum is within 20%.

The azimuthal direction of the missing transverse momentum ϕ^{miss} in Sub-Figure 4.6b highlights the excellent performance this variable has in terms of data and MC agreement with only minute fluctuations in the ratio panel. The two lower histograms displayed in Sub-Figures 4.6c and 4.6d have the $E_{\mathrm{T}}^{\mathrm{miss}}$ components in the x and y, $E_{\mathrm{x}}^{\mathrm{miss}}$ and $E_{\mathrm{y}}^{\mathrm{miss}}$. These two echo the performance seen in the standard $E_{\mathrm{T}}^{\mathrm{miss}}$ magnitude distribution but have positive and negative values while $E_{\mathrm{T}}^{\mathrm{miss}}$ is positive by construction.

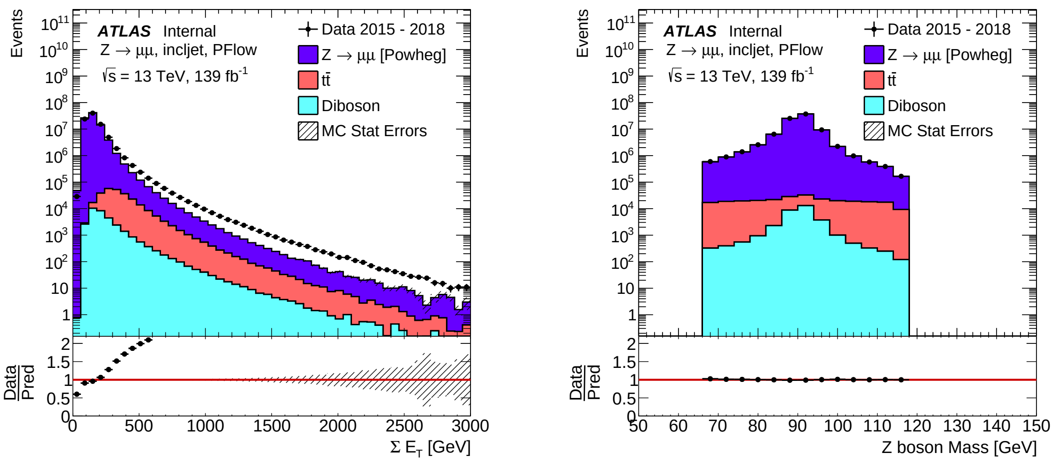

(a) $\sum E_{\mathrm{T}}$ **(b)** m_Z

Figure 4.7: The $\sum E_{\mathrm{T}}$ (a) quantity gives a measure of the activity in the event and the mass of the Z boson, m_Z, (b) indicates how well the Z is reconstructed from the two leptons.

As a further check on the MC modelling in the $Z \to \mu\mu$ channel the $\sum E_{\mathrm{T}}$

distribution and the reconstructed mass of the Z boson are considered in Figure 4.7. Sub-Figure 4.7a of $\sum E_{\mathrm{T}}$ has reasonable agreement for low values in the bulk, excluding the first bin's over-prediction, up to $\sim 200\,\mathrm{GeV}$. However, after this point significant discrepancies appear. This was observed in the early Run 2 performance paper [94] and as it was then this is a reflection of the mismodelling in the MC, particularly in terms of the hard object composition of a simulated event. The mass of the Z boson in the range specified by the event selection from Section 4.6.1 in Sub-Figure 4.7b indicates the high degree of accuracy with which these events are selected and modelled in terms of the Z. As expected the m_Z is dominated by the $Z \to \mu\mu$ process with some contribution from the $t\bar{t}$, although this is a smoothly falling spectrum and the peak is induced by the diboson histogram stacked underneath. The diboson contribution is indeed small and there is a slight peak from Z bosons decaying leptonically and being reconstructed.

4.7.1 $Z \to \mu\mu$ Event Selection - Object Terms

Each of the components entering $\mathbf{E}_{\mathrm{T}}^{\mathrm{miss}}$, seen in Equation 4.7, can be separated out and have its magnitude taken to evaluate its performance as in Figure 4.8. Sub-Figure 4.8a demonstrates the electrons that enter the $E_{\mathrm{T}}^{\mathrm{miss}}$ reconstruction. The large peak at zero represents the vast majority of events that do not contain any electrons for the $Z \to \mu\mu$ selection. The requirements for a $Z \to \mu\mu$ event, that exactly two muons are within $25\,\mathrm{GeV}$ of m_Z, does not preclude there being electrons in the event from other processes and these cases are what appear in the tail of the distribution that has a considerable fraction of diboson events. The modelling here fluctuates and tends to be under-predicted by the MC. The photons in Sub-Figure 4.8b have a distinctive peak at zero for all those events without any photons and a large gap caused by the p_{T} restriction on photons, $p_{\mathrm{T}}^{\gamma} > 130\,\mathrm{GeV}$. After this cut there is a consistent offset between the data and MC but there are very few events with photons of high enough p_{T} to enter the $E_{\mathrm{T}}^{\mathrm{miss}}$ reconstruction and so this should have very little impact on this selection but would require validation for analyses that select for photons.

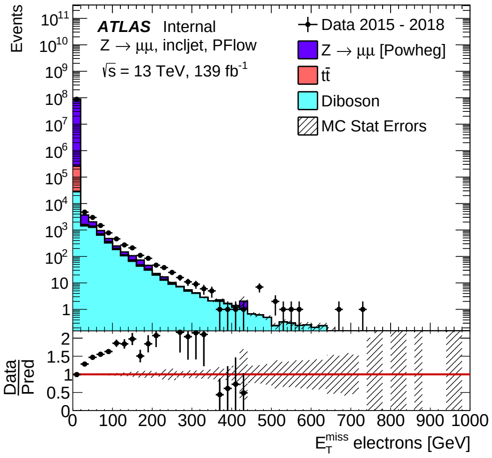

(a) Electrons

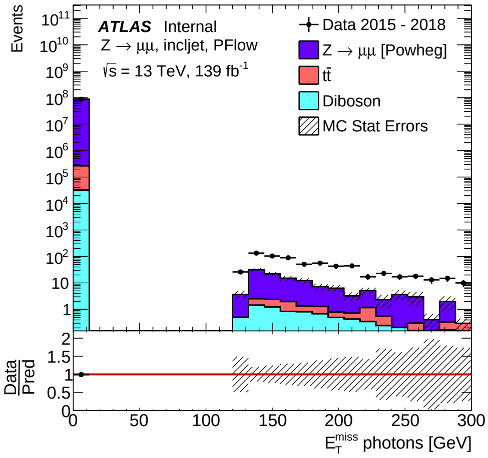

(b) Photons

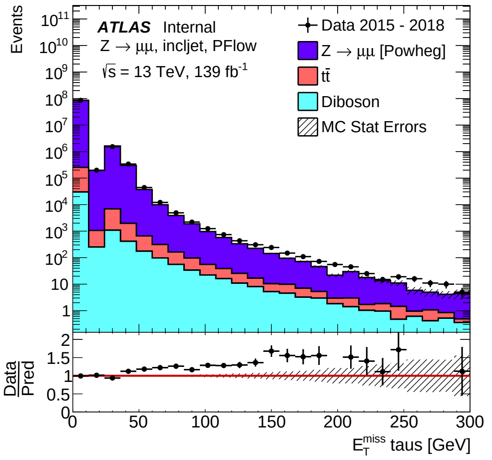

(c) Hadronic Taus

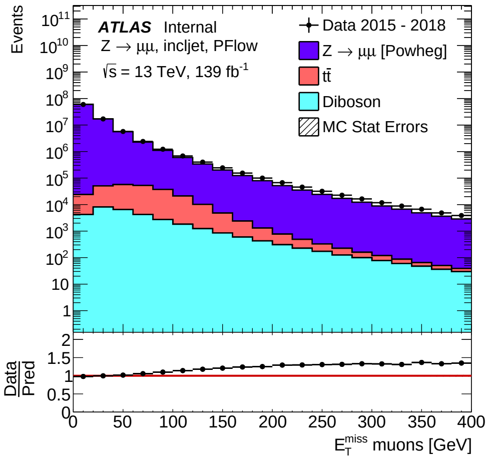

(d) Muons

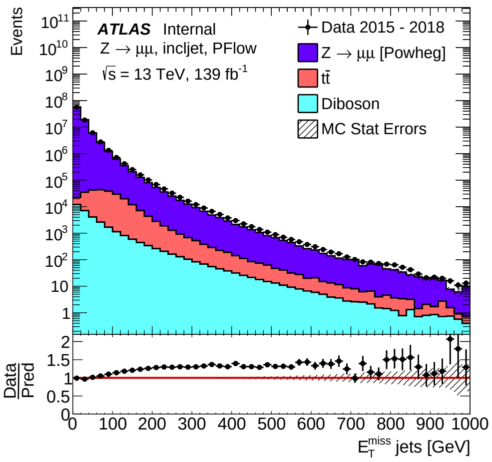

(e) PFlow Jets

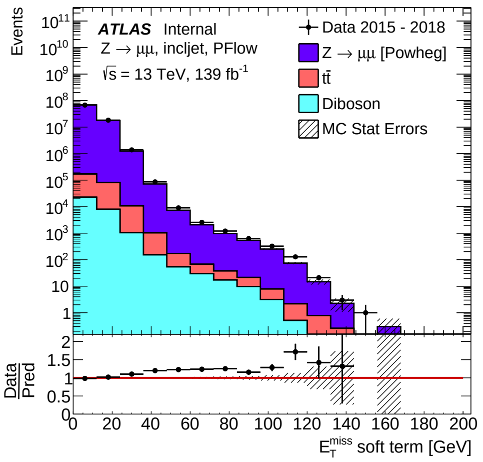

(f) Track Soft Term

Figure 4.8: $E_{\mathrm{T}}^{\mathrm{miss}}$ contributions from each of the object terms. The magnitude of the vector components in Equation 4.7 are taken in isolation for each of the hard objects and the track soft term with a $Z \to \mu\mu$ event selection applied.

Sub-Figure 4.8c indicates that there are quite a number of reconstructed tau particles that do enter the $\mathbf{E}_{\mathrm{T}}^{\mathrm{miss}}$ calculation, even with the large zero spike of events with no taus. The ratio agreement in this case is an improvement over the electrons and photons with only a few bins with more than a 50% disagreement. As one would expect the muon term is the most populated, Sub-Figure 4.8d. For $E_{\mathrm{T}}^{\mathrm{miss},\,\mu} < 50\,\mathrm{GeV}$ the ratio sticks close to the red unity line but after this begins to drift up to a plateau at Data/Pred ~ 1.4. The events are dominated by $Z \to \mu\mu$ simulation with a small but significant contribution of muons from the sub-dominant background processes.

In all of the metrics and distributions presented thus far the PFlow jet algorithm has been the method of choice for the jets due to its increased pile-up resistance aiding in the overall reconstruction of $E_{\mathrm{T}}^{\mathrm{miss}}$. Sub-Figure 4.8e indicates good performance of the PFlow jets entering the $E_{\mathrm{T}}^{\mathrm{miss,\,jet}}$ term. The previously seen under-prediction of the data by MC is again apparent and similarly to the $E_{\mathrm{T}}^{\mathrm{miss},\,\mu}$ term low values of $E_{\mathrm{T}}^{\mathrm{miss,\,jet}}$ have a ratio of 1 before drifting to a plateaued offset. Finally, the TST in Sub-Figure 4.8f has good agreement and extends only up to $\sim 150\,\mathrm{GeV}$ and is dominated by the $Z \to \mu\mu$ MC.

4.7.2 Generator Comparisons, $Z \to \mu\mu$

Outlined in Section 4.5 are the MC samples used for comparisons to data. Figure 4.9 shows the $E_{\mathrm{T}}^{\mathrm{miss}}$ distributions for the $Z \to \mu\mu$ using each type of MC generator. For both distributions the two MCs are very similar with only very minor differences and both can be said to have outstanding performance. There is much more of a difference when one considers the N_{jet} plots in Figure 4.10, Powheg is only able to accurately predict the number of jets in an event with three or less jets and after this the MC consistently underestimates the number of jets in an event compared to the data. Sherpa on the otherhand performs excellently even including the few extreme events with fourteen jets. This is the largest difference between the two and despite the misrepresentation of jets in Powheg there is still good agreement in $E_{\mathrm{T}}^{\mathrm{miss}}$.

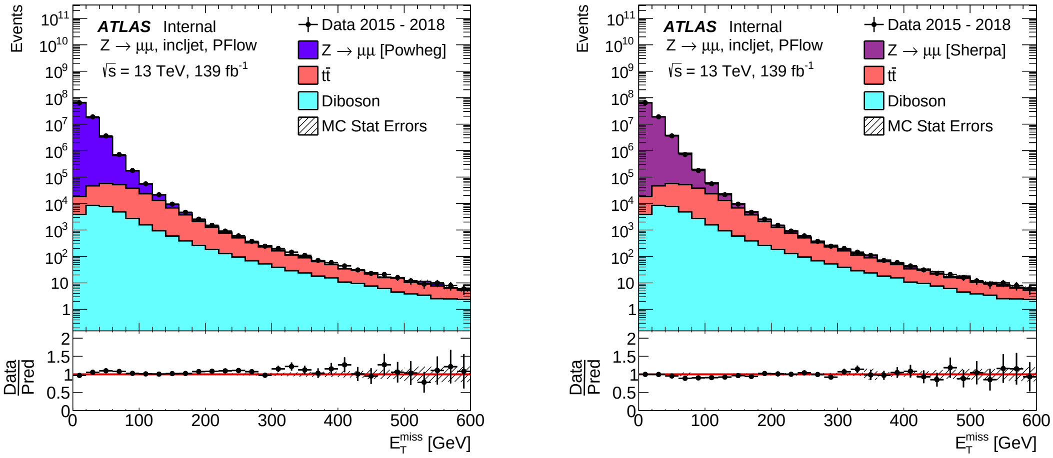

(a) Powheg **(b)** Sherpa

Figure 4.9: Calculated $E_{\mathrm{T}}^{\mathrm{miss}}$ for both data and Monte Carlo but using two different generators for the main $Z \rightarrow \mu\mu$ prediction. The left sub-figure (a) uses Powheg + Pythia8 while the right (b) is formed with Sherpa.

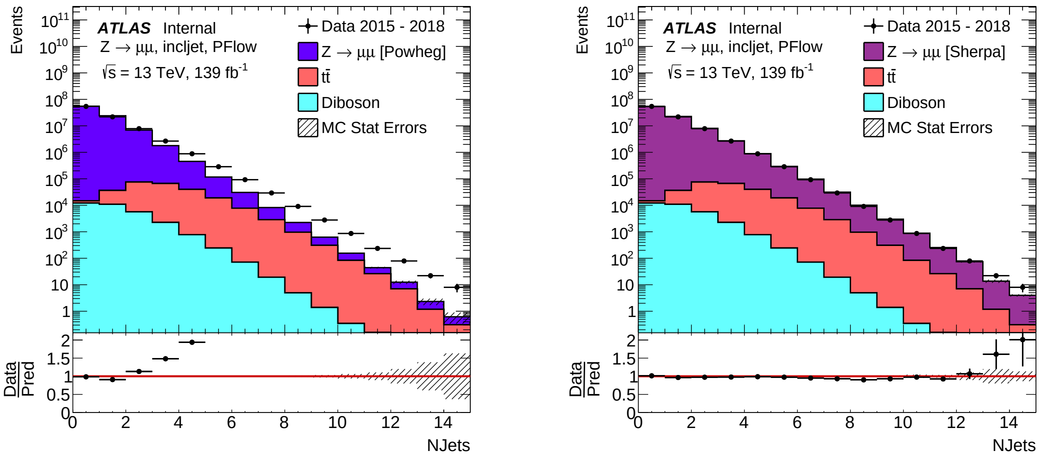

(a) Powheg **(b)** Sherpa

Figure 4.10: The number of jets in an event for both data and Monte Carlo but using two different generators for the main $Z \rightarrow \mu\mu$ prediction. The left sub-figure (a) uses Powheg + Pythia8 while the right (b) is formed with Sherpa.

4.7.3 Jet Collections, EMTopo v PFlow

Section 4.4.5 notes two jet collections, EMTopo and PFlow. The particle-flow jet collection is now the recommended method for ATLAS analyses due to its increased pile-up resistance, improved angular and energy resolution, and reduced systematics across the entire jet p_{T} spectrum. One of the leading contributions to the resolution limit of $E_{\mathrm{T}}^{\mathrm{miss}}$ reconstruction are the jets and so this new PFlow approach is well motivated for missing transverse momentum. The older, purely calorimeter based, EMTopo method is compared to PFlow in Figure 4.11 and in both cases the MC/data is very similar for the bulk of the distribution. However at higher values, $E_{\mathrm{T}}^{\mathrm{miss}} > 300\,\mathrm{GeV}$ there is a slight improvement when using PFlow jets.

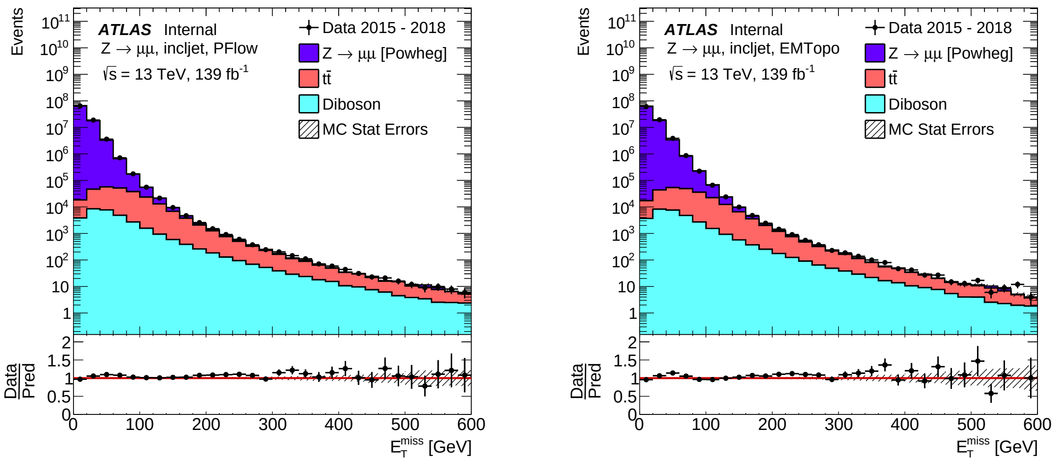

(a) PFlow Jets **(b)** EMTopo Jets

Figure 4.11: Two different jet reconstruction algorithms can be used to produce the jets entering the $E_{\mathrm{T}}^{\mathrm{miss}}$ calculation.

From Figure 4.11 the mean value for data and MC as well as the standard deviation give a numerical estimation of the differences between the two jet collections. Table 4.3 has the mean $E_{\mathrm{T}}^{\mathrm{miss}}$ values for $Z \to ee$ and $Z \to \mu\mu$ when using EMTopo and PFlow jet collections. In both cases the PFlow distributions have a smaller mean and standard deviation meaning that the distributions are narrower and closer to the $E_{\mathrm{T}}^{\mathrm{miss,\,true}} = 0$ value as one would expect as the PFlow jets have improved resolution and the bulk of the distribution comes from resolution effects contributing to an observational bias.

Event Type	Jet Collection	$\langle E_{\mathrm{T}}^{\mathrm{miss}} \rangle \pm \sigma$ [GeV] Data 2015-2018	MC Simulation
$Z \to \mu\mu$	PFlow	16.74 ± 12.90	16.27 ± 12.55
	EMTopo	17.36 ± 13.52	16.76 ± 13.15
$Z \to ee$	PFlow	16.45 ± 12.63	15.94 ± 12.22
	EMTopo	17.16 ± 13.31	16.59 ± 12.94

Table 4.3: Average values of $E_{\mathrm{T}}^{\mathrm{miss}}$, $\langle E_{\mathrm{T}}^{\mathrm{miss}} \rangle$, and the standard deviation, σ, for the two $Z \to \ell\ell$ channels and for both jet collections.

Figure 4.12 directly compares $E_{\mathrm{T}}^{\mathrm{miss,\,jet}}$ for the two collections and in this case there is again an improvement in the tails where PFlow indicates an, albeit small, improvement. In general the adoption of PFlow jets has improved the $E_{\mathrm{T}}^{\mathrm{miss}}$ reconstruction and led to a better prediction of the missing momentum observables.

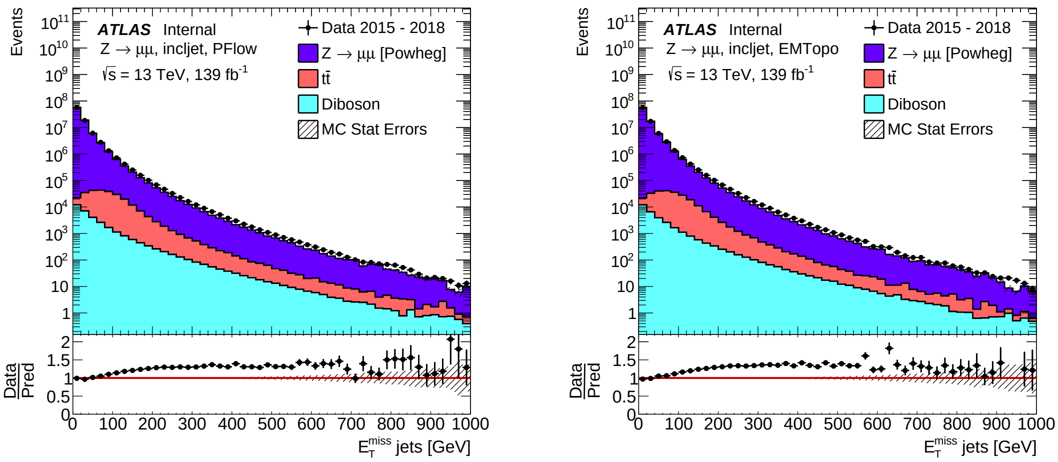

(a) PFlow $E_{\mathrm{T}}^{\mathrm{miss,\,jet}}$

(b) EMTopo $E_{\mathrm{T}}^{\mathrm{miss,\,jet}}$

Figure 4.12: Two different jet reconstruction algorithms can be used to produce the jets entering the $E_{\mathrm{T}}^{\mathrm{miss}}$ calculation.

4.7.4 Track Soft Term Performance

One can gain more insight into how well the soft term, $E_{\mathrm{T}}^{\mathrm{miss,\,Soft}}$, is performing by requiring that there be no jets in an event and so gain a more pure $Z \to \ell\ell$ dataset although there will be an impact on statistics. Sub-Figure 4.13a is the $E_{\mathrm{T}}^{\mathrm{miss}}$

spectrum for $Z \to \mu\mu$ with zero jets and one can see that the $t\bar{t}$ contributions are greatly suppressed as they will almost certainly have at least one jet present.

The number of events has been reduced quite considerably with the low values of $E_{\mathrm{T}}^{\mathrm{miss}}$ comprising mostly $Z \to \mu\mu$ events and the tails are dominated by diboson type events. The agreement between data and MC is still good with a fluctuation around $E_{\mathrm{T}}^{\mathrm{miss}} \approx 100\,\mathrm{GeV}$ and the tails are not as well populated as would be expected. Sub-Figure 4.13b demonstrates really strong performance for $E_{\mathrm{T}}^{\mathrm{miss,\,Soft}}$ when the jets are removed showing that soft contributions are coming predominantly from $Z \to \mu\mu$ final states.

Taking advantage of the jet removal again Figure 4.14 considers the two components of $\mathbf{E}_{\mathrm{T}}^{\mathrm{miss}}$ in the x and y directions. The distributions are again composed mostly of $Z \to \mu\mu$ events and the ratio is close to unity within statistical error. Importantly one would not expect intrinsic $E_{\mathrm{T}}^{\mathrm{miss}}$ with these selections and so the standard deviation or RMS of $E_{\mathrm{x(y)}}^{\mathrm{miss,\,Soft}}$ will give an estimate of the resolution; in both directions and, for data and MC the soft term resolution is approximately $7.5\,\mathrm{GeV}$.

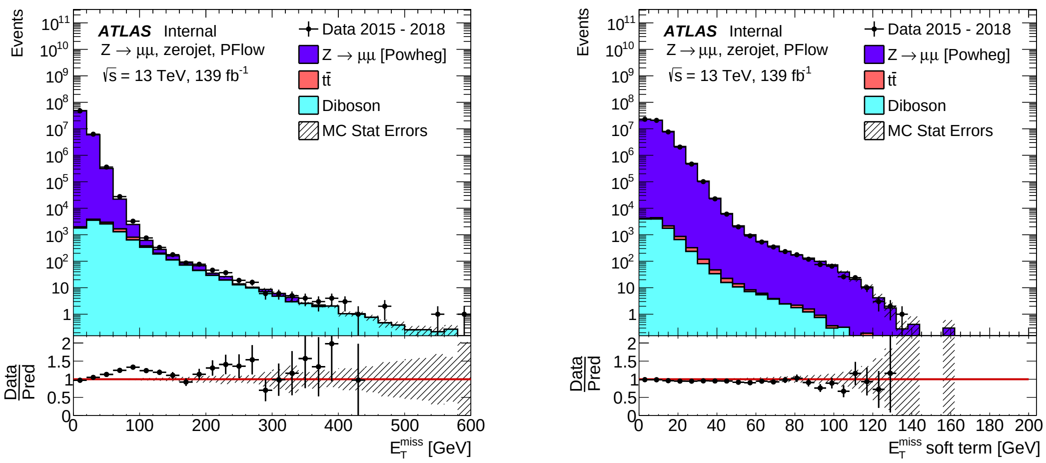

(a) 0 Jets, $E_{\mathrm{T}}^{\mathrm{miss}}$

(b) 0 Jets, $E_{\mathrm{T}}^{\mathrm{miss,\,Soft}}$

Figure 4.13: Zero jet selection to evaluate the performance of the $E_{\mathrm{T}}^{\mathrm{miss}}$ soft term, $E_{\mathrm{T}}^{\mathrm{miss,\,Soft}}$. The left sub-figure (a) is the missing transverse momentum histogram when events with jets are removed and to the right (b) is the track soft term, with the same zero jet requirement.

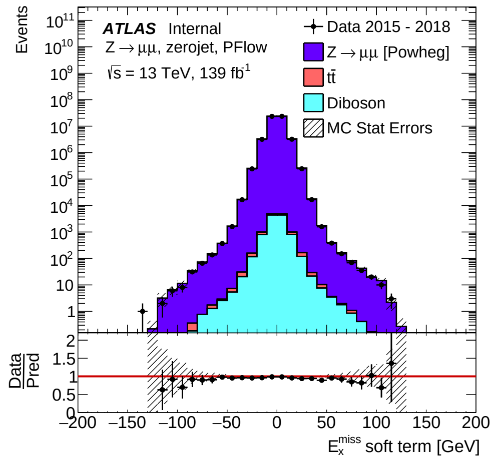

(a) 0 Jets, $E_{\mathrm{x}}^{\mathrm{miss,\,Soft}}$

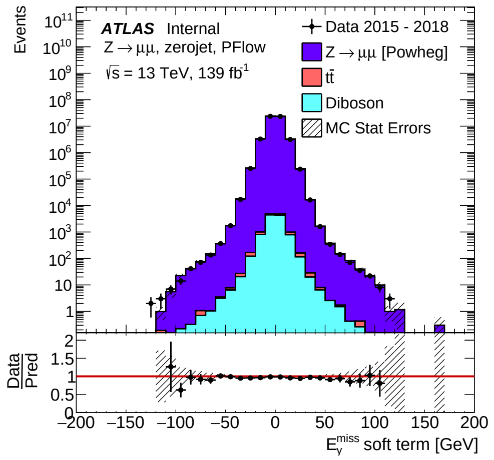

(b) 0 Jets, $E_{\mathrm{y}}^{\mathrm{miss,\,Soft}}$

Figure 4.14: Zero jet selection applied for the x (a) and y (b) components of the track soft term; $E_{\mathrm{x}}^{\mathrm{miss,\,Soft}}$ and $E_{\mathrm{y}}^{\mathrm{miss,\,Soft}}$.

In this part of the chapter almost all results considered the $Z \to \mu\mu$ event selection. The equivalent plots for the $Z \to ee$ event selections were produced by the author but these have not been included in this thesis as they are in many ways very similar to the $Z \to \mu\mu$ results.

4.8 The Significance of $E_{\mathrm{T}}^{\mathrm{miss}}$

The $E_{\mathrm{T}}^{\mathrm{miss}}$ calculation has been adroitly evolved to meet the increasingly complex and energetic environments generated by collisions of LHC beams delivered to the ATLAS experiment. The “standard candle” measurements using leptonically decaying Z bosons have demonstrated phenomenal data-prediction agreement but also shown that considerable values of $E_{\mathrm{T}}^{\mathrm{miss}}$ can appear in the tails of these distributions. These values often come from another process that has produced a neutrino and satisfied the event selection requirements for $Z \to \ell\ell$ but can also come from mismeasurement or limitations in object resolution. An important question, for standard model precision measurements and new physics searches alike, is how confident can we be that the observed $E_{\mathrm{T}}^{\mathrm{miss}}$ has come from a real invisible particle?

To address this question an heuristic definition was considered that approximated the resolution of $\mathbf{E}_{\mathrm{T}}^{\mathrm{miss}}$ using the square root of the scalar sum of all jet p_{T},

$$H_{\mathrm{T}} = \sum_{i} p_{\mathrm{T,i}}, \tag{4.9}$$

here the index runs over the jets. The approximation of $E_{\mathrm{T}}^{\mathrm{miss}}$ significance ($\mathcal{S}$), made possible because H_{T} scales with $\mathbf{E}_{\mathrm{T}}^{\mathrm{miss}}$ resolution, is written as

$$\mathcal{S} = \frac{E_{\mathrm{T}}^{\mathrm{miss}}}{\sqrt{H_{\mathrm{T}}}}. \tag{4.10}$$

Another approximation for the resolution was based on the sum of all the transverse energy in the detector, $\sqrt{\sum E_{\mathrm{T}}}$, and allowed the significance to be written as:

$$\mathcal{S} = \frac{E_{\mathrm{T}}^{\mathrm{miss}}}{\sqrt{\sum E_{\mathrm{T}}}}. \tag{4.11}$$

These definitions are formed from proxies for the resolution of $\mathbf{E}_{\mathrm{T}}^{\mathrm{miss}}$ and so are not true dimensionless significances. Both $\sqrt{H_{\mathrm{T}}}$ and $\sqrt{\sum E_{\mathrm{T}}}$ are event-by-event proxies for resolution that scale linearly with $\mathbf{E}_{\mathrm{T}}^{\mathrm{miss}}$ resolution under the assumption that only calorimeter signals are used to build $\mathbf{E}_{\mathrm{T}}^{\mathrm{miss}}$. This is not the case when one wishes to use the tracker for its improved pile-up rejection and better resolution for charged particles.

As the LHC moved to Run 2 the formulation of $\mathbf{E}_{\mathrm{T}}^{\mathrm{miss}}$ changed to cope with the environment, could a superior estimation of the significance also be determined? Thus enhancing the experimental ability to reject non-intrinsic values of missing transverse momentum and in doing so increase the power of ATLAS beyond that of the increased statistics?

4.8.1 Object-based $E_{\mathrm{T}}^{\mathrm{miss}}$ Significance

Section 4.3 introduced the concept of an object-based approach to $\mathbf{E}_{\mathrm{T}}^{\mathrm{miss}}$, fully described in Equation 4.7, can one form the significance in the same manner? One that encodes the resolutions of all objects, independent of which detector subsystems were used to build them, while also accounting for the correlations between each object in an event.

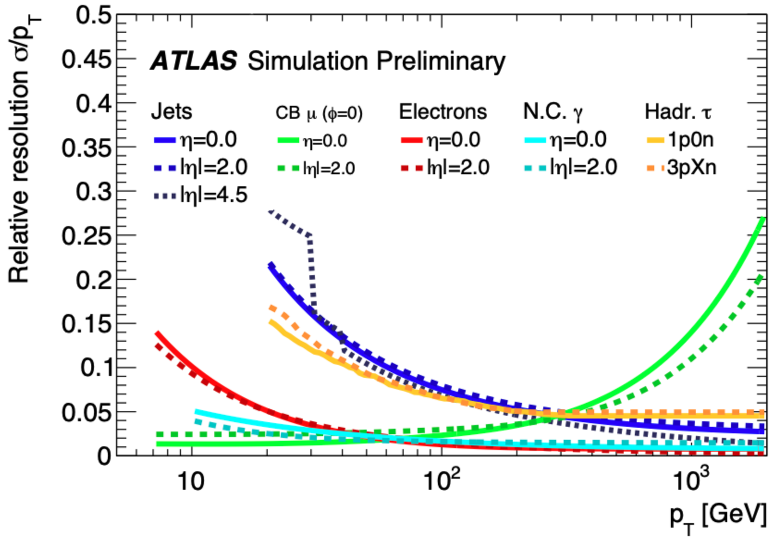

Figure 4.15: Each of the relative resolutions (σ/p_{T}) for the objects entering the $E_{\mathrm{T}}^{\mathrm{miss}}$, defined in Section 4.3. The lines are split by $|\eta|$ conditions and run with the p_{T} of the object in question. The muons are said to be combined (CB) meaning that they come from combined inner detector tracks and muon spectrometer hits. The photons are those which have not converted into an e^+e^- pair). Figure from [111]

This had been previously attempted by the Collider Detector at Fermilab (CDF) where the contribution to $E_{\mathrm{T}}^{\mathrm{miss}}$ resolution coming from unclustered energy deposits and jets was folded into the significance estimation [112]. The CMS collaboration has for many years employed a log likelihood ratio significance method [113][114]. Let's turn the discussion back towards ATLAS and the approach taken for Run 2.

The relative resolution of each of the physics objects as a function of their p_{T} motivates the use of an object-based approach to the significance in Figure 4.15. The relative resolutions can vary by a large amount across the p_{T} range and even in what $|\eta|$ region the candidate object is in.

With the objects and their respective resolutions used in Equation 4.7 in mind we can now formulate a true significance. To determine if the observed missing transverse momentum, $\mathbf{E}_{\mathrm{T}}^{\mathrm{miss}}$, is due to a real invisible particle, or instead caused by resolution effects and mismeasurement of detector objects, a hypothesis test between there being no momentum carried by invisible particles ($\mathbf{p}_{\mathrm{T}}^{\mathrm{inv}} = 0$) against there being genuine p_{T} carried by invisible particles ($\mathbf{p}_{\mathrm{T}}^{\mathrm{inv}} \neq 0$) is defined. This test forms the missing transverse momentum significance ($\mathcal{S}(E_{\mathrm{T}}^{\mathrm{miss}})$) definition,

$$\mathcal{S}^2 = 2\ln\left(\frac{\max_{\mathbf{p}_{\mathrm{T}}^{\mathrm{inv}}\neq 0}\mathcal{L}\left(\mathbf{E}_{\mathrm{T}}^{\mathrm{miss}}|\mathbf{p}_{\mathrm{T}}^{\mathrm{inv}}\right)}{\max_{\mathbf{p}_{\mathrm{T}}^{\mathrm{inv}}= 0}\mathcal{L}\left(\mathbf{E}_{\mathrm{T}}^{\mathrm{miss}}|\mathbf{p}_{\mathrm{T}}^{\mathrm{inv}}\right)}\right). \tag{4.12}$$

This log likelihood ratio, based on the Neyman-Pearson lemma [115], assumes that each of the likelihoods depends on all the objects measured in an event; how many there were, of what type and all their kinematic properties. In other words $\mathcal{S}$ is an event by event evaluation of the p-value that the observed $\mathbf{E}_{\mathrm{T}}^{\mathrm{miss}}$, is consistent with the null hypothesis that there is no true $\mathbf{E}_{\mathrm{T}}^{\mathrm{miss}}$, $\mathbf{E}_{\mathrm{T}}^{\mathrm{miss,\,true}} = 0$,

$$\mathcal{S}^2 = 2\ln\left(\frac{\mathcal{L}\left(\mathbf{E}_{\mathrm{T}}^{\mathrm{miss}}|\mathbf{E}_{\mathrm{T}}^{\mathrm{miss}}\right)}{\mathcal{L}\left(\mathbf{E}_{\mathrm{T}}^{\mathrm{miss}}|0\right)}\right). \tag{4.13}$$

This is all well and good but the functional form of $\mathcal{L}\left(\mathbf{E}_{\mathrm{T}}^{\mathrm{miss}}|\mathbf{p}_{\mathrm{T}}^{\mathrm{inv}}\right)$ is required to calculate $\mathcal{S}(E_{\mathrm{T}}^{\mathrm{miss}})$. Under a few assumptions a functional form can be found:

1. The p_{T} measurement for each object, $\mathbf{p}_{\mathrm{T}}^{\mathrm{Obj}}$, is independent from all others (where Obj $\in$ {e, γ, τ, μ, Jet}).

2. For each of the objects measuring $\mathbf{p}_{\mathrm{T}}^{\mathrm{Obj}}$ given it has a true value of $\mathbf{p}_{\mathrm{T}}^{\mathrm{Object,true}}$ has a particular probability distribution of the form $f\left(\mathbf{p}_{\mathrm{T}}^{\mathrm{Obj}} - \mathbf{p}_{\mathrm{T}}^{\mathrm{Object,true}}\right)$.

3. The probability distribution for each object is Gaussian and has a covariance matrix called $\mathbf{V}^{\mathrm{Obj}}$. This is the sum of covariances quantifying the resolutions of each object, in p_{T} and ϕ, entering the $\mathbf{E}_{\mathrm{T}}^{\mathrm{miss}}$ calculation.

4. Conservation of momentum in the transverse plane means that if the true momentum of each measured particle were to be summed this would balance with the negative signed invisible particle momentum (stemming from the very first idealised case at the beginning of the chapter, Equation 4.1):

$$\sum_{\mathrm{Objects}} \mathbf{p}_{\mathrm{T}}^{\mathrm{Obj}} = -\mathbf{p}_{\mathrm{T}}^{\mathrm{inv}}.$$

With these assumptions made the form of the likelihood is

$$\mathcal{L}\left(\mathbf{E}_{\mathrm{T}}^{\mathrm{miss}}|\mathbf{p}_{\mathrm{T}}^{\mathrm{inv}}\right) \propto \exp\left[-\frac{1}{2}\left(\mathbf{E}_{\mathrm{T}}^{\mathrm{miss}} - p_{\mathrm{T}}^{\mathrm{inv}}\right)^{\mathrm{T}}\left(\sum_{\mathrm{Objects}} \mathbf{V}^{\mathrm{Obj}}\right)^{-1}\left(\mathbf{E}_{\mathrm{T}}^{\mathrm{miss}} - p_{\mathrm{T}}^{\mathrm{inv}}\right)\right], \tag{4.14}$$

which is a two dimensional Gaussian distribution. Entering this into the maximised log likelihood ratio, Equation 4.13, results in the cancellation of any preceding coefficients and leaves:

$$\mathcal{S}^2 = \left(\mathbf{E}_{\mathrm{T}}^{\mathrm{miss}}\right)^{\mathrm{T}}\left(\sum_{\mathrm{Objects}} \mathbf{V}^{\mathrm{Obj}}\right)^{-1}\left(\mathbf{E}_{\mathrm{T}}^{\mathrm{miss}}\right). \tag{4.15}$$

This is now a sum of independent standard normal variables in two dimensions, or more simply a χ^2 hypothesis test in two dimensions. Equation 4.15 links $\mathbf{E}_{\mathrm{T}}^{\mathrm{miss}}$ to all the object resolutions which are encoded in the covariance matrix summation.

In this format the results of the χ^2 test are easily interpreted with a single value that indicates how likely it is that the null hypothesis (there is no real $\mathbf{E}_{\mathrm{T}}^{\mathrm{miss,\,true}}$) holds. With this in mind low values of $\mathcal{S}^2$ indicate that the $\mathbf{E}_{\mathrm{T}}^{\mathrm{miss}}$ comes from fake sources like mismeasurement or resolution effects while high values show that it is likely the $\mathbf{E}_{\mathrm{T}}^{\mathrm{miss}}$ comes from a real invisible particle leaving the detector without interaction.

The covariance matrix for each object is defined with an axis along the measured transverse momentum vector of the object under consideration, $\mathbf{p}_{\mathrm{T}}^{\mathrm{Obj}}$. This allows each object's covariance matrix to be simply written in terms of the resolution of the magnitude of $\mathbf{p}_{\mathrm{T}}^{\mathrm{Obj}}$ and the resolution in the azimuthal angle,

$$\mathbf{V}^{\mathrm{Obj}} = \begin{pmatrix} \sigma^2_{p_{\mathrm{T}}^{\mathrm{Obj}}} & 0 \\ 0 & {p_{\mathrm{T}}^{\mathrm{Obj}}}^2 \sigma^2_{\phi^{\mathrm{Obj}}} \end{pmatrix} \tag{4.16}$$

Under the condition that $p_{\mathrm{T}}^{\mathrm{Obj}}$ and ϕ^{Obj} are independent measurements. So far only the well defined hard objects have been considered but as was seen there is a soft term in Equation 4.5 with a resolution described in Figure 4.14. The covariance matrix for the soft term is defined in a similar fashion to the objects in Equation 4.16 and allows the complete covariance matrix to be written as:

$$\mathbf{V} = \sum_{\text{Objects}} \mathbf{V}^{\text{Obj}} + \mathbf{V}^{\text{Soft}}. \tag{4.17}$$

For the sake of brevity and ease the soft term will now be included in the "Objects" set so that Objects $\in \{\text{e}, \gamma, \tau, \mu, \text{Jet}, \text{Soft Term}\}$. The sum itself will be done in the $x-y$ coordinates as is usual for ATLAS. The total covariance matrix can be rotated using the two dimensional rotation matrix $R\left(\phi^{\text{Obj}}\right)$ in the azimuthal plane,

$$\mathbf{V}_{xy} = \sum_{\text{Objects}} R^{-1}\left(\phi^{\text{Obj}}\right) \mathbf{V}^{\text{Obj}}\, R\left(\phi^{\text{Obj}}\right) = \begin{pmatrix} \sigma_x^2 & \sigma_{xy}^2 \\ \sigma_{xy}^2 & \sigma_y^2 \end{pmatrix}. \tag{4.18}$$

Where the σ terms are now the combined resolutions of $E_{\text{T}}^{\text{miss}}$ in x and y. To simplify the situation even further it is prudent to again rotate the system to the frame of $\mathbf{E}_{\text{T}}^{\text{miss}}$. In this frame there are two components to the total $\mathbf{E}_{\text{T}}^{\text{miss}}$ resolutions; one longitudinal (or parallel) "L" and another transverse (or perpendicular) to $\mathbf{E}_{\text{T}}^{\text{miss}}$ "T". To do this another two dimensional rotation matrix is applied, $R\left(\phi\left(E_{\text{T}}^{\text{miss}}\right)\right)$, to end up with:

$$\mathbf{V}_{\text{LT}} = R\left(\phi\left(E_{\text{T}}^{\text{miss}}\right)\right) \mathbf{V}_{xy}\, R^{-1}\left(\phi\left(E_{\text{T}}^{\text{miss}}\right)\right) = \begin{pmatrix} \sigma_{\text{L}}^2 & \rho_{\text{LT}}\sigma_{\text{L}}\sigma_{\text{T}} \\ \rho_{\text{LT}}\sigma_{\text{L}}\sigma_{\text{T}} & \sigma_{\text{T}}^2 \end{pmatrix}. \tag{4.19}$$

The longitudinal variance is σ_{L}, the transverse variance is σ_{T} and ρ_{LT} represents the covariance between measurements in the longitudinal and transverse directions. Now almost all the pieces required to complete the calculation of Equation 4.15 are available. Note that Equation 4.15 takes the inverse of $\mathbf{V}$, this can be retrieved using the following relation for a two-by-two matrix,

$$\mathbf{V}^{-1} = \frac{1}{\det \mathbf{V}}\left[(\text{tr}\mathbf{V})\mathbf{I} - \mathbf{V}\right]. \tag{4.20}$$

Which gives,

$$\mathbf{V}_{\text{LT}}^{-1} = \frac{1}{\sigma_{\text{L}}^2\sigma_{\text{T}}^2 - \rho_{\text{LT}}^2\sigma_{\text{L}}^2\sigma_{\text{T}}^2} \begin{pmatrix} \sigma_{\text{T}}^2 & -\rho_{\text{LT}}\sigma_{\text{L}}\sigma_{\text{T}} \\ -\rho_{\text{LT}}\sigma_{\text{L}}\sigma_{\text{T}} & \sigma_{\text{L}}^2 \end{pmatrix}. \tag{4.21}$$

This can finally be substituted into a slightly more expanded version (for clarity) of Equation 4.15 with the total covariance matrix in the "LT" frame

$$\mathcal{S}^2 = \left(E_{\mathrm{T}}^{\mathrm{miss}}, 0\right) \mathbf{V}_{\mathrm{LT}}^{-1} \begin{pmatrix} E_{\mathrm{T}}^{\mathrm{miss}} \\ 0 \end{pmatrix}. \tag{4.22}$$

Finally entering Equation 4.21 and multiplying out the matrix one ends up with the much simpler definition of $\mathcal{S}(E_{\mathrm{T}}^{\mathrm{miss}})$:

$$\mathcal{S}^2 = \frac{|E_{\mathrm{T}}^{\mathrm{miss}}|^2}{\sigma_{\mathrm{L}}^2\,(1-\rho_{\mathrm{LT}}^2)} \tag{4.23}$$

or

$$\mathcal{S}(E_{\mathrm{T}}^{\mathrm{miss}}) = \frac{E_{\mathrm{T}}^{\mathrm{miss}}}{\sqrt{\sigma_{\mathrm{L}}^2\,(1-\rho_{\mathrm{LT}}^2)}}. \tag{4.24}$$

Equation 4.24 is final object-based missing transverse momentum significance and is a true significance. This variable contains the measured quantity in the numerator along with information on the variance of its measurement in the denominator in a dimensionless way [111].

4.9 $\mathcal{S}(E_{\mathrm{T}}^{\mathrm{miss}})$ Performance in Run 2

We can once again turn to the standard candle measurement of $Z \to \mu\mu$ to get an estimation of how well the various definitions are performing with data-MC comparisons. Figure 4.16 shows the older calorimeter dependent significance proxy defined in Equation 4.11. The behaviour of the distribution is as expected; the low values are dominated by events where we expect $E_{\mathrm{T}}^{\mathrm{miss,\,true}} = 0$ and so are due to resolution and mismeasurement that can occur when many jets are present. The high valued tails are mostly made up of events that can have a high energy neutrino produced.

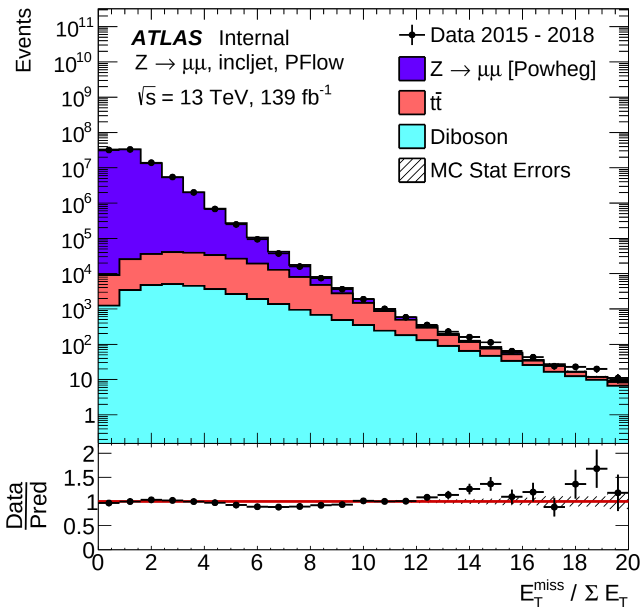

Figure 4.16: $E_{\mathrm{T}}^{\mathrm{miss}}$ over $\sqrt{\sum E_{\mathrm{T}}}$

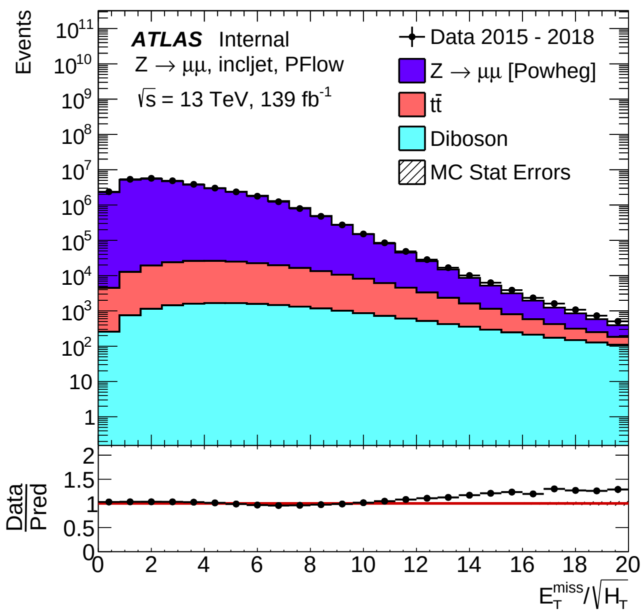

Figure 4.17: $E_{\mathrm{T}}^{\mathrm{miss}}$ over H_{T}

Figure 4.17 shows another of the older estimations of significance, defined in Equation 4.10, this version indicates that there are many more events which are likely to have real $E_{\mathrm{T}}^{\mathrm{miss}}$ in them. This is quite in opposition of what we have seen in Figure 4.16.

The complete object-based missing transverse momentum significance derived in Section 4.8.1 is presented in Figure 4.18. The behaviour here is very similar to that of Figure 4.16 and reinforces the statement that $\sqrt{\sum E_{\mathrm{T}}}$ is a good proxy for the resolution of $E_{\mathrm{T}}^{\mathrm{miss}}$. The performance of $\mathcal{S}(E_{\mathrm{T}}^{\mathrm{miss}})$ is very impressive indeed and even more so when one remembers that this is for the entire Run 2 data set.

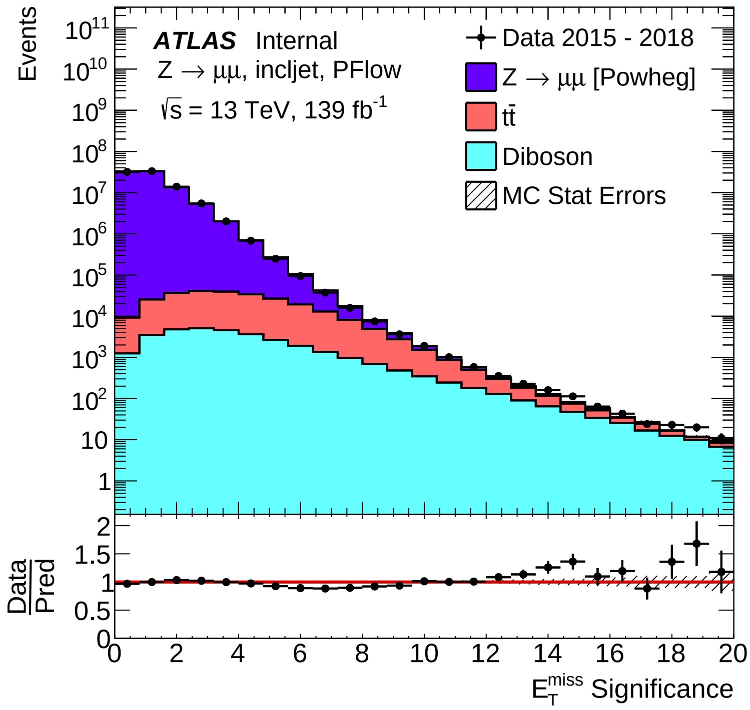

Figure 4.18: Object-based $E_{\mathrm{T}}^{\mathrm{miss}}$ significance

One can also investigate how the resolution terms in the denominator impact the agreement between data and prediction by defining a directional $E_{\mathrm{T}}^{\mathrm{miss}}$ significance that only has the longitudinal resolution in Equation 4.24 and so remove any input from σ_{T}. Figure 4.19 has some interesting features, considering only the longitudinal variance the over-prediction seen between $5 < \mathcal{S} < 10$ in Figure 4.18 is removed. Across almost the entire spectrum of Figure 4.19 there is an under-prediction.

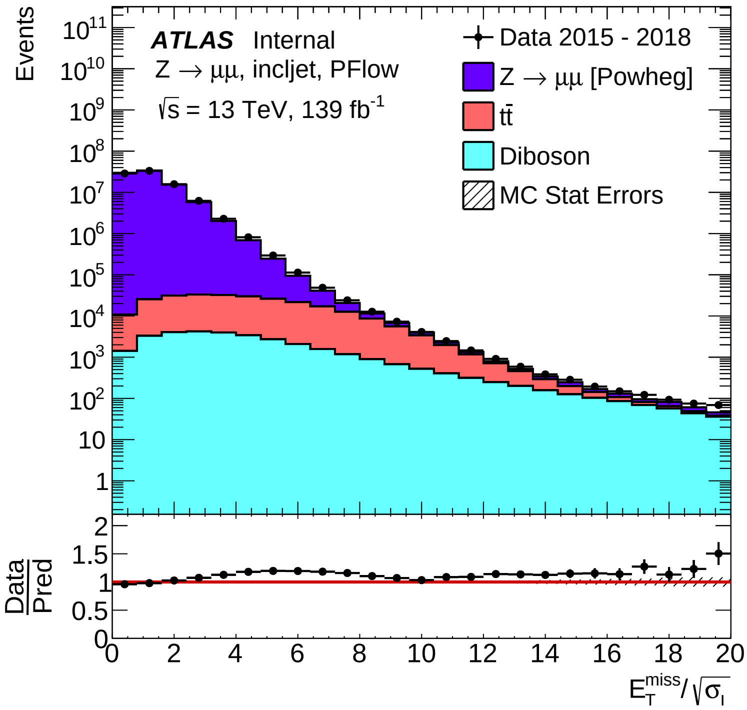

Figure 4.19: $E_{\mathrm{T}}^{\mathrm{miss}}$ significance directional

4.9.1 Jet Collections, EMTopo v PFlow

Section 4.7.3 compared the performance of $E_{\mathrm{T}}^{\mathrm{miss}}$ when using two different jet collections; EMTopo and PFlow. The same study for the $E_{\mathrm{T}}^{\mathrm{miss}}$ significance is shown in Figure 4.20. The two jet collections have a similar level of performance in $Z \to \mu\mu$ events but there are some important differences. The PFlow jet collection has a better agreement between data and prediction in the middle range of significance and the tail of the distributions are quite similar. The improved performance of PFlow is likely due to PFlow jet reconstruction having a better rejection of pile-up than EMTopo and so the $E_{\mathrm{T}}^{\mathrm{miss}}$ calculation will not be affected by this. The PFlow jets also have an improved resolution which will help with the determination of $\mathcal{S}$.

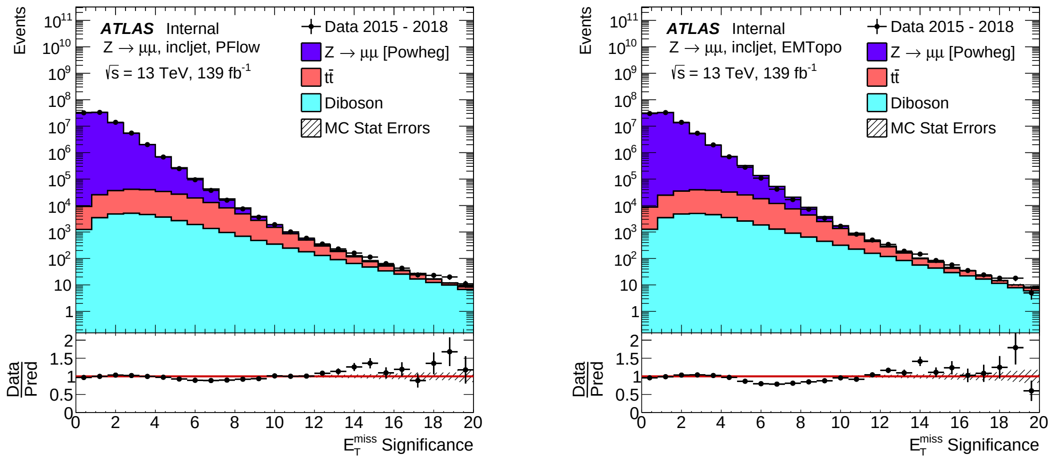

(a) PFlow Jets and PowhegPythia MC **(b)** EMTopo Jets and PowhegPythia MC

Figure 4.20: Object-based $E_{\mathrm{T}}^{\mathrm{miss}}$ Significance distributions for a Z boson decay into two oppositely charged muons. The left plot (a) shows the distribution when PFlow jets are used an the right (b) is with the EMTopo jet definition.

4.9.2 Generator comparison

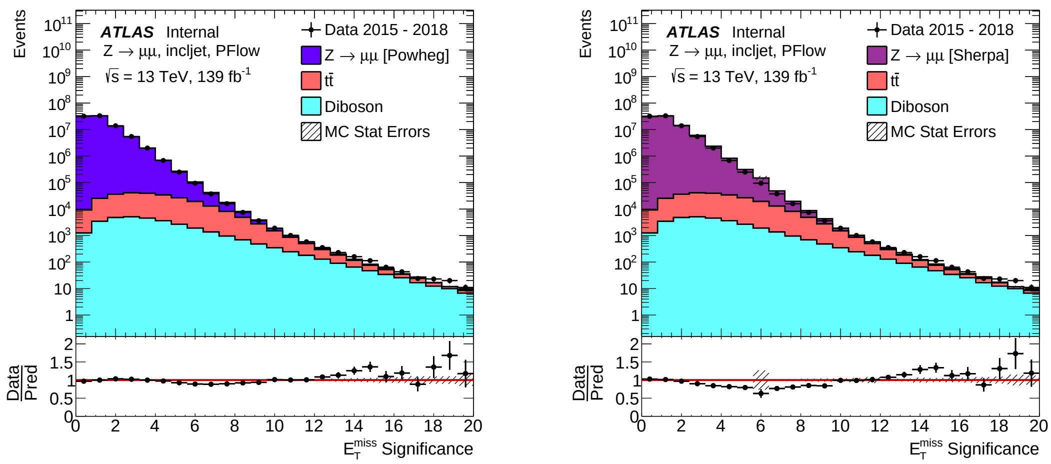

(a) PFlow Jets and PowhegPythia MC **(b)** PFlow Jets and Sherpa MC

Figure 4.21: Object-based $E_{\mathrm{T}}^{\mathrm{miss}}$ Significance distributions for a Z boson decay into two oppositely charged muons. The left plot (a) shows the distribution when PFlow jets are used with the PowhegPythia simulation and the right (b) is with the PFlow jets but using Sherpa for the $Z \to \mu\mu$ simulation.

As was done in Section 4.7.2 for $E_{\mathrm{T}}^{\mathrm{miss}}$ we can once again compare the difference between two MC generators; namely Powheg + Pythia8 [100][101] against Sherpa [104]. The MC generators are changed only for the main simulation of

$Z \to \mu\mu$. Figure 4.21 shows that the POWHEG + PYTHIA8 (left plot) performs better in the bulk of the distribution and the SHERPA simulation has a greater disagreement in that same region. There is a large statistical uncertainty fluctuation around $\mathcal{S} = 6$ caused by a small number of sherpa events with large weights. In the tails the performance is very similar for both.

4.10 $E_{\mathrm{T}}^{\mathrm{miss}}$ Scale Determination

The $Z \to \ell\ell$ events studied in this chapter are even more useful when one uses the transverse momentum of the Z boson as a measure of the hardness of the interaction. The momentum of the Z provides a handy scale for the evaluation of the $E_{\mathrm{T}}^{\mathrm{miss}}$ response in events with no true $E_{\mathrm{T}}^{\mathrm{miss}}$. First of all one can define an axis in the transverse plane from the $\mathbf{p}_{\mathrm{T}}$ of the Z which can be built using the $\mathbf{p}_{\mathrm{T}}$ of each of the leptons,

$$\hat{\mathbf{A}}_Z = \frac{\mathbf{p}_{\mathrm{T}}^{\ell+} + \mathbf{p}_{\mathrm{T}}^{\ell-}}{|\mathbf{p}_{\mathrm{T}}^{\ell+} + \mathbf{p}_{\mathrm{T}}^{\ell-}|} = \frac{\mathbf{p}_{\mathrm{T}}^{Z}}{p_{\mathrm{T}}^{Z}}. \tag{4.25}$$

With this reference axis the $\mathbf{E}_{\mathrm{T}}^{\mathrm{miss}}$ can be projected onto it with,

$$\mathcal{P}^Z = \mathbf{E}_{\mathrm{T}}^{\mathrm{miss}} \cdot \hat{\mathbf{A}}_Z. \tag{4.26}$$

This projection is highly sensitive to any mis-reconstruction in the $E_{\mathrm{T}}^{\mathrm{miss}}$ and provides an excellent way to gauge the performance of the $E_{\mathrm{T}}^{\mathrm{miss}}$ reconstruction. It is particularly sensitive to the impact of the hadronic recoil against the Z boson.

The expected value for a completely balanced reaction, Z boson produced with perfectly balancing hadronic recoil, is $\mathcal{P}^Z = 0$. If $\mathcal{P}^Z < 0$ then there is not enough hadronic recoil to balance the momentum of the Z and when $\mathcal{P}^Z > 0$ there is too much reconstructed recoil. The hardness of the interaction can be assessed by taking the average of the projection, $\langle \mathcal{P}^Z \rangle$, and binning it as a function of the magnitude of the transverse momentum of the Z boson, p_{T}^{Z}.

4.11 $E_{\mathrm{T}}^{\mathrm{miss}}$ Scale Performance

Figure 4.22 shows the average value of $\mathcal{P}^{Z}$ in bins of p_{T}^{Z} for data and MC with $Z \to ee$ selection using PFlow jets. In general there is an underestimation of the hadronic balance with the Z boson and an offset between data and prediction with Powheg + Pythia8. There are no systematics included here, however, they are expected to be rather large ($\sim 40\%$ with $p_{\mathrm{T}}^{Z} > 40\,\mathrm{GeV}$) as in the previous study in Reference [94] and would likely cover the difference between data and MC.

Including the rest of the backgrounds ($t\bar{t}$, Diboson) results in an improved performance as illustrated in Figure 4.23. This is due to a flattening of the magenta points between $40 < p_{\mathrm{T}}^{Z} < 120\,\mathrm{GeV}$.

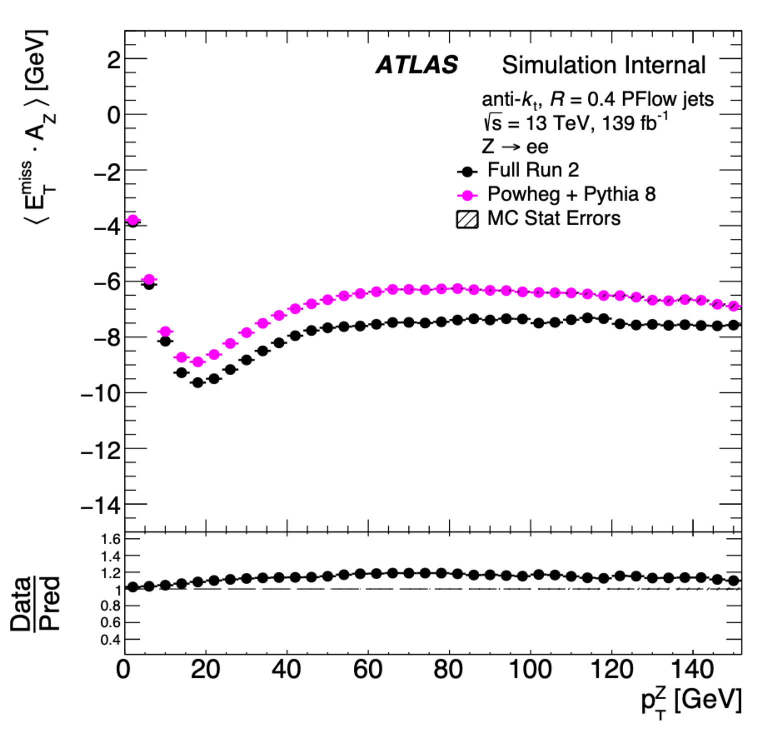

Figure 4.22: The average projection of $\mathbf{E}_{\mathrm{T}}^{\mathrm{miss}}$ on to $\mathbf{A}_{Z}$ as a function of the Z boson's transverse momentum. The full dataset is shown in black while the MC prediction for only the $Z \to ee$ process is shown in magenta. The two distributions show an offset towards the negative values which reaches a minimum at low p_{T}^{Z} before roughly levelling off. The MC is less offset but the data and prediction do agree to within 20%.

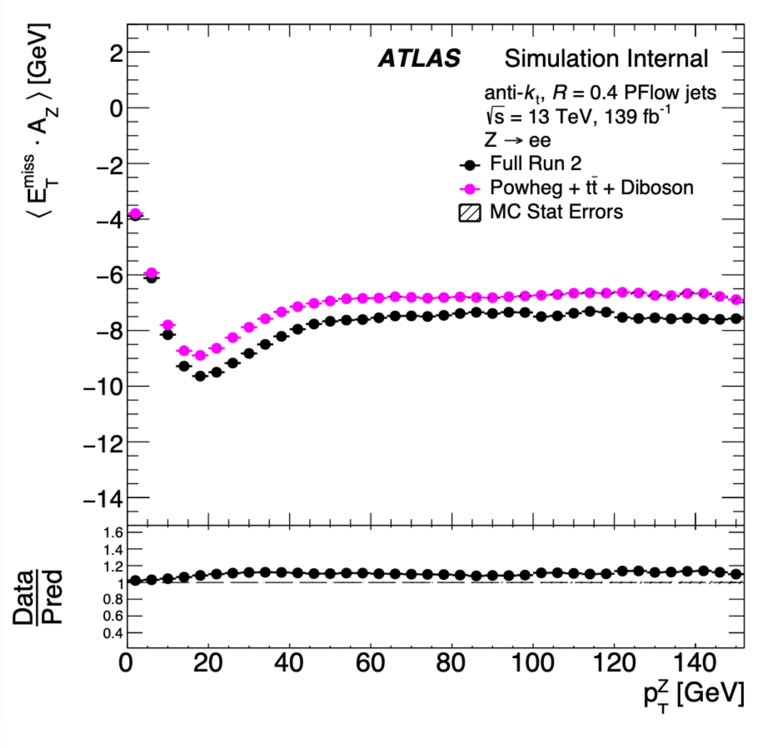

Figure 4.23: The average projection of $\mathbf{E}_{\mathrm{T}}^{\mathrm{miss}}$ on to $\mathbf{A}_Z$ as a function of the Z boson's transverse momentum. The MC simulation now includes the other background processes and this results in an improved agreement between data and prediction.

Figure 4.24 shows the average projection as a function of p_{T}^{Z} for the EMTopo jet collection with only $Z \to ee$ simulation on the left and the complete set of backgrounds are included on the right. Rather interestingly the agreement between data and prediction is superior to PFlow jets. The projection can also be estimated in events with the jets removed, in this case it would be expected that the projection would become increasingly negative, as p_{T}^{Z} increases, due to the hadronic recoil of the Z being removed and this is exactly the behaviour seen in Figure 4.25.

Figure 4.26 investigates the difference between the two jet collections a little more. Both lines in each of the figures represent the recorded data and the left figure is the $Z \to ee$ selections while the right shows $Z \to \mu\mu$. In both cases the agreement between the two degrades as p_{T}^{Z} increases. The EMTopo jet collection in black for both event types is closer to the ideal value of $\langle \mathbf{E}_{\mathrm{T}}^{\mathrm{miss}} \cdot \mathbf{A}_Z \rangle = 0$. For the PFlow jets show a maximum imbalance of 10 GeV and stabilise around $\langle \mathbf{E}_{\mathrm{T}}^{\mathrm{miss}} \cdot \mathbf{A}_Z \rangle \sim 9$ GeV.

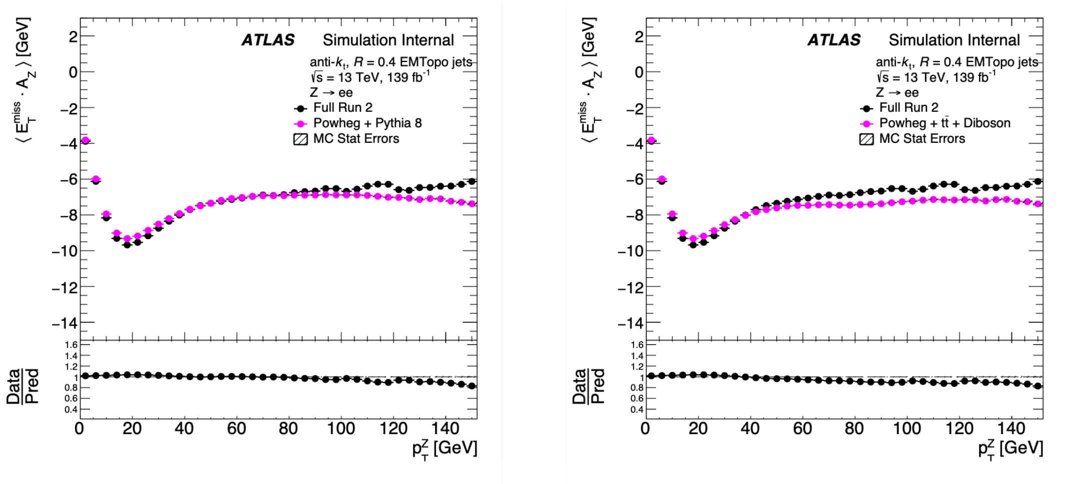

(a) $Z \to ee$ **(b)** $Z \to \mu\mu$

Figure 4.24: The projection, $\mathcal{P}^Z$, plotted against the transverse momentum of the Z boson. The left figure uses only the $Z \to ee$ simulation with Powheg + Pythia8 and on the right all of the other backgrounds ($t\bar{t}$ and Diboson) are included.

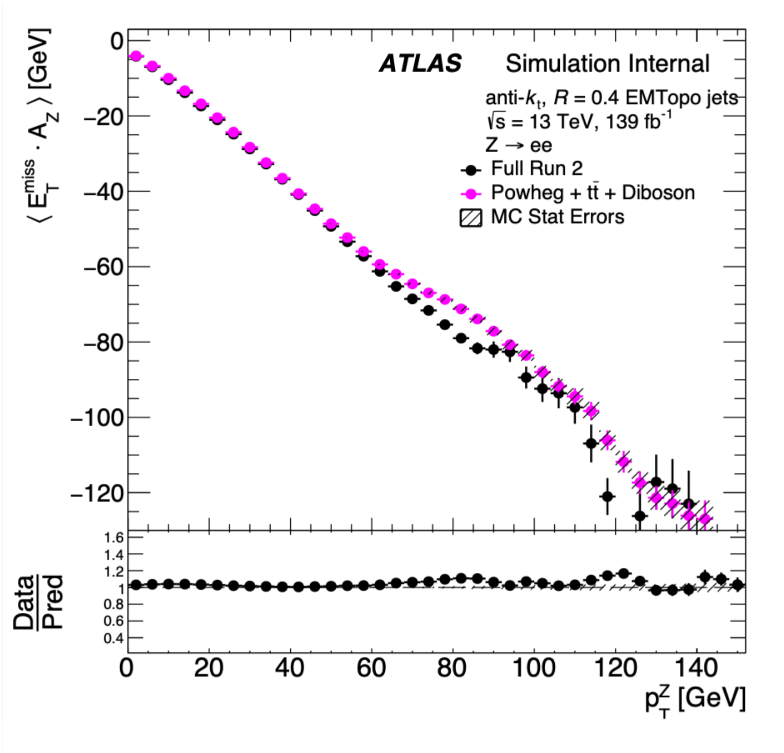

Figure 4.25: Average value of $\mathcal{P}^Z$ binned in p_{T}^{Z}. The jets are removed from consideration in these events and so one observes a linear decrease as the transverse momentum of the Z increases. The agreement between data and prediction in this case is good.

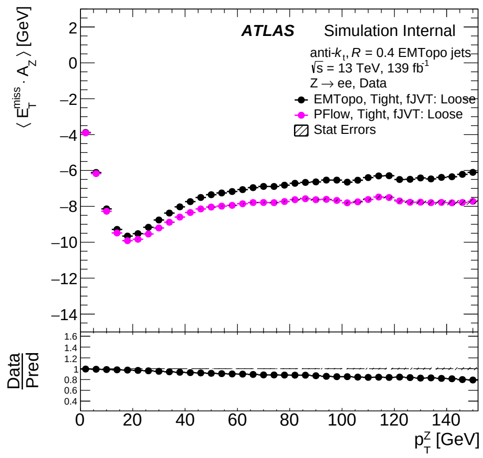

(a) $Z \rightarrow ee$

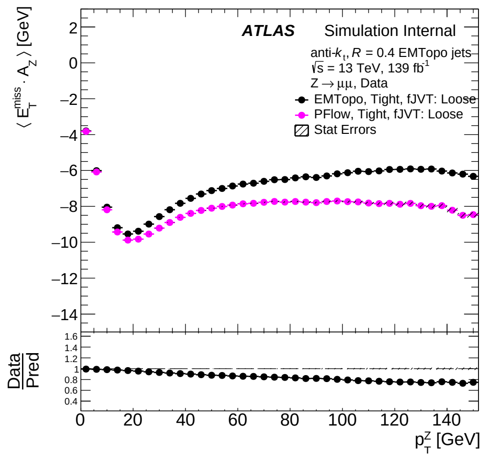

(b) $Z \rightarrow \mu\mu$

Figure 4.26: The projection, $\mathcal{P}^Z$, plotted against the transverse momentum of the Z boson. Two event types are included here, $Z \rightarrow ee$ (left) and $Z \rightarrow \mu\mu$ (right), using only data. The two jet collections are shown for each.

4.12 Conclusions and Future Work

Only one known class of particle in the standard model will evade detection by ATLAS and leave without interaction. Many theories for physics beyond the SM require the existence of massive non-interacting particles and the question arises, how does one know if such a particle has been produced in ATLAS? The technique of missing transverse momentum was introduced and the performance of the ATLAS object-based E_T^{miss} was investigated in this chapter. It was found that the performance for PFlow jets was excellent across the entire Run 2 dataset in $Z \rightarrow \ell\ell$ events.

Once the E_T^{miss} was calculated it was apparent that a method to test the reliability of the calculation was needed. Was the calculated value coming from a real invisible particle or simply mis-measurement or resolution effects. A significance test was previously estimated but these did not constitute a true dimensionless significance and so the object-based E_T^{miss} significance was derived based on the Neyman-Pearson lemma. This significance was found to perform excellently in terms of data-prediction agreement.

In both cases and many of the plots only the statistical error was included and work is ongoing to determine the systematic errors associated with the $E_{\mathrm{T}}^{\mathrm{miss}}$ and its significance. Many of the ratio panels indicated that many of the variables agreed to within, or close to, statistical error.

Study and evaluation of $E_{\mathrm{T}}^{\mathrm{miss}}$ and its significance is imperative to the functioning of many beyond the Standard Model (BSM) physics searches and SM measurements. This will become even more of a challenge as ATLAS moves in to the high-luminosity LHC era. The next chapter covers a search for supersymmetry in events with many jets and $E_{\mathrm{T}}^{\mathrm{miss}}$, highlighting the importance of this study in BSM searches.

If I had a world of my own, everything would be nonsense. Nothing would be what it is, because everything would be what it isn't. And contrary wise, what is, it wouldn't be. And what it wouldn't be, it would. You see?

— Lewis Carroll - *Through the Looking-Glass, 1871*

5

The Search for Supersymmetry in States with Many Hadronic Jets

Contents

5.1 Overview

Sifting through the mountains of data recorded by the ATLAS experiment [55] after being produced by proton-proton collisions at the LHC [53] occurring every 25 ns may seem like an impossible task but over the decades particle physicists have distilled the process into a few basic steps.

1. Select a small subset of collision data relevant for testing the hypothesis one is interested in.
2. Design some variable or set of variables that can discriminate between the hypothesis under examination and possible background processes.
3. Construct a statistical model.
4. Test hypothesis.

This short list describes the process in the broadest of strokes but does help give a big picture understanding of what is being undertaken. Supersymmetry (SUSY) analyses, those looking for a new theory of physics beyond the Standard Model (SM), follow along this same path and we can add some detail to the steps outlined above. In these analyses and in particular what is called a *search*, a region of kinematic space is sought that will maximise the number of signal events in comparison to the number of events coming from background processes. From this perspective the *signal* events are those coming from supersymmetric processes (identified by some feature of the process observable in the detector) and those events classified as *background* look much like the signal processes but are in fact due to some known SM process. Let's consider a generic example analysis, a simple schematic in Figure 5.1 shows how the distributions of background (grey) and signal (red) differ for some variable. In this case the data agree with the background prediction. This region of parameter space, in which the number of signal events is high, is known as the *signal region* (SR) and is the focus of any SUSY analysis. Although, there may be more than one region as we will see.

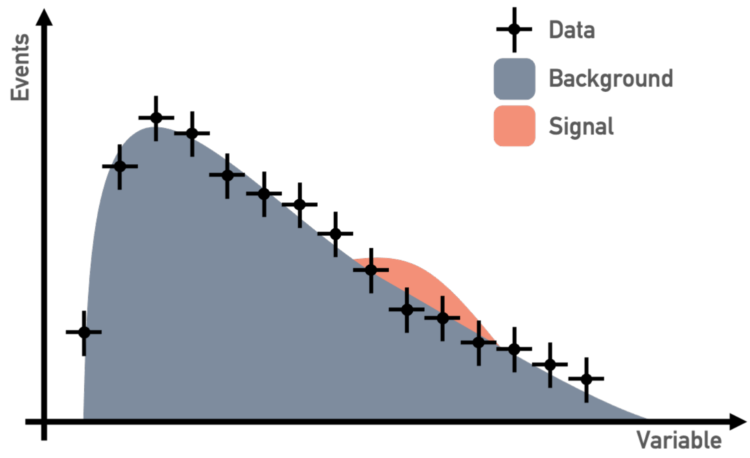

Figure 5.1: Schematic diagram of a generic variable and some distributions for background, in grey, and signal, in red. The data points in this example indicate agreement with the background hypothesis.

In general, once the SR has been defined the background contributions must be constrained and understood. This is done by defining a set of *control regions* (CRs) which are close to the SR and allow predictions of the SM to be compared to recorded data without any signal contamination but still allow for extrapolation to the SR. How well these background processes are modelled can be checked using another set of regions called *validation regions* (VRs). These are again ideally free of, or more realistically contain $\lesssim 1\%$, signal events. These are closer still to the SR, often being adjacent. The general structure of these regions can be seen in Figure 5.2.

The main focus of this chapter is a search for new physics beyond the SM that seeks a complex final state signature that would result from the long cascade decay of massive strongly produced gluinos ($\tilde{g}$), superpartner of the SM gluon. The hallmark of such a decay would be the observation of many hadronic jets along with a moderate amount of missing transverse momentum, $E_{\mathrm{T}}^{\mathrm{miss}}$, (see Section 5.4) in the detector. This signature presents challenges in background modelling and estimation. The principal background comes from QCD multi-jets and the sub-dominant background processes are $t\bar{t}$ and $W+$ jets. The estimation of the dominant background is achieved using a data-driven estimate while all others are simulated in Monte Carlo.

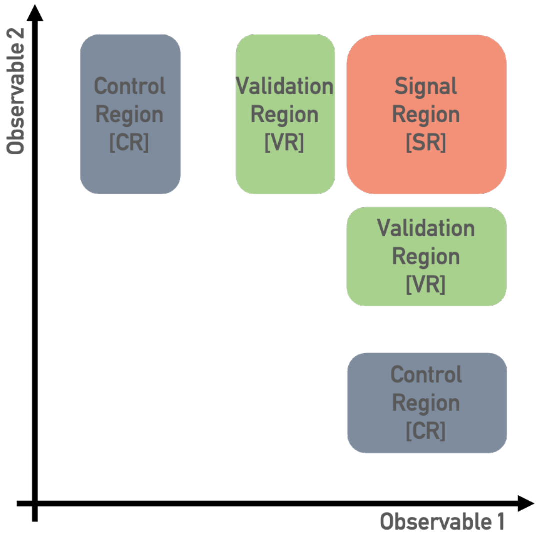

Figure 5.2: From the control regions (grey) the background modelling can be applied to data to test agreement without worry of signal contamination. These predictions are then tested by the validation regions, green, before finally being applied to the signal region in red.

During Run 2 (2015-2018) at the LHC the ATLAS experiment recorded *pp* collisions at 13 TeV corresponding to an integrated luminosity of 139 fb^{-1}. During, and in the wake of, the data taking runs, starting from 2015, related searches have been performed in four different incarnations corresponding to integrated luminosities of 3.2 fb^{-1}, 18.2 fb^{-1}, 36.1 fb^{-1} and 139 fb^{-1} [116][117][118][2]. In this chapter the analysis that uses the full Run 2 dataset of 139 fb^{-1} will be the focal point.

This most recent search includes some new techniques and parameter definitions to increase the discovery power. The first such addition is the use of particle-flow jets [70] that combine tracking and calorimeter information to form a more pile-up resistant and better resolved jet definition. This is the first such SUSY analysis to do so. Secondly an object-based definition of the missing transverse momentum significance [111], the development of which I was involved in, is now employed in ATLAS to enable better rejection of missing transverse momentum not originating from real invisible particles. Finally a new multi-bin fit [119] is employed in the results interpretation phase to increase the exclusion power for particular models by selecting signal regions most sensitive to each model.

5.2 Supersymmetric Signal Models

Three different types of Supersymmetry (SUSY) model are included in this search, and are illustrated in Figure 5.3. Two of these have the moderate missing transverse momentum signature due to a stable final state supersymmetric particle, these are R-parity[1] conserving (RPC) models [45]. The third signature has a small amount of missing transverse momentum, discussed below, and is an R-parity violating model (RPV) [48]. All three types of model are generated using the ATLAS fast simulation infrastructure [107]. Each of these represents a different aspect of the SUSY parameter space, but all show a common target signature with many hadronic jets. These simplified models are intended to capture some of the most important features of complete SUSY models. The focus here is on the production of pair produced gluinos, $\tilde{g}$, as these should have a high cross-section at a hadronic collider such as the LHC, and produce many jets.

5.2.1 Two-step

Gluinos can decay in a variety of ways. One such decay is to quarks and a chargino, $\tilde{\chi}_1^{\pm}$. This chargino may then cascade to produce a $W^{\pm}$ and Z boson along with the lightest neutralino $\tilde{\chi}_1^0$ which is stable (Figure 5.3 (a)). The masses of the SUSY particles represent the parameters of the model; $m_{\tilde{g}}$ and $m_{\tilde{\chi}_1^0}$. To reduce the number of free parameters the chargino mass, $m_{\tilde{\chi}_1^{\pm}}$, is constrained by $m_{\tilde{\chi}_1^{\pm}} = (m_{\tilde{g}} + m_{\tilde{\chi}_1^0})/2$ and in a similar fashion $m_{\tilde{\chi}_2^0}$ is determined by the relation $m_{\tilde{\chi}_2^0} = (m_{\tilde{\chi}_1^{\pm}} + m_{\tilde{\chi}_1^0})/2$. This decay mode will be known as the 'two-step' signal model.

5.2.2 Gtt

Another class of model to which this search has strong sensitivity is the decay of the gluino into top-quark rich final states mediated by the stop, $\tilde{t}_1$, known here as 'Gtt'. This can occur via an on- or off-shell stop, in the case of off-shell production the decay is assumed to have a 100% branching ratio to $t\bar{t} + \tilde{\chi}_1^0$ (Figure 5.3 (b)).

[1] $P_{\mathrm{R}} = (-1)^{3B+L+2s}$, where B is the baryon number, L is the lepton number and s is the quantum number of spin

5.2.3 RPV

Finally, permitting R-parity violation ('RPV' decay) allows the final state to be entirely SM quark dominated (Figure 5.3 (c)). These quarks can be detected and so the low values of $E_{\mathrm{T}}^{\mathrm{miss}}$ in these events, comes from the neutrinos produced in association with heavy quark decays and also from detector measurement. The low values of $E_{\mathrm{T}}^{\mathrm{miss}}$ are accessible due to the multi-jet triggers remaining fully efficient even at low values of missing transverse momentum. These events would not be accessible when using a dedicated $E_{\mathrm{T}}^{\mathrm{miss}}$ trigger as it only becomes fully efficient at higher values of missing transverse momentum.

Of the couplings that violate R-parity in the minimal supersymmetric standard model (MSSM) [48],

$$\int d^2\theta \lambda_1 U^C D^C D^C, \tag{5.1}$$

violate the baryon number by one unit and allows the all quark final state seen in Figure 5.3 (c). In this diagram the gluino decays via an intermediate top squark or stop ($\tilde{t}$) along with a standard model top quark. The $\tilde{t}$ is then able to further decay to two SM quarks, in this case b and s via the λ''_{323} coupling.

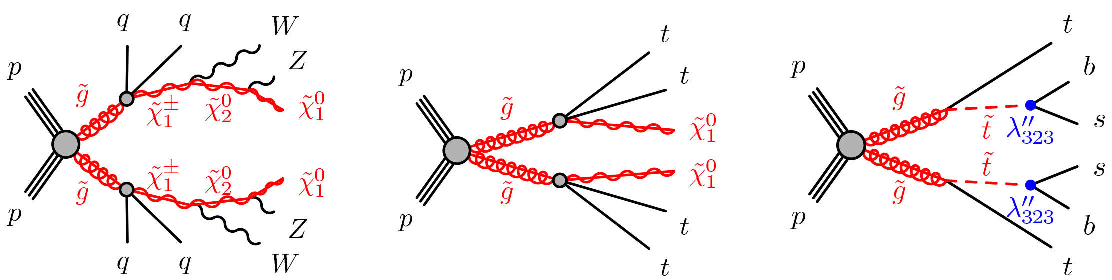

(a) Two-step **(b)** Gtt **(c)** RPV

Figure 5.3: The signal models sought by this analysis represented using pseudo-Feynman diagrams.

5.3 Event Selection

As discussed at the beginning of the chapter, one of the first steps in a particle physics analysis is to select a subset of the data to analyse. These first event selections are intended to select high quality events that are passed to a further selection stage. Here, an event must have at least one primary vertex with two reconstructed tracks, with $p_{\mathrm{T}} > 500\,\mathrm{MeV}$ measured by the ID [120]. Cleaning is required to remove backgrounds that are not due to any collision process from the beamline such as beam halo, cosmic ray particles incident on the detector and sporadic coherent energy spikes in the calorimeter. Jets originating from these unwanted processes are known as "fake jets" and those coming from $p-p$ collisions are "good jets". These "fake jets" are removed according to the "LooseBad" criteria as defined in [90] which selects "good jets" with an efficiency greater than 99.5% for jets with $p_{\mathrm{T}} > 20\,\mathrm{GeV}$. Any events failing these preliminary requirements are removed from further analysis.

Events early in LHC run 2 (2015 and 2016) were found to have had large amounts of transverse energy in particular $|\eta|$ ranges of the Liquid-Argon (LAr) calorimeter indicated by the measurement of unusual pulse shapes. This was caused by saturation of the endcap electromagnetic calorimeter and affected events were flagged such that they could be vetoed by analyses, including this one.

A large error ($> 20\%$) in the reconstructed momentum of muons indicates that an event is to be removed as these muons introduce high values of $E_{\mathrm{T}}^{\mathrm{miss}}$. Finally events containing a jet that is close to the *jet vertex tagger* JVT [121] selection are removed as they are likely from a non-vertex source and evade pile-up rejection later in the selection chain.

After any events failing the aforementioned conditions are removed, the physics objects used in the definition of various analysis sections are specified and used to further trim the sample.

5.4 Object Selection and Kinematic Variables

To identify final states of interest each physics object in the detector must be defined. These objects are constructed using a predefined set of characteristics in the detector. The reconstruction and calibration of objects removed from consideration by the analysis as well as the overlap removal procedure are detailed in Appendix B. The primary object considered by the analysis is the jet and the procedure for identifying and calibrating is outlined below along with definitions of important parameters.

Jets

For this analysis the primary jet collection is the new PFlow technique, whereas the EMTopo jet collection was used in the previous iteration using 36 fb^{-1} of 2015 and 2016 data [118]. The EMTopo jet collection is considered in a performance comparison with particle flow to determine any change in performance particularly in discovery and exclusion power. Both jet types are described in Section 3.4.5.

The jets are defined in two categories; "baseline" and "signal" and the latter is a subset of the former. Baseline jets are required to have a minimum transverse momentum cut of $p_{\mathrm{T}} > 20\,\mathrm{GeV}$ and to be within the pseudo-rapidity range $|\eta| < 2.8$. To be considered signal jets, several more constraints are added to the baseline according to the Jet Vertex Tagger (JVT) [121] criteria. In addition to this the analysis adds a final set of conditions that the jet must have $p_{\mathrm{T}} > 50\,\mathrm{GeV}$ or $p_{\mathrm{T}} > 80\,\mathrm{GeV}$ and also $|\eta| < 2.0$. The two transverse momentum cuts define two separate signal region streams as is later discussed in full in section 5.5.

b-Tagged Jets

The jet collections described above may also be tagged as resulting from a bottom quark using the MV2c10 algorithm[89]. MV2c10 combines track-based variables to form a multivariate discriminant designed to identify jets as being b-flavoured while rejecting those of c or light-flavour in simulated $t\bar{t}$ events. Jets are deemed to be b-flavour if they pass a 70% efficiency working point provided that they have satisfied the JVT conditions along with the kinematic and detector cuts of $p_{\mathrm{T}} > 20\,\mathrm{GeV}$ and $|\eta| < 2.5$. As this algorithm is optimised using simulation, scale factors are applied to correct for the differences in selecting b-jets in data [89].

Large Radius Jets

Small-R jets ($R = 0.4$) that have passed the overlap removal procedure with a transverse momentum $p_{\mathrm{T}} > 20$ GeV and fall within the pseudo-rapidity range $|\eta| < 2.0$ are used as inputs to the anti-k_t algorithm [85] to be reclustered into jets with a larger radius of $R = 1.0$ [122]. Large-R jets with $p_{\mathrm{T}} > 100$ GeV and $|\eta| < 1.0$ are defined as signal quality and used in analysis selections.

Object-based Missing Transverse Momentum And Its Significance

An improvement over previous analyses is the introduction of the object-based missing transverse momentum, $E_{\mathrm{T}}^{\mathrm{miss}}$, and its significance, $\mathcal{S}(E_{\mathrm{T}}^{\mathrm{miss}})$ or $E_{\mathrm{T}}^{\mathrm{miss}}$ significance). This replaces an older heuristic definition ($E_{\mathrm{T}}^{\mathrm{miss}}/\sqrt{H_{\mathrm{T}}}$) that approximated the resolution of $E_{\mathrm{T}}^{\mathrm{miss}}$ using the square root of the hard term which is a scalar sum of all jet p_{T},

$$H_{\mathrm{T}} = \sum_{i} p_{\mathrm{T,i}}, \tag{5.2}$$

here the index runs over the jets. The $E_{\mathrm{T}}^{\mathrm{miss}}$ and its significance and discussed in detail in Chapter 4.

Event-level (Large-R) Jet Mass

All of the reconstructed large-R jets ($R = 1.0$) have their masses calculated ($m_j^{R=1.0}$) and summed to find a total mass of large-R jets in the event:

$$M_{\mathrm{J}}^{\Sigma} = \sum_{j} m_j^{R=1.0}. \tag{5.3}$$

SM processes involving jets with masses significantly larger than the top quark mass are rare and such final states would be an indication of BSM physics. This variable is used in a separate stream of the analysis, the jet-mass channel, which targets decays of SUSY particles that have enough mass to produce massive, highly-boosted SM particles. The definitions of the jet mass regions using the event level jet mass are described later in Section 5.5.

Transverse Mass

To enhance the contribution of leptonically decaying W bosons, that will increase the number of events in the control regions and so better constrain this background, one can utilise the transverse mass

$$m_{\mathrm{T}} \simeq_{m_l \to 0} \sqrt{2 p_{\mathrm{T}}^{l} E_{\mathrm{T}}^{\mathrm{miss}} \cos\left(\Delta\phi_{l,E_{\mathrm{T}}^{\mathrm{miss}}}\right)}. \tag{5.4}$$

Under the assumption that a heavy resonance decays into two particles, one of which is massless, the above equation is found. The transverse momentum is that of the detected lepton (p_{T}^{l}) and the missing transverse momentum is that of the neutrino escaping undetected ($E_{\mathrm{T}}^{\mathrm{miss}}$). Finally the cosine function acts on the angular difference between the lepton and neutrino in the azimuthal plane recovering the directional information necessary to construct a bound on the mass of the parent particle, which, in this case is a W boson.

Trigger Selections

Multi-jet triggers are used in this analysis and the triggers are outlined in Table 5.1. The triggers select events based on the appearance of a certain number of jets (each having $|\eta| < 2.4$), with a particular transverse momentum. The trigger strategy can vary from year to year. The consequences of this, in terms of the analysis, are discussed in Sections 5.6.1 and 5.6.4.

Trigger Thresholds	
N_{jet}^{50}	N_{jet}^{80}
2015-2016: $N_{\text{jet}} = 6$ with $p_{\text{T}} > 45$ GeV	2015: $N_{\text{jet}} = 5$ with $p_{\text{T}} > 70$ GeV
2017-2018: $N_{\text{jet}} = 7$ with $p_{\text{T}} > 45$ GeV	2016: $N_{\text{jet}} = 5$ with $p_{\text{T}} > 65$ GeV
	2018: $N_{\text{jet}} = 5$ with $p_{\text{T}} > 70$ GeV

Table 5.1: The trigger conditions used to select events for the analysis shown by year with the jet and transverse momentum conditions, for a definition of N_{jet}^{50} and N_{jet}^{80} refer to Section 5.5.

5.5 Signal Regions

This analysis targets final states that would indicate the presence of physics beyond the SM in the form of Supersymmetry. These events would form long cascade decays with many hadronic jets along with a moderate amount of missing transverse momentum carried away by the lightest supersymmetric particle, LSP. The $E_{\text{T}}^{\text{miss}}$ carried by such an invisible particle would be much larger than that caused by the resolution of the detector and so have an $E_{\text{T}}^{\text{miss}}$ significance value indicating that this missing transverse momentum was indeed due to a real source.

Events are chosen through a series of selections, summarised in Table 5.2. The first such selection is that there are no reconstructed baseline leptons present (Section 5.4). This reduces the contribution of events with real $E_{\text{T}}^{\text{miss}}$ from neutrinos that are produced in addition to the lepton (electron or muon) from a W boson decay. The jet multiplicity (N_{jet}) is the next important event selection parameter and is key in the definition of the signal regions (SRs).

SRs are split into two categories based on the jet multiplicity and the transverse momentum cut imposed on the jets. All of the signal-jets must have a pseudo-rapidity cut of $|\eta| < 2.0$. Events are first selected on the number of signal jets each having $p_{\text{T}} > 50$ GeV (N_{jet}^{50}). These regions contain events with greater than or equal to 8, 9, 10, 11 and 12 jets above the p_{T} cut. Events with, progressively more jets, having $p_{\mathrm{T}} > 80\,\mathrm{GeV}$ form another count, N_{jet}^{80}, where events may have 9 or more jets.

In order to boost the sensitivity to models that couple strongly to heavy flavour quarks a b-jet requirement is overlaid on to the jet multiplicity restrictions. The $N_{\mathrm{jet}}^{50,80}$ regions can be subdivided according to the b-jet multiplicity $N_{b-\mathrm{jet}}^{50,80}$ with values $= 0$, $= 1$ or ≥ 2.

A third dimension is applied to the selection stream defining the signal regions with N_{jet}^{50} to increase sensitivity to the decay of massive gluinos that cause heavy SM particles to become boosted. These boosted particles will produce large radius jets with an unusually high mass. The selections are applied using M_{J}^{Σ} (Section 5.4) and target ranges defined approximately by the top mass (m_t). They exploit the observation that few SM processes produce jets with masses significantly above m_t. The ranges for the event level jet mass are defined to be up to about twice m_t ($0 < M_{\mathrm{J}}^{\Sigma} \leq 340\,\mathrm{GeV}$), between about twice and three times the mass of the top quark ($340\,\mathrm{GeV} < M_{\mathrm{J}}^{\Sigma} \leq 500\,\mathrm{GeV}$) and all masses above $\sim 3m_t$ with no upper bound ($M_{\mathrm{J}}^{\Sigma} > 500\,\mathrm{GeV}$). In the $p_{\mathrm{T}} > 80\,\mathrm{GeV}$ SRs there are no such additional requirements on M_{J}^{Σ}.

The final condition imposed on signal region events is a restriction in the $E_{\mathrm{T}}^{\mathrm{miss}}$ significance designed to remove sources of fake missing transverse momentum and is $\mathcal{S}\left(E_{\mathrm{T}}^{\mathrm{miss}}\right) > 5$. Rejecting low values of $E_{\mathrm{T}}^{\mathrm{miss}}$ significance removes most events with the missing transverse momentum largely originating from detector resolution. The chosen threshold discards much of the SM multi-jet processes in the SR while allowing intermediate values of $E_{\mathrm{T}}^{\mathrm{miss}}$ associated with potential signal to remain.

Selection	Conditions		
Lepton veto	0 baseline leptons (μ or e) with $p_{\mathrm{T}} > 10\,\mathrm{GeV}$		
Jet momentum	$p_{\mathrm{T}} > 50\,\mathrm{GeV}$ **or** $p_{\mathrm{T}} > 80\,\mathrm{GeV}$, both $\lvert\eta\rvert < 2.0$		
N_{jet}	$N_{\mathrm{jet}}^{50} \geq 8, 9, 10, 11, 12, \ldots$ **or** $N_{\mathrm{jet}}^{80} \geq 7, 8, 9, \ldots$		
$N_{b-\mathrm{jet}}$	$= 0$	$= 1$	≥ 2
M_{J}^{Σ}	0-340 GeV	340-500 GeV	≥ 500 GeV
$E_{\mathrm{T}}^{\mathrm{miss}}$ significance	$\mathcal{S}\left(E_{\mathrm{T}}^{\mathrm{miss}}\right) > 5$		

Table 5.2: A summary of the selection criteria that define the signal regions. The first three rows define the basic cuts for every signal region, every jet multiplicity with $p_{\mathrm{T}}^{\mathrm{jet}} > 50\,\mathrm{GeV}$ is split by each b-jet selection forming three flavour selections per N_{jet}^{50}. These sub-regions are then further divided by the event level jet mass (M_{J}^{Σ}) requirements. The $p_{\mathrm{T}} > 80\,\mathrm{GeV}$ regions are only subdivided by b-jet multiplicity. In both cases there must be greater than ten SM background events in the region, if this is not the case the regions are merged together starting from the M_{J}^{Σ} bins and working back up the table. The final $E_{\mathrm{T}}^{\mathrm{miss}}$ significance condition defines the signal range in the distributions and hence the blinded regions.

Signal Region	Target Model
8ij50-0ib-MJ500	pMSSM
9ij50-0ib-MJ340	Gtt
10ij50-0ib-MJ340	2-step
10ij50-0ib-MJ500	2-step
10ij50-1ib-MJ500	RPV, Gtt
11ij50-0ib-MJ0	2-step
12ij50-2ib-MJ0	Extreme SM
9ij80-0ib-MJ0	2-step

Table 5.3: Certain SRs are chosen to be used in the single-bin discovery fit to increase sensitivity to the target models and provide a good coverage of the phase space. Furthermore the 12 jet region, *12ij50-2ib-MJ0*, is a previously unexplored, and extreme, region in data while the 8 jet region, *8ij50-0ib-MJ500*, is sensitive to a model considered in the previous analysis.

For each N_{jet}^{50} selection there are 9 sub regions divided by $N_{b-\text{jet}}$ and M_{J}^{Σ} for the selection shown in Table 5.5. A condition that a given N_{jet} SR must have at least 10 events predicted means that regions with fewer than 10 events are merged with other regions starting with a merge of the M_{J}^{Σ} bins.

To improve the discovery potential of the analysis, a statistical test [119] is applied to a subset of signal regions designed to target each of the signal models discussed in section 5.2. These regions and the target model are shown in Table 5.3. For a description of the SR naming conventions see Section 5.5.1.

Multi-bin Fit Region					
N_{jet}^{50}	SR Name	$N_{b-\text{jet}}$	SR Name	M_{J}^{Σ}	Multi-bin SR Name
≥ 8	8ij50	$= 0$	8ij50-0eb	$(0, 340]$	8ij50-0eb
				$(340, 500]$	8ij50-0eb-MJ340
				$(500, \text{inf})$	8ij50-0eb-MJ500
		$= 1$	8ij50-1eb	$(0, 340]$	8ij50-1eb
				$(340, 500]$	8ij50-1eb-MJ340
				$(500, \text{inf})$	8ij50-1eb-MJ500
		≥ 2	8ij50-2ib	$(0, 340]$	8ij50-2ib
				$(340, 500]$	8ij50-2ib-MJ340
				$(500, \text{inf})$	8ij50-2ib-MJ500

Table 5.4: An example of one of the multi-bin fits, the regions are formed in much the same way as the general SRs except with the modified $b-$jet selections that impose orthogonality. The same logic applies to the other two multi-bin fits that use $N_{\text{jet}} \geq \{9, 10\}$. For complete summary of the region nomenclature go to Section 5.5.1

For an enhanced exclusion potential with respect to the selected signal models another fit method is employed, the multi-bin fit. This technique uses the $N_{\text{jet}}^{50} \geq 8, 9, 10$ regions and for these jet multiplicities the $N_{b-\text{jet}}$ selections are similar but contain explicit, rather than exclusive cuts, $N_{b-\text{jet}}^{50} = 0, = 1, \geq 2$. This modification to the $b-$jet conditions prevents any overlap between the signal regions and ensures that they are orthogonal thus allowing the probability density functions (PDF) to be treated as uncorrelated. The SRs are again divided by M_{J}^{Σ}, resulting in 9 SRs per jet multiplicity as shown in Table 5.4 for the $N_{\mathrm{jet}}^{50} \geq 8$ regions.

5.5.1 Signal Region Nomenclature

A condensed method for identifying each region is employed to simplify communication.

- Each region type is specified using a two letter acronym e.g. *signal region* becomes 'SR' and *control region* is 'CR'.
- The jet multiplicity, N_{jet}, is classified as being inclusive 'ij' ($N_{\mathrm{jet}} \geq a$) or exclusive 'ej' ($N_{\mathrm{jet}} = a$).
- The jet p_{T} cut is reduced to the numerical value in GeV, 50 or 80.
- b-jet multiplicity is split into inclusive and exclusive in a similar manner to N_{jet} using 'ib' and 'eb'.
- The M_J^{Σ} specification for a range ($0 < M_{\mathrm{J}}^{\Sigma} < 340\,\mathrm{GeV}$) becomes 'MJ0TO340' and any threshold ($M_{\mathrm{J}}^{\Sigma} > 500\,\mathrm{GeV}$) reduces to 'MJ500'.

This notation allows regions to be written in a compact fashion in which each selection is separated by a hyphen such as 'SR-10ij50-2ib-MJ500'. This region requires $N_{\mathrm{jet}} \geq 10$ all having $p_{\mathrm{T}} > 50\,\mathrm{GeV}$, $N_{b-\mathrm{jet}} \geq 2$ and $M_{\mathrm{J}}^{\Sigma} > 500\,\mathrm{GeV}$. Note that the absence of 'MJ' in a region string is indicative of there being no restriction on M_{J}^{Σ}. A full set of regions for $N_{\mathrm{jet}}^{50} \geq 8$ can be seen in Table 5.5, the same logic applies to all higher jet multiplicity regions.

N_{jet}^{50}	SR Name	$N_{b-\text{jet}}$	SR Name	M_{J}^{Σ}	Complete SR Name
≥ 8	8ij50	≥ 0	8ij50-0ib	$(0, 340]$	8ij50-0ib
				$(340, 500]$	8ij50-0ib-MJ340
				$(500, \infty)$	8ij50-0ib-MJ500
		≥ 1	8ij50-1ib	$(0, 340]$	8ij50-1ib
				$(340, 500]$	8ij50-1ib-MJ340
				$(500, \infty)$	8ij50-1ib-MJ500
		≥ 2	8ij50-2ib	$(0, 340]$	8ij50-2ib
				$(340, 500]$	8ij50-2ib-MJ340
				$(500, \infty)$	8ij50-2ib-MJ500

Table 5.5: Tabular illustration of how the selections for the signal regions are applied for $p_{\text{T}} > 50\,\text{GeV}$ jets. Moving from left to right the various conditions are applied starting with jet multiplicity, then the $b-$jet conditions and finally the ranges of M_{J}^{Σ} are imposed. The rightmost column displays the final signal region name and demonstrates that there are 9 regions per N_{jet} selection. This structure repeats for $N_{\text{jet}} \geq \{9, 10, 11, 12\}$ as long as the minimum event number condition is met (mentioned above in Section 5.5).

5.6 Backgrounds

With the SRs defined according to the signal models, the background contributions in these regions can be estimated as was outlined in the general SUSY analysis summary (5.1). This is done using a set of *Control Regions*, CRs, that will allow the predicted or estimated background contributions to be tested in a region with minimal signal contamination. These regions should be placed such that extrapolation to the SRs is reliable. The main background contribution comes from QCD multi-jets, particularly at low $E_{\text{T}}^{\text{miss}}$, followed by two other major contributions from $t\bar{t}$ and $W+$jets. Figure 5.4 shows the primary production modes for these two background types.

The production of top quarks results in the appearance of a bottom quark and a W boson almost 100% of the time. This decay will result in an all hadronic final state of the form $t\bar{t} \rightarrow b\bar{b}WW \rightarrow b\bar{b}q\bar{q}q\bar{q}$ in 44% [11] of cases and so can be detected as a 6 jet final state with more jets possible due to final and initial state radiation (FSR and ISR). Figure 5.5 (a) shows the fully hadronic decay of a top quark diagrammatically; the semi-leptonic decay (Figure 5.5 (b)) is used to constrain the $t\bar{t}$ contribution to the SRs.

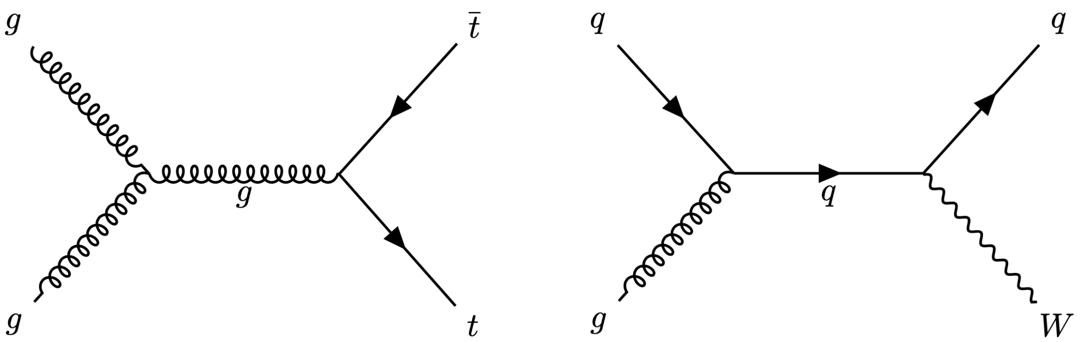

(a) $t\bar{t}$ **(b)** $W+\text{jets}$

Figure 5.4: The two most dominant SM background contributions to the SRs after QCD multi-jet. The main production of $t\bar{t}$ is by the gluon fusion mechanism [11] (a) while a production mode for $W+$jets is shown in (b) [123].

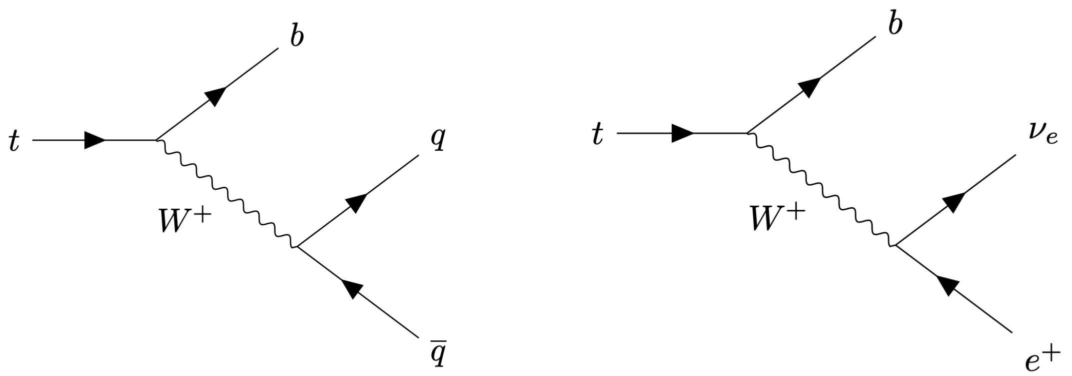

(a) Fully Hadronic top decay **(b)** Semi-leptonic top decay

Figure 5.5: The fully hadronic decay of a top quarks (a) contribute to the signal regions the decay of the anti-top is very similar in its final state signature except the decay goes by $\bar{t} \to \bar{b}W^-$. The semi-leptonic decay (b) is targeted by the control regions to constrain $t\bar{t}$ in the SRs [123].

Another sub-dominant background comes from the production of a W boson in conjunction with a quark (Figure 5.4 (b)). This process, with a hadronically decaying W, would ideally produce only three jets in the detector. However as mentioned in the case of $t\bar{t}$ more jets can be produced by the emission of a gluon. This gluon emission is proportional to the strong coupling constant ($\alpha_\mathrm{s}(M_Z) = 1.1181$ [11]) and becomes even further suppressed with the emission of N gluons being proportional to α_s^N. This naturally reduces the contribution of this process to the high multiplicity SRs but it still must be estimated and again the semi-leptonic decay $qW \to q'\ell\nu$ is used for the CRs.

To estimate the background processes entering in to the signal regions the leptonic contributions briefly mentioned above and further discussed in Section 5.6.1 are constrained using CRs while the QCD multi-jets contribution is estimated using a template method built from the *template regions* (TR). The template estimation and other background processes are then tested in a set of *validation regions* (VR), covered in Section 5.6.2.

There is a final set of sub-dominant processes that are estimated with sufficient accuracy using the Monte Carlo simulations with no control regions. Backgrounds in this category include single top quark contributions and $t\bar{t}$ production accompanied by intermediate vector bosons or other heavy particles such as $t\bar{t}t\bar{t}$, $t\bar{t}+W$, $t\bar{t}+Z$ and $t\bar{t}+WW$; collectively known as $t\bar{t}+X$. The final contribution to the lesser background category is the production of two vector bosons, known as di-boson, such as WW, WZ and ZZ.

Once the $W+\text{jets}$ and leptonically or semi-leptonically decaying $t\bar{t}$ backgrounds have been simulated in Monte Carlo they are compared to data in a set of control regions (defined in Section 5.6.1) and, to correct for any mismodelling of the simulation, HistFitter [119] performs a simultaneous background only fit to calculate normalisation factors $\mu_{W+\text{jets}}$ and $\mu_{t\bar{t}}$ for $W+\text{jets}$ and $t\bar{t}$ respectively. Due to the construction of the leptonic control regions there is almost no contribution from multi-jets and so these factors are independent of the template estimation which is considered in Section 5.6.4. The multi-jets estimation also has a set of control regions known as QCRs and these are covered in full in Section 5.6.2. In a similar way to the leptonic contributions, a normalisation factor $\mu_{\mathrm{multi-jets}}$ is used to correct for inaccuracies in the template method (Section 5.6.4). This factor is also sensitive to the mismodelling in the leptonic backgrounds. All three normalisation factors result from a simultaneous fit of leptonic and multi-jet control regions which also accounts for systematic uncertainty related to MC predictions and uncertainty on the template method.

5.6.1 Leptonic Background Estimation

The leptonic backgrounds from $W+$ jets and leptonically and semi-leptonically decaying $t\bar{t}$ are estimated using Monte Carlo Simulation. They also form an important contribution to the dominant QCD multi-jet's (largest background) data-driven estimation method. The Monte Carlo generators are summarised in Table 5.6 and all simulated events have multiple p–p collisions simulated with soft QCD processes of Pythia8 [101] overlaid. The detector response is simulated using Geant4 [108]. The two largest MC contributions are expected to be $t\bar{t}$ and $W+$ jets and further detail on the MC simulations is available in [2].

Background Process	Generator
$t\bar{t}$	Powheg [100] and Pythia8 [101] for the parton shower
Single top	Powheg [100] and Pythia8 [101] for the parton shower
W or $Z+$ jets	Sherpa [104]
Diboson	Sherpa [104]
$t\bar{t}+X$	MadGraph5 [124]

Table 5.6: A summary of the MC generators used to determine the main leptonic backgrounds. The $t\bar{t}+X$ row represents the production of $t\bar{t}$ with additional heacy particles.

Control regions (CR) are constructed to determine the normalisation of these backgrounds. The CRs are split into two and each is designed to be enriched in either $W+$ jets (WCR) or $t\bar{t}$ (TCR) and a full summary is provided in Table 5.7.

The first selection is on the jet multiplicity: this must be $N_{\mathrm{jet}} - 1$ where N_{jet} is the multiplicity of the signal region in which the leptonic background contribution is being calculated. The same jet p_{T} cuts of 50 GeV and 80 GeV are used as well as the same M_{J}^{Σ} conditions in the case of the N_{jet}^{50} SRs. Placing the control regions at N_{jet} one below the SR is used to increase the yields available to these regions and hence have an improved background estimation after the simultaneous fit. However, in the low N_{jet} regions this is not possible due to the desire for an unprescaled trigger in the 50 GeV regions. In 2017 the unprescaled trigger was changed from 6j45 to 7j45 (Table 5.1) meaning that the CRs for the 8ij50 SR necessarily have the same jet multiplicity.

These CRs also require exactly one lepton and this can be either an electron or a muon, in either case with $p_{\mathrm{T}} > 10$ GeV. The control regions are subdivided by the lepton flavour and follow the naming convention *CR1e* or *CR1m* with the rest of the nomenclature the same as explained in Section 5.5.1. In order to enhance the contribution from a single leptonically decaying W boson in an event and reduce signal contamination, the transverse mass (m_{T} in Section 5.4), calculated from the lepton p_{T} and the missing transverse momentum, has to be less than 120 GeV.

The main difference between the $t\bar{t}$ and $W+$jets background types, and so the criterion by which they are partitioned, is the presence or absence of a $b-$jet. Events containing zero $b-$jets will have a higher occurrence of a single leptonically decaying W boson with hadronic jets (WCR) while the appearance of one or more $b-$jets indicates the production of $t\bar{t}$ due to the top quark having branching ratio to bottom quarks that is close to unity. To form the corresponding CR, each of the $b-$jet regions the bins are subdivided into M_{J}^{Σ} bins in the same manner as the SRs discussed above and these 3 bins per control region are used in the multi-bin fit process.

Selection	Conditions
Leptons	Exactly 1 baseline lepton (μ or e) with $p_{\mathrm{T}} > 10\,\mathrm{GeV}$
m_{T}	$< 120\,\mathrm{GeV}$
N_{jet}	$N_{\mathrm{jet}}^{\mathrm{SR}} - 1$, p_{T} same as SR and $\lvert\eta\rvert < 2.0$
$N_{b-\mathrm{jet}}$	$= 0$ for $W+$ jets (WCR) ≥ 1 for $t\bar{t}$ (TCR)
M_{J}^{Σ}	Same as SR
$E_{\mathrm{T}}^{\mathrm{miss}}$ significance	$\mathcal{S}\left(E_{\mathrm{T}}^{\mathrm{miss}}\right) > 4$

Table 5.7: The selections summary for the leptonic control regions that normalise the background contributions from $W+$ jets and $t\bar{t}$. To increase statistics and therefore improve the constraint of these backgrounds the $\mathcal{S}(E_{\mathrm{T}}^{\mathrm{miss}})$ cut is relaxed. As a further measure to increase the number of events in the CRs any lepton passing the jet kinematic requirements may enter the CR reconstructed as a jet.

There is a restriction on the $E_{\mathrm{T}}^{\mathrm{miss}}$ significance in the SRs to remove fake sources of $E_{\mathrm{T}}^{\mathrm{miss}}$ that would otherwise contaminate the SRs. In the CRs to increase the statistics and improve background estimation compared to the SR value, this restriction is loosened to $\mathcal{S}(E_{\mathrm{T}}^{\mathrm{miss}}) > 4.0$.

Using these regions, the contributions from leptonically decaying W as well as semi- and leptonically decaying $t\bar{t}$ events entering the signal regions can be normalised. The simulation is compared to data with the same cuts for each control region and then the multi-bin fit is performed to determine normalisation factors that correct for any mismodelling. Most of the leptons entering the signal regions come from mis-reconstructed electrons, leptons that fall outside of the detector's acceptance or hadronically decaying taus that could not be differentiated from a parton seeded jet. All of these can contribute $E_{\mathrm{T}}^{\mathrm{miss}}$ to the signal regions so these backgrounds must be understood and constrained.

To illustrate the control regions contributing to a particular signal region, SR-9ij50-1ib for example, the two control regions each requiring one electron (according to the criteria above) are shown in Figure 5.6 after the background fit procedure is applied. The left hand sub-figure shows the TCR (CR1e-8ij50-1ib) with the imposition that the number of b-jet(s) be one or more to enrich top processes and the right sub-figure has the zero b-jet restriction that specifies the WCR. The Monte Carlo prediction representing each targeted process is larger in the appropriate control region. Overall the data and prediction agree and many of the data points are covered by the combined statistical and systematic uncertainties. The figure also demonstrates the negligible amount of signal contamination by plotting one model point from each of the RPV and 2-step signal models. The dashed signal contribution lines are found to be $< 1\%$ consistently in across the distributions. A full summary of the predictions and yields in each of the TCRs and WCRs is available in Figure 5.7. All of the control regions are presented for both backgrounds with the single-electron and single-muon events shown separately.

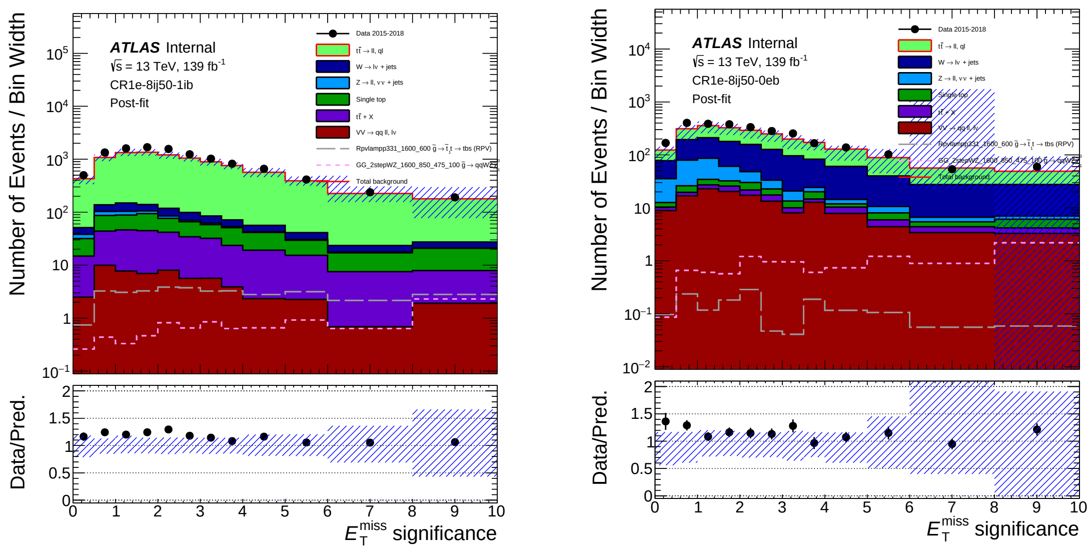

(a) 50 GeV inclusive b-jet control region with $N_{\text{jet}}^{50} \geq 8$ and no M_{J}^{Σ} cuts for top control.

(b) 50 GeV $N_{b-\text{jet}}^{50} = 0$ control region with $N_{\text{jet}}^{50} \geq 8$ and no M_{J}^{Σ} requirement for W control.

Figure 5.6: $\mathcal{S}\left(E_{\text{T}}^{\text{miss}}\right)$ distributions for the two electron control regions. The background normalisation factor from the background-only multi-bin fit has been applied. The $t\bar{t}$ (left) and W (right) control regions show good agreement with data and most points in the are covered by the combined statistical and systematic errors. The dashed lines represent chosen signal models and demonstrate the low signal contamination in these regions.

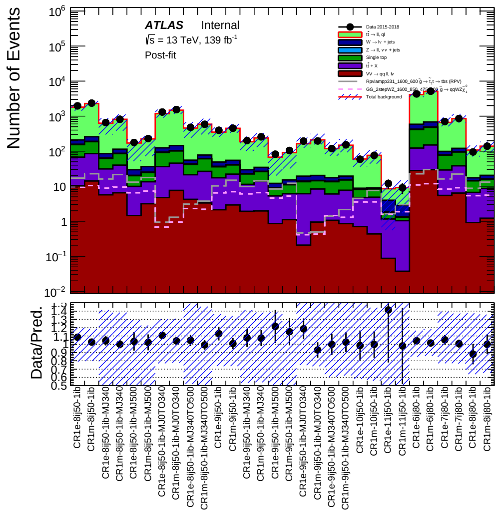

(a) 50 and 80 GeV inclusive b-jet control regions summary for TCRs.

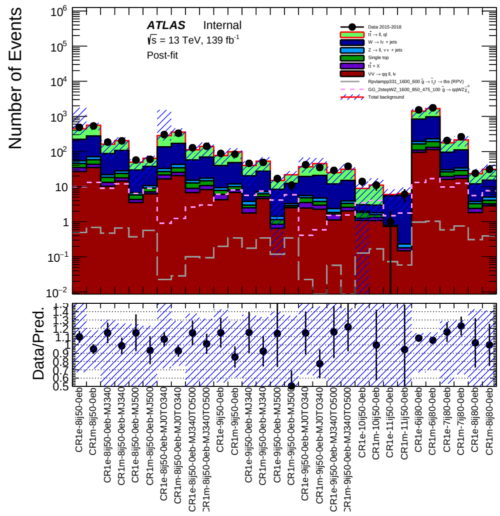

(b) 50 and 80 GeV zero b-jet control regions summary for WCRs.

Figure 5.7: A summary of the predicted and observed yields for TCRs (left) with the $p_{\mathrm{T}} > 50\,\mathrm{GeV}$ and $p_{\mathrm{T}} > 80\,\mathrm{GeV}$ jet selections. The sub-figure shows both the electron and muon regions agree well with data after the normalisation factors have been applied. The signal contamination is generally below 10%. The WCRs (right) have the same format except with $N_{b-\mathrm{jet}} = 0$ and again show good prediction of the $W+$ jets background.The signal contamination for the two-step model is higher than 10% in some of the more statistically limited bins and this is due to the signal model requiring a W in the final state 5.3.

All of the regions are modelled well after the normalisation factors μ_{W+jets} and $\mu_{t\bar{t}}$ are applied. Showing that these backgrounds are well understood and can be constrained in the SRs.

5.6.2 Multi-jet Background Estimation

The dominant background in the analysis comes from QCD multi-jet events. This contribution to the signal regions is extracted using a data-driven template method. Although named the template method in the context of this analysis this technique is more broadly known as the ABCD, or matrix, method. The signal models indicate that there will be a great many jets in the signal regions of this search, this introduces some problems in estimating the SM multi-jet contribution in these areas of phase space.

The simulation of these complex QCD objects can quickly become very computationally expensive and for many analyses there is simply not enough precision at such high multiplicities. It must be said that a great deal of progress has been made on this front [125], however, the lack of statistics and large systematic errors that come with high numbers of jets force analysers to choose a different path; often data-driven methods like the one discussed here.

5.6.3 The ABCD Method

The core idea of many, if not all, data-driven techniques is to use information from several separate background dominated regions to extrapolate or infer those same properties in a signal dominated region. Firstly, two variables must be chosen (call them f and g) that have different behaviour for signal and background, ideally localising the signal to one region. These variables must also be statistically independent to good approximation, this property can be manually ensured. Once these variables are identified the two-dimensional space can be partitioned using the intelligent application of simple cuts on each axis. In this method the regions are defined by their signal content, the signal is localised to one region A and then there are three background dominated regions (B, C, D) as shown in Figure 5.8. With all of this in place the background contribution to the signal region, A, can be estimated using the three background dominated regions, B, C, D, with the simple relation

$$N_A = \frac{N_B N_C}{N_D}, \tag{5.5}$$

where N_i is the number of events in the i-th region and $i \in \{A, B, C, D\}$. For the multi-jets analysis the two variables chosen for use in the ABCD method are N_{jet} and $\mathcal{S}(E_{\text{T}}^{\text{miss}})$.

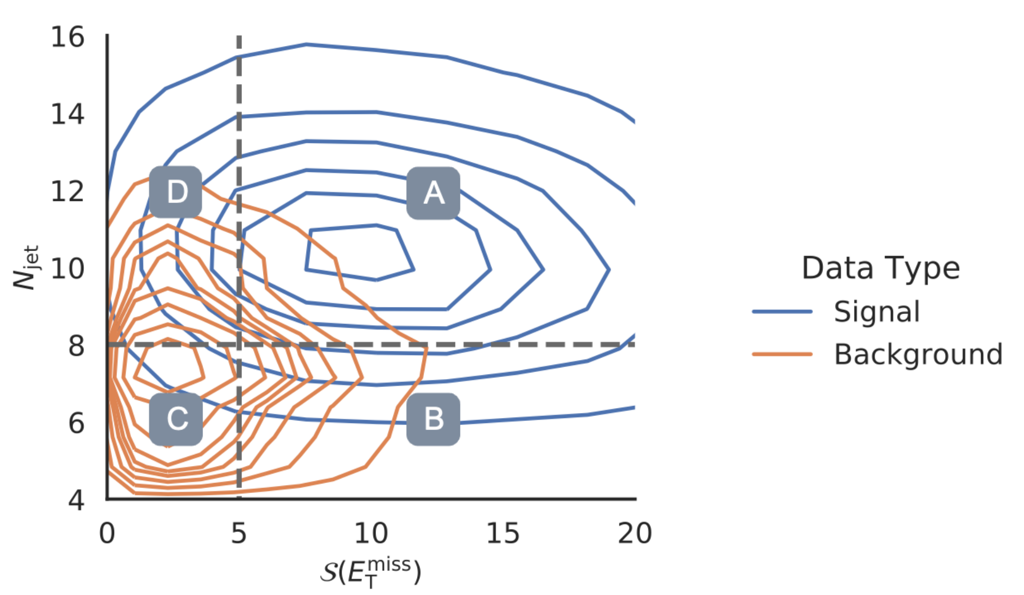

Figure 5.8: Contours for signal (blue) and background (orange) distributions using the number of jets in an event N_{jet} and the missing transverse momentum significance $\mathcal{S}(E_{\mathrm{T}}^{\mathrm{miss}})$ variables. These quantities are used for the multi-jets data-driven estimation of QCD multi-jets in the signal regions. Simple cuts to define the ABCD regions are demonstrated with the dashed grey lines.

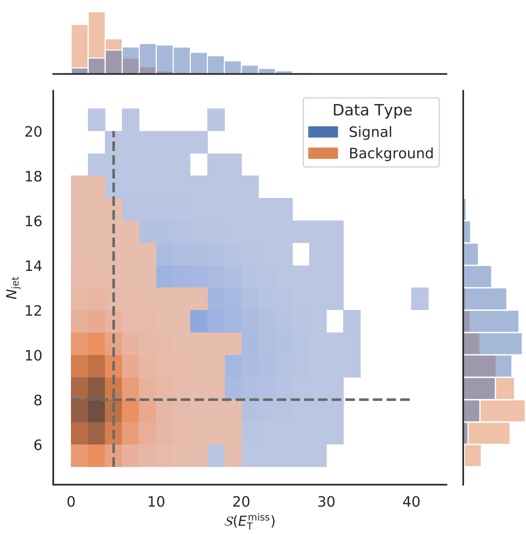

Figure 5.9: Histograms, centrally in two-dimensions and one-dimension on the peripheries, for signal (blue) and background (orange) simulation. The number of jets in an event N_{jet} and the missing transverse momentum significance $\mathcal{S}(E_{\mathrm{T}}^{\mathrm{miss}})$ are the ordinate and abscissa respectively in the two-dimensional histogram. Simple cuts to define the ABCD regions are demonstrated with the dashed grey lines and these show how good separation between signal and background dominated regions can be achieved with relative ease.

5.6.4 The Template Method

The primary assumption at the heart of this data-driven technique is that the shape of the $\mathcal{S}\left(E_{\mathrm{T}}^{\mathrm{miss}}\right)$ spectrum is invariant as the number of jets is increased, an assumption that is tested using the procedure described below.

The measurement of such a high number of jets means that the amount of $E_{\mathrm{T}}^{\mathrm{miss}}$ originating from detector effects, principally jet mismeasurement, will contaminate the SRs. This is another important use of the $E_{\mathrm{T}}^{\mathrm{miss}}$ significance parameter in that these unwanted events can be removed as they have low values of $\mathcal{S}\left(E_{\mathrm{T}}^{\mathrm{miss}}\right)$ (Section 5.4).

After the determination of all other SM processes in SRs is complete, as described above in Sections 5.6 and 5.6.1, these events are subtracted from data in each of the regions leaving only the contribution from QCD multi-jet events. In short, the template method for multi-jet background estimation can be outlined as:

1. Extract the shape of the $\mathcal{S}\left(E_{\mathrm{T}}^{\mathrm{miss}}\right)$ at low N_{jet}.
2. Validate the prediction of the $\mathcal{S}\left(E_{\mathrm{T}}^{\mathrm{miss}}\right)$ spectrum at the desired jet multiplicity but with lower $\mathcal{S}\left(E_{\mathrm{T}}^{\mathrm{miss}}\right)$ values than the signal region definition.
3. Validate the extraction of $\mathcal{S}\left(E_{\mathrm{T}}^{\mathrm{miss}}\right)$ to higher N_{jet} and the extrapolation to high $\mathcal{S}\left(E_{\mathrm{T}}^{\mathrm{miss}}\right)$ for a particular N_{jet}.
4. Calculate the prediction of QCD multi-jets in each of the signal regions, using the template normalised at low $\mathcal{S}\left(E_{\mathrm{T}}^{\mathrm{miss}}\right)$, but with the same N_{jet} as the corresponding SR.

The shape of the $\mathcal{S}\left(E_{\mathrm{T}}^{\mathrm{miss}}\right)$ distribution is measured at low N_{jet}, which, is determined by the lowest jet multiplicity recorded by the trigger. There are two triggers, one for each p_{T} cut, that define the shape extraction template region or $\texttt{TR}_{\mathrm{shape}}$ and these are $N_{\mathrm{jet}} = 7$ for the $p_{\mathrm{T}} > 50\,\mathrm{GeV}$ stream and $N_{jet} = 5$ for the $p_{\mathrm{T}} > 80\,\mathrm{GeV}$

jets. The $\mathtt{TR}_{\text{shape}}$ yields are found after the subtraction, from data, of the predicted number of events due to the Monte Carlo modelled processes.

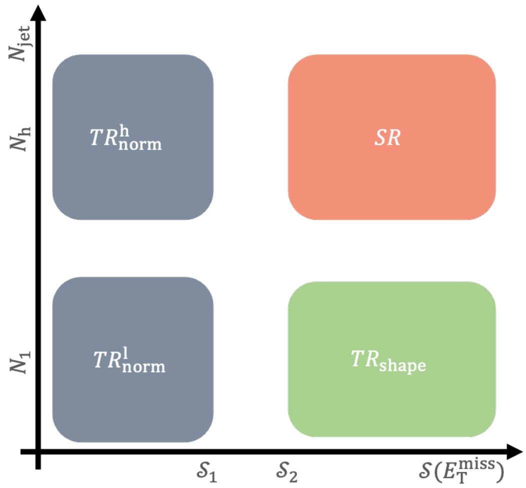

Figure 5.10: A schematic demonstrating the regions used to estimate the multi-jet contribution to the signal regions. The shape template region, $\mathtt{TR}_{\text{shape}}$, and lower normalisation region, $\mathtt{TR}^{\text{l}}_{\text{norm}}$, remain fixed while SR can be any signal region and the upper template region, $\mathtt{TR}^{\text{h}}_{\text{norm}}$, is at the same jet multiplicity as the SR. In the analysis the optimal $\mathcal{S}(E_{\text{T}}^{\text{miss}})$ cuts were found to be $\mathcal{S}_1 = 2$ and $\mathcal{S}_2 = 5$.

Given the assumption that the shape of the $\mathcal{S}\left(E_{\text{T}}^{\text{miss}}\right)$ spectrum is approximately independent of any changes in the number of jets, the prediction may be scaled to fit the yields of each signal region jet multiplicity by applying a normalisation factor derived from two template normalisation regions $\mathtt{TR}^{\text{l}}_{\text{norm}}$ and $\mathtt{TR}^{\text{h}}_{\text{norm}}$ where the superscripts l and h denote low and high N_{jet} respectively. The "high" N_{jet} normalisation region will have the same multiplicity as its respective SR and the "low" template normalisation region will have the same N_{jet} as $\mathtt{TR}_{\text{shape}}$ (Figure 5.10). In both cases there is an upper bound on the $E_{\text{T}}^{\text{miss}}$ significance of $\mathcal{S}\left(E_{\text{T}}^{\text{miss}}\right) < 2.0$ to prevent contamination from signal signatures. The entire yield of a signal region ($\hat{N}_{\text{SR}}$) is determined using the ratio of the yields from $\mathtt{TR}^{\text{h}}_{\text{norm}}$ and $\mathtt{TR}^{\text{l}}_{\text{norm}}$ in order to scale the measured yield in data from the template shape extraction ($\mathtt{TR}_{\text{shape}}$) to the desired jet multiplicity:

$$\hat{N}_{\text{SR}} = \frac{N_{TR^{h}_{\text{norm}}}}{N_{TR^{l}_{\text{norm}}}} N_{TR_{\text{shape}}}. \tag{5.6}$$

This method may also be applied to other regions in $\mathcal{S}\left(E_{\mathrm{T}}^{\mathrm{miss}}\right)$ and so provide the yields for each bin in the $\mathcal{S}\left(E_{\mathrm{T}}^{\mathrm{miss}}\right)$ distribution of a given SR:

$$\hat{N}_{\mathrm{SR}}\left[x<\mathcal{S}\left(E_{\mathrm{T}}^{\mathrm{miss}}\right)<y\right]=\frac{N_{TR^{h}_{\mathrm{norm}}}}{N_{TR^{l}_{\mathrm{norm}}}}N_{TR_{\mathrm{shape}}}\left[x<\mathcal{S}\left(E_{\mathrm{T}}^{\mathrm{miss}}\right)<y\right]. \tag{5.7}$$

With the template normalised to any particular region a further correction can be applied by defining a set of quality control regions known as QCRs. These QCRs are required to have the same jet multiplicity as the signal region and are bound by the range, $3.0<\mathcal{S}\left(E_{\mathrm{T}}^{\mathrm{miss}}\right)<4.0$. In this range a correction factor for the normalisation is defined, $\mu_{\mathrm{multi-jets}}$ and used in a multi-bin likelihood fit with HistFitter [119] along with the normalisation factors μ_{W+jets} and $\mu_{t\bar{t}}$ for the leptonic backgrounds (Section 5.6.1).

The template prediction is validated in two dedicated validation regions (VR). One is constructed to test the invariance of TR_{shape} when extrapolated to higher N_{jet}. It is denoted by $VR_{\mathcal{S}\left(E_{\mathrm{T}}^{\mathrm{miss}}\right)}$ and has $N_{\mathrm{jet}}^{\mathrm{SR}}$ the same $N_{b-\mathrm{jet}}$ and M_{J}^{Σ} requirements as each SR but a restricted range in missing transverse momentum significance of $4.0<\mathcal{S}\left(E_{\mathrm{T}}^{\mathrm{miss}}\right)<5.0$. The other component to validate for the template method is the projection to high $\mathcal{S}\left(E_{\mathrm{T}}^{\mathrm{miss}}\right)$. These regions are known as $VR_{N-\mathrm{jet}}$ and the validation is performed on a jet multiplicity one above TR_{shape} and below that of the first signal region N_{jet} for each jet momentum stream. In the case of N_{jet}^{50} the first signal region begins at $N_{\mathrm{jet}}^{50}=8$ (SR-8ij50), only one above TR_{shape}^{50}, due to the limitations of unprescaled triggers (Table 5.1). To test the reliability of the $\mathcal{S}\left(E_{\mathrm{T}}^{\mathrm{miss}}\right)$ prediction a trigger that records only a small subset of ATLAS data with 6 jets, termed a prescaled trigger, is used to form a template for this test with $VR_{N-\mathrm{jet}}^{50}$ having $N_{\mathrm{jet}}^{50}=7$. For the $p_T>80\,\mathrm{GeV}$ channels things are simpler as the lowest SR is at $N_{\mathrm{jet}}^{80}=7$ and as the shape is extracted from $N_{\mathrm{jet}}^{80}=5$ the $VR_{N-\mathrm{jet}}$ is able to reside in the $N_{\mathrm{jet}}^{80}=6$ multiplicity.

The template prediction for TR-7ej50-1ib is demonstrated in the left sub-figure of Figure 5.11 and shows the multi-jet estimation to be extracted well for $p_{\mathrm{T}}>50\,\mathrm{GeV}$

jets. The Monte Carlo modelled backgrounds are first subtracted from the region so that the remaining events are due to QCD multi-jet processes. In the figure these backgrounds are added back and each background is displayed separately. The data agrees with the prediction perfectly in these template regions by definition. The right sub-figure shows the template extraction for $p_{\mathrm{T}} > 80\,\mathrm{GeV}$ jets.

The accuracy of the template prediction when scaled to higher jet multiplicity and $\mathcal{S}\left(E_{\mathrm{T}}^{\mathrm{miss}}\right)$ must be tested and the complete summary of validation regions for $N_{\mathrm{jet}}^{50} = 7$ is shown in Figure 5.12. The VR_{N-jet} regions (left) validate the template prediction from the 6 jet prescaled trigger. The $VR_{\mathcal{S}\left(E_{\mathrm{T}}^{\mathrm{miss}}\right)}$ (right) summaries with a $\mathcal{S}\left(E_{\mathrm{T}}^{\mathrm{miss}}\right)$ range adjacent to the signal region cut show that the extraction to higher jet multiplicity signal regions is well founded. The dashed lines show that the signal contamination in the validation regions is minimal ($< 1\%$).

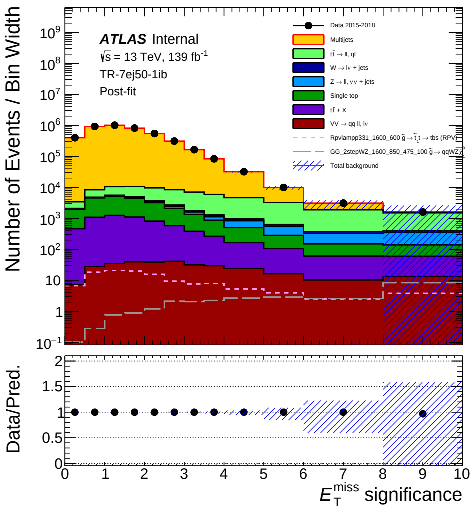

(a) TR-7ej50-1ib with no M_{J}^{Σ} requirement - post-fit

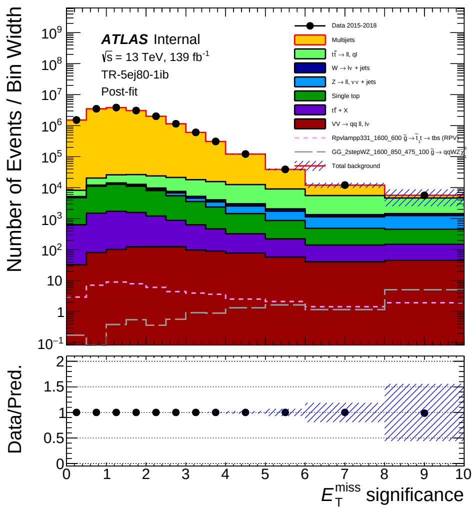

(b) TR-5ej80-1ib with no M_{J}^{Σ} requirement - post-fit

Figure 5.11: The $\mathcal{S}\left(E_{\mathrm{T}}^{\mathrm{miss}}\right)$ template extractions for $p_{\mathrm{T}} > 50\,\mathrm{GeV}$ (left) and $p_{\mathrm{T}} > 80\,\mathrm{GeV}$ (right) jets after the simultaneous background normalisation correction fit, where $\mu_{t\bar{t},W+\mathrm{jets},\mathrm{multi-jets}}$ normalisation factors have been applied.

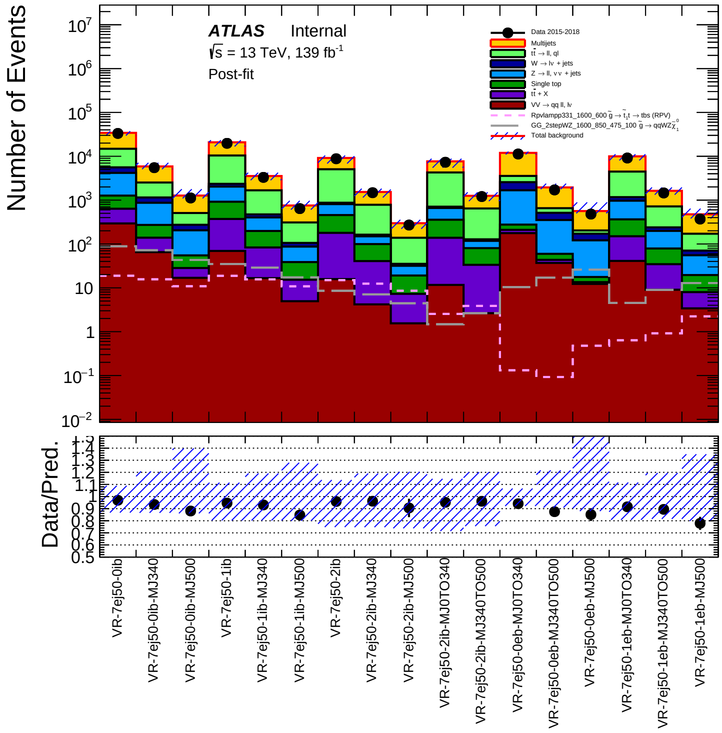

(a) 50 GeV Validation regions VR_{N-jet} summary - post-fit

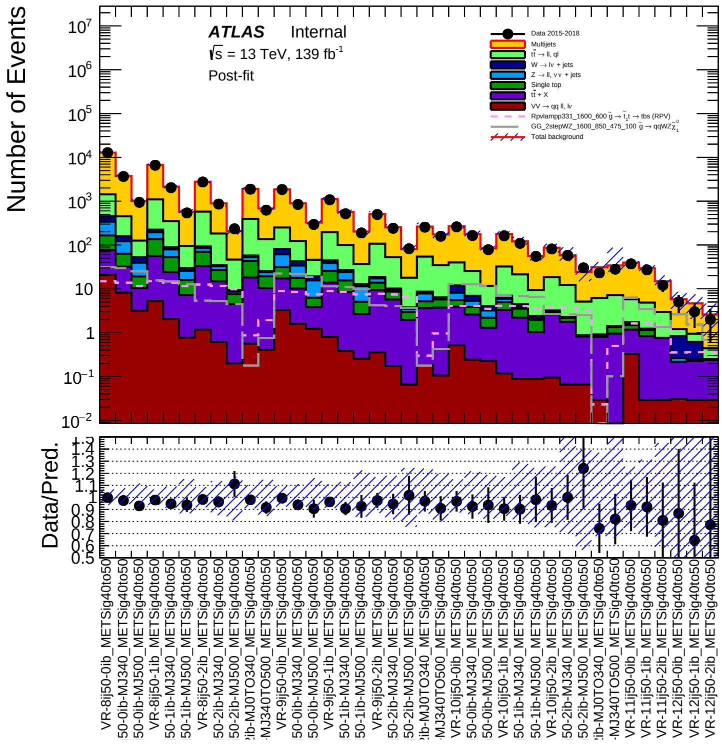

(b) 50 GeV Validation regions $VR_{\mathcal{S}(E_{\mathrm{T}}^{\mathrm{miss}})}$ summary - post-fit

Figure 5.12: A summary of the two validation region types VR_{N-jet} and $VR_{\mathcal{S}(E_{\mathrm{T}}^{\mathrm{miss}})}$ demonstrating the validity of the template prediction with all data agreeing with prediction within systematic and statistical error. Each bin represents one of the validation regions and contains the entire yield, this is split up by background type including the Monte Carlo determined backgrounds as well as the multi-jet prediction in yellow. These validation regions are only for the $p_{\mathrm{T}} > 50\,\mathrm{GeV}$ jets and an equivalent plot exists for $p_{\mathrm{T}} > 80\,\mathrm{GeV}$ jets.

5.7 Systematic Uncertainties

To quantify the accuracy of the background estimation in the signal regions one must use systematic uncertainties. These, broadly, come in three types:

1. *Experimental systematic uncertainties* allow the determination of the impact of detector mis-measurement.

2. *Theoretical systematic uncertainties* account for the precision of the theoretical models used to produce the MC simulations.

3. *Template systematic uncertainties* quantify the uncertainties that come from the data-driven template method.

The systematic uncertainties are applied to the simulations in general except for the template systematics which are applied to data. These uncertainties are then considered to be nuisance parameters in a profile likelihood fit using HistFitter [119].

5.7.1 Experimental Uncertainties

Experimental systematic uncertainties allow one to quantify the accuracy of measurement for the various physics objects. These uncertainties are on the resolution and energy scales of the objects as well as identification and reconstruction efficiencies. The large number of jets in the signal regions of the analysis mean that the dominant systematics related to jet reconstruction. The veto on leptons means that the uncertainties on their energy scales and resolutions only enter through the control regions. The most important systematics are summarised here:

JET ENERGY SCALE

Nuisance parameters related to the jet energy scale correction, described in Section 3.4.5.

JET ENERGY RESOLUTION

The jet resolution uncertainties are estimated by smearing jet energies using a Gaussian. The mean and width of which are determined using the difference between the resolutions measured in data and MC.

JET VERTEX TAGGER

The efficiencies of tagging hard scatter jets with the JVT discriminant are corrected in MC by applying scale factors taken from pile-up depleted regions.

FLAVOUR TAGGING

To make the simulated b-tagging efficiencies better match the data scale factors are applied. The uncertainty on these scale factors are derived from variations in the jet flavour components.

$E_{\mathrm{T}}^{\mathrm{miss}}$ **Soft Term**

The uncertainties on the hard term components of $E_{\mathrm{T}}^{\mathrm{miss}}$ are determined by propagating the systematics that are applied to each of the objects. The soft term systematics are determined by applying variations to the scale of the track soft term. The TST is also smeared, by the difference between data and MC, in two orthogonal directions to the soft term.

PILE-UP REWEIGHTING

Apply two variations to the data scale factor used for pile-up reweighting this accounts for uncertainties and mismodelling in the minimum bias overlay used in the MC pile-up simulation.

5.8 Results

The backgrounds have been constrained and tested, now what remains is to project the predictions into the SRs. Up to this point no data has been included in the SR plots beyond $\mathcal{S}(E_{\mathrm{T}}^{\mathrm{miss}}) = 5$ in the SRs as this denotes the beginning of the signal region proper and has been blinded to data. Now that all the backgrounds are well understood data can be added in the signal region in a process known as unblinding. This represents the testing of our signal hypotheses; agreement between data and prediction indicates that the SM is accurate and models the phenomena observed. A disagreement between data and prediction to a high statistical significance would suggest the presence of new physics. Figures 5.13 and 5.14 are two examples, containing 13 and 16 signal jets respectively, of what these events actually look like in the detector and demonstrate how complex the signal really is.

As an example of the distribution of $\mathcal{S}(E_{\mathrm{T}}^{\mathrm{miss}})$ the yield and prediction shown in Figure 5.15 is for *SR-9ij50-1ib*. The example regions used in the leptonic (5.6.1) and multi-jet (5.6.4) background determination sections contribute towards this signal region with $N_{\mathrm{jet}}^{50} \geq 9$ and $N_{b-\mathrm{jet}} \geq 1$. A background-only fit was able to scale the background contributions to account for any mismodelling in the MC and a summary of these scale factors for the multi-bin and single-bin regions is available in Figure 5.16. These scale factors can be approximated summarised as

$$\mu_{\mathrm{multi-jet}} \approx 0.95, \quad \mu_{t\bar{t}} \approx 0.9, \quad \mu_{W+\mathrm{jets}} \approx 0.6. \tag{5.8}$$

In general the background is overestimated with respect to the data, in particular for $W+\mathrm{jets}$ due to poor modelling at such high N_{jet} and low event numbers in many regions, and this is reflected in the large error bands. Figure 5.15 reveals the complete combination of all background predictions and data above the SR cut of $\mathcal{S}\left(E_{\mathrm{T}}^{\mathrm{miss}}\right) > 5.0$. Data above this point for this SR show no disagreement with the SM.

All regions contributing to the statistical fit for this SR are shown in Figure 5.18 with the total yield in data and each contributing background process in each bin starting, leftmost, with the SR itself. All contributing regions show excellent agreement and the dashed signal lines indicate that contamination is low in control and validation regions. This region is not particularly sensitive to the two signal points chosen as a standard demonstration on all plots, however, it is sensitive to other mass points and models. A comprehensive summary of all N_{jet}^{50} SRs complete with bottom quark jet and event-level large-R jet mass bins is in the left sub-figure of Figure 5.17 while the N_{jet}^{80} SRs are on the right.

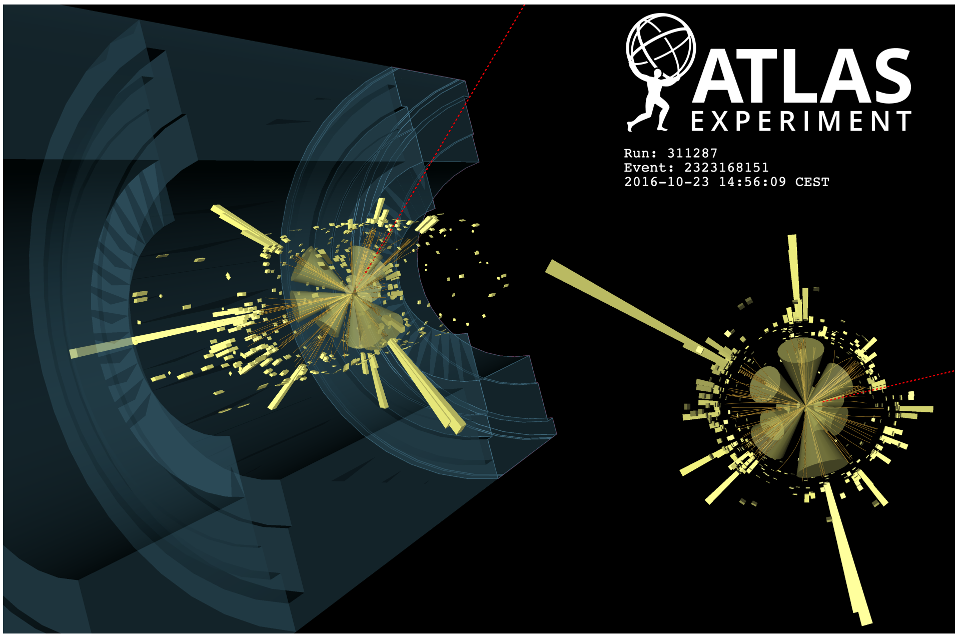

Figure 5.13: Visualisation of the highest jet multiplicity event selected in the analysis signal regions. This event was recorded by ATLAS on 23 October 2016, and contains 16 signal jets. Of these jets, 13 (11) have transverse momenta above 50 GeV (80 GeV), with 3 (2) being b-tagged. The leading jet has a transverse momentum of 507 GeV, and the sum of jet transverse momenta $H_{\mathrm{T}} = 2.9\,\mathrm{TeV}$. A value of 343 GeV is observed for the $E_{\mathrm{T}}^{\mathrm{miss}}$, producing $\mathcal{S}\left(E_{\mathrm{T}}^{\mathrm{miss}}\right) = 6.4$. The large-radius jet mass sum $M_{\mathrm{J}}^{\Sigma} = 1070\,\mathrm{GeV}$.

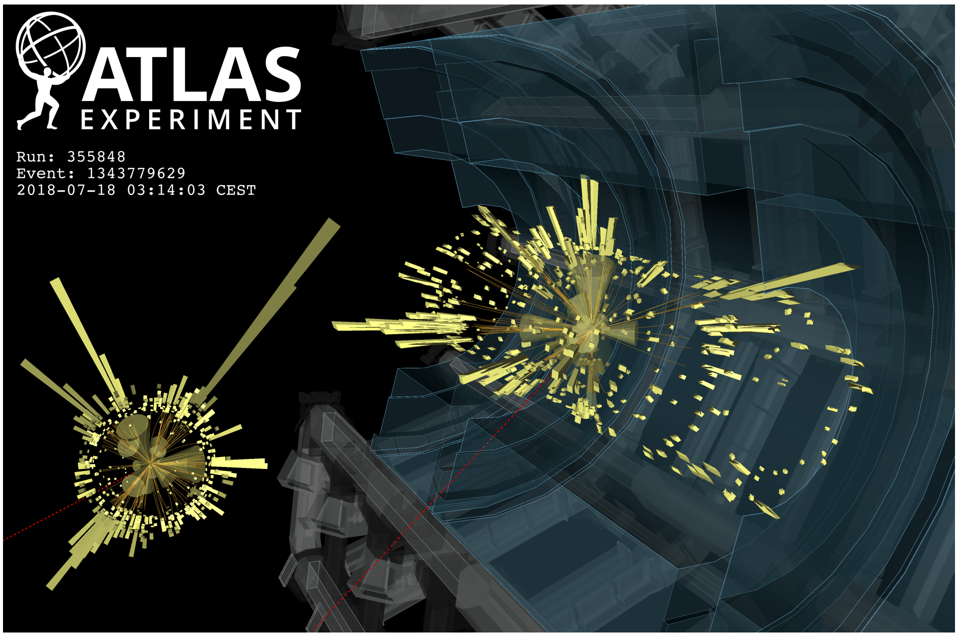

Figure 5.14: Visualisation of the highest jet multiplicity event selected in the analysis template region. This event was recorded by ATLAS on 18 July 2018, and contains 19 signal jets, of which 16 (10) have transverse momenta above 50 GeV (80 GeV). No jets were b-tagged. The leading jet has a transverse momentum of 371 GeV, and the sum of jet transverse momenta $H_{\mathrm{T}} = 2.2\,\mathrm{TeV}$. A value of 8 GeV is observed for the $E_{\mathrm{T}}^{\mathrm{miss}}$, producing $\mathcal{S}\left(E_{\mathrm{T}}^{\mathrm{miss}}\right) = 0.2$. The large-radius jet mass sum $M_{\mathrm{J}}^{\Sigma} = 767\,\mathrm{GeV}$.

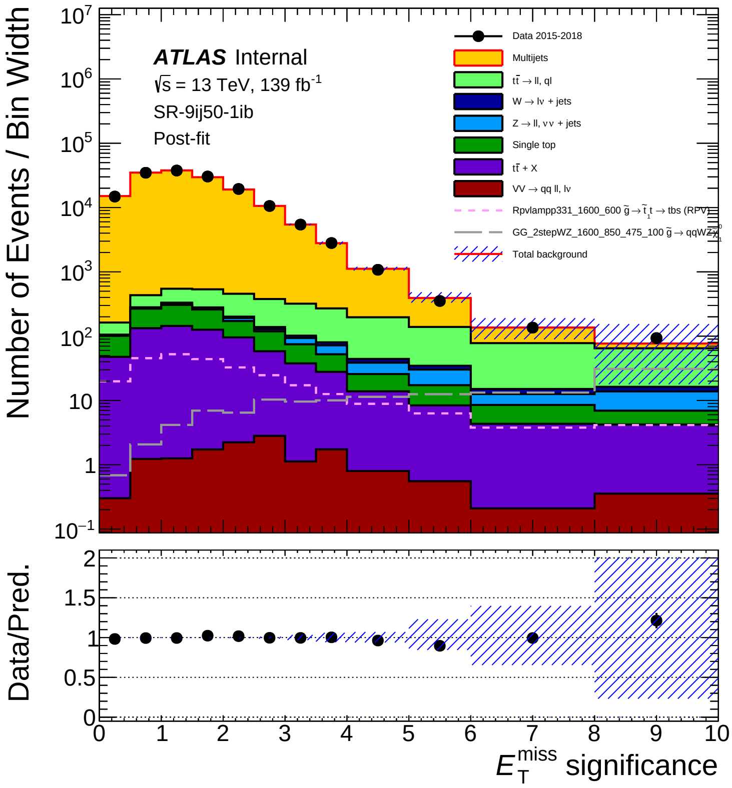

Figure 5.15: The unblinded data in this SR ($N_{\text{jet}}^{50} \geq 9$ and $N_{b-\text{jet}} \geq 1$) show agreement with SM prediction within total systematic error. Each background is shown separately and the multi-jet prediction in this region is found to be excellent, the QCD contribution dominates the low $\mathcal{S}\,(E_{\text{T}}^{\text{miss}})$ as expected. In these low $E_{\text{T}}^{\text{miss}}$ significance values the missing transverse momentum is largely due to mismeasurement of jets and not the presence of an invisible particle. Two signal points are plotted with dashed lines.

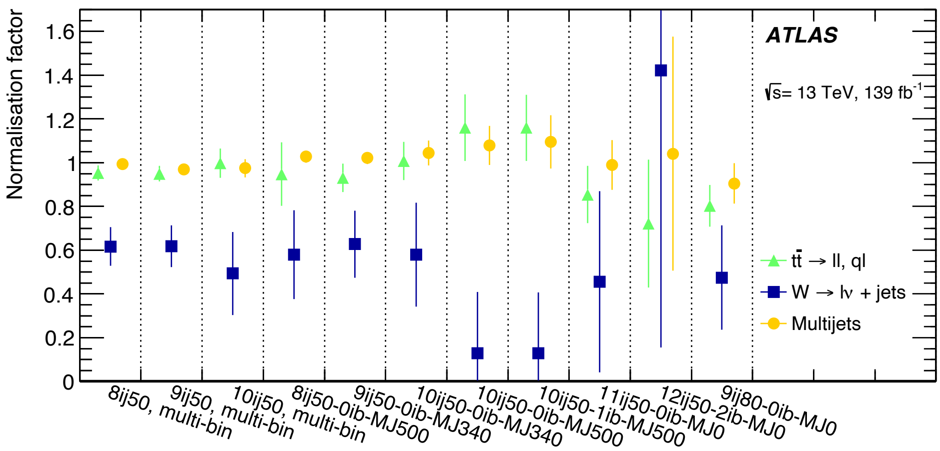

Figure 5.16: The fitted normalisation factors for each of the main background types; multi-jet, $t\bar{t}$ and $W+$jets. This summary shows the multi-bin fit regions as well as those regions used in the single-bin fits with the error bands representing the combined statistical and systematic errors.

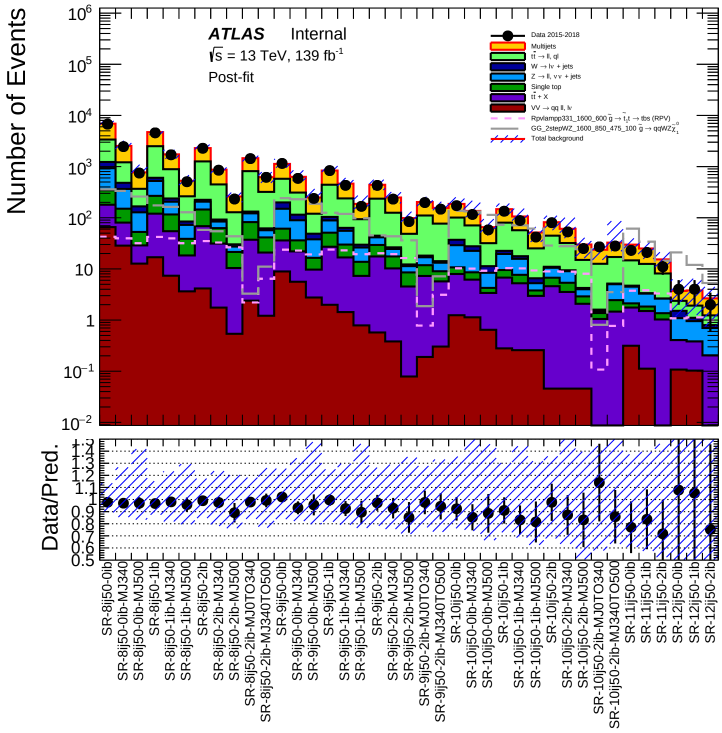

(a) 50 GeV Signal Regions Summary

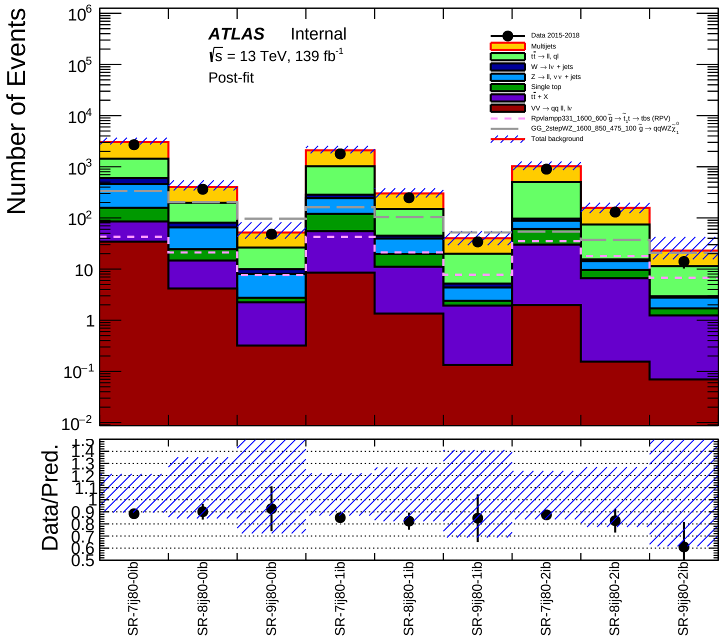

(b) 80 GeV Signal Regions Summary

Figure 5.17: A summary of all yields and SM predictions in the 50 GeV jet momentum channel including all b-jet and M_J^{Σ} cuts (top). The 80 GeV signal regions (bottom) are only split by b-jet multiplicity and show that the data are consistent with SM prediction. Several of the 80 GeV regions show good sensitivity to the demonstration models.

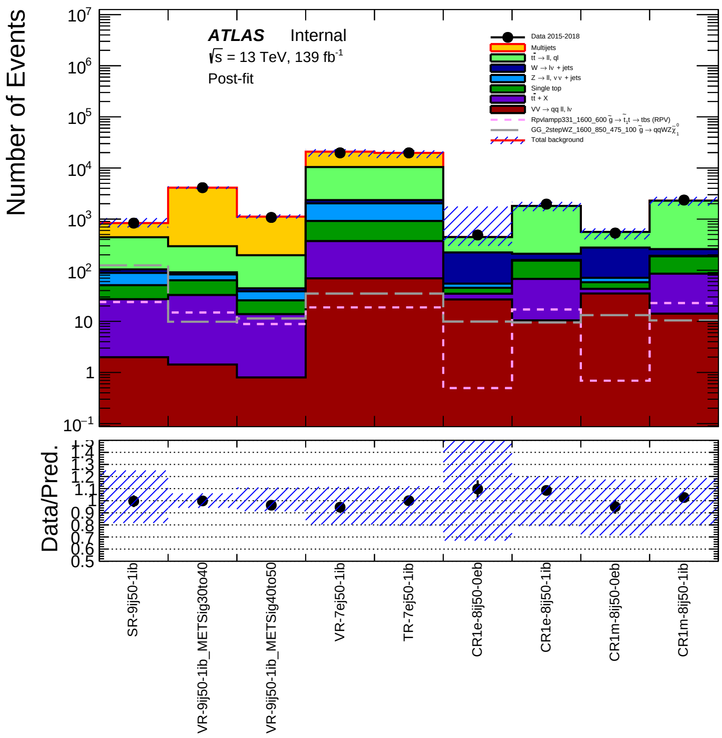

Figure 5.18: Yields and SM prediction for SR-9ij50-1ib along with all of the contributing regions to the various background estimations. These include the leptonic control regions for electrons and muons, the template region and all template method validation regions.

The summary shows that the agreement with the standard model is seen across all multiplicities, and for different numbers of b-jets and cuts on M_{J}^{Σ}. Again the two demonstration signal models are shown with dashed lines, for the two-step (grey line) the analysis shows good sensitivity at the highest jet multiplicities ($N_{\mathrm{jet}}^{50} > 11$). In this extreme phase space the background prediction shows that the number of standard model events that can produce this final state is low while in the presence of a supersymmetric decay there would be an increased number of events. All $p_{\mathrm{T}} > 50\,\mathrm{GeV}$ and $p_{\mathrm{T}} > 80\,\mathrm{GeV}$ regions show agreement with the standard model.

Exclusion Limits

As no significant excess from the standard model is observed, the signal regions can be used in a fit to provide exclusion limits for each of the models outlined in Section 5.2. There were two approaches involved in the fitting of exclusion limits the previous version of the analysis [118] used a single bin fit approach. For this analysis a new exclusion fitting technique is introduced, the multi-bin fit.

In the case of the single-bin fit each selection in jet multiplicity, the number of b-jets and M_{J}^{Σ} forms a channel to fit a high confidence limit exclusion limit for each of the models in Figure 5.3. These limits constrain the masses of two SUSY particles; the gluino ($m_{\tilde{g}}$) and the lightest neutralino ($m_{\tilde{\chi}_1^0}$). A multi-bin fit aims to improve the exclusion power of the analysis and uses regions with $N_{\mathrm{jet}}^{50} \geq 8, 9, 10$. Each of these is a channel in the fit and there may be up to 9 SR bins per channel when the subdivisions in $N_{b-\mathrm{jet}}$ and M_J^{Σ} are applied. The regions for the multi-bin fit are summarised in Table 5.8.

Multi-bin Channel	N_{jet}	$N_{b-\mathrm{jet}}$	M_{J}^{Σ}
SR-8ij50	≥ 8		
SR-9ij50	≥ 9	$= 0, = 1, \geq 2$	$(0, 340]$, $(340, 500]$, $(500, \mathrm{inf})$
SR-10ij50	≥ 10		

Table 5.8: A tabular summary of the multi-bin fit regions, the leftmost column defines the jet multiplicity channel for 50 GeV jets. Within each channel there are 9 bins defined by the sub-selections in b-jet multiplicity and M_{J}^{Σ}.

The exclusion limits for each of the signal models are shown in figures 5.19, 5.20 and 5.21. In each of these figures the grey area represents the limit in exclusion from the previous version of the analysis [118], while the blue and red lines represent 95% CL exclusion for the single- and multi-bin fit respectively. In all cases below the improvement from the multi-bin fit over the previously used single bin approach is very apparent. All exclusion values quoted below will be 95% CL limits from the multi-bin fit exclusion curves (red).

The largest exclusion on gluino mass comes from the two step decay ($\tilde{g} \rightarrow qqWZ\tilde{\chi}_1^0$, Figure 5.19 (a)) and indicates that the gluino mass must be in the range $m_{\tilde{g}} > 2.0\,\mathrm{TeV}$ assuming massless neutralinos. This limit remains relatively constant as the neutralino is raised in mass values up to $m_{\tilde{\chi}_1^0} = 800\,\mathrm{GeV}$.

In a model with a gluino decaying to $t\bar{t}$ (Figure 5.20 (b)) all masses below $m_{\tilde{g}} = 1.8\,\text{TeV}$ for low mass neutralinos are excluded. This is a large improvement from the last version of the analysis using this model.

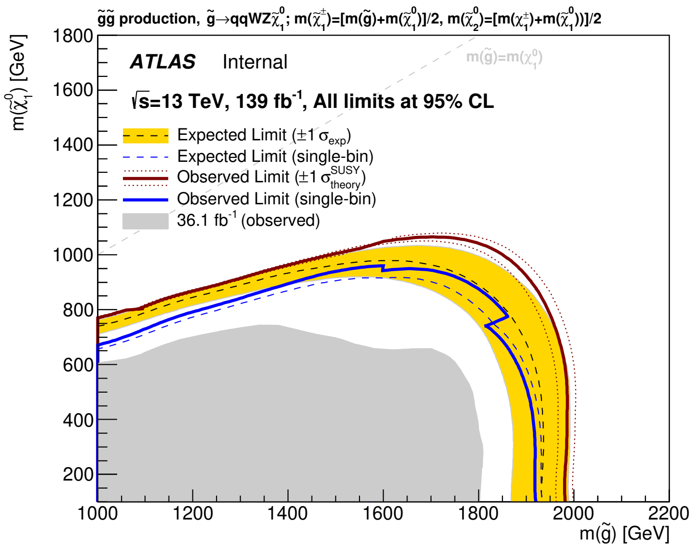

Figure 5.19: Exclusion limits determined for the two-step decay to quarks with mixed diboson production (Figure 5.3 (a)) where the grey area represents the old limit on exclusion from the last version of the analysis, while the blue and red lines represent the single- and multi-bin fit respectively.

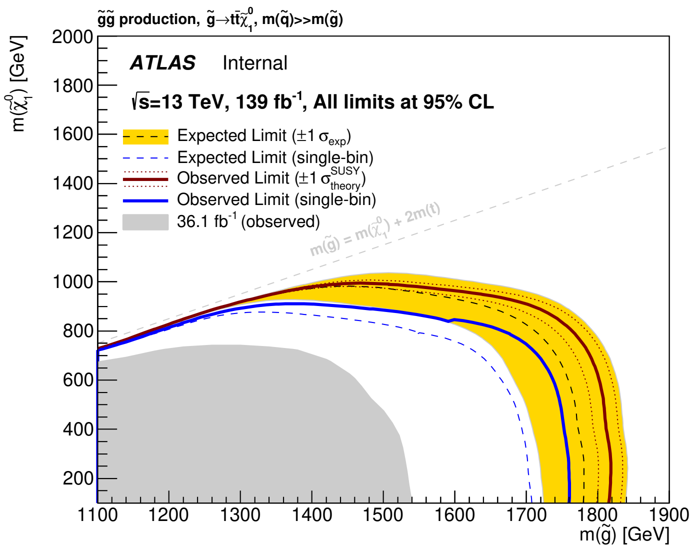

Figure 5.20: Exclusion limits determined for the Gtt decay mode (Figure 5.3 (b)) where the grey area represents the old limit on exclusion from the last version of the analysis, while the blue and red lines represent the single- and mutli-bin fit respectively.

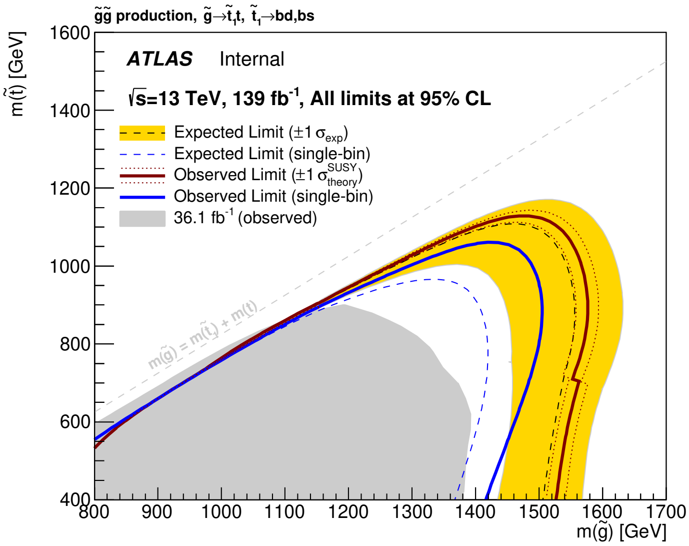

Figure 5.21: Exclusion limits determined for the R-parity violating decay (Figure 5.3 (c)) where the grey area represents the old limit on exclusion from the last version of the analysis, while the blue and red lines represent the single- and multi-bin fit respectively.

In the R-parity violating scenario (Figure 5.21 (c)) the greatest reach is up to $m_{\tilde{g}} = 1.62\,\text{TeV}$ and $m_{\tilde{t}} = 1.1\,\text{TeV}$ for the stop. The optimised exclusion for both particles is $m_{\tilde{g}} < 1.54\,\text{TeV}$ and $m_{\tilde{t}} < 1\,\text{TeV}$.

5.8.1 A Comparison of Jet Definitions

The analysis used particle-flow (PFlow) jets instead of the electromagnetic topocluster (EMTopo) jets. PFlow jets are proven to be more pile-up resistant and provide better resolution across the entire p_{T} range detectable by ATLAS [70]. A comparison between the two jet definitions shows quantitatively the improvement in analysis performance given by PFlow jets. The results are summarised in Table 5.9.

The multi-jet backgrounds are reduced by $25 - 30\%$ when using PFlow, while the other backgrounds that produce SM neutrinos remain largely unchanged. The reduction in multi-jet background indicates a suppression of the $E_{\mathrm{T}}^{\mathrm{miss}}$ from mismeasurement effects. The reduction also demonstrates the removal of pile-up jets by the PFlow algorithm, EMTopo generally identifies more jets, which are likely to be from from pile-up. The template closure uncertainty when using PFlow is improved by 50% showing that the main background in the analysis is better constrained. All of these improvements translate to a 30% increase in sensitivity (1σ) for the analysis and an excellent demonstration of the power of PFlow jets.

Signal channel	Jet type	Total SM	Multijet yield	$\sigma_{\text{nonClosure}}$	$\delta\sigma^{\text{rel}}_{\text{bkg}}$	S^{95}_{exp}	$\Delta S^{95}_{\text{exp}}$
`8ij50-0ib-MJ500`	PFlow	747 ± 47	372 ± 42	10	5%	99^{+36}_{-26}	1.2
	EMTopo	956 ± 63	552 ± 45	17		143^{+175}_{-52}	
`9ij50-0ib-MJ340`	PFlow	612 ± 36	295 ± 35	5.8	-1%	91^{+33}_{-25}	0
	EMTopo	738 ± 43	393 ± 32	13		90^{+35}_{-25}	
`10ij50-0ib-MJ340`	PFlow	136 ± 14	62 ± 9	1.2	-3%	34^{+14}_{-9}	0.3
	EMTopo	161 ± 16	84 ± 10	3.1		38^{+15}_{-10}	
`10ij50-0ib-MJ500`	PFlow	68 ± 10	33 ± 6	0.9	72%	24^{+11}_{-7}	0.8
	EMTopo	83 ± 21	46 ± 7	2.5		32^{+13}_{-13}	
`10ij50-1ib-MJ500`	PFlow	56 ± 10	27 ± 6	2.7	-5%	19^{+8}_{-5}	0.6
	EMTopo	65 ± 11	35 ± 7	2.7		24^{+10}_{-7}	
`11ij50-0ib-MJ0`	PFlow	27 ± 5	12 ± 3	0.6	24%	15^{+6}_{-4}	1.2
	EMTopo	39 ± 9	18 ± 4	1.5		22^{+8}_{-6}	
`12ij50-2ib-MJ0`	PFlow	2.4 ± 1.6	1.0 ± 0.9	0.3	8%	$5.1^{+2.6}_{-1.6}$	0
	EMTopo	2.5 ± 1.8	1.1 ± 0.9	0.2		$5.1^{+2.6}_{-1.6}$	
`9ij80-0ib-MJ0`	PFlow	46 ± 7	20 ± 4	2.2	15%	20^{+8}_{+6}	0.25
	EMTopo	57 ± 10	29 ± 5	2.5		22^{+9}_{+6}	

Table 5.9: Comparison of analysis results for calorimeter (EMTopo) and particle flow (PFlow) jet reconstruction. For each single-bin signal region, results for the two reconstruction methods are compared for the following quantities. Total SM: the total background yield in the signal region; Multijet yield: the estimated SR contamination from multijet production; $\sigma_{\text{nonClosure}}$: the systematic uncertainty due to non-closure in the multijet template estimate; $\delta\sigma^{\text{rel}}_{\text{bkg}}$: the relative increase in the normalised uncertainty on the total background $\sigma^{\text{rel}}_{\text{EMTopo}}/\sigma^{\text{rel}}_{\text{PFlow}} - 1$; S^{95}_{exp}: the expected limit on the number of signal events falling in the SR; $\Delta S^{95}_{\text{exp}}$: the relative increase in S^{95}_{exp} when using EMTopo. Only jet energy scale/resolution and multijet template closure systematic uncertainties have been considered.

5.9 Conclusion

A search for new physics beyond the standard model of particle physics was conducted using the full Run 2 p–p collision data set at $\sqrt{s} = 13$ TeV recorded by the ATLAS experiment of $139\,\mathrm{fb}^{-1}$. The analysis targeted events that contained many hadronic jets with zero leptons as well as a moderate amount of missing transverse momentum. To further increase the sensitivity to new physics, and particular supersymmetric models, extra signal-region requirements were added. Including a b-jet requirement to probe models with a stronger coupling to heavy flavour quarks. M_{J}^{Σ} also expanded the scope of the analysis to decays of massive particles that could boost large mass SM particles.

In this analysis, novel techniques were implemented to improve discovery potential and exclusion power. These included the adoption of particle-flow jets that could resolve lower momentum jets with an increase in pile-up reduction. The object-based $E_{\mathrm{T}}^{\mathrm{miss}}$ significance allowed for a better rejection of missing transverse momentum from unwanted sources. The data are found to match prediction with no significant deviations from the SM. The standard model performs remarkably well up to the most extreme phase space regions of this analysis. The large increase in data as well as the introduction of novel definitions and techniques allowed for a large increase in excluded masses particularly for the gluino in the two-step cascade ($m_{\tilde{g}} > 2.0$ TeV).

For the next phase of this analysis it will be combined with other similar searches to constrain models ranging from complete R-parity violation to those with stable final state SUSY particles (RPC). The extreme phase space regions that are probed here make the measurement of hadronic cross-sections in the SM a logical next step. As well as these objectives further research in to quark-gluon discrimination is a high priority in order to suppress gluon background that mimics signal in the all-quark signal states. This and other additions will be included in anticipation of Run 3 at the LHC and the next frontier of high energy physics.

Three quarks for Muster Mark!

Sure he has not got much of a bark

And sure any he has it's all beside the mark. ...

— James Joyce *Finnegans Wake, 1939*

6
Quark and Gluon-Tagging

Contents

6.1 Introduction

To most people outside the scientific community "quark" is a type of German cheese or an interesting quote from an old Irish writer's back catalogue in which some

Dublin seagulls recommend that a Mr Mark be given some beer. In the field of high energy physics however, quarks are enigmatic objects that form the basis of matter in our universe. Since the discovery that the proton was not a fundamental particle but comprised of three point like particles physicists have sought the underlying theory that governs this colourful world. A huge leap forward was taken by the prominent physicist Murray Gell-Mann when he planted the seeds for the quark model with *the eightfold way* [126] a system to bring order to the apparent chaos of the hadrons at the time, as well as reputedly coining the name "quark". Quantum Chromodynamics quickly rose to prominence and along with it the mediator of the strong force, the gluon, came into view [127–130]. Physicists have spent decades untangling the mysteries of the strong interaction. While the phenomenology of this area of particle physics has been somewhat tamed by the Goliath of modern computational methods some of the details continue to present a challenge to the modern experimentalist and theorist alike.

Discrimination between quarks and gluons has been attempted many times before in particle physics experiments and the current generation of high energy physics experiments are no exception [131][132]. The number of particles inside the decay cone of a quark or gluon produced in a high energy collision would, on average, be larger for a gluon and so presents an opening that could be exploited to differentiate between these objects. The ability to reliably pick out either object would greatly enhance the physics capability for measurements of the standard model (SM) and even open new avenues for discovery of new physics.

6.2 Quarks and Gluons in QCD

To determine why the number of constituents differs between quark and gluon initiated jets we can turn to a set of parton splitting functions, the Dokshitzer-Gribov-Lipatov-Altarelli-Parisi (DGLAP) splitting functions [133–135]. These functions were written down around the same time in the early 1970's by different physicists around Europe, hence the long acronym. The overall DGLAP evolution equation [136] is

$$\mu\frac{d}{d\mu}f_i\left(x,\mu\right)=\frac{\alpha_s}{\pi}\int_x^1\frac{d\xi}{\xi}f_i\left(\xi,\mu\right)P_{qq}\left(\frac{x}{\xi}\right) \tag{6.1}$$

where ξ is the momentum of the parton, x is the Bjorken-x and μ is the factorisation scale. The final two pieces are $f_i\left(x,\mu\right)$ which represents the parton distribution functions (PDFs) and $P_{qq}\left(\frac{x}{\xi}\right)$ denoting the splitting kernel. This allows the formulation of splitting functions for processes such as: $q\rightarrow qg$ and $g\rightarrow qq$ at leading order [136]:

$$P_{qq}(z)=C_F\left[\frac{1+z^2}{[1-z]_+}+\frac{3}{2}\delta(1-z)\right], \tag{6.2}$$

$$P_{qg}(z)=T_F\left[z^2+(1-z)^2\right], \tag{6.3}$$

$$P_{gq}(z)=C_F\left[\frac{1+(1-z)^2}{z}\right], \tag{6.4}$$

$$P_{gg}(z)=2C_A\left[\frac{z}{[1-z]_+}+\frac{1-z}{z}+z(1-z)\right]+\frac{\beta_0}{2}\delta(1-z), \tag{6.5}$$

where $z=\frac{Q^2}{2p_i\cdot q}$ and $\beta_0=\frac{11}{3}C_A-\frac{4}{3}T_Fn_f$. In physical terms z is the splitting parameter and dictates the momentum fraction in the light cone of the emitted parton with respect to the emitter. The indices of P_{ji} represent a process of the form $i\rightarrow jk$ and here the parton type of k is fixed by the types of i and j [16]. The two processes we are most interested in ($q\rightarrow qg$ and $g\rightarrow gg$) for the sake of demonstration are shown in Figure 6.1. Looking more closely at the two emissions highlighted in Figure 6.1, a quark emitting a gluon and a gluon emitting a gluon, we see that there is a factor of C_F for the $q\rightarrow qg$ process in Equation 6.4 and a factor of C_A for the $g\rightarrow gg$ process in Equation 6.5.

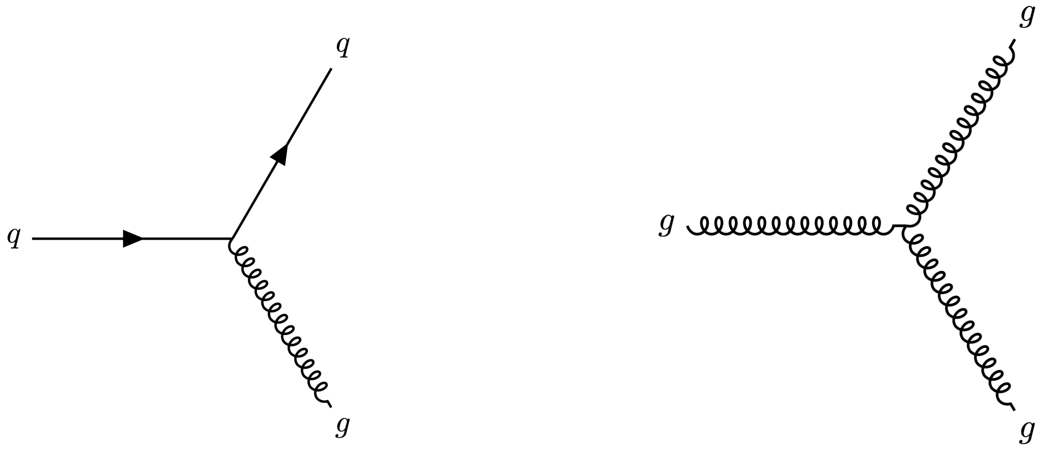

(a) $q \to qg$ **(b)** $q \to qg$

Figure 6.1: A quark (a) and a gluon (b) can be produced in high energy collisions at the LHC through myriad processes. Due to colour confinement these particles will go through the process of hadronisation to form colourless particles. During this process each particle type can emit a gluon with a certain probability [123].

In the simplest terms the probability of a gluon emission from a quark is proportional to C_F and for the emission of a gluon from a gluon we have C_A. The colour ("Casimir") factor, which has its origins in group theory, associated with the emission of a gluon from a quark is

$$C_F \equiv \frac{N_C^2 - 1}{2N_C} = \frac{4}{3}, \tag{6.6}$$

where N_C is the number of colours in the model and is equal to three. The colour factor associated with a gluon being emitted to a gluon is simply

$$C_A \equiv N_C = 3. \tag{6.7}$$

Inspecting the ratio of these two factors leads to a simple yet powerful result,

$$\frac{C_A}{C_F} = \frac{9}{4}. \tag{6.8}$$

This means that a gluon is roughly more than twice as likely to emit another gluon as a quark is to do the same, ignoring the dependency on z. Indicating that a quark forming a jet would have more radiation as well as a wider spread in the pattern of that radiation. In terms of a general purpose detector one would find that, on average, gluon jets would have more constituents with a broader pattern than jets from quarks. In a more specific sense, gluon jets would have a larger number of charged particle constituents within the jet cone than a jet originating from a quark. This, for a long time, has been the primary approach to quark-gluon discrimination.

6.2.1 Hadronisation

The extra radiation of gluons from gluons over the same emission from quarks mean that, on average, there will be more constituents in a jet from a gluon. This occurs through a process called hadronisation. Light quarks are not truly isolated entities and will hadronise on a very short time scale. This hadronisation time-scale can be approximated in the laboratory frame, with a few assumptions [16], as

$$t_{\text{had}} \approx \frac{ER}{m_Q}, \tag{6.9}$$

in natural units. Here E denotes the energy at which the quark is produced, R is the typical size of a hadron and is of the order of 1 fm while m_Q represents the mass of the quark. For the light quarks the appropriate mass is the dynamical mass, close to the QCD scale ($\Lambda_{\text{QCD}} \approx 250\,\text{MeV}$) and this in turn is approximately R^{-1}. This introduces two slightly different hadronisation time scales [16],

$$t_{had} \approx ER^2, \tag{6.10}$$

for the light quarks while Equation 6.9 holds for heavy quarks of mass m_Q. A notable exception to this rule is the most massive of all the quarks, the top quark. In this case we can write its lifetime as [16]

$$\tau_t \sim \left(\frac{m_W}{m_t}\right)^3 \frac{E}{m_t}, \tag{6.11}$$

where m_W is the mass of the W boson ($m_W = 80.379 \pm 0.012\,\text{GeV}$ [11]) which mediate the flavour changing decay, and all other symbols retain their previous definitions except that the generic quark mass subscript Q is now specifically the mass of the top quark ($m_t = 173.0 \pm 0.4\,\text{GeV}$) [11]. If we approximate the hadronisation time for the top quark as $t_{had,t} \sim E/M_t$, for the sake of comparison, it is clear that $\tau_t \ll t_{had,t}$. This indicates that the top quark will decay before it can hadronise to a bottom quark. Physically this means that the top quark is the only quark able to behave as a free particle and is excepted from this rapid hadronisation.

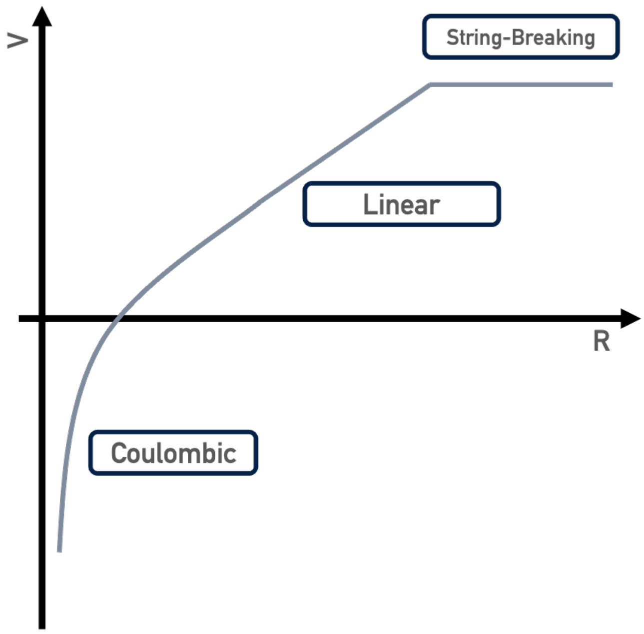

Figure 6.2: The static quark potential in QCD shown in a qualitative fashion to highlight the main features [137].

The process of hadronisation can be linked closely to the concept of colour confinement. The force between the a pair of static quarks, also called the "static quark potential", is qualitatively described in Figure 6.2. At very small distances (R) the static quark potential (V) is Coulomb-like due to asymptotic freedom causing the strong force to become weaker at these short distances and so be dominated by the Coulombic component. Asymptotic freedom can be likened to a spring (connecting two balls or "quarks" if you like) at its natural length; no force is exerted unless one attempts to extend the spring. Increasing R to intermediate distances the potential grows in a linear manner as the pair are separated. As a consequence more and more energy is required to separate the two (an infinite amount of energy is required to separate the quarks to infinite distance). Eventually it becomes energetically favourable to spontaneously produce a quark anti-quark pair and move into the “string breaking” phase [137].

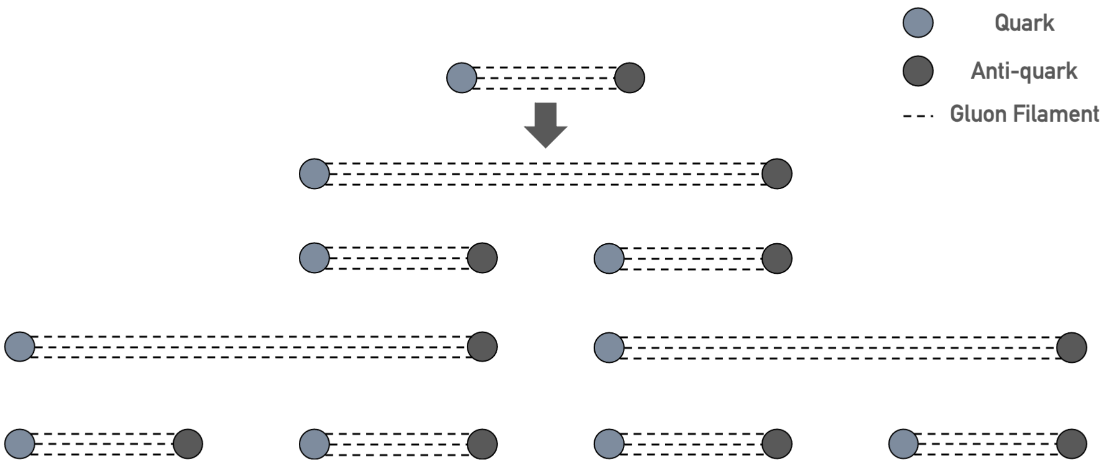

Figure 6.3: Starting at the top with a quark and anti-quark pair the flux tube is represented by the dashed lines of gluon filaments. As the quark pair move apart due to having some velocity from their initial production more energy is stored in the flux tube and this is represented by its elongation. Once there is enough energy to create a new quark and anti-quark pair the tube splits and forms the third row. This process occurs until all quarks combine to form colourless hadrons [137][138].

Another representation of how this process can occur is demonstrated in Figure 6.3. On the top line of this schematic the quark and anti-quark pair are connected via a flux tube, this tube results when the colour field is squeezed into a cylindrical region between the quarks. Using this idea, and returning to the spring analogy used to idealise asymptotic freedom earlier, it is possible to estimate the energy in the flux tube in a simple way; the energy in the colour electric field (E_c) will increase with separation as $E_c = \sigma R$, where σ is effectively the tension in the tube ($\sim 1\,\mathrm{GeV\,fm^{-1}}$) [138]. This very simple picture allows us to imagine that as the energy in the flux tube increases with separation, the second line of the schematic, at a certain threshold enough energy is stored to allow for the spontaneous production of another quark and anti-quark pair, the third line. This process will continue, as seen in the lower part of the diagram, until the energy is low enough that the quarks and anti-quarks combine to form colourless mesons and hadrons. This is a hugely simplified picture of an extremely complex phenomenon but allows for some intuitive thought about the underlying physics.

6.2.2 Detection of Hadronic Interactions

The processes briefly described in Sections 6.2 and 6.2.1 have taken us from the microscopic production of partons that exist only fleetingly to the beginnings of hadronisation. As this process evolves ever towards lower energies by producing more and more partons a new regime appears in which these partons are bound together in hadrons that can propagate a measurable distance. It is these showers of energetic particles that will be detected by a high energy physics (HEP) experiment.

The entire process can be broken down into a series of steps in the case of a collider experiment like the LHC [53], from production to detection:

1. Collision

   Proton-proton collisions occurring at $\sqrt{s} = 13\,\mathrm{TeV}$ in the LHC allow for partonic interactions and production of quarks and gluons via channels like that in Figure 6.4. The highest energy interaction from the $p - p$ collision is known as the *hard interaction* or *hard process*. This initial stage as well as all subsequent evolution of the particles coming from a particular collision is known as an *event*.

2. Hadronisation

   The partons form showers of colourless hadrons through the mechanisms described in Section 6.2.1 and these particles propagate in a collimated sprays forming a conical shape. The issue is further complicated with the existence of *initial state radiation* (ISR) and this is the radiation coming from the incident particles before the collision. Another similar phenomena, *final state radiation* (FSR), also contributes to the number of partons in the final state when the produced particles emit radiation (if one or both of the quarks in Figure 6.4 were to emit a gluon for example). All of these particles will contribute to this hadronisation process in an event forming a greater number of particle showers.

3. Detection

   All of the particles produced from a single collision remain unobserved until a detector is placed in the way to measure them. Of particular interest here is the detection of *jets*, these are the result of the parton production and the following hadronisation to form the collimated sprays of particles. In measured data, jets are the final objects observed from the initial quarks and gluons and they will have to furnish us with all the information needed to determine which parton they came from or were *seeded* by.

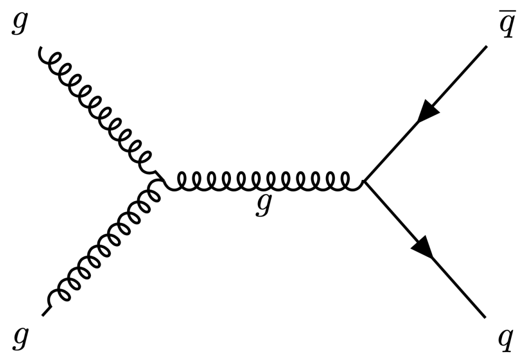

Figure 6.4: Two protons incident on one another can emit two gluons which, consequently fuse and finally produce a quark and anti-quark pair [123].

It is clear that the challenge is a formidable one and that one must work backwards through several degrees of separation from measured jets, formed using detector subsystems, to the originating parton. This is certainly true of recorded data however, there is a way in which the processes inbetween may be modelled using Monte Carlo (MC).

An example of an entire event through the lens of MC is given in Figure 6.5. As mentioned in the whistle-stop tour of this whole process it is useful to think of this process after the protons are incident on one another as beginning from the highest energy or hardest component; the hard interaction and this is represented by the central red circle (Figure 6.5). The ISR activity is apparent in the radiation coming from the two gluons before they interact at the red circle. The produced, “final state”, partons are indicated with the red lines and show the splitting and emission of radiation described earlier. Finally the hadronisation is shown with the green ovals that then emit the showers of particles. This representation demonstrates just how complex hadronic collisions can be before the detector is even involved. The green circles are what can be measured and these measurements will form the starting point of the effort to differentiate quarks from gluons.

All of the following work will now become more specific to the ATLAS detector [55] using the data recorded from collisions produced by the LHC and simulation intended to model proton collisions through the eyes of ATLAS (Chapter 3).

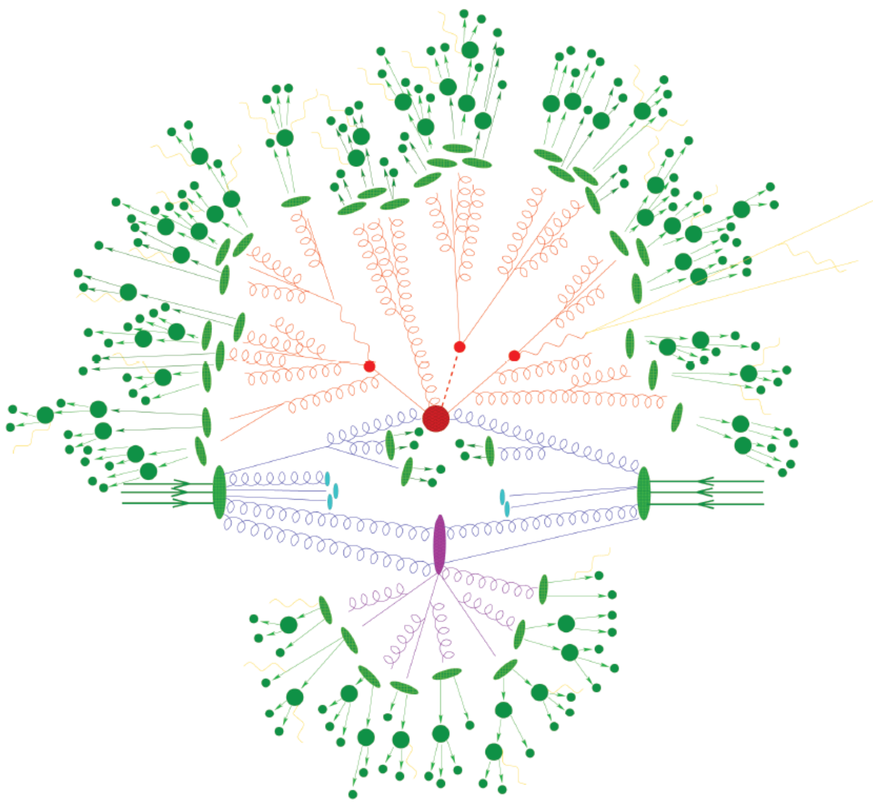

Figure 6.5: A structural view of a proton-proton collision with the three arrows ending in a green oval representing each of the incident protons. The hard process is the the red circle and the red lines moving outward represent the outgoing partons and other particles. The further splitting from these few red lines indicate radiative processes (FSR) before all of the partons move to the hadronisation phase in green. The highest energy regions are in the centre of the diagram while the lower scales are found as one moves outward to the green. Image source: [16].

6.3 Quark-Gluon Discrimination

Now that there is an outlined theoretical and experimental basis to work forward from, the chapter will move on to look at the practicalities of quark-gluon discrimination. There are many reasons to press on with this kind of work including increasing the power an analyser of ATLAS events has to select the desired final states. There has been more specialised work done in the past in particular on the subject of identifying $b-$jets [89][139] to great success. The tagging of $b-$jets was heavily involved in one of the channels contributing to the discovery of the Higgs boson in 2012 [5][6]. Since the discovery, measurements have been performed to accurately constrain the properties of the Higgs and even a dedicated analysis to observe the decay of the Higgs to bottom quarks, $H \to b\bar{b}$, a channel that is the dominant decay mode of the Higgs ($\sim 58\%$) [140]. Not only has the bottom quark been the subject of these kinds of efforts but also its heaviest-generation partner the top quark [141]. The "heavy" quarks can be grouped in this way due to their ability to act in a free-quark manner as was touched upon in Section 6.2.1 however, in an ideal scenario physicists would have the ability to classify quark and gluon jets and even label the quark-flavour of any jet in question.

The pseudo-Feynman diagrams (Figures 6.6a to 6.6c) represent three scenarios for SUSY to present an all quark final state. Each of these models require the production of a particle known as the gluino the superpartner of the standard model's gluon. There is a substantial cross section for the production of gluinos ($\tilde{g}$) from proton-proton collisions (Section 2.4.4). Once produced these gluinos decay either promptly or through cascades with both processes ending in a substantial number of quarks that will be observed in the detector as jets.

Figures 6.6a shows the example of the production of a gluino ($\tilde{g}$) pair, each of which subsequently decays directly via the R-parity[1] violating (RPV) [48] UDD

[1] $P_{\mathrm{R}} = (-1)^{3B+L+2s}$, where B is the baryon number, L is the lepton number and s is the quantum number of spin

coupling λ'' to three quarks. Figure 6.6b is a similar process with the added step that the $\tilde{g}$ decays to a neutralino ($\tilde{\chi}_1^0$) and two extra quarks before using the same RPV coupling to produce three further quarks [142].

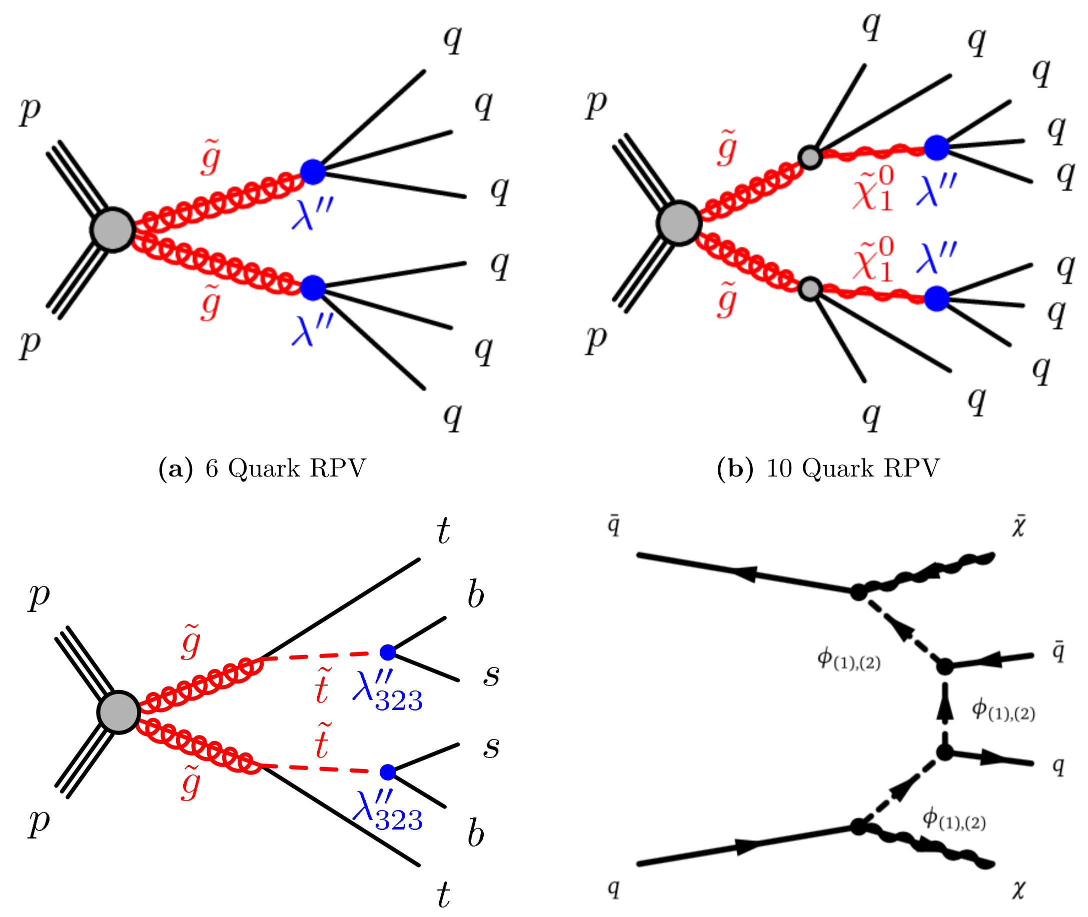

(a) 6 Quark RPV

(b) 10 Quark RPV

(c) 6 Quark RPV via $\tilde{t}$

(d) Quarks and Dark Matter

Figure 6.6: Models for physics beyond the standard model that present quark dominated final states.

In Figure 6.6c the gluino decays via an intermediate top squark or stop ($\tilde{t}$) along with a standard model top quark. The $\tilde{t}$ is then able to further decay to two SM quarks, in this case b and s via the λ''_{323} coupling [2]. Finally in an example of a dark matter model there can be the production of a dark matter particle χ in conjunction with a quark pair as in Figure 6.6d [143][144].

The SM backgrounds for these kinds of processes are gluon dominated and so in this context this brief summary of some signal models demonstrates just how powerful effective quark-gluon discrimination would be in the search for physics beyond the standard model. Due to the low cross sections for high jet multiplicity events in the SM the background is naturally suppressed and this is advantageous in its own right but could be greatly improved by reliably identifying events with only quark jets. These kinds of pure quark signatures present an ideal use case for an effective quark-gluon tagger.

6.3.1 Previous Work

Initially, attempts made to determine whether a jet is quark- or gluon-initiated have involved simulating collider events, since in such simulations the initiating particle can be known. Using this information, distributions of the number of associated tracks for a jet are plotted for quarks and gluons as in Figure 6.7. The number of tracks associated to a particular jet, or the track multiplicity, (n_{track}) is shown for quarks with a solid line and a dashed line for gluons. These two distributions are then displayed for different momentum ranges, showing that the average number of tracks in a jet increases with the p_{T} of a jet. What should also be noted is that the gluon distribution, in every p_{T} range shown, sits to the right of the quark histogram. Another feature of the gluon distributions is that the tails stretch out to much higher track multiplicity than the quark jets, particularly for the high p_{T} range. Both features are a validation of the behaviour predicted by the DGLAP functions (Section 6.2) that a gluon should radiate more readily and so have more particles in jet cone, this coupled with the increased radiation due to the higher p_{T} gives rise to these long tails.

These distributions are produced in different transverse momentum ranges (p_{T}). In each range a track number (n_{track}) cut is found that separates between quark and gluon. The authors of [131] studied a final state in which only two jets were detected from the primary vertex. Once these cut values on track number were determined in each p_{T} range for Monte Carlo one could look at similar dijet states measured in data. The n_{track} and p_{T} values of each jet measured in data would be compared to the n_{track} cut value in each momentum range and the jet "tagged" as being from a quark or a gluon if the track values were lower or higher than the cut respectively.

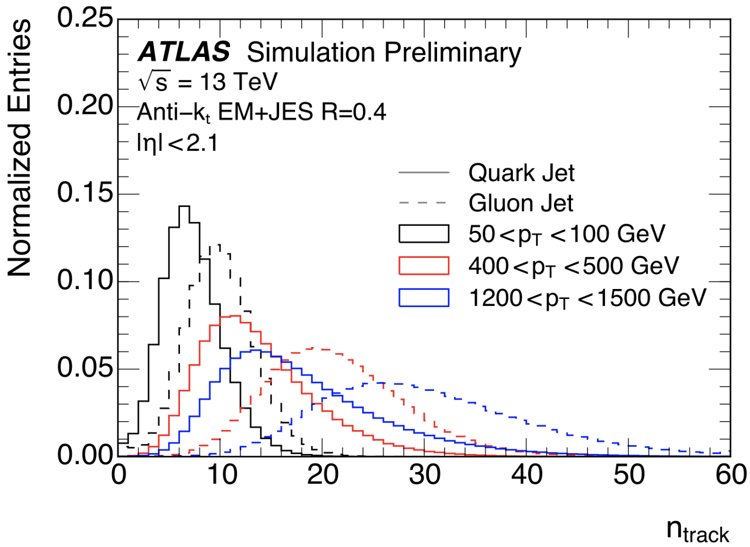

Figure 6.7: The number of charged tracks, with $p_{\mathrm{T}} > 500\,\mathrm{MeV}$, associated to a jet. This is also know as the reconstructed track multiplicity of a jet, n_{track}. The distributions are split into different p_{T} ranges and also show the n_{track} distributions for the quark (solid lines) or gluon (dashed lines) truth labels [131].

This method is desirable as it is simple and easy to implement. The number of charged tracks associated with a jet forms the basis of this and almost all more complex methods. The authors of the existing ATLAS method [131] report a quark tagging efficiency of 60% and a gluon tagging efficiency of $10 - 20\%$ over a substantial p_{T} range (up to $p_{\mathrm{T}} = 1.5\quad\mathrm{TeV}$). The total systematic uncertainty placed on these results is 5%, increasing for higher numbers of jets in an event. We note that an efficiency of 0.6 per jet very rapidly becomes insufficient for high jet multiplicity events.

The CMS collaboration has made similar, slightly more complex, efforts with about the same success [132][145]. CMS uses not only the track multiplicity of the jet but also some extra theoretically motivated variables. The first such quantity is the *jet energy sharing*,

$$p_{\mathrm{T}}D = \frac{\sqrt{\sum_i p_{\mathrm{T},i}^2}}{\sum_i p_{\mathrm{T},i}}, \tag{6.12}$$

where the index, i, here runs over the jet constituents. This is an interesting variable as it encodes information about the fragmentation of the jet. The quarks are less likely to radiate than the gluons so a quark jet can be observed with one, or very few hard constituents. If a jet is made up of only one constituent carrying all of the momentum $p_{\mathrm{T}}D = 1$ but as $p_{\mathrm{T}}D \to 0$ the number of constituents approaches infinity. A third addition to track multiplicity is extracted from the jet shapes and is a measure of the angular spread of the jet in the $\eta - \phi$ plane, σ_2. The spread of the jet is again motivated by the points in Section 6.2 as the gluon emits more radiation the electromagnetic interaction between constituents will increase the spread of the jet.

A different approach has been taken in a more recent publication by Y. Sakaki [146]. Instead of identifying initiator particles jet-by-jet the author instead looks at the event as a whole. A"quarkiness" variable, Q, is defined based on the result of a boosted decision tree (BDT) output operating on Monte Carlo samples and using primarily the same variables as the simpler techniques (n_{track}). This Q is used to form a normalised quadratic sum for all the jets in the event and hence an event-level value running between zero and one. Zero represents the case where it is certain there are no quarks in the event and one corresponds to the case in which only quarks are present. The overall event-level variable is shown to have good discriminating power for a toy model. The model is such that two gluons or a quark and anti-quark pair produce a heavy resonance X ($gg/u\bar{u} \to XX$). The two heavy particles decay in to a final state containing 10 quarks. The event-level variable for background (coming from QCD jets) had a value of roughly 0.45 for ten jets and for the signal state of 10 quarks the value was 0.6. This is a very similar model to those identified as ideal use cases above and is a very promising result.

The most promising and powerful methods to date exploit simple, physically well-motivated variables to achieve some form of tagging or labelling. The results have shown promise but do not have the same efficiencies as the likes of a $b-$jet tagger does. Can the situation be improved? A good starting point is to review some of the variables at our disposal in the ATLAS experiment.

6.3.2 Useful Variables

To summarise the important global quantities of a jet a four-vector, in terms of energy and momentum, can be specified as $(p_{\mathrm{x}}, p_{\mathrm{y}}, p_{\mathrm{z}}, E)$ or by other coordinates, such as $(p_{\mathrm{T}}, \eta, \phi, M)$ where M is the jet mass. The second version is the most useful in the ATLAS detector since it respects the geometry of the detector and longitudinal boosts. Figure 6.8 shows the distributions of p_{T}, η, ϕ and jet mass M_{jet} using $t\bar{t}$ MC.

The $t\bar{t}$ events are simulated using matrix elements with next-to-leading order calculation and using the POWHEG BOX V2 generator [100] as well as the *NNPDF3.0NLO* parton distribution function (PDF) set [105]. MadSpin [147] was used to conserve all spin correlations while all parton showering, fragmentation and the underlying event are handled by Pythia8 [101] which utilised the *NNPDF2.3LO PDF* set [148] along with the ATLAS A14 tune [106]. Finally the detector interactions are processed by GEANT4 [108] after the simulation of the hadronisation processes for all final state particles.

In order to select useful and "good" events some initial selection criteria are imposed on the events. An event must have at least one primary vertex with two reconstructed tracks, with $p_{\mathrm{T}} > 500\,\mathrm{MeV}$ measured by the inner detector (ID) [120], before being considered for the event cleaning process. Cleaning is required to remove backgrounds that are not due to any collision process from the beamline such as cosmic particles incident on the detector and sporadic coherent energy spikes in the calorimeter. Jets originating from these unwanted background processes are known as "fake jets" and those coming from pp collisions are "good jets". These "fake jets" are removed according to the "LooseBad" criteria as defined in [90] which selects “good jets” with an efficiency greater than 99.5% for jets with $p_{\mathrm{T}} > 20\,\mathrm{GeV}$. Any events failing these preliminary requirements are removed from further analysis.

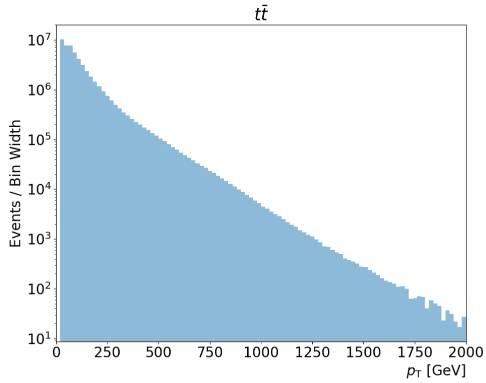

(a) Jet p_{T}

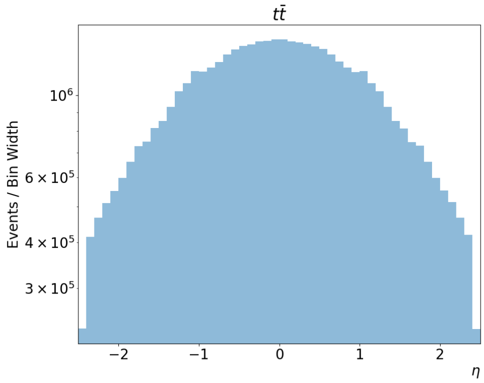

(b) Jet η

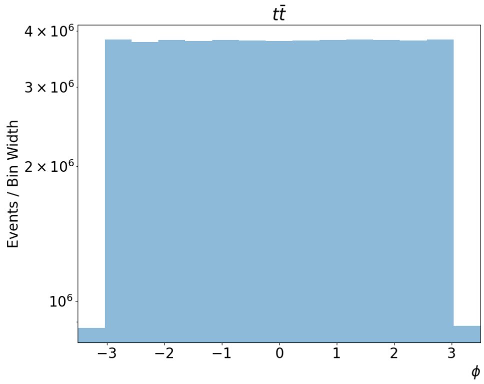

(c) Jet ϕ

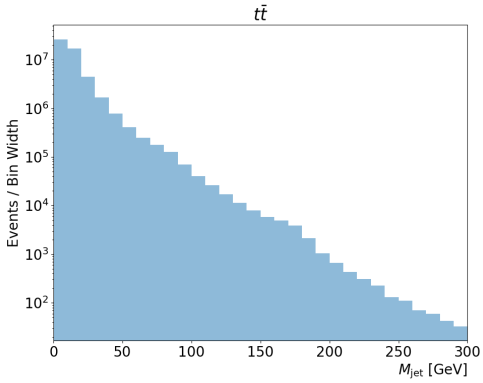

(d) Jet Mass, M_{jet}

Figure 6.8: Simulated $t\bar{t}$ events are used to summarise some of the primary quantities that define a jet. All of the distributions shown here, in semi-log scale, are after the cleaning process and show no unusual features.

As well as the event conditions the jets are reconstructed to ensure that we have a high quality dataset to work with. The jets in question are reconstructed using the particle-flow method (PFlow) [70], Section 3.4.5.

The results of this cleaning are apparent in Figure 6.8 in which, each of the quantities associated with a typical jet four-vector are shown. The p_{T} spectrum in Figure 6.8a shows a smoothly falling distribution out towards a very high p_{T} of $2\,\mathrm{TeV}$ while the bulk of the distribution lies within $p_{\mathrm{T}} < 500\,\mathrm{GeV}$. The next plot shows the behaviour in pseudo-rapidity η (Figure 6.8b) and here high positive or negative values indicate jets forward or backward in the detector respectively and a value of zero indicates a jet is perpendicular to the beam line. There is a preference here for jets to be very central ($|\eta| < 1.0$). Next comes a plot of the azimuthal angle ϕ, which indicates the angular displacement from the detectors y-axis in the $x - y$ plane. Figure 6.8c is expected to be flat as there is no reason for jets to have a particular directional preference in this plane, the very small bins on the outer edges ($|\phi| > 3.0$) are a consequence of the binning regime as ϕ runs from $-\pi$ to π. Finally Figure 6.8d shows the jet mass and this histogram does have a feature around the top quark mass $m_t \approx 173\,\mathrm{GeV}$ but this is to be expected given that $t\bar{t}$ simulation has been used and indicates the cases in which the jet contains the entire mass of the top quark $M_{\mathrm{jet}} \sim 173\,\mathrm{GeV}$.

These histograms show expected behaviour however, these features are relatively insensitive to the initiating parton. In Section 6.2.2 it was noted that there is a window into simulation that is not available in data, the MC contains information about all the particles that were produced in the initial interaction and those in the final state. This picture of an event was described in Figure 6.5 and it allows the labelling of a particular jet with a designation in *truth*. Truth level is the generator stage of the simulation before any detector effects are applied and the collection of truth particles can be stored in the MC data. The truth partons can be matched to the reconstructed jets (jets built using the PFlow algorithm) in order to label them as a particular type. The entire set of truth partons is considered and each one in turn is compared to each of the reconstructed jets in an event. If the truth parton falls within $R = 0.3$ of a jet it is matched to that jet and removed from further consideration. This process continues until all partons are matched to jets; once complete all of the *children* are removed (truth particles coming from another particle's decay) so that only the *parent* particles remain associated to a jet. The jet is then labelled with the parton type of the highest energy truth particle matched to that jet and gives a proxy for the initiator of a jet. We note that this process is very dependent on the simulation of something which is, when considered with care, theoretically ill-defined.

The partons matched to jets are numbered using a scheme that sets $1-6$ as the quark flavours and 21 as a gluon [11] and this number is then stored along with all other information for any given jet. The truth-matched jets are restricted to those coming from partons, other numbers in this scheme represent leptons and all other particles, and we will exclude the top quark label for now. Ignoring the top label is legitimate due to its assumed 100% branching ratio to the bottom quark. The labelled jets can be extracted from the simulation and the results for $t\bar{t}$ are in Figure 6.9. In red the quark labels show that the majority of quark jets are bottom type as is expected in this data set and there is a considerable contribution from the lightest generation quarks likely coming from the decay of the W boson produced in association with the b. In blue there is a huge contribution from gluon jets and these will be from the underlying event as well as ISR and FSR.

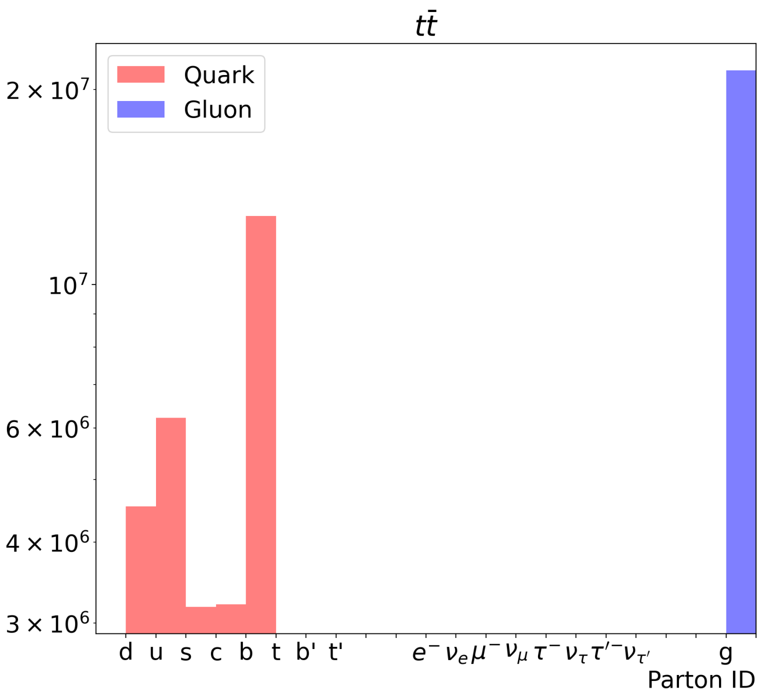

Figure 6.9: Distrbution of the number of truth labelled quarks, by flavour, and gluons.

Using the truth-labelling scheme the distributions of Figure 6.8 can be split into quark and gluon-labelled jets as in Figure 6.10 with the same configuration as before. Now some striking differences between the two jet types become apparent. Starting with the jet p_{T}, Figure 6.10a, the gluons tend to have lower p_{T} and have a peak at very low values of transverse momentum. Moving into the tails the difference becomes increasingly accentuated as the jet p_{T} rises. In the η plot there is again a noticeable difference, particularly in the ratio panel, with the quark jets tending to be more central in the detector while the gluon jets have a slightly more flat distribution.

Moving on to Figure 6.10c the azimuthal angle remains flat across the full range of values and this behaviour is the same for both jet types. There is an offset of ~ 1.4 in the ratio and this is due to there simply being more quark jets in the dataset than gluon which, is apparent when looking at Figure 6.9 and considering all quark bins as one. The same consideration must be applied to the other sub-figures and focus on the shape of the ratio rather than the offset. The final component of our four-vector of plots is M_{jet} (Figure 6.10d). The gluon jet mass falls off in a smooth manner, in contrast the quark jets show some important features. The first such deviation in the ratio panel appears at $M_{\mathrm{jet}} \sim 80\,\mathrm{GeV}$ and this is likely due to a hadronically decaying W boson with its decay products captured in a single jet.

Further out in the distribution the peak around the top quark mass is again obvious and is in fact accentuated due to the removal of background gluons. A final peak in the ratio plot is visible in the far tail of M_{jet}. Investigating this simple selection of attaching a truth label to the jets has revealed that there is indeed classification power in these standard quantities but this method has relied on information that is not available in real ATLAS data.

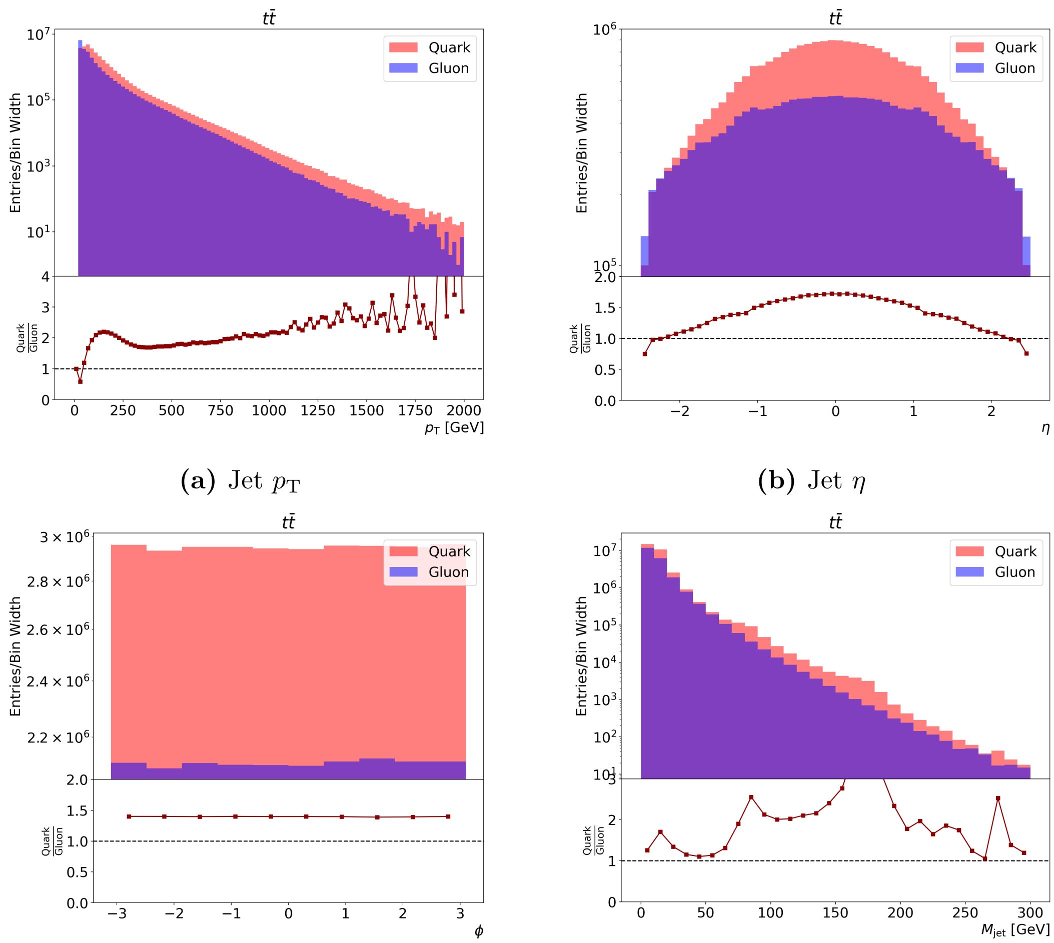

(a) Jet p_{T}

(b) Jet η

(c) Jet ϕ

(d) Jet Mass, M_{jet}

Figure 6.10: The same $t\bar{t}$ events as used in Figure 6.8 but now they are split into two distributions based on truth label. The red indicates jets that have had a truth quark marked as the seed of the jet and the blue shows those jets that are gluon initiated in term of truth. The lower panel of each plot is the ratio of each bin to highlight any differences between the quark and gluon plots.

The variables discussed above are not the only pieces of information available to assist in this effort and also quite $t\bar{t}$ specific. Attempts in the past have relied on the physically well-motivated n_{track} variable. The quark and gluon truth labelled distribution is shown in Figure 6.11. The difference in n_{track} between quarks and gluons that is to be expected from previous results [131] and shows why this quantity is preferred as a simple discrimination method.

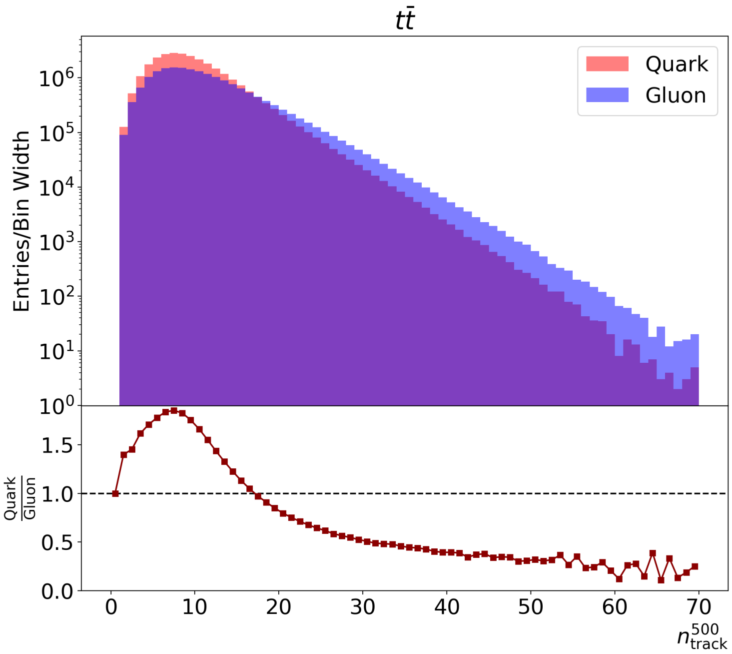

Figure 6.11: Two distributions of n_{track}^{500} using $t\bar{t}$ MC, the blue distribution represents the jets that have a truth tag for gluon. These often have a very large number of tracks in the jet. The red shows the same distribution only for a jet truth labelled as a quark, here the average value lies towards the lower values of n_{track}^{500}. This difference is highlighted in the ratio plot in the lower panel. This distribution is for all jet and has no condition on p_{T}.

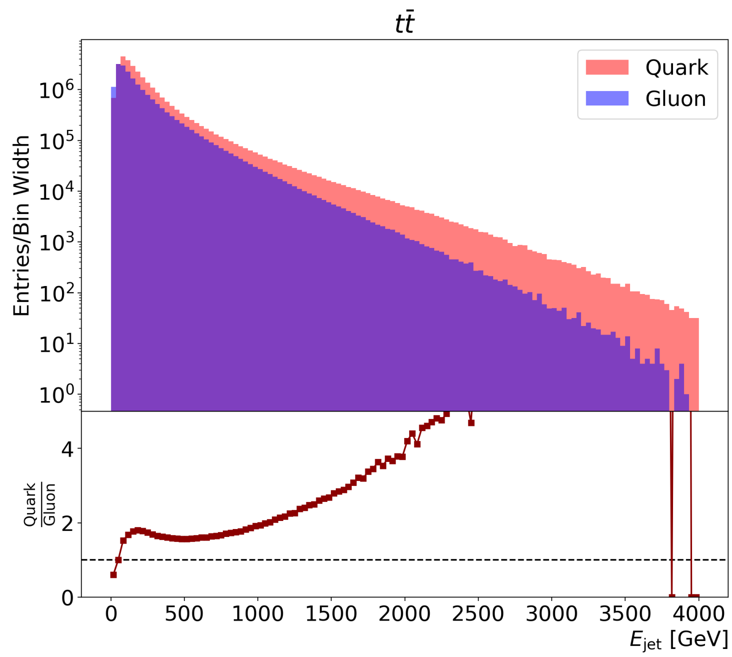

Figure 6.12: The measured jet energy for quark and gluon truth-labelled jets.

One other quantity that shows good discrimination power is the jet energy E_{jet} shown in Figure 6.12. Here the energy is shown over a large range, up to 4 TeV and at low values there is a large difference before heading to a region of overlap. After the $E_{\text{jet}} \sim 600\,\text{GeV}$ point the shapes of the two distributions begin to differ wildly and the high energy region is heavily quark dominated. This hints at good promise as a useful variable in the future analysis.

After splitting the jets into truth labelled sets a small subset of potentially useful variables showed good promise in being able to discriminate between quark and gluon jets. This investigation relied on the truth information being available and this is only true of simulation. The objective is to have the same ability in data in order to isolate the interesting events that may hide new signal models like those in Figure 6.6. The behaviour of these variables while classed under the truth categories could reveal features that are unique to quark or gluon jets, aside from knowing the simulation label, and so be applicable to data.

6.3.3 Likelihood Method

Beginning on the premise that n_{track} is indeed the most appropriate way to classify jets as quark and gluon one can add a little more complexity by folding in some information about the p_{T} of the jet. As was demonstrated in Figure 6.7 there is a p_{T} dependence for the n_{track} cut. Using the $t\bar{t}$ MC a two-dimensional histogram of n^{500}_{track} against p_{T} would visually demonstrate how these two quantities behave together, Figure 6.13.

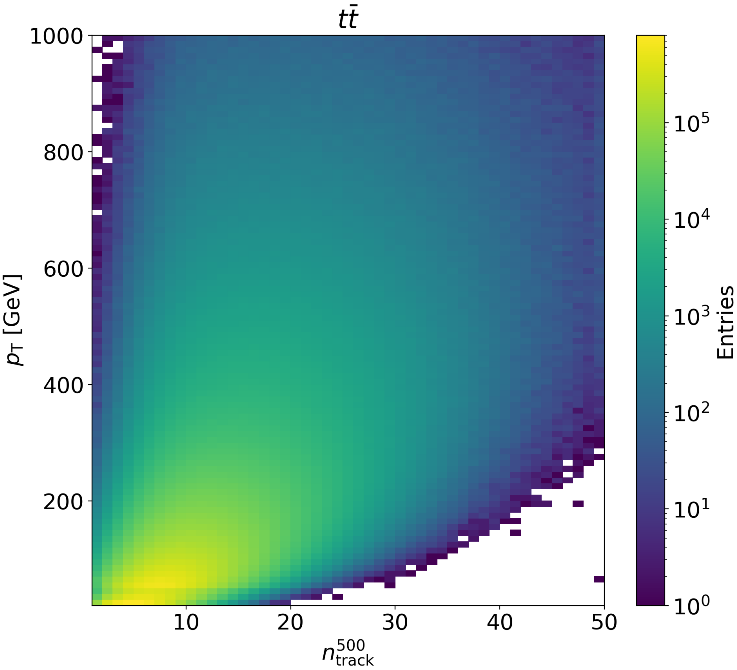

Figure 6.13: Two dimnesional histogram of p_{T} and n_{track}^{500}, the z-axis quantifies the number of jets that enter into each bin. The interdependency of p_{T} and n_{track}^{500} is apparent.

Each bin here indicates how many jets fell within that p_{T} and n_{track} range, the vast majority of jets are concentrated in the lower left corner before the spreading out in both n_{track} and p_{T}. There is indeed a dependence between the two that can be seen even by eye.

To inspect the behaviour of truth labelled quark and gluon jets, Figure 6.14 has zoomed in to a smaller region of the kinematic space and adds a striking colour change to accentuate some of the details. There are now two MC types; the original $t\bar{t}$ that has been used thus far and an additional dijet simulation.

The upper two panels of Figure 6.14 are the jets from simulated $t\bar{t}$ events and the lower two contain jets from dijet simulated events. Both panels on the left are the quark jets and the right two are the gluon. The red and orange coloured bins show where the highest concentration of jets are in n_{track}^{500} and p_{T} space. For the truth-labelled quark jets in both event types the n_{track} and p_{T} do increase in a dependent fashion for low values of n_{track}. The red region then turns upward indicating that the number of tracks in a jet becomes less independent of the p_{T}, in a very loose sense as there are still considerable number of jets with high p_{T} and high n_{track}. This upwards turn behaviour is most striking for the dijet data and while still apparent for the $t\bar{t}$ data there is a larger spread in n_{track} values at high p_{T}.

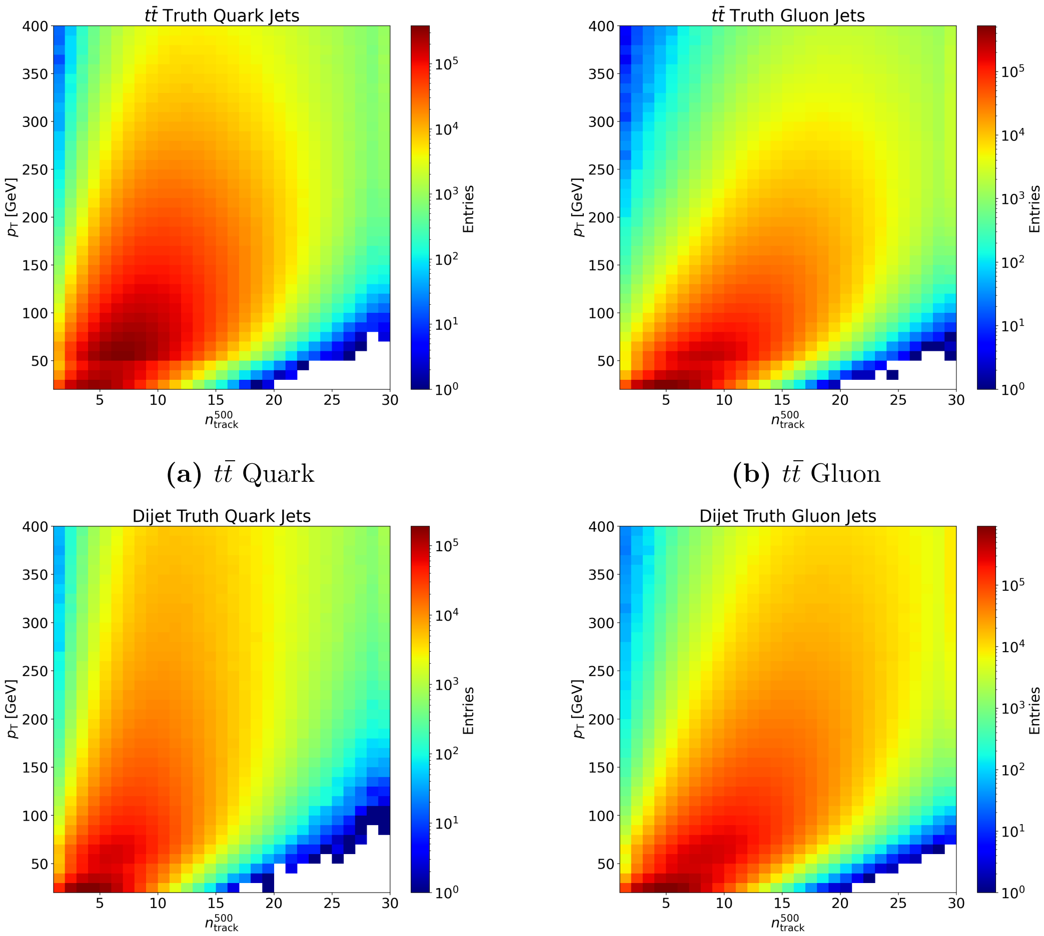

(a) $t\bar{t}$ Quark

(b) $t\bar{t}$ Gluon

(c) Dijet Quark

(d) Dijet Gluon

Figure 6.14: Quark and gluon truth labelled jets are split into different figures, left and right respectively. The upper two panels show the $t\bar{t}$ event type and the lower panels illustrate the same distributions for dijet events.

The two gluon distributions for $t\bar{t}$ and dijets (Figures 6.14b and 6.14d respectively) tend to maintain the dependence between n_{track} and p_{T} up into the high values of both quantities. At high values of n_{track}, across a large range of the p_{T}, for both event types there are large numbers of gluons. While for low n_{track} and higher p_{T}

the quarks form the bulk of the distribution. The main issue is in the lower left hand corner where there is a lot of overlap between the two jet types. Having observed this interdependence of the two primary variables in a two-dimensional way can the discriminant also be formed in a similar fashion?

All of the quark and gluon plots in Figure 6.14 show the number of jets in each bin. Earlier we saw that the quarks were more numerous in the $t\bar{t}$ sample and if a different selection were to be considered, like dijet events, we would see gluons as more common. To remove any effect that one jet type being more common than the other might have these plots are normalised to one for each p_{T} bin (all entries of n_{track} for that p_{T} range sum to one) for the next part of the discussion. If one considers the normalised entries of a p_{T} slice in each distribution to represent the probability that given a certain n_{track} the highest energy parton is quark for a each p_{T} value. It then becomes possible to define a likelihood that a given jet is quark initiated,

$$L(q \mid n_{\mathrm{track}}) = \frac{P(n_{\mathrm{track}} \mid q)}{P(n_{\mathrm{track}} \mid q) + P(n_{\mathrm{track}} \mid g)}. \tag{6.13}$$

This means that each p_{T} slice has a normalised one dimensional histogram in n_{track}. The value between zero and one for any n_{track} then represents the probability a quark jet is found if using the truth quark jet distribution or a gluon jet if we started with the truth gluon distribution. The gluon likelihood would be the same except with $P(n_{\mathrm{track}} \mid g)$ in the numerator. This definition makes it simple to combine the quark and gluon n_{track} versus p_T plots of Figure 6.14 into a likelihood distribution. Each bin of the quark plot is added to the same bin in the gluon figure to form a total and this is the denominator of Equation 6.13. The total obtained is divided into the quark distribution bin by bin to form the final likelihood as in the right hand plot of Figure 6.15.

Initially each of the different MC event types were considered separately and formed their own likelihoods. Each of these likelihood distributions did behave differently as can be inferred by a quick inspection of the differences between dijet and $t\bar{t}$ in Figure 6.14. Only having one event type is not representative of LHC data which combines a great number of different event types distributed in a probabilistic way. One solution to this is that the simulation types be combined to have a more representative data set although, any gain in discrimination based on the event type would be lost. Figure 6.15 is the result of mixing the $t\bar{t}$ and dijet events together. Further work is required to assess the best combination of MC types and to add other event selections into the mixture.

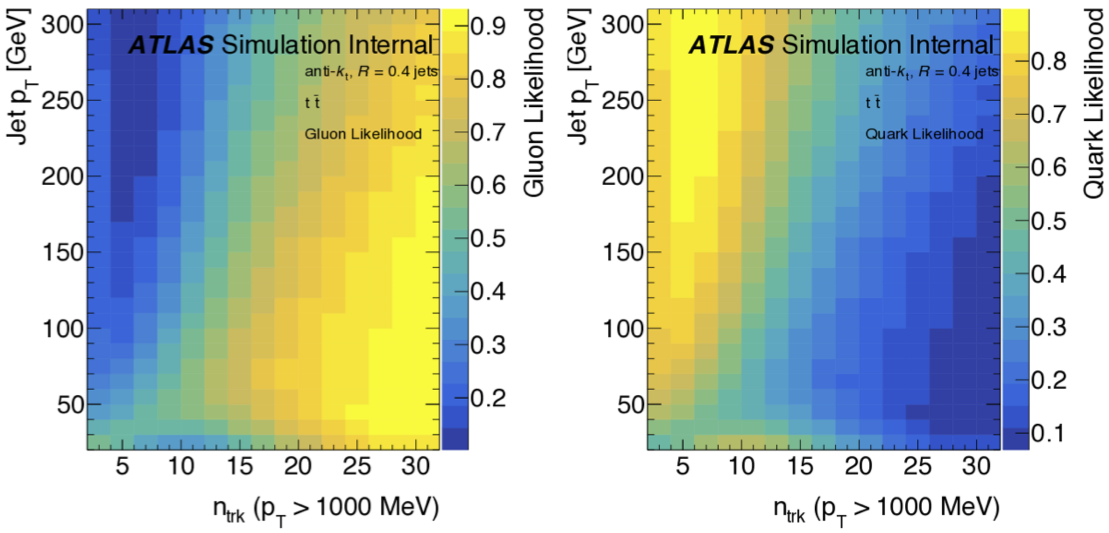

Figure 6.15: The constructed likelihood plots for gluon (left) and quark (right). The x-axis describes the n_{track} values with $p_{\text{T}} > 1\,\text{GeV}$ and the y-axis shows the p_{T} of the jet

The likelihood as defined in Equation 6.13 ranges by definition between zero and one. By construction these two likelihood plots when added together bin by bin will be equal to one. Hence, only the quark likelihood is needed and $L = 0$ represents that the jet is 100% gluon initiated and $L = 1$ is a quark jet. Inspection of Figure 6.15 indicates that jets with a small number of tracks ($n_{\text{track}} < 10$) with $p_{\text{T}} > 50$ GeV are very likely to be quarks. Those with higher values of n_{track} are more probably gluon jets.

The green regions are the areas in which $L \approx 0.5$ and are jets that have a similar likelihood to be either quark or gluon initiated. As noted previously the bottom left corner region with a lot of overlap between the quark and gluon truth jets is in the green ambiguous region. Perhaps another variable added into the likelihood would allow this region to be better classified. It is important that this area is disentangled as a large fraction of the jets reside here. If we continue to add new variables or select different areas of kinematic space the discrimination will improve but this problem seems rather well suited to the application of machine learning (ML).

6.4 Machine Learning for Quark-Gluon Tagging

Machine learning (ML) [149][150] can be succinctly summarised as the ability for computer algorithms to self-improve through experience [151]. The technique has been used by the high energy physics community for decades to improve the sensitivity of searches, measurements and reconstruction techniques [152]. In the beginning of this journey it was common to use *multivariate* techniques that would dynamically optimise kinematic cuts and utilise the full information of an event. It was the arrival of deep learning [153] along with private industry developments that opened the flood gates to ML in HEP.

The problem of quark gluon tagging, in the truth matched form so far discussed, lends itself perfectly to supervised learning. In this case there is a discrete binary output, the jet is a truth quark or it is a truth gluon. This further restricts the scope of these first steps to the subset of supervised learning known as *classification*. The other possibility is *regression* and this is used for continuous variables, probability that we have a quark or gluon jet for example. There are also unsupervised learning techniques but for now the discussion will be limited to a supervised learning classification problem. Supervised learning is the idea that the machine can learn to map an input onto an output given a set of labelled data points. If X is the input space and Y the output, supervised learning attempts to form a mapping function f

$$f : X \to Y. \tag{6.14}$$

In this case the extrapolation into the quark-gluon format is straightforward; there is complete set of labelled data, the truth tagged jets which form the output space

Y. The variables mentioned in Section 6.3.2 along with a few carefully selected additions would easily form the input set X. To approximate the mapping function between input and output the model needs a set of labelled outputs as a *training set* [150]. The *training* of the model is an iterative process in which the model is corrected whenever the prediction is wrong. The training phase continues until the appropriate level of accuracy is achieved. Once the model is trained it can then be validated on a labelled set, the time the model is asked to predict the output and this result is compared with the label of that data point. In this way the accuracy of the trained model can be found.

There is a huge variety of models and techniques available in modern ML. For this investigation we can begin with two of the more common approaches; Artificial Neural Networks (ANN), or Neural Networks (NN), and Random Forest Classifiers (RFC).

6.4.1 Neural Network (NN)

These networks are famously inspired by the operations of neurons in a living brain. The network is composed of layers of artificial neurons, each neuron can take inputs and it then produces a single output. This output can be sent to several other neurons. Figure 6.16 presents the general structure of a neural network, the first layer of neurons takes the inputs and there are as many neurons as there are input parameters to the model. The middle stage consists of layers of neurons (multiple layers are what make it deep learning), each neuron in these layers can have multiple inputs from different neurons. The final layer is the output layer and the result of the network.

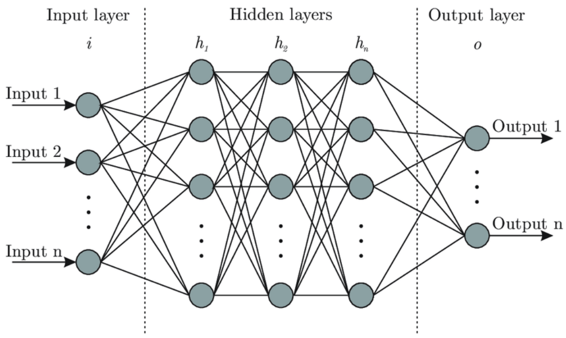

Figure 6.16: Schematic diagram demonstrating the structure of a neural network. The three main layers are the input, hidden layers and the output. This is an example of a NN with three hidden layers and so is an example of deep learning. Image Source: [154].

6.4.2 Random Forest

Random forests or *random decision forests* [155] are a collection of decision trees and the concept of a decision tree has existed for some time. The decision tree, as the name aptly suggests, consists of a set of decision nodes that make some decision based on the input and then branch out to other nodes, a schematic representation would show that these nodes continue to branch out into a tree-like shape. This technique is simple and is related to the concept of a multivariate analysis [156].

The random forest is a collection of many trees constructed during training for classification the result is the mode of all the trees. Random forests arose to combat the tendency for decision trees to *overfit* the data, overfitting is what occurs when the algorithm learns the data in too fine a detail and ends up predicting features of noise in the data rather than actual data trends.

6.4.3 Semi-supervised Learning

To remove some of the reliance on truth matching a semi-supervised machine learning approach was also employed. Semi-supervised learning combines a small amount of labelled data with a large amount of unlabelled data and it is a special case of weak supervision [157]. This approach allows one to gain a deeper understanding of the data by training a model to label the unlabelled real data.

Assuming that the data is clustered in the parameter space we define; quarks close to quarks and the same for gluons. This approach is broken down into a series of steps:

1. Use the labelled data to train a model.
2. Use that model to predict the labels for an unlabelled set.
3. Using the predictions calculate a loss on the unlabelled data.
4. Combine the loss of labelled and unlabelled and then back-propagate.

6.4.4 Setup and Architecture of ML Models

Two approaches are taken to address the quark gluon classification problem; a NN using a code framework known as Keras [158] and a random forest classifier from SciKit learn [159]. Firstly the random forest classifier has 30 trees and each of these trees has a maximum depth of 5. The maximum depth is how many consecutive nodes are allowed from the *root node* (first node) to the furthest leaf, in simpler terms it is the height of the tree. The neural network was built with a Keras sequential model and designed to take the 14 input variables summarised in Table 6.1. After that there are 2 hidden layers each with 20 neurons and these both use the Rectified Linear Units (ReLU) as the activation function [160]

$$R(x) = \begin{cases} 0 & \text{if } x \leq 0 \\ x & \text{if } x \geq 0 \end{cases}. \tag{6.15}$$

The output layer consists of a single neuron with the Sigmoid activation function [161]

$$S(x) = \frac{x}{1+e^{-x}}. \tag{6.16}$$

A subset of the available data, e.g. $t\bar{t}$ MC, was presented to the model and the training was allowed to run for 10 epochs, which indicates how many times the data set is given to the model. This sample was further subdivided into training and validation sets with 80% being given to the training and the remaining 20% used to validate. In the semi-supervised version the NN could have three hidden layers and there were 8 input neurons. The NN could then be trained on a mixture of

MC backgrounds which were the same as the multi-jets and described in Section 5.6.1 and 6 jet RPV SUSY (Section 2.4.2) signal samples as seen in Figure 6.6a, these are generated as detailed in Reference [142].

6.4.5 Useful Variables

Variable Name	Text Name	Definition
Jet p_{T}	jetPt	Transverse momentum of the jet.
Jet η	jetEta	The pseudo-rapidity η of the jet.
Jet ϕ	jetPhi	The azimuthal angle of the jet.
Jet Mass	jetMass	The mass of the jet in GeV, M_{jet}.
Jet Energy	jetEnergy	The total energy of the jet in GeV, E_{jet}.
Jet EM Fraction	jetEMFrac	The fraction of the jet's energy measured in the EM calorimeter.
Jet HEC Fraction	jetHECFrac	Fraction of the jet's energy measured in the hadronic calorimeter.
Jet Charge Fraction	jetChFrac	Fraction of the jet's energy coming from the charged particle tracks. $\frac{\sum_i p^i_{\mathrm{T,i}}}{p_{\mathrm{T,jet}}}$ where $i \in$ tracks.
Jet n^{500}_{track}	jetNumTrkPt500	Track multiplicity ($p_{\mathrm{T}}^{\mathrm{track}} > 500\,\mathrm{MeV}$).
Jet $n^{1000}_{\mathrm{track}}$	jetNumTrkPt1000	Track multiplicity ($p_{\mathrm{T}}^{\mathrm{track}} > 1000\,\mathrm{MeV}$).
Track Width 500	jetTrackWidthPt500	$w^{500}_{\mathrm{track}} = \frac{\sum_i \Delta R(\mathrm{jet},\mathrm{track_i}) p^{\mathrm{track}}_{\mathrm{T,i}}}{\sum_i p^{\mathrm{track}}_{\mathrm{T,i}}}$ where $i \in$ tracks ($p_{\mathrm{T}}^{\mathrm{track}} > 500\,\mathrm{MeV}$).
Track Width 1000	jetTrackWidthPt500	$w^{1000}_{\mathrm{track}} = \frac{\sum_i \Delta R(\mathrm{jet},\mathrm{track_i}) p^{\mathrm{track}}_{\mathrm{T,i}}}{\sum_i p^{\mathrm{track}}_{\mathrm{T,i}}}$ where $i \in$ tracks ($p_{\mathrm{T}}^{\mathrm{track}} > 1000\,\mathrm{MeV}$).
Total Track Momentum 500	jetSumTrkPt500	$\sum_i p^{\mathrm{track}}_{\mathrm{T,i}}$ where $i \in$ tracks ($p_{\mathrm{T}}^{\mathrm{track}} > 500\,\mathrm{MeV}$).
Total Track Momentum 1000	jetSumTrkPt500	$\sum_i p^{\mathrm{track}}_{\mathrm{T,i}}$ where $i \in$ tracks ($p_{\mathrm{T}}^{\mathrm{track}} > 1000\,\mathrm{MeV}$).

Table 6.1: Table of the input variables to the ML models with their definitions.

Quite a few more variables have been added to the classification process since the likelihood method was detailed and some of these variables were shown in Section 6.3.2. It is useful to check correlations between the quantities in order to reduce the dimensionality of the problem. The viability of this reduction can be assessed by producing a correlation matrix for all the values that can be used like that illustrated in Figure 6.17. This matrix was constructed from the $t\bar{t}$ dataset and as a validation we see that the diagonal has all values of one which, is expected as each variable is perfectly correlated with itself.

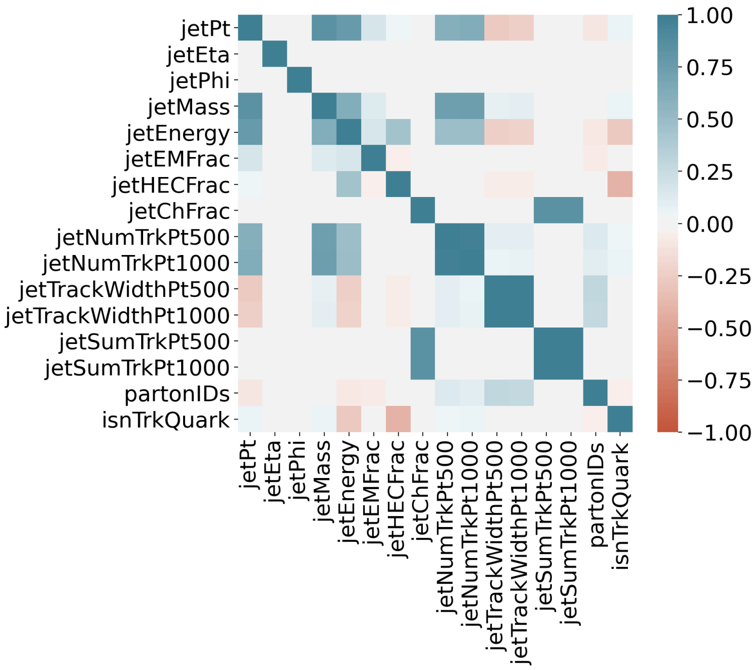

Figure 6.17: Variables used in the ML models and how they correlate to each other.

There are a few extra quantities displayed outside of those summarised in Table 6.1. A simple n_{track} cut is applied to the MC jets as a benchmark of performance (isnTrkQuark). The jet is labelled a track quark if it falls below this cut. Another intriguing result is the strong anti-correlation the track quark label has with the jet charge fraction.

6.5 Results

Training the Keras NN over 10 epochs on 10% of the $t\bar{t}$ Monte Carlo shows promising results with very little optimisation of the hyperparameters. This sample of the data gave a training sample of $1,856,367$ jets which could then be validated on $464,092$ jets. For both the NN and the random forest all 14 variables were given even though the quantities with differing $p_{\mathrm{T}}^{\mathrm{track}}$ cuts are highly correlated. The accuracy and loss of the NN are displayed in Figure 6.18 as a function of training epoch for the training and validation sets. The loss indicates how badly the model is doing after each iteration, for both training and validation this drops rapidly during the first iteration and remains fairly consistent. The accuracy displays the same properties but does increase gradually with epoch up to $\sim 70\%$. As a first attempt this is already on a par with, and indeed slightly better than, the n_{track} method noted in Section 6.3.1 which had 60% accuracy for quark jets.

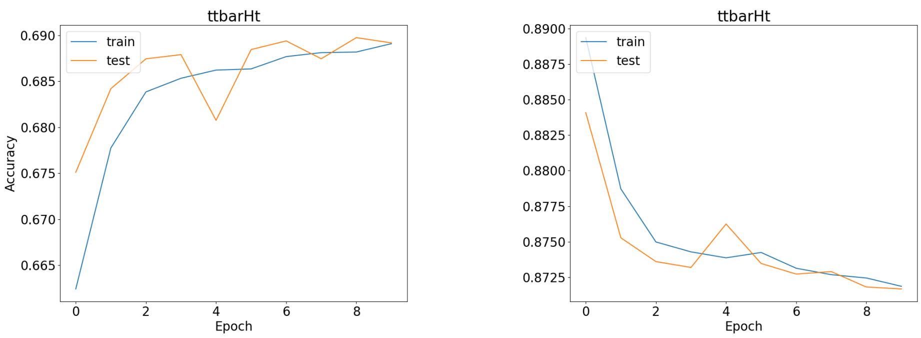

(a) $t\bar{t}$ NN Accuracy **(b)** $t\bar{t}$ NN Loss

Figure 6.18: The accuracy and loss values as a function of epoch, or iteration. The results from the training set are in blue and the validation is in orange. A subset of the $t\bar{t}$ MC was used in this training process (10%).

Looking at the output of the network's labelling (Figure 6.19) there are two distributions; in red the output score for truth labelled quark jets and blue the same for gluons. The model has output continuous values which is perfectly natural for a NN but we want binary classification, that was motivation for using a Simoid output function as it ranges from 0 to 1. At this point a cut would have to be applied to the NN output values to approximate the binary classification. The network has performed well and shows good separation in predicting quark and gluon jets but there is still considerable overlap. Overall, low network scores indicate that the jet is likely to be gluon initiated and high score values indicate the presence of a quark jet. In this case a cut of say 0.75 would do a reasonable job of isolating majority quark jets.

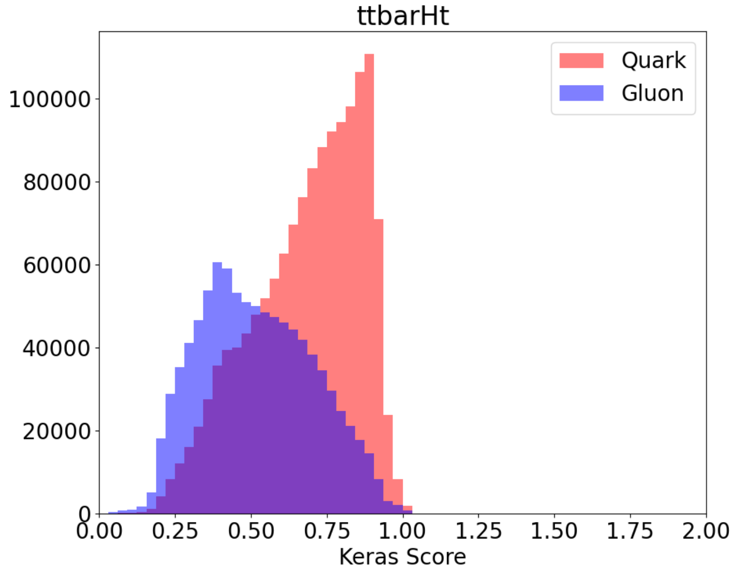

Figure 6.19: The NN prediction for quarks and gluons, the red indicates that the jets in question are labelled as truth quarks and in blue the truth gluons.

The random forest classifier (RFC) also performed well given that it is unoptimised, it achieved an accuracy of 68.9% which is comparable to the NN. One advantage of the RFC is that it is relatively easy to access a ranking of the inputs from most import to least, Table 6.2 shows the ranking of the features in the eyes of the RFC.

This list provides some intriguing results. The RFC indicates that the two most important variables were the track widths with two different $p_{\mathrm{T}}^{\mathrm{track}}$ requirements. Some way behind that appear the n_{track} values that have dominated a lot of previous attempts at the quark-gluon discrimination problem, n_{track} is followed closely by the jet p_{T}. All the other variables fill a supporting role but all in combination provide more power to the RFC's ability to classify. The least important, in the eyes of the RFC, are the jet HEC fraction, the jet η and of absolutely zero importance is the jet ϕ, as one would hope.

Rank	Variable	Feature Importance
1	jetTrackWidthPt500	0.264904
2	jetTrackWidthPt1000	0.203263
3	jetNumTrkPt500	0.107982
4	jetPt	0.105385
5	jetSumTrkPt1000	0.094718
6	jetNumTrkPt1000	0.072480
7	jetSumTrkPt500	0.047901
8	jetMass	0.032219
9	jetEnergy	0.025865
10	jetEMFrac	0.020631
11	jetChFrac	0.014252
12	jetHECFrac	0.006909
13	jetEta	0.003492
14	jetPhi	0.000000

Table 6.2: A ranked list of the input variables to the RFC with the corresponding feature importance value.

The two methods used in this section can be compared using a receiver operating characteristic (ROC) curve. The ROC curve indicates the diagnostic ability of a binary classifier as the cut threshold is varied. ROC curves are plotted against the true positive rate, probability of detection, which indicates the number of positive results that are correct and the false positive rate, probability of false alarm, which is the number of positives that should have been negative.

The ROC curves for the Keras NN and the RFC, or RF, are given in Figure 6.20. The NN has marginally better performance than the RFC, where perfect performance resides in the top left corner of the diagram. A numerical comparison is available with the area values under the curve in the legend and these reinforce the observation that the NN outperforms the RFC.

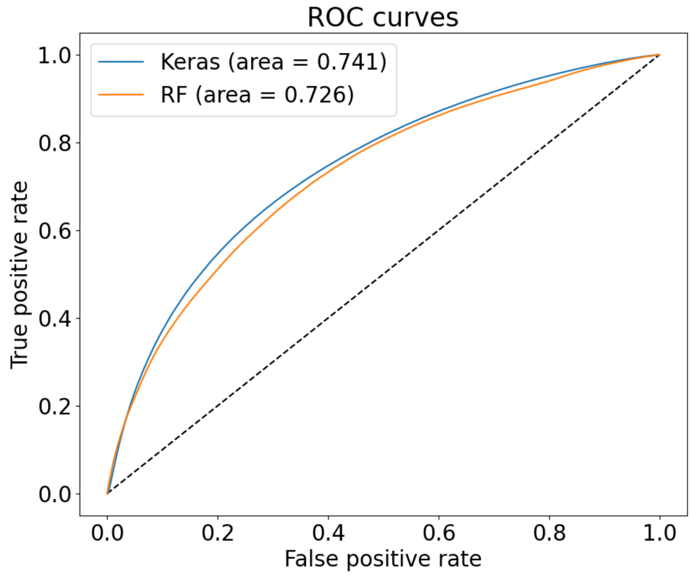

Figure 6.20: The ROC curves for the trained Keras models as well as the random forest classifier.

6.5.1 Semi-Supervised Learning and Shapley Values

Using the semi-supervised machine learning technique one can again gauge the performance using ROC curves. In Figure 6.21 the model has been trained on the mixture of "background" processes from the multi-jets analysis [2] and also a "signal" set. The signal in this case are simulated events of the RPV process shown in Figure 6.6a. Figure 6.21 contains ROC curves for three standard NN architectures and the optimal structure was trained in the semi-supervised manner, this done for quark tagging (left) and gluon tagging (right). The final component of the figure is the BDT currently available to the ATLAS experiment. For all NN cases, including the semi-supervised approach, the performance is roughly similar. Encouragingly there is quite an improvement over the currently available ATLAS BDT.

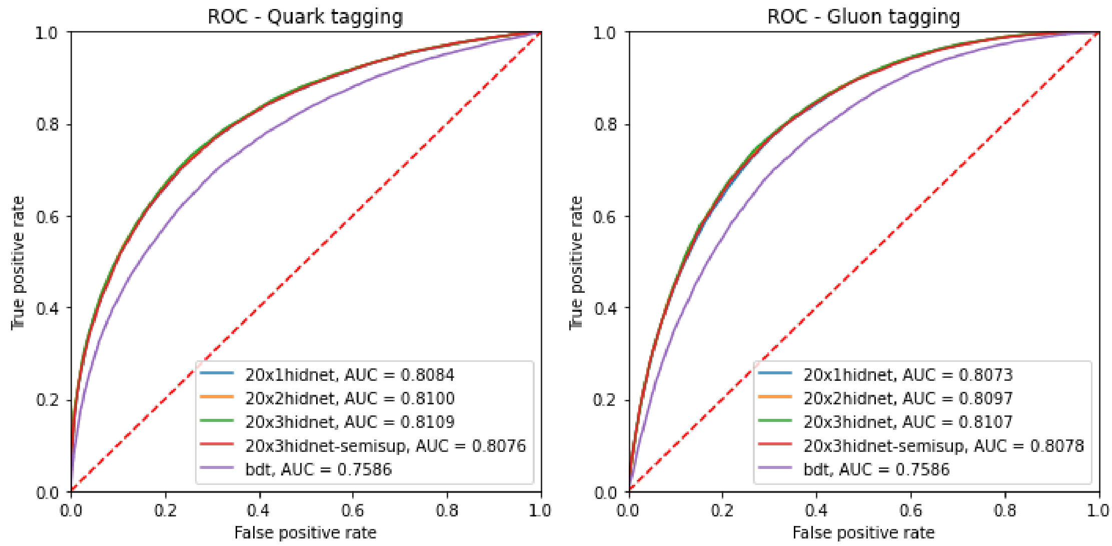

Figure 6.21: The ROC curve for the NN when trained on a mixture of background and RPV signal, the test set is also a mixture of background and signal.

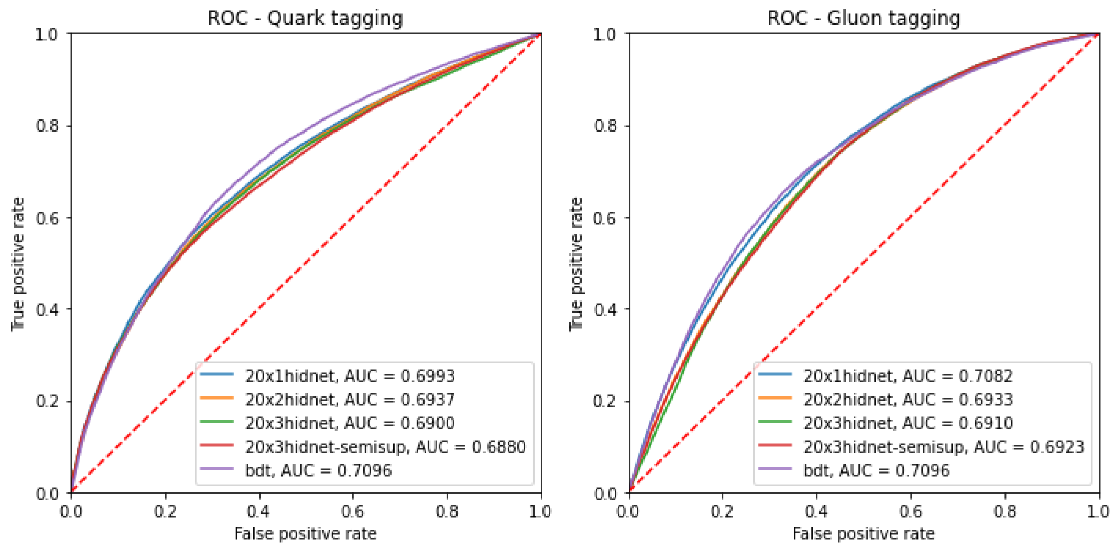

Figure 6.22: The ROC curve for the NN when trained on a mixture of background and RPV signal, now the test set only contains the RPV signal MC.

What if one wished to target the signal directly and determine the performance only on our ideal use case of the RPV signal samples one can remove those from the testing samples. Figure 6.22 shows the case in which the models are all trained as before but the testing sample only contains the pure quark signal final state. In this case all the performance gain is lost and all of the algorithms perform in much the same way. The BDT seems to be more resistant to this change and this is trained on jets from dijet events. A useful feature of the RFC was the ability to extract the feature importances of the input variables to determine which were of most importance to the algorithm, can one do something similar for the more complex semi-supervised machine learning approach?

Using Shapley values [162] from coalitional game theory, a method that indicates how the payout of a game should be divided amongst the players involved one can infer which features are important. A game involving N players with some payout at the end, the players can cooperate in different combinations and so the payout to that coalition will vary depending on its members. Shapley values are a way to assign the appropriate amount of payout to each player in the game depending on their value to the coalition. The same idea can be applied to machine learning but now the players are the feature values and the optimal payout is a correct prediction by the algorithm.

So in the context of these results the Shapley value is the average contribution of a feature value across all possible coalitions of the input features. This was done using the SHapley Additive exPlanations (SHAP) library [163]. Figure 6.23 (left) shows the full SHAP values for a set of 7 input variables, each point on this figure represents an event and the corresponding SHAP value is given on the x-axis. The z-axis colour bar indicates how important that particular feature instance was to the prediction, as this is a quark classifier red is related to "quarkiness" and blue to "gluoniness".

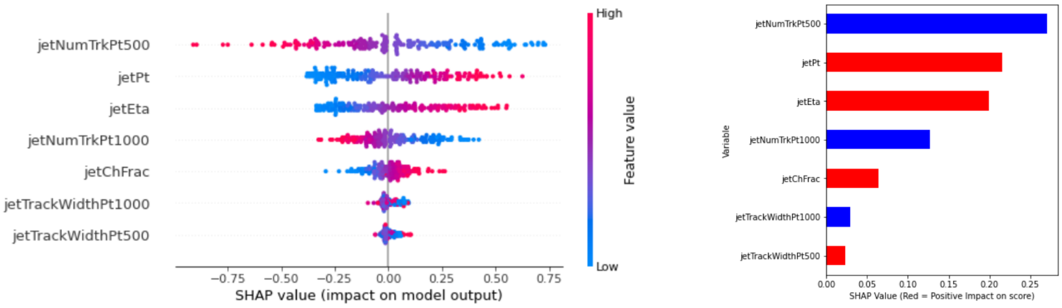

(a) Shapley Values **(b)** Absolute Shapley Values

Figure 6.23: The Shapley values for the semi-supervised learning quark-gluon classifier, the left shows the actual SHAP values

A slightly more easily understood version of this figure is given in the right sub-figure of Figure 6.23 with the absolute SHAP values presented in a bar chart. In this figure red again indicates quarkiness and so one sees that as predicted n_{track} is the most important feature of a jet closely followed by p_{T} and η. This is reassuring as the ML algorithm is learning what was theoretically motivated and applying this knowledge to discriminate. The added power comes from the algorithms ability to use the lower importance variables to aid in the classification of jets that would have been ambiguous in previous methods.

6.6 Errors

Total systematic error in quark-gluon tagging has several contributing factors. These errors are dependent on the event characteristics because quarks and gluons have different colour charge. In the dijet final state using a track multiplicity cut the total systematic error was calculated to be 5% for a broad p_{T} range [131]. The main considerations when calculating this error could be split into two categories [131]. The first is the modelling uncertainty in the simulations and the second is an experimental uncertainty. The experimental uncertainty is further subdivided into reconstruction efficiency of the jets, the fake rate (trajectories which cannot be easily associated to one particle) and detector resolution.

The main contribution to modelling uncertainty is in the modelling of QCD processes, particularly modelling of the non-perturbative regime and mis-modelling at high jet multiplicities. There are several ways to address the calculation of these errors. The approach taken in [131] was to plot the average charged track multiplicity inside a jet against the p_{T} of the jet from simulations. From these distributions the authors extracted a quark and gluon jet fraction by using the angular dependence of quark and gluon emission. The jet fraction uncertainty could then be calculated by comparing different generators (Pythia8 and Herwig). The most thorough work in quantifying these errors has been done by [164] and focuses on a Monte Carlo generator comparison method. The authors define quark and gluon enriched samples using kinematic selection. The gluon enriched sample is the same as presented in this work ($pp \rightarrow$ dijets) and the quark enriched sample is $pp \rightarrow Z +$jets. The jets in seven different generators are compared by plotting the charged track multiplicity within a jet. The errors for our analysis will be addressed in much the same way.

6.7 Conclusions and Future Work

Starting from the theoretically motivated technique of using the number of charged track constituents in a jet as the base of a discrimination method. This has been expanded to a likelihood calculation by condensing the one-dimensional distributions of n_{track} in various p_{T} ranges into a two-dimensional plot of n_{track} versus p_{T}. These two-dimensional plots were produced for quark- and gluon-initiated jets in simulation. The next step was to use these distributions to calculate a likelihood distribution in the same format. Each bin in this likelihood plot for a particular n_{track} and p_{T} corresponded to a value between zero and one. These values indicated how likely a jet with those properties was to be gluon or quark initiated.

With the large overlap between quark and gluon jets at low values of p_{T} and n_{track} extra variables were needed to assist in classifying quark and gluon jets. It was at this point that the problem became an obvious target for machine learning classification. Two initial ML methods were applied to a host of variables associated to quark and gluon jets; a random forest classifier and a neural network. Both methods were found to be effective without any optimisation.

To reduce the reliance on MC truth labelling a semi-supervised learning approach was introduced. This method used a small amount of labelled data to train a model to classify the jets on the assumption that quarks and gluons are clusters nearby themselves in the parameter space. This method proved to be highly effective but the performance did drop dramatically when applied only to an RPV signal set. The impact of the input variables in this complex model were calculated using Shapley values from coalitional game theory and it was found that the theoretically well motivated features of a jet were the most important.

Quark-gluon tagging is certainly quite the challenge but with the rise of machine learning techniques it is one that can be achieved with great success in the near future. The combination of data-driven quark-gluon sample extraction with these robust ML techniques is an excellent strategy for progress. Approaching this problem in a multi-layered fashion could also be fruitful. Tagging detector level inputs, a topic of current research, then combining this with the high-level variables used here and finally an event type identification technique to isolate those events that are quark dominated for example.

Cracking this problem would have a hugely positive effect on high energy particle physics analysis and in particular on searches beyond the Standard Model. This is certainly a reasonable goal in Run 3 and into the HL-LHC and is a well motivated route to discovering physics beyond the standard model.

So long and thanks for all the fish . . .

— Douglas Adams - *1984*

7 Conclusions

The LHC delivered a record breaking number of collisions to the ATLAS experiment over the course of Run 2, of this data ATLAS recorded a staggering $139\,\mathrm{fb}^{-1}$ of $\sqrt{\mathrm{s}} = 13\,\mathrm{TeV}$ p–p data. With this dataset ATLAS physicists have been able to test the Standard Model to very high precision and this incredible theory has stood up to the tests. There are known fundamental shortcomings (lack of gravitation, no explanation of dark matter etc.) that need to be addressed to form a complete picture of our universe at its most fundamental scale. Many theories have been put forward to solve the problems inherent in the SM and one well motivated example is supersymmetry (SUSY). SUSY theories can predict a massive, gravitationally interacting and weakly interacting particle that would serve as a dark matter candidate particle.

Such particles may be produced in the LHC and although they would leave the detector without interaction, this does not preclude the fact that they can be searched for. In this thesis, Chapter 4, the performance of the missing transverse momentum was studied in detail as a way to not only infer the presence of standard model neutrinos but also as a method to search for invisible particles beyond the standard model. The performance of this complex and powerful technique was found to be remarkable for the entire Run 2 dataset and although (at the time of writing) no new physics has been found this technique has aided in the measurement of the SM.

Following on from the study of $E_{\mathrm{T}}^{\mathrm{miss}}$ and its significance $\mathcal{S}(E_{\mathrm{T}}^{\mathrm{miss}})$ this thesis presented a search for new physics using the 13 TeV ATLAS data, Chapter 5. This analysis targeted events in which massive SUSY particles produced in pairs would decay via cascades of SUSY particles that would appear as many jets and a moderate amount of $E_{\mathrm{T}}^{\mathrm{miss}}$. The dominant background for such a search comes in the form of QCD multijets that would also produce $E_{\mathrm{T}}^{\mathrm{miss}}$ through mismeasurement and resolution effects. This prompted the use of the $\mathcal{S}(E_{\mathrm{T}}^{\mathrm{miss}})$ calculation as a powerful discriminant to isolate only those events with $E_{\mathrm{T}}^{\mathrm{miss}}$ likely coming from a real invisible particle. No significant deviation from the standard model was observed, the analysis was able to increase the exclusion of gluino masses up to 2 TeV.

The plethora of quark jets produced in the aforementioned search prompted the study of quark-gluon discrimination in Chapter 6. The multi-jets analysis and many other models predict final states that contain quarks coming from a particular process and gluons present in such events would be a background. If one were able to efficiently tag light-quark jets this would be of great help in isolating such events in a signal region. Machine learning techniques were applied to the problem of quark-gluon tagging and shown to be an improvement over the classic n_{track} cut method. Further work is need to isolate a high purity sample of quarks or gluons that one could train a ML classifier on. This problem is challenging, however, the benefits of success would be tremendous.

No physics beyond the Standard Model was found in this thesis but the LHC is to continue operations for many more years recording evermore data. The work of today aids in the successes of the future and with perseverance, dedication to the scientific method, and a hint of luck the high energy physics community can be confident in uncovering the mysteries of the universe at this machine or the next.

Appendices

A
Theory

A.0.1 Electroweak Sector

Neutral Interactions

The neutral interactions under this regime are the diagonal terms of Equation 2.19. These are described by the diagonal terms of the $SU(2)_L$ generators, the Pauli matrices of Equation 2.18. Under inspection it is clear that the diagonal terms couple to the right handed spinors and those proportional to σ_3. One can derive a formulation of the neutral weak and electromagnetic interactions by rotating the fields B^μ and W_3^μ by some angle with,

$$\begin{pmatrix} B^\mu \\ W_3^\mu \end{pmatrix} = \begin{pmatrix} \cos\theta_W & -\sin\theta_W \\ \sin\theta_W & \cos\theta_W \end{pmatrix} \begin{pmatrix} A^\mu \\ Z^\mu \end{pmatrix} \tag{A.1}$$

where θ_W is known as the *Weinberg angle* or *weak mixing angle* and is the angle by which the W^0 and B^0 fields are rotated in spontaneous symmetry breaking (Section A.0.2), thus generating the Z^0 boson and a massless photon. The weak mixing angle can be expressed in terms of the coupling constants of the $U(1)_Y$ and $SU(2)_L$ symmetries, g and g':

$$\theta_W = \arctan\left(\frac{g'}{g}\right), \cos\theta_W = \frac{g}{\sqrt{g^2+g'^2}} \text{ and } \sin\theta_W = \frac{g'}{\sqrt{g^2+g'^2}}. \tag{A.2}$$

The Z_μ boson and photon fields can also be written in terms of the Weinberg angle,

$$A_\mu = B_\mu \cos\theta_W + W_\mu^3 \sin\theta_W \tag{A.3}$$

and

$$Z_\mu = -B_\mu \sin\theta_W + W_\mu^3 \cos\theta_W. \tag{A.4}$$

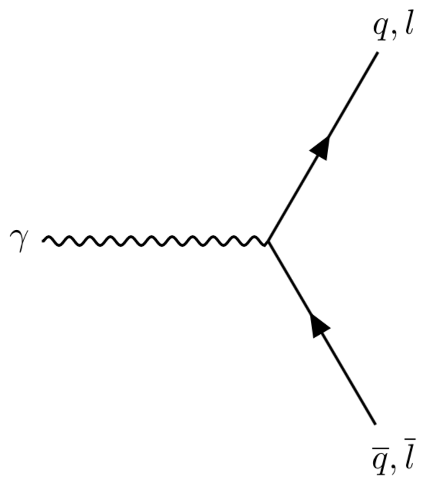

(a) $\propto eQ$

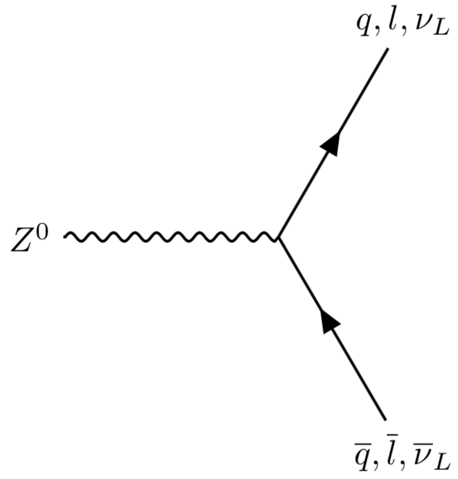

(b) $\propto eQ_z$

Figure A.1: The neutral current interactions in the electroweak sector. Here the A^μ field of Equation A.3 is the photon field and Z^μ is the massive Z^0 after rotation of the B^μ and W_3^μ fields.

Figure A.1 shows the form of the neutral current electroweak interactions with the possible final particles indicated on the right as well as the proportionality of the diagram to the electric charge for the photon coupling, detailed in Equation 2.17, the Z^0 coupling is proportional to the weak charge,

$$Q_Z = \frac{1}{\sin\theta_W \cos\theta_W}\left(T_3 - Q\sin^2\theta_W\right). \tag{A.5}$$

Charged Interactions

Now looking more closely at the W boson fields the charged current interactions can be identified. Again using Equation 2.19 the charged interactions come from the off diagonal terms of the $SU(2)_L$ generators (Pauli matrices again). The two

Pauli matrices with off diagonal elements are σ_1 and σ_2. The off diagonal elements prompt a rewrite of the interaction terms of Equation 2.19 in a complete diagonal basis to define the new gauge fields W^μ_+ and W^μ_-,

$$W^\mu_\pm = \frac{1}{\sqrt{2}}\left(W^1_\mu \mp iW^2_\mu\right). \tag{A.6}$$

These represent the positive and negative W boson fields; W^+ and W^-. Inspection of the gauge covariant derivative, Equation 2.16, allows the specification of the unit of positive electric charge in terms of the weak mixing angle and the coupling strengths of the weak and electromagnetic fields:

$$e = g' \cos\theta_W = g\sin\theta_W. \tag{A.7}$$

Equipped with these tools one can show that the interaction term of Equation 2.19 can be written in the compact, yet informative, form of

$$\begin{aligned}\mathcal{L}_{CC,\, int} = \frac{g}{2\sqrt{2}}\left(\bar{\nu_e},\, \bar{\nu_\mu},\, \bar{\nu_\tau}\right)\gamma_\mu(1-\gamma_5)W^\mu_+\begin{pmatrix} e \\ \mu \\ \tau \end{pmatrix} \\ - \frac{g}{2\sqrt{2}}\left(\bar{u},\, \bar{c},\, \bar{t}\right)\gamma_\mu(1-\gamma_5)W^\mu_+ V_{\mathrm{CKM}}\begin{pmatrix} d \\ s \\ b \end{pmatrix} + h.c.\end{aligned} \tag{A.8}$$

where γ_μ are the Dirac matrices with $\mu \in \{0,1,2,3\}$ and the fifth gamma matrix is defined as $\gamma_5 = i\gamma_0\gamma_1\gamma_2\gamma_3$. The Hermitian conjugate encodes the same type of interactions but for the negative W boson. The final part of this expression comes up in the quark term and this is a unitary matrix called the Cabbibo-Kobayashi-Masakawa (CKM) matrix [165][166][11] that allows for the quark mixing:

$$\begin{pmatrix} d' \\ s' \\ b' \end{pmatrix} = V_{\mathrm{CKM}}\begin{pmatrix} d \\ s \\ b \end{pmatrix} = \begin{pmatrix} V_{ud} & V_{us} & V_{ub} \\ V_{cd} & V_{cs} & V_{cb} \\ V_{td} & V_{ts} & V_{tb} \end{pmatrix}\begin{pmatrix} d \\ s \\ b \end{pmatrix}. \tag{A.9}$$

Figure A.2 demonstrates the charged current interactions for the positive W boson for the leptonic mode as well as via quarks, an equivalent set of diagrams exists for the W^- with the anti-particle bar symbols reversed. These diagrams also demonstrate the universality of quark and lepton interactions that comes as a direct consequence of the gauge symmetry.

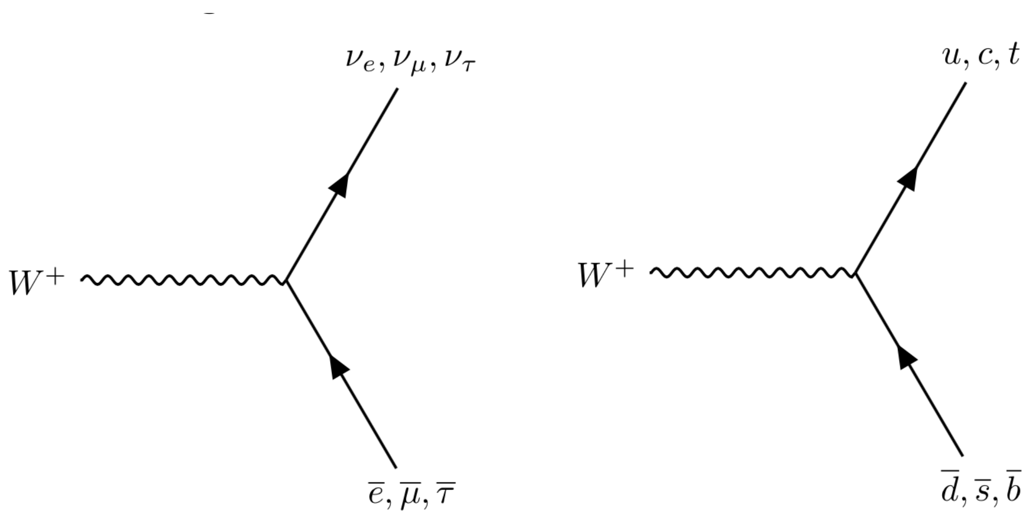

(a) $\propto \frac{g}{2\sqrt{2}}\gamma_\mu(1-\gamma_5)$ **(b)** $\propto \frac{g}{2\sqrt{2}}\gamma_\mu(1-\gamma_5)V_{ud}$

Figure A.2: The charged current interactions for electroweak interactions. The term V_{ud} corresponds to the CKM matrix elements that relate the up-type and down-type quarks.

Gauge Self-interaction

The electroweak Lagrangian of Equation 2.19 when expanded out to its fullest also contains some boson self interaction terms. These terms allow for the self-coupling of the W, Z and γ fields. Figure A.3 shows the Feynman diagrams associated to these terms.

Now we shall jump out of order in this summary of the terms in the Lagrangian density as it is now apparent that inserting a mass term in the fermion sector is not gauge invariant under $SU(3)_C \otimes SU(2)_L \otimes U(1)_Y$ and so, forbidden. The weak bosons are observed to be massive, again with no way to insert a mass term that respects the symmetries imposed. So, there must be a missing piece. Well, there *was* as missing piece.

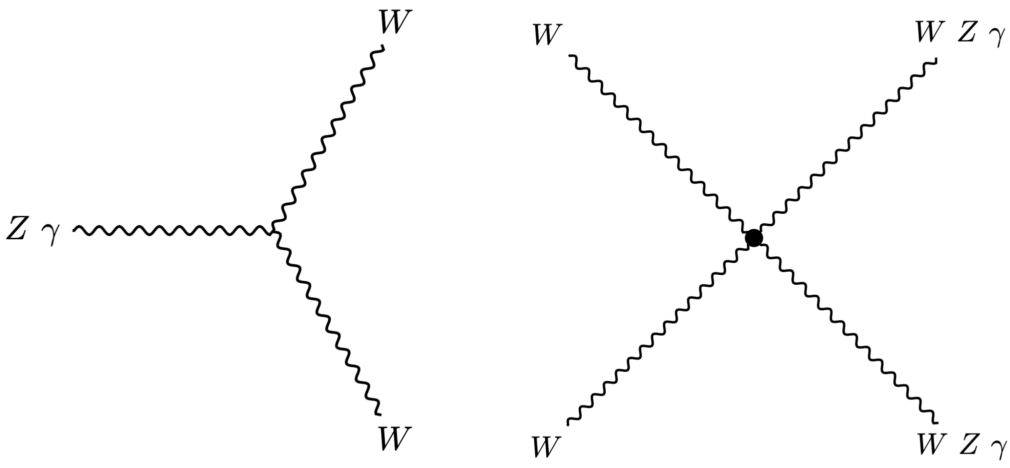

(a) (b)

Figure A.3: The self-interactions of the electroweak boson fields. Although not included in the diagram charge conservation is respected here.

A.0.2 The Higgs Mechanism and Spontaneous Symmetry Breaking

To generate the masses required by observations of the boson processes another method must be included that does not violate the gauge symmetry. One solution is to keep the Lagrangian invariant under the stated symmetries but not the vacuum state. To achieve this let us introduce a new complex scalar doublet into the $SU(2)_L \otimes U(1)_Y$ symmetry that has a non-zero vacuum expectation value. This maintains our symmetry but allows the mass terms to appear when one takes small excursions away from the vacuum, like in the presence of the gauge fields.

Spontaneous symmetry breaking shows itself when the Lagrangian is symmetric but the vacuum is not. The new complex scalar doublet is:

$$\Phi = \begin{pmatrix} \phi^+ \\ \phi^0 \end{pmatrix} = \frac{1}{\sqrt{2}} \begin{pmatrix} \phi_1 + i\phi_2 \\ \phi_3 + i\phi_4 \end{pmatrix}. \tag{A.10}$$

Where each of the fields ϕ_i are the normalised real scalar fields. Now we have a complex scalar field one can add it to the EW Lagrangian of Equation 2.19, also seen in the complete SM Lagrangian of Equation 2.9, in the form:

$$\mathcal{L}_{Higgs} = (D_\mu \Phi)^\dagger D_\mu \Phi - V(\Phi). \tag{A.11}$$

Where $V(\Phi)$ is the Higgs potential which is defined as:

$$V(\Phi) = \mu^2 \Phi^\dagger \Phi + \lambda \left(\Phi^\dagger \Phi\right)^2. \tag{A.12}$$

The complex scalar field is a $SU(2)_L$ doublet and so one can define a covariant derivative in a similar fashion to the left-handed quarks and leptons,

$$D^\mu \Phi = \left(\partial^\mu - ig\frac{\sigma_i}{2} W_i^\mu - ig'\frac{Y_W}{2} B^\mu\right)\Phi. \tag{A.13}$$

The sign of μ in Equation A.12 can be positive or negative and one must select the appropriate range. In this case forcing $\mu^2 < 0$ while also having $\lambda > 0$ means that the minimum of the potential is not at $\Phi = 0$ but instead there are an infinite degenerate set of states where

$$\Phi^\dagger \Phi = \frac{\mu^2}{2\lambda}. \tag{A.14}$$

This allows for the mechanism of spontaneous symmetry breaking, the vacuum must select one of these states and so no longer respect $SU(2)_L \otimes U(1)_Y$ symmetry which is *spontaneously broken*. Now, setting the vacuum state to be,

$$\phi^0 = \sqrt{-\frac{\mu^2}{2\lambda}}, \tag{A.15}$$

a real-valued quantity that allows us to rewrite Φ in terms of excursions around a central point. The equation

$$\Phi = \frac{1}{\sqrt{2}} \exp\left[i\frac{\sigma_i}{2}\theta_i\right] \begin{pmatrix} 0 \\ v + H(x) \end{pmatrix} \tag{A.16}$$

contains four real fields: $\theta_{1,2,3}$ and $H(x)$ and the vacuum expectation is $v = \sqrt{-\frac{\mu^2}{\lambda}}$. The three θ_i fields are in fact Goldstone bosons that are absorbed by the W and Z fields in order to give them mass, while $H(x)$ is a new massive scalar field representing the Higgs boson. Using the new formulation of Φ shown in Equation A.16 and inserting it into the kinetic term of Equation A.11 yields:

$$\begin{aligned}(D_\mu\Phi)^\dagger D_\mu\Phi = &\frac{1}{2}\partial^\mu H\partial_\mu H \\ &+ (v+H)^2\left(\frac{g^2}{4}\left(W_\mu^+\right)^\dagger W_\mu^+ + \frac{g^2}{4}\left(W_\mu^-\right)^\dagger W_\mu^- + \frac{g^2}{8\cos^2\theta_W}Z_\mu Z^\mu\right).\end{aligned} \quad (A.17)$$

So giving the masses of the W and Z bosons in the terms proportional to v^2 while the electroweak boson interactions with the Higgs field are contained in the terms proportional to vH and v^2. It is through this rotation that the B_μ and W_3^μ fields generate the Z_μ and A_μ fields as was seen previously in Equation A.1. The masses of the W and Z are now [11]:

$$m_W = \frac{vg}{2} = 80.379 \pm 0.012\,\text{GeV} \quad (A.18)$$

and

$$m_Z = \frac{vg}{2\cos\theta_W} = 91.1876 \pm 0.0021\,\text{GeV}. \quad (A.19)$$

The photon has remained massless here and due to the single generator of the $U(1)_{EM}$ symmetry remaining a symmetry of the vacuum. Taking a closer look at the Higgs potential of Equation A.12 with the new formulation one finds:

$$V(\Phi) = \frac{m_H^2}{2}H^2 + \frac{m_H^2}{2v}H^3\frac{m_H^2}{8v^2}H^4. \quad (A.20)$$

The mass of the Higgs is then [11]:

$$m_H = \sqrt{-2\mu^2} = \sqrt{2\lambda}v = 125.10 \pm 0.14\,\text{GeV}. \quad (A.21)$$

The higher order terms of H^3 and H^4 indicate that there are Higgs self-interactions that are a consequence of the spontaneous symmetry breaking mechanism.

Masses of the Fermions

Previously it was found that a mass term for the fermions of the form $\mathcal{L} = -m\bar{\psi}\psi = -m\left(\bar{\psi}_L\psi_R + \bar{\psi}_R\psi_L\right)$ is forbidden as it mixed left and right chiral components. Now there is an additional scalar doublet in the model and so a new part of the Lagrangian can be added, corresponding to the third term of Equation 2.9, with:

$$\mathcal{L}_Y = -c^d(\bar{u},\bar{d})_L\Phi d_r - c^u(\bar{u},\bar{d})_L\Phi u_r - c^e(\bar{\nu}_e,\bar{e})_L\Phi e_r + h.c.. \tag{A.22}$$

In actuality there will be a term like this for each matter generation. Once SSB takes place the Yukawa Lagrangian simplifies to,

$$\mathcal{L}_Y = -\frac{1}{\sqrt{2}}(v+H)\sum_i(c_i^d\bar{d}_i d_i + c_i^u\bar{u}_i u_i + c_i^e\bar{e}_i e_i) \tag{A.23}$$

where the sum is over the three generations. The masses of the fermions are given in the terms that are proportional to the vacuum expectation value

$$m_{d_i} = c_i^d\frac{v}{\sqrt{2}}, \quad m_{u_i} = c_i^u\frac{v}{\sqrt{2}}, \quad m_{e_i} = c_i^e\frac{v}{\sqrt{2}}. \tag{A.24}$$

The c parameters are unknown theoretically and so they are arbitrary and are measured from experiment.

This ingenious and elegant solution was proposed by R. Brout, F. Englert, P. Higgs, G. Guralnik, C. Hagen and T. Kibble [167–169], and the boson in question was discovered at the LHC in 2012 [5][6].

A.0.3 Quantum Chromodynamics

Quantum Chromodynamics (QCD) is the theory of how quarks and gluons interact. Quarks are the fermionic component of this theory and come in three generations, each progressively more massive than the previous. They do share certain attributes with each generation containing an "up type" quark with a fractional electric charge of $+2/3e$ and a "down type" with fractional electric charge of $-1/2e$. These particles interact not only via electromagnetic interactions but also the strong force. The strong interaction is mediated by gluons, eight massless electronically neutral bosons. The gluons come from the eight generators of the $SU(3)_C$ symmetry and can be seen in the structure of the field strength tensor $\mathbb{G}^a_{\mu\nu}$. Importantly there exists a colour charge which each of these particles carries and as this is a non-abelian gauge theory, or a Yang-Mills theory, the gluons can self interact.

The Lagrangian for QCD can be summarise succinctly as:

$$\mathcal{L}_{QCD} = -\frac{1}{4}\mathbb{G}^{\mu\nu}_a \mathbb{G}^a_{\mu\nu} + \sum_j i\bar{\psi}_j \left(i\not{\partial} - m_j - \frac{1}{2} i g_s \lambda^a \not{G}^a \right) \psi_j, \tag{A.25}$$

where the gauge invariant strong field strength tensor, $\mathbb{G}^a_{\mu\nu}$, was defined previously in Equation 2.13 and the transformation of the tensor addressed in Table 2.2. The three elements of the ψ vector are the three colour charges and the index, j, runs over the six mass eigenstates of the quarks. The matrices, λ^a are the Gell-Mann matrices, defined as:

$$\begin{gathered}
\lambda_1 = \begin{pmatrix} 0 & 1 & 0 \\ 1 & 0 & 0 \\ 0 & 0 & 0 \end{pmatrix}, \quad \lambda_2 = \begin{pmatrix} 0 & -i & 0 \\ i & 0 & 0 \\ 0 & 0 & 0 \end{pmatrix}, \quad \lambda_3 = \begin{pmatrix} 1 & 0 & 0 \\ 0 & -1 & 0 \\ 0 & 0 & 0 \end{pmatrix}, \\
\lambda_4 = \begin{pmatrix} 0 & 0 & 1 \\ 0 & 0 & 0 \\ 1 & 0 & 0 \end{pmatrix}, \quad \lambda_5 = \begin{pmatrix} 0 & 0 & -i \\ 0 & 0 & 0 \\ i & 0 & 0 \end{pmatrix}, \quad \lambda_6 = \begin{pmatrix} 0 & 0 & 0 \\ 0 & 0 & 1 \\ 0 & 1 & 0 \end{pmatrix}, \\
\lambda_7 = \begin{pmatrix} 0 & 0 & 0 \\ 0 & 0 & -i \\ 0 & i & 0 \end{pmatrix} \quad \text{and} \quad \lambda_8 = \frac{1}{\sqrt{3}} \begin{pmatrix} 1 & 0 & 0 \\ 0 & 1 & 0 \\ 0 & 0 & -2 \end{pmatrix}.
\end{gathered} \tag{A.26}$$

The interaction vertices that result from this component of the SM are demonstrated in Figure A.4.

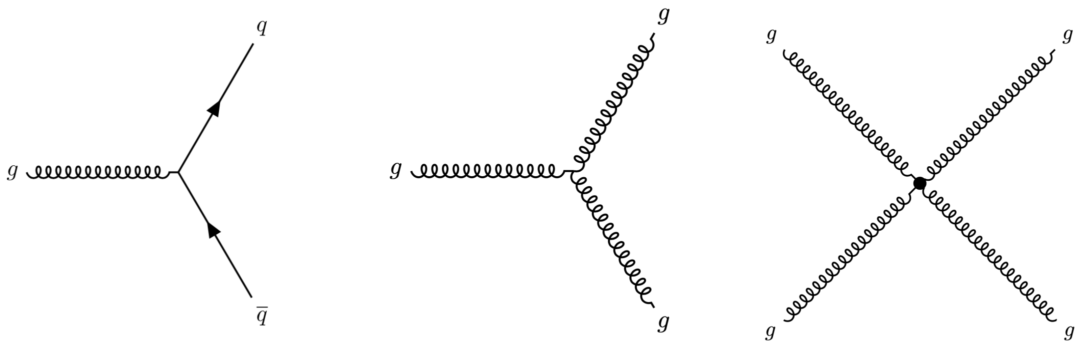

(a) $\propto g_s \frac{\lambda^a}{2}\gamma_\mu$ (b) $\propto g_s f^{abc}$ (c) $\propto g_s^2 f^{abc} f^{ade}$

Figure A.4: The interaction vertices generated by QCD theory.

The self-interaction of the gluons has some important consequences. Considering the running of the strong coupling one sees that it is decreasing with the momentum scale, which is the opposite of the electromagnetic coupling. This simple fact produces two important features of the strong interaction, namely; *colour confinement* and *asymptotic freedom*.

At low momentum the strong coupling is $\alpha_s = \frac{g_s^2}{4\pi}$, which approaches one. This means that perturbation theory no longer applies and the quarks are bound together forming colourless states called hadrons as discussed briefly in Section 2.2. This is the phenomenon of colour confinement. At the opposite end of the spectrum, at high momentum scales, the strong coupling reduces and then quarks and gluons can become asymptotically free. These behaviours and their consequences for the formation of detectable objects known as *jets* are discussed in more detail in Chapter 6.

A.0.4 Renormalisation

When actually calculating the matrix element for a process a problem arises; all possible diagrams that have the same in and out-going lines also contribute to the calculation. This allows for an infinite amount of loops to appear in a given matrix element calculation and this gives rise to an infinite sum that cannot be calculated. These loops represent a cloud of virtual particles that interact with the "bare" particle and these form divergences.

This is effectively the same as integrating up to very high momentum scales that are not currently accessible to modern colliders, at those scales new physics contributions will become important and the current version of the SM is not expected to be predictive. There are a few techniques to avoid this: firstly perturbation theory only considers up to a limited to some order of vertex factor (where the contributions of those diagrams are much less than one), the second method imposes some scale, Λ, to cut off the integral and this is known as *renormalisation*.

With the cut off scale the calculation may be separated out into divergent and finite components, the divergent components are removed by placing an opposite and counter term in the Lagrangian but now the finite term depends on the momentum of the interaction. To get around this problem the theoretical quantities are replaced with those measured in experiments, renormalised values.

The emission of a massless particle with very low momentum compared to the parent also causes divergences as the amplitude for this process increases as the momentum of the daughter, relative to the parent, approaches zero. Again applying the renormalisation technique and inserting the counter terms to the divergent members of the series one will again see that the finite components depend on the momentum scale, this low energy version is called *factorisation*. The scales for factorisation and renormalisation must be chosen carefully and typically these range from $Q/2$ to $2Q$ respectively. The differences in the calculations at each of these scales compared to the nominal value of Q can then be taken as a systematic uncertainty.

B
Physics Object Definitions

Electrons

Electrons are reconstructed using topo-clusters, these clusters are formed from sets of calorimeter cells containing an energy deposit above a noise threshold which is a similar method to that used in jet building. The topo-clusters are then matched to tracks reconstructed while considering the effects of bremsstrahlung radiation in the tracker [83].

The electrons are then calibrated using regression boosted decision trees (BDT) trained to correct the energies of the uncalibrated electron candidates. Using particles that have propagated through full detector simulation a true energy value can be obtained and the multivariate approach is able to derive a correction factor that is applied to the raw detector energy to obtain the calibrated value [83].

There are two quality classifications of an identified electron, the first stage is to define a “baseline” electron. These must have $p_{\mathrm{T}} > 10\,\mathrm{GeV}$, $|\eta_{\mathrm{clus}}| < 2.47$ to remove electrons from the crack region between the barrel and end-cap calorimeter, satisfy the “LooseAndBLayerLLH” quality selections [95] and an impact parameter restriction of $|z_0 \sin\theta| < 0.5\,\mathrm{mm}$. These baseline electrons are promoted to signal quality if they satisfy $d_0/\sigma(d_0) < 5$ and the higher transverse momentum cut of $p_{\mathrm{T}} > 20\,\mathrm{GeV}$. The signal electrons must also be isolated according to the "GradientLoose" working point and pass the "TightLLH" quality criteria [96].

Muons

Muons are found by combining hits in the muon spectrometer's (MS) various subsystems where coordinates can be measured in, and orthogonal to, the bending plane of the detectors magnetic field. These hits are combined to form segments in each of the MS layers that may then be gathered into track candidates and after a χ^2 fit these candidates are accepted if the requisite selections are met. Independently of the MS reconstruction the tracks in the inner detector (ID) are processed and in most cases a combined fit is achieved by extrapolating the MS track inwards and associated with an ID track [84].

Baseline muons are found to have $p_{\mathrm{T}} > 10\,\mathrm{GeV}$, $|\eta| < 2.7$ and $|z_0 \sin\theta| < 0.5\,\mathrm{mm}$. The baseline muon candidates must also have passed the overlap removal procedure and pass the "Medium" quality criteria. Extending these criteria signal quality muons must also satisfy the conditions of "GradientLoose" isolation [84] and a cut on the transverse impact parameter significance of $d_0/\sigma(d_0) < 3$.

Taus

Tau leptons are considered in two separate categories; hadronically and leptonically decaying. In both cases no selection procedure is applied so that in the hadronic case these tau particles are not distinguished from jets and for leptonic decays, if the daughter particle is reconstructed as a signal muon or electron, these events are removed from consideration by the lepton veto of the analysis. However, the τ-leptons can contribute to the unwanted background of the analysis and this is discussed in section 5.6.

Photons

Reconstruction of photons follows a similar procedure to that of the electrons. The topo-clusters are seeded in the same manner [83] but after this the inclusion of tracking information is the main difference. There are two main photon reconstruction types; a photon will be reconstructed as being converted and the resulting particles will leave tracks in the ID modules that can be subdivided into single or double-track conversions or the photon will remain unconverted and appear only as an EM calorimeter deposit [82].

Calibration of the photons and electrons is done in the same manner [97]. "Tight" identification settings in conjunction with $p_{\mathrm{T}} > 10\,\mathrm{GeV}$ and $|\eta_{\mathrm{clus}}| < 2.37$ give baseline photons and the "FixedCutTight" isolation criteria are added to form the signal photons.

B.1 Overlap Removal Procedure

To prevent double counting of energy deposits in the calorimeter or using objects reconstructed that did not originate from the hard scatter (HS) but instead were the result of some secondary physics process like the production of a Bremsstrahlung photon, an overlap removal procedure is employed. Objects are considered in relation to one another and removed when these conditions are met in the following order:

1. When an electron and muon share an ID track, remove the electron. If the muon is a calo-muon and shares a track with an electron then remove the muon.
2. Photons within $\Delta R < 0.4$ of an electron or muon are removed.
3. Remove any jet that is within $\Delta R < 0.2$ of an electron.
4. Remove any electron that is within $0.2 < \Delta R < 0.4$ of a jet.
5. If a muon track is associated with a jet or the muon is within $\Delta R < 0.2$ of a jet then remove the jet if the number of tracks n_{track} in it is less than 3 and if the jet p_{T} is consistent with muon final state radiation or energy loss.
6. Remove any muon that is within $0.2 < \Delta R < 0.4$ of a jet.

7. If a jet is within $\Delta R < 0.4$ of a photon, remove the jet.

As well as this overlap removal procedure to ensure that energy deposits are not associated with more than one object a bug in the PFlow algorithm was discovered meaning that the ID tracks from muons were not correctly removed and so the these muons could be reconstructed as jets (except the highest p_{T} muon). The overlap procedure described above removes the vast majority of these fake jets initiated by muons.

References

[1] Aaron Paul O'Neill. "Missing Transverse Momentum Significance For Full Run 2 using 13 TeV pp data". In: (Feb. 2019). URL: `https://cds.cern.ch/record/2660341`.

[2] The ATLAS Collaboration. "Search for new phenomena in final states with large jet multiplicities and missing transverse momentum using $\sqrt{s} = 13$ TeV proton-proton collisions recorded by ATLAS in Run 2 of the LHC". In: *Journal of High Energy Physics* 2020.10 (Oct. 2020). URL: `http://dx.doi.org/10.1007/JHEP10(2020)062`.

[3] Aaron Paul O'Neill. "When jets MET SUSY: ATLAS Searches for Squarks and Gluinos". In: (Aug. 2020). URL: `https://cds.cern.ch/record/2727570`.

[4] Aaron Paul O'Neill. "When jets MET SUSY: ATLAS searches for squarks and gluinos". In: *PoS* ICHEP2020 (2021), p. 269.

[5] The ATLAS Collaboration. "Observation of a new particle in the search for the Standard Model Higgs boson with the ATLAS detector at the LHC". In: *Physics Letters B* 716.1 (Sept. 2012), pp. 1–29. URL: `http://dx.doi.org/10.1016/j.physletb.2012.08.020`.

[6] The CMS Collaboration. "Observation of a new boson at a mass of 125 GeV with the CMS experiment at the LHC". In: *Physics Letters B* 716.1 (Sept. 2012), pp. 30–61. URL: `http://dx.doi.org/10.1016/j.physletb.2012.08.021`.

[7] Jeanneret Guillaume. "WANDERING THE IMMEASURABLE. PÉRÉGRINATIONS À L'INFINI". In: (Oct. 2014). General Photo. URL: `https://cds.cern.ch/record/1957174`.

[8] Antonio Pich. "The Standard Model of Electroweak Interactions; rev. version". In: (Feb. 2005), 48 p. URL: `http://cds.cern.ch/record/819632`.

[9] Martijn Mulders and Giulia Zanderighi, eds. *Proceedings, 2016 European School of High-Energy Physics (ESHEP2016): Skeikampen, Norway, June 15-28 2016.* Vol. 5. CERN Yellow Reports: School Proceedings. Geneva: CERN, 2017. arXiv: `1805.00935 [hep-ph]`.

[10] Heather E. Logan. *TASI 2013 lectures on Higgs physics within and beyond the Standard Model.* 2017. arXiv: `1406.1786 [hep-ph]`.

[11] P.A. Zyla et al. "Review of Particle Physics". In: *PTEP* 2020.8 (2020), p. 083C01.

[12] M. Robinson et al. *A Simple Introduction to Particle Physics.* 2008. arXiv: `0810.3328 [hep-th]`.

[13] Matthew Dean Schwartz. *Quantum field theory and the standard model [electronic resource].* eng. Cambridge, 2014.

[14] Julia Woithe, Gerfried J Wiener, and Frederik F Van der Veken. “Let’s have a coffee with the Standard Model of particle physics!” In: *Physics Education* 52.3 (Mar. 2017), p. 034001. URL: `https://doi.org/10.1088/1361-6552/aa5b25`.

[15] Richard P Feynman and Albert R Hibbs. *Quantum mechanics and path integrals*. eng. International series in pure and applied physics. New York: McGraw-Hill, 1965.

[16] John Campbell et al. *The Black Book of Quantum Chromodynamics: A Primer for the LHC Era*. eng. Oxford University Press, 2017.

[17] C. P Burgess and Guy David Moore. *The standard model : a primer [electronic resource]*. eng. Cambridge core. Cambridge, 2007.

[18] W. N. Cottingham and D. A. Greenwood. *An Introduction to the Standard Model of Particle Physics*. 2nd ed. Cambridge University Press, 2007.

[19] Stephen P. Martin. “A SUPERSYMMETRY PRIMER”. In: *Advanced Series on Directions in High Energy Physics* (July 1998), pp. 1–98. URL: `http://dx.doi.org/10.1142/9789812839657_0001`.

[20] Ian Aitchison. “Supersymmetry and the MSSM: An Elementary Introduction”. In: (June 2005).

[21] Sudhir K. Vempati. *Introduction to MSSM*. 2012. arXiv: `1201.0334 [hep-ph]`.

[22] Andrew Purcell. “Go on a particle quest at the first CERN webfest. Le premier webfest du CERN se lance à la conquête des particules”. In: (Aug. 2012), p. 10. URL: `https://cds.cern.ch/record/1473657`.

[23] S.-K. Choi et al. “Observation of a Resonancelike Structure in the $\pi^{\pm}\Psi'$Mass Distribution in Exclusive $B \to K\pi^{\pm}\Psi'$ Decays”. In: *Physical Review Letters* 100.14 (Apr. 2008). URL: `http://dx.doi.org/10.1103/PhysRevLett.100.142001`.

[24] The LHCb Collaboration. “Observation of $J/\psi p$ Resonances Consistent with Pentaquark States in $\Lambda_b^0 \to J/\psi K^- p$ Decays”. In: *Physical Review Letters* 115.7 (Aug. 2015). URL: `http://dx.doi.org/10.1103/PhysRevLett.115.072001`.

[25] E. Noether. “Invariante Variationsprobleme”. ger. In: *Nachrichten von der Gesellschaft der Wissenschaften zu Göttingen, Mathematisch-Physikalische Klasse* 1918 (1918), pp. 235–257. URL: `http://eudml.org/doc/59024`.

[26] Emmy Noether. “Invariant variation problems”. In: *Transport Theory and Statistical Physics* 1.3 (Jan. 1971), pp. 186–207. URL: `http://dx.doi.org/10.1080/00411457108231446`.

[27] *Standard Model Summary Plots March 2021*. Tech. rep. All figures including auxiliary figures are available at https://atlas.web.cern.ch/Atlas/GROUPS/PHYSICS/PUBNOTES/ATL-PHYS-PUB-2021-005. Geneva: CERN, Mar. 2021. URL: `http://cds.cern.ch/record/2758261`.

[28] E. Corbelli and P. Salucci. “The extended rotation curve and the dark matter halo of M33”. In: *Monthly Notices of the Royal Astronomical Society* 311.2 (Jan. 2000), pp. 441–447. URL: `http://dx.doi.org/10.1046/j.1365-8711.2000.03075.x`.

[29] A. Bosma. “The distribution and kinematics of neutral hydrogen in spiral galaxies of various morphological types”. PhD thesis. -, Jan. 1978.

[30] Stephen P. Martin and David G. Robertson. "Standard model parameters in the tadpole-free pure $\overline{\text{MS}}$ scheme". In: *Phys. Rev. D* 100.7 (2019), p. 073004. arXiv: `1907.02500 [hep-ph]`.

[31] The SNO Collaboration. "Measurement of the Rate of $\nu_e + d \to p + p + e^-$ Interactions Produced by B8 Solar Neutrinos at the Sudbury Neutrino Observatory". In: *Physical Review Letters* 87.7 (July 2001). URL: `http://dx.doi.org/10.1103/PhysRevLett.87.071301`.

[32] Stefano Dell'Oro et al. "Neutrinoless Double Beta Decay: 2015 Review". In: *Advances in High Energy Physics* 2016 (2016), pp. 1–37. URL: `http://dx.doi.org/10.1155/2016/2162659`.

[33] Andrei D Sakharov. "Violation ofCPin variance,Casymmetry, and baryon asymmetry of the universe". In: *Soviet Physics Uspekhi* 34.5 (May 1991), pp. 392–393. URL: `https://doi.org/10.1070/pu1991v034n05abeh002497`.

[34] R.D. Peccei and Helen Quinn. "CP Conservation in the Presence of Pseudoparticles". In: *Physical Review Letters - PHYS REV LETT* 38 (June 1977), pp. 1440–1443.

[35] Howard Georgi and S. L. Glashow. "Unity of All Elementary-Particle Forces". In: *Phys. Rev. Lett.* 32 (8 Feb. 1974), pp. 438–441. URL: `https://link.aps.org/doi/10.1103/PhysRevLett.32.438`.

[36] The LHCb Collaboration. "Test of Lepton Universality Using $B^+ \to K^+\ell^+\ell^-$ Decays". In: *Physical Review Letters* 113.15 (Oct. 2014). URL: `http://dx.doi.org/10.1103/PhysRevLett.113.151601`.

[37] The LHCb Collaboration. "Test of lepton flavor universality by the measurement of the $B^0 \to D^{*-}\tau^+\nu_{tau}$ branching fraction using three-prong τ decays". In: *Physical Review D* 97.7 (Apr. 2018). URL: `http://dx.doi.org/10.1103/PhysRevD.97.072013`.

[38] $g - 2$ Collaboration. "Measurement of the Positive Muon Anomalous Magnetic Moment to 0.46 ppm". In: *Phys. Rev. Lett.* 126 (14 Apr. 2021), p. 141801. URL: `https://link.aps.org/doi/10.1103/PhysRevLett.126.141801`.

[39] J. Wess and B. Zumino. "Supergauge Invariant Extension of Quantum Electrodynamics". In: *Nucl. Phys. B* 78 (1974), p. 1.

[40] A. Salam and J. Strathdee. "Super-symmetry and non-Abelian gauges". In: *Physics Letters B* 51.4 (1974), pp. 353–355. URL: `http://www.sciencedirect.com/science/article/pii/0370269374902263`.

[41] S. Ferrara and B. Zumino. "Supergauge Invariant Yang-Mills Theories". In: *Nucl. Phys. B* 79 (1974), p. 413.

[42] P. Fayet. "Supersymmetry and weak, electromagnetic and strong interactions". In: *Physics Letters B* 64.2 (1976), pp. 159–162. URL: `https://www.sciencedirect.com/science/article/pii/0370269376903191`.

[43] Pierre Fayet. "Spontaneously Broken Supersymmetric Theories of Weak, Electromagnetic and Strong Interactions". In: *Phys. Lett. B* 69 (1977), p. 489.

[44] A. Djouadi et al. "The Minimal supersymmetric standard model: Group summary report". In: *GDR (Groupement De Recherche) - Supersymetrie*. Dec. 1998. arXiv: `hep-ph/9901246`.

[45] Glennys R. Farrar and Pierre Fayet. "Phenomenology of the production, decay, and detection of new hadronic states associated with supersymmetry". In: *Physics Letters B* 76.5 (1978), pp. 575–579. URL: http://www.sciencedirect.com/science/article/pii/0370269378908584.

[46] Borut Bajc et al. "Threshold corrections to dimension-six proton decay operators in non-minimal SUSY SU (5) GUTs". In: *Nuclear Physics B* 910 (Sept. 2016), pp. 1–22. URL: http://dx.doi.org/10.1016/j.nuclphysb.2016.06.017.

[47] Gerard Jungman, Marc Kamionkowski, and Kim Griest. "Supersymmetric dark matter". In: *Physics Reports* 267.5-6 (Mar. 1996), pp. 195–373. URL: http://dx.doi.org/10.1016/0370-1573(95)00058-5.

[48] Herbi Dreiner. "An introduction to explicit R-parity violation". In: *Pramana* 51.1 (1998), pp. 123–133. URL: https://doi.org/10.1007/BF02827485.

[49] Carola F Berger et al. "Supersymmetry without prejudice". In: *Journal of High Energy Physics* 2009.02 (Feb. 2009), pp. 023–023. URL: http://dx.doi.org/10.1088/1126-6708/2009/02/023.

[50] the ATLAS Collaboration. "Summary of the ATLAS experiment's sensitivity to supersymmetry after LHC Run 1 — interpreted in the phenomenological MSSM". In: *Journal of High Energy Physics* 2015.10 (Oct. 2015). URL: http://dx.doi.org/10.1007/JHEP10(2015)134.

[51] Christoph Borschensky et al. "Squark and gluino production cross sections in pp collisions at $\sqrt{s} = 13, 14, 33$ and 100 TeV". In: *The European Physical Journal C* 74.12 (Dec. 2014). URL: http://dx.doi.org/10.1140/epjc/s10052-014-3174-y.

[52] Jonathan L. Feng. "Naturalness and the Status of Supersymmetry". In: *Annual Review of Nuclear and Particle Science* 63.1 (Oct. 2013), pp. 351–382. URL: http://dx.doi.org/10.1146/annurev-nucl-102010-130447.

[53] Lyndon Evans and Philip Bryant. "LHC Machine". In: *Journal of Instrumentation* 3.08 (Aug. 2008), S08001–S08001. URL: http://dx.doi.org/10.1088/1748-0221/3/08/S08001.

[54] Maximilien Brice. "Aerial View of the CERN taken in 2008." July 2008. URL: https://cds.cern.ch/record/1295244.

[55] The ATLAS Collaboration. "The ATLAS Experiment at the CERN Large Hadron Collider". In: *Journal of Instrumentation* 3.08 (Aug. 2008), S08003–S08003. URL: http://dx.doi.org/10.1088/1748-0221/3/08/S08003.

[56] The CMS Collaboration. "The CMS Experiment at the CERN LHC". In: *JINST* 3 (2008), S08004.

[57] The ALICE Collaboration. "The ALICE experiment at the CERN LHC". In: *JINST* 3 (2008), S08002.

[58] The LHCb Collaboration. "The LHCb Detector at the LHC". In: *JINST* 3 (2008), S08005.

[59] Esma Mobs. "The CERN accelerator complex - 2019. Complexe des accélérateurs du CERN - 2019". In: (July 2019). General Photo. URL: https://cds.cern.ch/record/2684277.

[60] Werner Herr and B Muratori. “Concept of luminosity”. In: (2006). URL: https://cds.cern.ch/record/941318.

[61] G Apollinari et al. *High-Luminosity Large Hadron Collider (HL-LHC): Preliminary Design Report*. CERN Yellow Reports: Monographs. Geneva: CERN, 2015. URL: https://cds.cern.ch/record/2116337.

[62] *Luminosity determination in pp collisions at $\sqrt{s} = 13$ TeV using the ATLAS detector at the LHC*. Tech. rep. Geneva: CERN, June 2019. URL: https://cds.cern.ch/record/2677054.

[63] The ATLAS Collaboration. “Luminosity Public Results Run 2”. In: (Apr. 2021). URL: https://twiki.cern.ch/twiki/bin/view/AtlasPublic/LuminosityPublicResultsRun2#Pileup_Interactions_and_Data_Tak.

[64] The ATLAS Collaboration. “Luminosity Public Results Run 1”. In: (Mar. 2020). URL: https://twiki.cern.ch/twiki/bin/view/AtlasPublic/LuminosityPublicResults.

[65] M Capeans et al. *ATLAS Insertable B-Layer Technical Design Report*. Tech. rep. Sept. 2010. URL: https://cds.cern.ch/record/1291633.

[66] Alessandro La Rosa. “The ATLAS Insertable B-Layer: from construction to operation”. In: *JINST* 11.12 (2016). Ed. by Claudia Gemme and Leonardo Rossi, p. C12036. arXiv: 1610.01994 [physics.ins-det].

[67] A Vogel. *ATLAS Transition Radiation Tracker (TRT): Straw Tube Gaseous Detectors at High Rates*. Tech. rep. Geneva: CERN, Apr. 2013. URL: https://cds.cern.ch/record/1537991.

[68] Nikiforos Nikiforou. *Performance of the ATLAS Liquid Argon Calorimeter after three years of LHC operation and plans for a future upgrade*. 2013. arXiv: 1306.6756 [physics.ins-det].

[69] *ATLAS liquid-argon calorimeter: Technical Design Report*. Technical design report. ATLAS. Geneva: CERN, 1996. URL: https://cds.cern.ch/record/331061.

[70] The ATLAS Collaboration. “Jet reconstruction and performance using particle flow with the ATLAS Detector”. In: *The European Physical Journal C* 77.7 (July 2017). URL: http://dx.doi.org/10.1140/epjc/s10052-017-5031-2.

[71] *ATLAS tile calorimeter: Technical Design Report*. Technical design report. ATLAS. Geneva: CERN, 1996. URL: https://cds.cern.ch/record/331062.

[72] *Performance of the muon spectrometer alignment in 2017 and 2018 data*. Tech. rep. All figures including auxiliary figures are available at https://atlas.web.cern.ch/Atlas/GROUPS/PHYSICS/PUBNOTES/ATL-MUON-PUB-2021-002. Geneva: CERN, Mar. 2021. URL: https://cds.cern.ch/record/2753329.

[73] The ATLAS Collaboration. “Standalone Vertex Finding in the ATLAS Muon Spectrometer. ” In: *JINST* 9 (Nov. 2013), P02001. 22 p. arXiv: 1311.7070. URL: https://cds.cern.ch/record/1631701.

[74] ATLAS Collaboration. “ATLAS Experiment Briefing: aligning the ATLAS muon spectrometer”. General Photo. Mar. 2021. URL: https://cds.cern.ch/record/2753549.

[75] The ATLAS Collaboration. “Performance of the ATLAS trigger system in 2015”. In: *The European Physical Journal C* 77.5 (May 2017). URL: http://dx.doi.org/10.1140/epjc/s10052-017-4852-3.

[76] Joao Pequenao and Paul Schaffner. “How ATLAS detects particles: diagram of particle paths in the detector”. Jan. 2013. URL: https://cds.cern.ch/record/1505342.

[77] *Performance of the reconstruction of large impact parameter tracks in the ATLAS inner detector*. Tech. rep. All figures including auxiliary figures are available at https://atlas.web.cern.ch/Atlas/GROUPS/PHYSICS/PUBNOTES/ATL-PHYS-PUB-2017-014. Geneva: CERN, July 2017. URL: https://cds.cern.ch/record/2275635.

[78] *Performance of the ATLAS Silicon Pattern Recognition Algorithm in Data and Simulation at $\sqrt{s} = 7$ TeV*. Tech. rep. All figures including auxiliary figures are available at https://atlas.web.cern.ch/Atlas/GROUPS/PHYSICS/CONFNOTES/ATLAS-CONF-2010-072. Geneva: CERN, July 2010. URL: https://cds.cern.ch/record/1281363.

[79] *Performance of primary vertex reconstruction in proton-proton collisions at $\sqrt{s}$ =7 TeV in the ATLAS experiment*. Tech. rep. All figures including auxiliary figures are available at https://atlas.web.cern.ch/Atlas/GROUPS/PHYSICS/CONFNOTES/ATLAS-CONF-2010-069. Geneva: CERN, July 2010. URL: https://cds.cern.ch/record/1281344.

[80] The ATLAS Collaboration. “Topological cell clustering in the ATLAS calorimeters and its performance in LHC Run 1”. In: *The European Physical Journal C* 77.7 (July 2017). URL: http://dx.doi.org/10.1140/epjc/s10052-017-5004-5.

[81] The ATLAS Colaboration. “Electron and photon performance measurements with the ATLAS detector using the 2015–2017 LHC proton-proton collision data”. In: *Journal of Instrumentation* 14.12 (Dec. 2019). URL: http://dx.doi.org/10.1088/1748-0221/14/12/P12006.

[82] The ATLAS Collaboration. “Measurement of the photon identification efficiencies with the ATLAS detector using LHC Run-1 data”. In: *The European Physical Journal C* 76.12 (Dec. 2016). URL: http://dx.doi.org/10.1140/epjc/s10052-016-4507-9.

[83] The ATLAS Collaboration. *Electron and photon reconstruction and performance in ATLAS using a dynamical, topological cell clustering-based approach*. Tech. rep. ATL-PHYS-PUB-2017-022. Geneva: CERN, Dec. 2017. URL: https://cds.cern.ch/record/2298955.

[84] The ATLAS Collaboration. “Muon reconstruction performance of the ATLAS detector in proton–proton collision data at $\sqrt{s} = 13$ TeV”. In: *The European Physical Journal C* 76.5 (May 2016). URL: http://dx.doi.org/10.1140/epjc/s10052-016-4120-y.

[85] Matteo Cacciari, Gavin P Salam, and Gregory Soyez. “The anti-k_t jet clustering algorithm”. In: *Journal of High Energy Physics* 2008.04 (Apr. 2008), pp. 063–063. URL: http://dx.doi.org/10.1088/1126-6708/2008/04/063.

[86] The ATLAS Collaboration. "Jet energy scale measurements and their systematic uncertainties in proton-proton collisions at $\sqrt{s} = 13$ TeV with the ATLAS detector". In: *Physical Review D* 96.7 (Oct. 2017). URL: http://dx.doi.org/10.1103/PhysRevD.96.072002.

[87] *Tagging and suppression of pileup jets with the ATLAS detector*. Tech. rep. All figures including auxiliary figures are available at https://atlas.web.cern.ch/Atlas/GROUPS/PHYSICS/CONFNOTES/ATLAS-CONF-2014-018. Geneva: CERN, May 2014. URL: https://cds.cern.ch/record/1700870.

[88] The ATLAS Collaboration. "Identification and rejection of pile-up jets at high pseudorapidity with the ATLAS detector". In: *The European Physical Journal C* 77.9 (Sept. 2017). URL: http://dx.doi.org/10.1140/epjc/s10052-017-5081-5.

[89] The ATLAS Collaboration. *Optimisation of the ATLAS b-tagging performance for the 2016 LHC Run*. Tech. rep. ATL-PHYS-PUB-2016-012. Geneva: CERN, June 2016. URL: https://cds.cern.ch/record/2160731.

[90] The ATLAS Collaboration. *Selection of jets produced in 13TeV proton-proton collisions with the ATLAS detector*. Tech. rep. ATLAS-CONF-2015-029. Geneva: CERN, July 2015. URL: https://cds.cern.ch/record/2037702.

[91] The ATLAS Collaboration. "What happens when energy goes missing". In: (Nov. 2016). URL: https://atlas.cern/updates/blog/what-happens-when-energy-goes-missing.

[92] The ATLAS Collaboration. "Performance of missing transverse momentum reconstruction in proton-proton collisions at $\sqrt{s} = 7$ TeV with ATLAS". In: *The European Physical Journal C* 72.1 (Jan. 2012). URL: http://dx.doi.org/10.1140/epjc/s10052-011-1844-6.

[93] The ATLAS Collaboration. "Performance of algorithms that reconstruct missing transverse momentum in $\sqrt{s} = 8$ TeV proton–proton collisions in the ATLAS detector". In: *The European Physical Journal C* 77.4 (Apr. 2017). URL: http://dx.doi.org/10.1140/epjc/s10052-017-4780-2.

[94] The ATLAS Collaboration. "Performance of missing transverse momentum reconstruction with the ATLAS detector using proton–proton collisions at $\sqrt{s} = 13$TeV". In: *The European Physical Journal C* 78.11 (Nov. 2018). URL: http://dx.doi.org/10.1140/epjc/s10052-018-6288-9.

[95] The ATLAS Collaboration. "Electron reconstruction and identification in the ATLAS experiment using the 2015 and 2016 LHC proton–proton collision data at $\sqrt{s} = 13$ TeV." In: *The European Physical Journal C* 79.8 (Aug. 2019). URL: http://dx.doi.org/10.1140/epjc/s10052-019-7140-6.

[96] The ATLAS Collaboration. "Electron efficiency measurements with the ATLAS detector using 2012 LHC proton–proton collision data". In: *The European Physical Journal C* 77.3 (Mar. 2017). URL: http://dx.doi.org/10.1140/epjc/s10052-017-4756-2.

[97] The ATLAS Collaboration. “Electron and photon energy calibration with the ATLAS detector using LHC Run 1 data”. In: *The European Physical Journal C* 74.10 (Oct. 2014). URL: http://dx.doi.org/10.1140/epjc/s10052-014-3071-4.

[98] *Measurement of the tau lepton reconstruction and identification performance in the ATLAS experiment using pp collisions at* $\sqrt{\mathrm{s}} = 13\,\mathrm{TeV}$. Tech. rep. ATLAS-CONF-2017-029. Geneva: CERN, May 2017. URL: https://cds.cern.ch/record/2261772.

[99] G. Avoni et al. “The new LUCID-2 detector for luminosity measurement and monitoring in ATLAS”. In: *JINST* 13.07 (2018), P07017.

[100] C. Oleari. “The POWHEG BOX”. In: *Nuclear Physics B - Proceedings Supplements* 205-206 (Aug. 2010), pp. 36–41. URL: http://dx.doi.org/10.1016/j.nuclphysbps.2010.08.016.

[101] Torbjörn Sjöstrand et al. “An introduction to PYTHIA 8.2”. In: *Computer Physics Communications* 191 (June 2015), pp. 159–177. URL: http://dx.doi.org/10.1016/j.cpc.2015.01.024.

[102] G. Aad et al. “Measurement of the $Z/\gamma*$ boson transverse momentum distribution in pp collisions at $\sqrt{s} = 7$ TeV with the ATLAS detector”. In: *Journal of High Energy Physics* 2014.9 (Sept. 2014). URL: http://dx.doi.org/10.1007/JHEP09(2014)145.

[103] Jonathan Pumplin et al. “New Generation of Parton Distributions with Uncertainties from Global QCD Analysis”. In: *Journal of High Energy Physics* 2002.07 (July 2002), pp. 012–012. URL: http://dx.doi.org/10.1088/1126-6708/2002/07/012.

[104] T Gleisberg et al. “Event generation with SHERPA 1.1”. In: *Journal of High Energy Physics* 2009.02 (Feb. 2009), pp. 007–007. URL: http://dx.doi.org/10.1088/1126-6708/2009/02/007.

[105] Richard D. Ball et al. “Parton distributions for the LHC run II”. In: *Journal of High Energy Physics* 2015.4 (Apr. 2015). URL: http://dx.doi.org/10.1007/JHEP04(2015)040.

[106] *ATLAS Pythia 8 tunes to 7 TeV data.* Tech. rep. ATL-PHYS-PUB-2014-021. Geneva: CERN, Nov. 2014. URL: https://cds.cern.ch/record/1966419.

[107] The ATLAS Collaboration. “The ATLAS Simulation Infrastructure”. In: *The European Physical Journal C* 70.3 (Sept. 2010), pp. 823–874. URL: http://dx.doi.org/10.1140/epjc/s10052-010-1429-9.

[108] S. Agostinelli et al. “Geant4 - a simulation toolkit”. In: *Nuclear Instruments and Methods in Physics Research Section A: Accelerators, Spectrometers, Detectors and Associated Equipment* 506.3 (2003), pp. 250–303. URL: http://www.sciencedirect.com/science/article/pii/S0168900203013688.

[109] The ATLAS Collaboration. “Performance of the ATLAS muon triggers in Run 2”. In: *JINST* 15.09 (2020), P09015. arXiv: 2004.13447 [physics.ins-det].

[110] The ATLAS Collaboration. “Performance of electron and photon triggers in ATLAS during LHC Run 2”. In: *Eur. Phys. J. C* 80.1 (2020), p. 47. arXiv: 1909.00761 [hep-ex].

[111] The ATLAS Collaboration. *Object-based missing transverse momentum significance in the ATLAS detector*. Tech. rep. ATLAS-CONF-2018-038. Geneva: CERN, July 2018. URL: `https://cds.cern.ch/record/2630948`.

[112] T. Aaltonen et al. "Search for anomalous production of events with two photons and additional energetic objects at CDF". In: *Physical Review D* 82.5 (Sept. 2010). URL: `http://dx.doi.org/10.1103/PhysRevD.82.052005`.

[113] The CMS Collaboration. "Missing transverse energy performance of the CMS detector". In: *Journal of Instrumentation* 6.09 (Sept. 2011), P09001–P09001. URL: `http://dx.doi.org/10.1088/1748-0221/6/09/P09001`.

[114] The CMS Collaboration. "Performance of the CMS missing transverse momentum reconstruction in pp data at $\sqrt{s} = 8\,\mathrm{TeV}$". In: *JINST* 10.02 (2015), P02006. arXiv: `1411.0511 [physics.ins-det]`.

[115] Jerzy Neyman, Egon Sharpe Pearson, and Karl Pearson. "IX. On the problem of the most efficient tests of statistical hypotheses". In: *Philosophical Transactions of the Royal Society of London. Series A, Containing Papers of a Mathematical or Physical Character* 231.694-706 (1933), pp. 289–337. eprint: `https://royalsocietypublishing.org/doi/pdf/10.1098/rsta.1933.0009`. URL: `https://royalsocietypublishing.org/doi/abs/10.1098/rsta.1933.0009`.

[116] The ATLAS collaboration. "Search for new phenomena in final states with large jet multiplicities and missing transverse momentum with ATLAS using $\sqrt{s}$=13 TeV proton–proton collisions". English. In: *Physics Letters B* 757 (June 2016), pp. 334–355.

[117] *Pursuit of new phenomena in final states with high jet multiplicity, high jet masses and missing transverse momentum with ATLAS at $\sqrt{s} = 13$ TeV*. Tech. rep. ATLAS-CONF-2016-095. Geneva: CERN, Sept. 2016. URL: `https://cds.cern.ch/record/2212161`.

[118] The ATLAS Collaboration. "Search for new phenomena with large jet multiplicities and missing transverse momentum using large-radius jets and flavour-tagging at ATLAS in 13 TeV *pp* collisions". In: *Journal of High Energy Physics* 2017.12 (Dec. 2017). URL: `http://dx.doi.org/10.1007/JHEP12(2017)034`.

[119] M. Baak et al. "HistFitter software framework for statistical data analysis". In: *The European Physical Journal C* 75.4 (Apr. 2015). URL: `http://dx.doi.org/10.1140/epjc/s10052-015-3327-7`.

[120] The ATLAS Collaboration. *Vertex Reconstruction Performance of the ATLAS Detector at $\sqrt{s} = 13$TeV*. Tech. rep. ATL-PHYS-PUB-2015-026. Geneva: CERN, Aug. 2015. URL: `https://cds.cern.ch/record/2037717`.

[121] The ATLAS Collaboration. "Performance of pile-up mitigation techniques for jets in *pp* collisions at $\sqrt{s} = 8$ TeV using the ATLAS detector". In: *The European Physical Journal C* 76.11 (Oct. 2016). URL: `http://dx.doi.org/10.1140/epjc/s10052-016-4395-z`.

[122] The ATLAS Collaboration. *Jet reclustering and close-by effects in ATLAS run II*. Tech. rep. ATLAS-CONF-2017-062. Geneva: CERN, July 2017. URL: `https://cds.cern.ch/record/2275649`.

[123] Joshua P. Ellis. "Ti k Z-Feynman: Feynman diagrams with Ti k Z". In: *Computer Physics Communications* 210 (Jan. 2017), pp. 103–123. URL: http://dx.doi.org/10.1016/j.cpc.2016.08.019.

[124] J. Alwall et al. "The automated computation of tree-level and next-to-leading order differential cross sections, and their matching to parton shower simulations". In: *Journal of High Energy Physics* 2014.7 (July 2014). URL: http://dx.doi.org/10.1007/JHEP07(2014)079.

[125] *Multijet simulation for 13 TeV ATLAS Analyses*. Tech. rep. ATL-PHYS-PUB-2019-017. Geneva: CERN, Apr. 2019. URL: https://cds.cern.ch/record/2672252.

[126] M Gell-Mann. "THE EIGHTFOLD WAY: A THEORY OF STRONG INTERACTION SYMMETRY". In: (Mar. 1961). URL: https://www.osti.gov/biblio/4008239.

[127] R. Brandelik et al. "Evidence for planar events in e+e- annihilation at high energies". In: *Physics Letters B* 86.2 (1979), pp. 243–249. URL: https://www.sciencedirect.com/science/article/pii/037026937990830X.

[128] D. P. Barber et al. "Discovery of Three Jet Events and a Test of Quantum Chromodynamics at PETRA Energies". In: *Phys. Rev. Lett.* 43 (1979), p. 830.

[129] Ch. Berger et al. "Jet analysis of the Υ(9.46) decay into charged hadrons". In: *Physics Letters B* 82.3 (1979), pp. 449–455. URL: https://www.sciencedirect.com/science/article/pii/037026937990265X.

[130] John Ellis. "The discovery of the gluon". In: *International Journal of Modern Physics A* 29.31 (Dec. 2014), p. 1430072. URL: http://dx.doi.org/10.1142/S0217751X14300725.

[131] *Quark versus Gluon Jet Tagging Using Charged Particle Multiplicity with the ATLAS Detector*. Tech. rep. ATL-PHYS-PUB-2017-009. Geneva: CERN, May 2017. URL: http://cds.cern.ch/record/2263679.

[132] Tom Cornelis. *Quark-gluon Jet Discrimination At CMS*. 2014. arXiv: 1409.3072 [hep-ex].

[133] V. N. Gribov and L. N. Lipatov. "Deep inelastic e p scattering in perturbation theory". In: *Sov. J. Nucl. Phys.* 15 (1972), pp. 438–450.

[134] Yuri L. Dokshitzer. "Calculation of the Structure Functions for Deep Inelastic Scattering and e+ e- Annihilation by Perturbation Theory in Quantum Chromodynamics." In: *Sov. Phys. JETP* 46 (1977), pp. 641–653.

[135] G. Altarelli and G. Parisi. "Asymptotic freedom in parton language". In: *Nuclear Physics B* 126.2 (1977), pp. 298–318. URL: http://www.sciencedirect.com/science/article/pii/0550321377903844.

[136] Matthew Dean Schwartz. *Quantum field theory and the standard model*. eng. Cambridge, 2014.

[137] Jeff Greensite. *An Introduction to the confinement problem [electronic resource]*. eng. Lecture notes in physics ; 821. Heidelberg ; New York: Springer, 2011.

[138] Mark Thomson. *Modern particle physics*. eng. Cambridge, 2013.

[139] The ATLAS Collaboration. “Measurements of $b-$jet tagging efficiency with the ATLAS detector using $t\bar{t}$ events at $\sqrt{\mathrm{s}} = 13\,\mathrm{TeV}$ ”. In: *Journal of High Energy Physics* 2018.8 (Aug. 2018). URL: http://dx.doi.org/10.1007/JHEP08(2018)089.

[140] Camilla Vittori. *Observation of Higgs in $b\bar{b}$ channel from ATLAS and CMS*. Tech. rep. ATL-PHYS-PROC-2019-028. Geneva: CERN, Mar. 2019. URL: https://cds.cern.ch/record/2669538.

[141] The ATLAS Collaboration. “Performance of top-quark and W-boson tagging with ATLAS in Run 2 of the LHC”. In: *The European Physical Journal C* 79.5 (Apr. 2019). URL: http://dx.doi.org/10.1140/epjc/s10052-019-6847-8.

[142] The ATLAS Collaboration. “Search for R-parity-violating supersymmetric particles in multi-jet final states produced in p–p collisions at $\sqrt{s} = 13$ TeV using the ATLAS detector at the LHC”. In: *Physics Letters B* 785 (Nov. 2018), pp. 136–158. URL: http://dx.doi.org/10.1016/j.physletb.2018.08.021.

[143] Michele Papucci, Alessandro Vichi, and Kathryn M. Zurek. “Monojet versus the rest of the world I: t-channel models”. In: *Journal of High Energy Physics* 2014.11 (Nov. 2014). URL: http://dx.doi.org/10.1007/JHEP11(2014)024.

[144] The ATLAS and CMS Collaborations. “Dark Matter benchmark models for early LHC Run-2 Searches: Report of the ATLAS/CMS Dark Matter Forum”. In: *Physics of the Dark Universe* 27 (2020), p. 100371. URL: http://www.sciencedirect.com/science/article/pii/S2212686419301712.

[145] “Performance of quark/gluon discrimination in 8 TeV pp data”. In: (Oct. 2013).

[146] Yasuhito Sakaki. “Quark jet rates and quark-gluon discrimination in multijet final states”. In: *Physical Review D* 99.11 (June 2019). URL: http://dx.doi.org/10.1103/PhysRevD.99.114012.

[147] Pierre Artoisenet et al. “Automatic spin-entangled decays of heavy resonances in Monte Carlo simulations”. In: *Journal of High Energy Physics* 2013.3 (Mar. 2013). URL: http://dx.doi.org/10.1007/JHEP03(2013)015.

[148] Richard D. Ball et al. “Parton distributions with LHC data”. In: *Nuclear Physics B* 867.2 (Feb. 2013), pp. 244–289. URL: http://dx.doi.org/10.1016/j.nuclphysb.2012.10.003.

[149] A. L. Samuel. “Some Studies in Machine Learning Using the Game of Checkers”. In: *IBM Journal of Research and Development* 3.3 (1959), pp. 210–229.

[150] Trevor Hastie, Robert Tibshirani, and Jerome Friedman. *The Elements of Statistical Learning*. Springer Series in Statistics. New York, NY, USA: Springer New York Inc., 2001. URL: https://web.stanford.edu/~hastie/ElemStatLearn/.

[151] Tom M Mitchell. *Machine learning*. eng. International edition. McGraw-Hill computer science series. New York ; London: McGraw-Hill, 1997.

[152] Alexander Radovic et al. “Machine learning at the energy and intensity frontiers of particle physics”. In: *Nature* 560 (Aug. 2018).

[153] Ian Goodfellow, Yoshua Bengio, and Aaron Courville. *Deep Learning*. http://www.deeplearningbook.org. MIT Press, 2016.

[154] Facundo Bre, Juan Gimenez, and Víctor Fachinotti. “Prediction of wind pressure coefficients on building surfaces using Artificial Neural Networks”. In: *Energy and Buildings* 158 (Nov. 2017).

[155] Tin Kam Ho. “Random decision forests”. In: *Proceedings of 3rd International Conference on Document Analysis and Recognition*. Vol. 1. 1995, 278–282 vol.1.

[156] L. Breiman et al. *Classification and Regression Trees*. Monterey, CA: Wadsworth and Brooks, 1984.

[157] Vivien Cabannes, Francis Bach, and Alessandro Rudi. *Disambiguation of weak supervision with exponential convergence rates*. 2021. arXiv: `2102.02789 [cs.LG]`.

[158] François Chollet et al. *Keras*. `https://keras.io`. 2015.

[159] F. Pedregosa et al. “Scikit-learn: Machine Learning in Python”. In: *Journal of Machine Learning Research* 12 (2011), pp. 2825–2830.

[160] Abien Fred Agarap. *Deep Learning using Rectified Linear Units (ReLU)*. 2019. arXiv: `1803.08375 [cs.NE]`.

[161] Jun Han and Claudio Moraga. “The influence of the sigmoid function parameters on the speed of backpropagation learning”. In: *From Natural to Artificial Neural Computation*. Ed. by José Mira and Francisco Sandoval. Berlin, Heidelberg: Springer Berlin Heidelberg, 1995, pp. 195–201.

[162] Lloyd S. Shapley. *Notes on the N-Person Game - II: The Value of an N-Person Game*. Santa Monica, CA: RAND Corporation, 1951.

[163] Scott M Lundberg and Su-In Lee. “A Unified Approach to Interpreting Model Predictions”. In: *Advances in Neural Information Processing Systems 30*. Ed. by I. Guyon et al. Curran Associates, Inc., 2017, pp. 4765–4774. URL: `http://papers.nips.cc/paper/7062-a-unified-approach-to-interpreting-model-predictions.pdf`.

[164] Philippe Gras et al. “Systematics of quark/gluon tagging”. In: *Journal of High Energy Physics* 2017.7 (July 2017). URL: `http://dx.doi.org/10.1007/JHEP07(2017)091`.

[165] Makoto Kobayashi and Toshihide Maskawa. “CP-Violation in the Renormalizable Theory of Weak Interaction”. In: *Progress of Theoretical Physics* 49.2 (Feb. 1973), pp. 652–657. eprint: `https://academic.oup.com/ptp/article-pdf/49/2/652/5257692/49-2-652.pdf`. URL: `https://doi.org/10.1143/PTP.49.652`.

[166] Nicola Cabibbo. “Unitary Symmetry and Leptonic Decays”. In: *Phys. Rev. Lett.* 10 (1963), pp. 531–533.

[167] F. Englert and R. Brout. “Broken Symmetry and the Mass of Gauge Vector Mesons”. In: *Phys. Rev. Lett.* 13 (9 Aug. 1964), pp. 321–323. URL: `https://link.aps.org/doi/10.1103/PhysRevLett.13.321`.

[168] Peter W. Higgs. “Broken Symmetries and the Masses of Gauge Bosons”. In: *Phys. Rev. Lett.* 13 (16 Oct. 1964), pp. 508–509. URL: `https://link.aps.org/doi/10.1103/PhysRevLett.13.508`.

[169] G. S. Guralnik, C. R. Hagen, and T. W. B. Kibble. “Global Conservation Laws and Massless Particles”. In: *Phys. Rev. Lett.* 13 (1964). Ed. by J. C. Taylor, pp. 585–587.